Faculty of Science and Engineering
School of Earth and Planetary Sciences

Development and application of atom probe tomography to complex zircon grains

Stephanie Dannett Montalvo Delgado
0000-0003-0601-2881

This thesis is presented for the Degree of
Doctor of Philosophy
of
Curtin University

March 2020

DECLARATION

To the best of my knowledge and belief this thesis contains no material previously published by any other person except where due acknowledgment has been made.

This thesis contains no material which has been accepted for the award of any other degree or diploma in any university.

Signature: _____

Date: 18/03/2020

DEDICATION

To my partner Danny Fleming.

You are an amazing person, always there to support me, even through tough times. Without you this thesis would not have been completed.

For that and much more, I thank you.

ABSTRACT

Atom probe tomography (APT) is a 3D analytical technique that provides the elemental composition of materials at sub-nanometre resolutions. Although originally developed for material science applications, recent advances in APT technology has expanded the applicability to other disciplines, including geological samples. The high spatial resolution of APT opens new avenues of geochemical studies. The few APT studies conducted on zircon have focussed on the nanogeochemistry and nanogeochronology of standards, igneous and metamorphic grains. However, the current applications of APT with zircon grains are limited with no systematic studies conducted on complex grains. This project is aimed at further developing APT techniques to zircon through the novel application of APT to meteoritic, altered and shocked zircon grains.

Microscale zircon grains from the Bunburra Rockhole meteorite were analysed using APT to better understand the origin and formation history of the meteorite. The APT geochemical results suggested a similar source melt for the different clast that made up the meteorite. This data was later used to discern between the parent body of Bunburra Rockhole and the asteroid 4 Vesta.

An altered zircon from the Lalla Rookh Sandstone formation was analysed with APT to understand the composition of the hydrothermal alteration zones. The nanogeochemistry of the grain showed a high concentration of trace elements in metamict areas, Pb clusters in crystalline areas, and it revealed a connection between the U, radiation damage and APT specimen yield. The APT data was also used to confirm the age of the metamorphic event that affected the grain.

The use of APT in shocked zircons from the Stac Fada impact structure (Scotland) provided evidence of trace element mobility associated with the zircon-to-reidite transformation. These results were used to develop a new model for the phase transformation that includes the martensitic transformation and short-range diffusion components that occurs during an impact event.

This PhD project has developed new applications for APT in the analysis of complex zircon grains and provides a basis and lessons learnt for further nanoscale geochemical and geochronological studies. The project results offer an improved understanding of how APT may be applied to certain complex grains and provides a framework for new geological applications and to other minerals.

ACKNOWLEDGEMENTS

The decision of pursuing a PhD in Earth and Planetary Sciences at Curtin University was an easy one for me. However, the path was not as easy. Along the way, I encountered unexpected ups and downs involving my PhD research and my personal life. Yet, that is how science (and life) works. Nonetheless, I stand by my decisions and, even though there were some frustrating moments, I am pleased and proud of what I have learned and accomplished throughout my PhD years.

The completion of this thesis could not have been possible without the help of the people I have met along this journey. First, I would like to thank my partner for all his support, understanding and editing help. This thesis would have been very different without his help. Secondly, I would also like to thank my mother, younger sister and stepfather for supporting my decision to move to the furthest place from them I can possibly think of. I know it was not easy for them, but they still supported me.

My supervisors Steven M. Reddy, David W. Saxey, William D. Rickard and Denis Fougerouse have provided me their guidance (scientific writing, technical instruments, general knowledge) during my PhD, which has contributed to my growth as a scientist. They gave me the opportunity to work, learn and gain experience with state-of-the-art instruments at Curtin University. The knowledge I have acquired thanks to them is invaluable and much appreciated.

I would also like to thank my co-authors and collaborators for their input and assistance in the individual case studies. They are Zakaria Quadir (Curtin Univ.), Tim E. Johnson (Curtin Univ.), Gretchen K. Benedix (Curtin Univ.), Chris Kirkland (Curtin Univ.), Thorsten Geisler (Univ. of Bonn, Germany) and Alexander G. Webb (China Univ. of Geosciences). Of course, this project relied upon the assistance and guidance of the technical staff of the John de Laeter Centre, which includes Ms Elaine Miller, Ms Kelly Merigot, Ms Veronica Avery and Mr Hao Gao.

Other professors, technical staff and PhD students provided me with additional guidance, encouragement and friendship during my PhD at Curtin University. These are Aaron Cavosie, Andrew Putnis, Nick Timms, Pete Kinny, Adam Frew, Rick Verberne, Jennifer Porter, Sonia Armandola, Cilva Joseph, Johanna Heeb, Tommaso Tacchetto, Tobias Wengorsch, Morgan Cox, Alexander Walker, Tania Hidalgo, Ellie Sansom and Timmons Erickson.

LIST OF PUBLICATIONS

- *Nanoscale constrains on the shock-induced transformation of zircon to reidite*

  Montalvo, S. D., Reddy, S. M., Saxey, D. W., Rickard, W. D. A., Fougerouse, D., Quadir, Z., and Johnson, T. E., 2019, Nanoscale constraints on the shock-induced transformation of zircon to reidite: Chemical Geology, v. 507, p. 85-95.

I warrant that I have obtained, where necessary, permission from the copyright owners to use any third-party copyright material reproduced in the thesis (e.g. artwork), or to use any of my own published works (e.g. journal articles) in which the copyright is held by another party (e.g. publishers, co-author).

TABLE OF CONTENTS

LIST OF FIGURES

LIST OF SUPPLEMENTARY FIGURES

LIST OF TABLES

LIST OF SUPPLEMENTARY TABLES

Chapter 1 INTRODUCTION AND OVERVIEW

Background

Atom probe tomography (APT) is a three-dimensional (3D) analytical technique that works through the field evaporation of ions from a nanoscale needle-shaped specimen to a position-sensitive detector, offering the chemical composition and position of each detected ion (Fig. 1.1) (Gault et al., 2012; Larson et al., 2013). Field evaporation is caused by the ionisation and desorption of surface atoms from the tip of the specimen by an electric field (Müller, 1956; Gault et al., 2012). This process is initiated by applying a high voltage to the specimen that creates an electric field close to the threshold of what is needed for the atoms to evaporate, and either voltage pulses (voltage-pulse mode) or ultra-violet (UV) laser pulses (laser-assisted mode) to the apex of the specimen. For non-conducting geological samples (e.g. zircon), the laser-assisted mode is used.

The exact mechanics of the field evaporation process for non-conducting materials remains a subject of on-going research (Miller and Forbes, 2014; Karahka and Kreuzer, 2015). Increasing the electric field reduces the energy barrier of the atoms, while increasing the temperature contributes thermal energy that allows atoms to hop over the energy barrier (Fig. 1.2) (Miller and Forbes, 2009; Gault et al. 2012). This results in the atoms transitioning to a lower energy state and detaching from the surface of the specimen. The electric field and the temperature of the specimen controls the evaporation rate of the atoms. In the voltage-pulse mode, the voltage pulses can briefly increase the electric field, while in the laser-assisted mode, the laser pulses increase the thermal energy, hence the temperature of the specimen. Once the ions are released, they are accelerated toward the detector by the electric field, which records the ions evaporation sequence and hit position (X, Y).

Aside from the physical and chemical properties of the analysed material, the APT acquisition parameters influence the yield of the specimen and the quality of the APT data. The main parameters for non-conductive samples (laser-assisted mode) are the specimen base temperature (K), the laser pulse energy (pJ), laser pulse frequency (kHz) and the targeted detection rate (ions/pulse). Larson et al. (2013) provides information on the considerations, quality of data and the trade-offs of the different parameters, and these are briefly summarised here. In the laser-assisted

mode, the specimen base temperature affects the mass resolving power (MRP) and the background noise. An increase in the base temperature would produce a better specimen yield, while a lower temperature would improve the spatial resolution. Increasing the laser pulse energy would lower the required electric field and thus the stress on the specimen, increasing the MRP and decreasing the background noise, resulting in a better specimen yield. On the other hand, a lower laser pulse energy would improve the spatial resolution. For the laser pulse frequency and the detection rate, higher values are preferred. However, if ions with a long time-of-flight (ToF, time from the pulse to the detection) are not being detected within the pulse or the sample tends to result in a low yield, these parameters are lowered. Details on the optimisation of these parameters for geological samples can be found in Reddy et al. (2020).

Besides the base temperature, the other three parameters can be readjusted during the first stages of the acquisition process. Once the acquisition process is fully automated, the software maintains the detection rate by adjusting the applied voltage on the specimen to keep the surface electric field at the threshold level. A simple formula to express the surface electric field (E) on the specimen is represented by:

$$E = {}^{V}/_{kR}$$

where V is the applied voltage, R is the radius of the tip of the specimen and k is a geometric field reduction factor constant (Gomer, 1994). As the acquisition proceeds, the radius of the tip of the specimen increases due to the removal of material, resulting in a decrease in the electric field, thus a decrease in the detection rate of the ions. Once the software detects this, it increases the applied voltage to maintain the targeted detection rate and the electric field at the threshold level. The acquisition process ends when the user-defined number of ions or the maximum voltage has been reached. Another way to end the process is by the premature fracture of the specimen, or specimen failure, due to the field-induced high stress on the tip.

After the acquisition, the data is processed and reconstructed into a 3D representation in real space (x,y,z) of the analysed volume from the specimen. The spatial reconstruction involves converting the hit position (X, Y) in the detector into real-space coordinates (x,y; lateral coordinates) with a direct reverse-projection model, producing a virtual spherical cap that represents the specimen. The depth direction (z) is determined by back projecting the sequence of evaporation of the

detected ions. Certain information of the specimen and the sample material needs to be known beforehand to obtain an accurate reconstruction (e.g. the specimen radius and the mean atomic density of the sample).

The traveling distance (flight path) and the ToF of the detected ion are used to determine its mass-to-charge ratio. The resulting histogram, or the mass spectrum, is a series of signal peaks that is later calibrated by the user to determine the identity of the single (or molecular) ions. The chemical identification process (mass spectrum ranging) requires the user to relate a peak to an ion, along with picking out the lower and upper limits of the range. Once the reconstruction process is completed, the user can investigate the composition and the structure of the specimen from the 3D image.

The use of APT has grown since its development (refer to Figure 2 in Reddy et al., 2020). APT derived from the field electron emission microscope (FEEM) was developed in 1935 by Erwin Müller (Larson et al., 2013). The technique has since evolved into what is now known as APT (Table 1.1), with the most common system being the local electrode atom probe (LEAP) (Kelly et al., 2004; Kelly and Larson, 2012; Larson et al., 2013). This type of atom probe system uses a local electrode (Fig. 1.1) to enhance and localise the electric field on the specimen, allowing field evaporation at lower voltages (Kelly et al., 1996). In addition, the introduction of the local electrode allowed for a higher mass resolution across an increased field of view and an increased data collection rate (Kelly et al., 2004; Larson et al., 2013).

The commercialisation of the laser-pulsed LEAP allowed the scientific community to analyse non-conducting geological material, resulting in an increasing development of APT in geosciences. The general technical capabilities of APT for geological samples are a mass resolving power ~1000 (the instruments ability to distinguish between two peaks), a field of view of 100x100x1000 nm, a detection limit of ~10 ppm and a high spatial resolution of ~1 nm (Fig. 1.3) (Reddy et al., 2020). APT is a technique that can analyse a small volume (< 0.02 μm^3) (Reddy et al., 2020), offering the location and identification of the atoms. In addition, APT can provide new geochemical and geochronological information that has not been previously recorded due to low resolutions of conventional techniques, small sample area (grain size) or small regions of interest (microstructures and complicated textures in the grain).

Incorporating APT into the common analytical workflow can result in the discovery of geological processes that have disturbed the grain (Valley et al., 2014;

Peterman et al., 2016; Fougerouse et al., 2019), findings of new mechanisms associated with the grains chemistry (e.g. Piazolo et al., 2016; Reddy et al., 2016; Dubosq et al., 2019; Montalvo et al., 2019; Peterman et al., 2019), or in the discovery of new micro and nanostructures (Weber et al., 2016; Cao et al., 2019) that shed light on the grain formation. For example, combining APT analysis with transmission electron microscopy (TEM) analysis has already proven useful for studying and linking the chemistry and structure of a sample (Gin et al., 2017; Rout et al., 2017; Montalvo et al., 2019; Seydoux-Guillaume et al., 2019). When these two techniques are used together, APT offers the location, chemistry and isotopic composition of the sample, while TEM offers structural information (e.g. microstructure, defects, porosity).

A series of macro and microscale investigations need to occur prior the APT nanoscale study. For example, to identify targeting areas for the APT study, techniques like scanning electron microscopy (SEM) imaging, electron backscatter diffraction (EBSD), cathodoluminescence (CL), time-of-flight secondary ion mass spectrometer (ToF-SIMS) and nanometre scale secondary ion mass spectrometer (NanoSIMS) can be used. Transmission Kikuchi diffraction (TKD) mapping on the APT specimens can offer crystallographic information, aiding in the mineral identification and providing the crystallographic misorientation of the specimen. Furthermore, APT is a destructive technique that requires a complex sample preparation. Overall, the advantages of APT surpass its limitations, which makes it an important complementary technique to conventional analytical methods conducted on geologic samples, and in the case of this project, to the characterisation of zircon ($ZrSiO_4$) grains.

Zircon is a common accessory mineral found in igneous, sedimentary and metamorphic crustal rocks. The ability of zircon to incorporate trace and rare elements, including radioactive elements, makes it a valuable geochemical repository for examining the conditions and processes of crustal evolution. Because of this, zircon grains, both natural and synthetic, have been studied extensively with several analytical techniques, including but not limited to the techniques in Fig. 1.4 (Table 1.2). Depending on the type of investigation, whether geochemical, geochronological or microstructural, various techniques with different spatial resolutions can be implemented, each containing their own advantages and limitations. Incorporating APT to the standard analytical workflow offers the possibility to analyse the

geochemistry and geochronology of a sample at the nanoscale. In addition, this information can be correlated to the micro and macroscopic features seen on the grains offering insights of the geological processes.

Table 1.1 Predecessors of atom probe instruments

FEEM *Field electron emission microscope*		Developed in 1935	E. W. Müller (Larson et al., 2013)
FIM *Field ion microscope*		1st image in 1951	E. W. Müller (Larson et al., 2013)
APFIM *Atom probe field ion microscope*	1st 1D atom probe	Developed in 1967	J. A. Panitz, S. Brooks McLane and G. L. Fowler with E. W. Müller's supervision (Müller et al., 1968)
IAP *Imaging atom probe*	3D atom probe (series of 2D maps)	Developed in 1972	J. A. Panitz (Panitz, 1973)
PLAP *Pulsed-laser atom probe*	Semiconductors could be analysed	Developed 1979	GL. Kellogg and T.T. Tsong (Kellogg and Tsong, 1980)
Mapping atom probe	3D atom probe	Developed in 1986	M. K. Miller (Miller, 1986)
PoSAP *Position sensitive atom probe*	3D atom probe	Developed in 1988	A. Cerezo, T.J. Godfrey and G.D.W. Smith (Cerezo et al., 1988)
Tomographic atom probe	3D atom probe	Developed in 1989	A Bostel, D. Blavette, A. Menand and J.M. Sarrau (Bostel et al., 1989)
SAP *Scanning atom probe*	3D atom probe	Developed in 1994	O. Nishikawa (Nishikawa and Kimoto, 1994)
LEAP *Local electrode atom probe*	3D atom probe minerals	Developed from 1993-2001 1st commercial laser-pulsed AP in 2006	Millennium Instruments/Imago Scientific Instruments (Larson et al., 2013)

Table 1.2 Historical uses of different techniques on zircon grains

Technique	classification		Year	First publication
TIMS	analytical	bulk isotopic analysis	1955	Tilton et. al, 1955, Isotopic composition and distribution of lead, Uranium, and Thorium in a Precambrian granite
XRD	analytical	bulk structural analysis	1963	Silver and Deutsch, 1963, Uranium-lead isotopic variations in zircons: a case study
EMP	analytical	chemical mapping	1964	Marvin and Klein, 1964, Meteoritic Zircon
TEM	imaging	sub-µm imaging /structural analysis	1966	Bursill and McLaren, 1966, Transmission electron microscope study of natural radiation damage in zircon (ZrSiO4)
SEM	imaging	sub-µm imaging	1974	Neves et. al, 1974, High hafnium members of the zircon-hafnon series from the granite pegmatites of Zambézia, Mozambique
Raman	analytical	chemical bonding	1970	Griffith, 1970, Raman studies on rock-forming minerals. Part II. Minerals containing MO3, MO4, and MO6 groups
CL	imaging	grain scale imaging	1976	Ono, 1976, Chemistry and zoning of zircon from some Japanese granitic rocks
SHRIMP	analytical	µm-scale isotopic analysis	1983	Compston and Williams, 1983, U-Pb Geochronology of Zircons from Breccia 73217 Using a Sensitive High Mass-Resolution Ion Microprobe (shrimp)
Analytical TEM	analytical/ mapping	sub-µm chemical /structural analysis	1992	McComb et. Al, 1992, Qualitative interpretation of electron energy-loss near-edge structure in natural zircon
LA-ICPMS	analytical	µm-scale chemistry /isotopic analysis	1993	Feng et.al 1993, Lead geochronology of zircon by LaserProbe-inductively coupled plasma mass spectrometry (LP-ICPMS)
EBSD	mapping	microstructural analysis	2005	Ma and Rossman, 2005, Microanalysis of hafnian zircon
NanoSIMS	analytical/ mapping	sub-µm chemistry /isotopic analysis	2005	Stern et. Al, 2005, Ion microprobe (NanoSIMS 50) Pb-isotope geochronology at <5µm scale
ToF-SIMS	analytical/ mapping	sub-µm chemistry /isotopic analysis	2007	Meredith, 2007, An investigation of chemical mobility and variability within a metamict zircon from the Georgeville Granite, Nova Scotia, using ToF-SIMS
APT	analytical/ mapping	sub-nm chemistry /isotopic analysis	2014	Valley et. Al, 2014, Hadean age for a post-magma-ocean zircon confirmed by atom-probe tomography
TKD	mapping	sub-µm structural analysis	2015	Reddy et al. 2015, Precambrian reidite discovered in shocked zircon from the Stac Fada impactite, Scotland

Rationale

Limited published work exists on APT studies of natural geological zircon grains (~15 thus far). The few published studies have focused on standards (reference material), igneous and metamorphic zircon grain (e.g. Valley et al., 2014; Peterman et al., 2016; Exertier et al., 2018; Saxey et al., 2018; Moser et al., 2019). A comprehensive study using APT on complex zircon grains has not been conducted.

This Ph.D. project aims to further develop the use of APT on complex zircon grains from different environments, with varying deformation characteristics and radiation damage. New applications of this technique include studying the geochemistry and geochronology of μm zircon grain from a meteorite, hydrothermal altered zones of a few microns, and phase transformations in shocked zircon grains.

Thesis structure

This thesis is composed of three individual chapters (Ch. 2-4) in the form of manuscripts for publication, and three additional chapters. Chapter 1 introduces the main points of the project, chapter 5 explores the effectiveness of APT analyses on zircon grains that have been deformed by shock metamorphism and chapter 6 concludes with the main findings of the project. The arrangement of the three main chapters is based on the complexity of the zircon grains analysed, from least to most complex grains. Chapter 4 has been published in Chemical Geology (Montalvo et al., 2019), while the other two (Ch.2,3) are nearing submission to Meteoritics and Planetary Science and Chemical Geology journals, respectively.

Chapter 2 was primarily written by the lead author of this manuscript in collaboration with Steven Reddy, Gretchen Benedix, David Saxey, William Rickard and Denis Fougerouse. The chapter focusses on the geochemistry of zircon grains from the Bunburra Rockhole meteorite. The aim of this research was to analyse micrometre zircon grains that have not been studied previously due to the spatial limitations of conventional techniques using APT. The geochemical information obtained from the grains with APT offered a more comprehensive understanding of the origin and formation of the grains and the parent body. It was also hoped that the Pb isotopic composition of the grains would provide age constraints on different meteoritic components. However, the zircon grains proved to be low in U, and therefore radiogenic Pb, and isotopic data could not be constrained.

Chapter 3 was written by the lead author of this manuscript in collaboration with Steven Reddy, David Saxey, William Rickard, Denis Fougerouse, Thorsten Geisler, Tim Johnson, Chris Kirkland and Alexander Webb. This chapter focused on an altered zircon grain from the Lalla Rookh Sandstone formation on the Pilbara Craton, Western Australia. This grain shows evidence of fluid alteration in its internal structure. APT was used to obtain the geochemistry of different regions within the convoluted textures for comparison. By combining APT with other techniques (SHRIMP, TEM, CL and SEM imaging), two events were found to have altered the grain. A crystallization age of 3.5 Ga was obtained for the grain, with a 3.3 Ga metamorphic event forming the core-rim structure and causing Pb mobility and clustering. A younger hydrothermal event is believed to have caused the convoluted textures seen in the rim, along with the enhancement of U through fractures. In addition, it was identified that the APT specimen yield was affected by the amount of radiation damage and defects the different regions contained.

Chapter 4 was written by the lead author of this manuscript in collaboration with Steven Reddy, David Saxey, William Rickard, Denis Fougerouse, Zakaria Quadir and Tim Johnson as co-authors. This chapter was published in Chemical Geology (Montalvo et al., 2019) and focused on the mechanisms and the geochemistry associated with the zircon-reidite transformation. When looking at the zircon grains with reidite lamellae, the interfaces were found to be enriched in trace elements with a heterogeneous distribution. The distribution of trace elements was found to be associated with the microstructures present at the interface (e.g. quasi-periodic structures, dislocations and amorphous features). The geochemical data obtained revealed a connection between trace element mobility to the reidite lamellae formation, which was later used to propose a new model for the transformation of zircon to reidite lamellae.

Chapter 5 was written by the lead author of this research. This chapter detailed the distribution of trace elements in shocked zircon, the limitations of several techniques for shocked zircon analysis and it summarises the recorded contribution of sample integrity on the yield of the APT specimen, with an emphasis on crystallinity, deformation and amount of radiation damage. Shocked zircon grains from the Stac Fada ejecta deposit were analysed with APT as these grains had different textures, microstructures, uranium concentration and radiation damage, proving to be the perfect sample suite for the study.

Figures

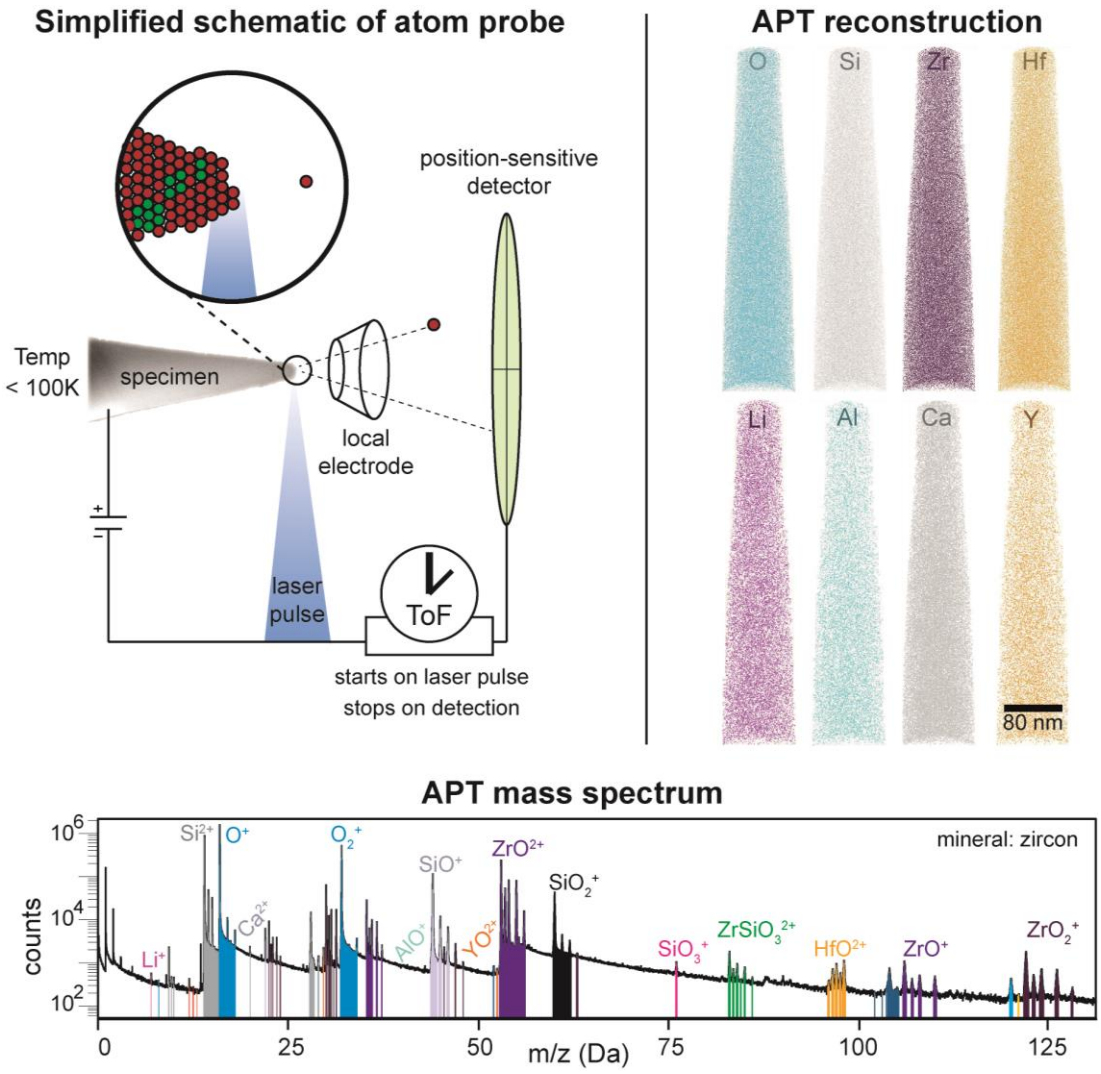

Figure 1.1 Schematic diagram of a local electrode atom probe, the mass spectrum of a zircon sample with peaks identified and 3D APT reconstructions of major and trace elements identified in the zircon sample.

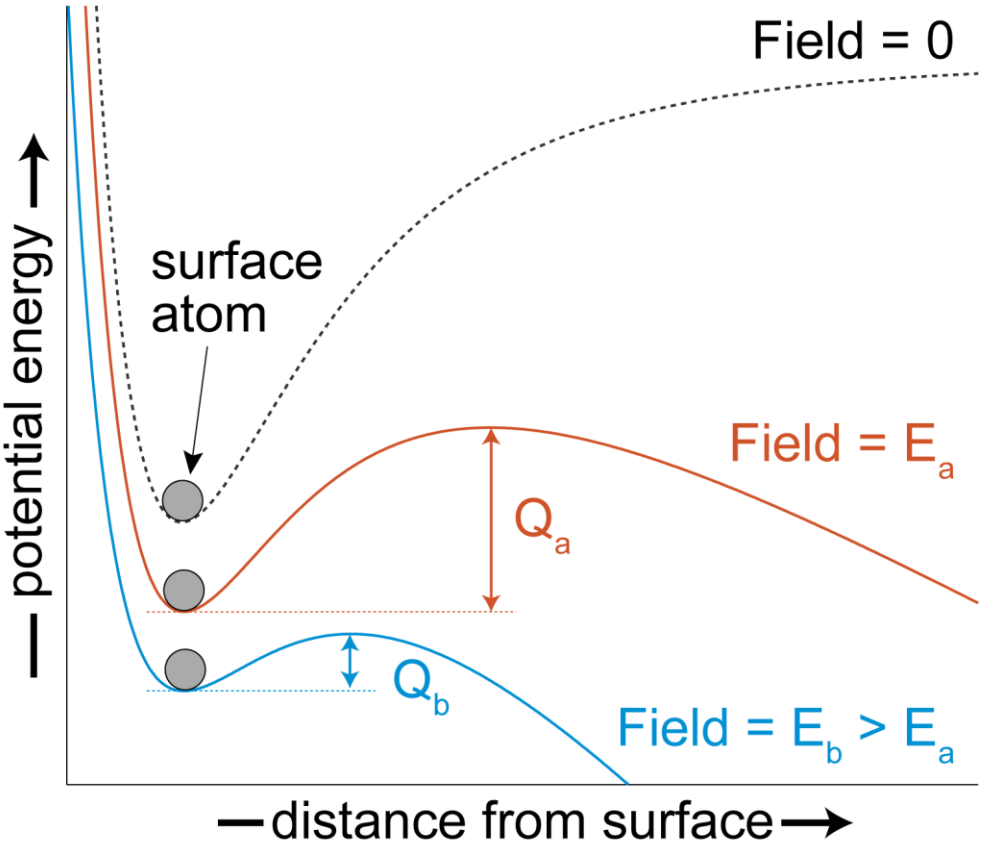

Figure 1.2 Potential energy curve diagram of an ion at the surface of the APT specimen. Dashed black line represents the energy curve when there is no electric field (E) applied, orange represents when the electric field is E_a and blue is when the electric field is E_b (higher than E_a). The energy barrier of each energy curve is depicted by Q. Modified from Reddy et al. (2020).

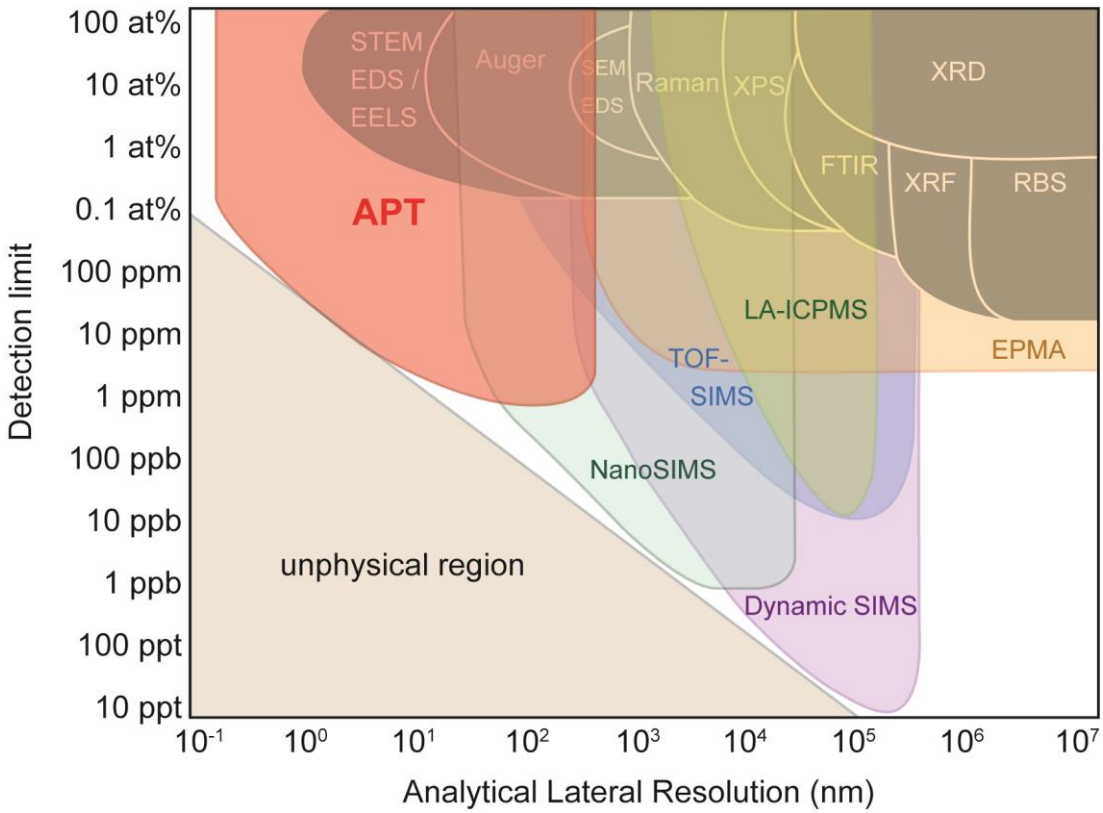

Figure 1.3 Analytical lateral resolution and the detection limit of several techniques used for geochemical and geochronological studies. Modified from Reddy et al. (2020). APT = atom probe tomography, NanoSIMS = nanometre scale secondary ion mass spectrometer, ToF-SIMS = time-of-flight secondary ion mass spectrometer, Dynamic SIMS = dynamic secondary ion mass spectrometer, LA-ICPMS = laser ablation inductively coupled plasma mass spectrometry, EPMA= electron probe micro-analyser, STEM-EDS = scanning transmission electron microscopy - energy dispersive X-ray spectroscopy, EELS = electron energy loss spectroscopy, Auger = auger electron spectroscopy, SEM EDS = scanning electron microscopy - energy dispersive X-ray spectroscopy, Raman = raman spectroscopy, XPS = X-ray photoelectron spectroscopy, FTIR = Fourier-transform infrared spectroscopy, XRF = energy dispersive X-ray fluorescence spectroscopy, and RBS = Rutherford backscattering spectrometry.

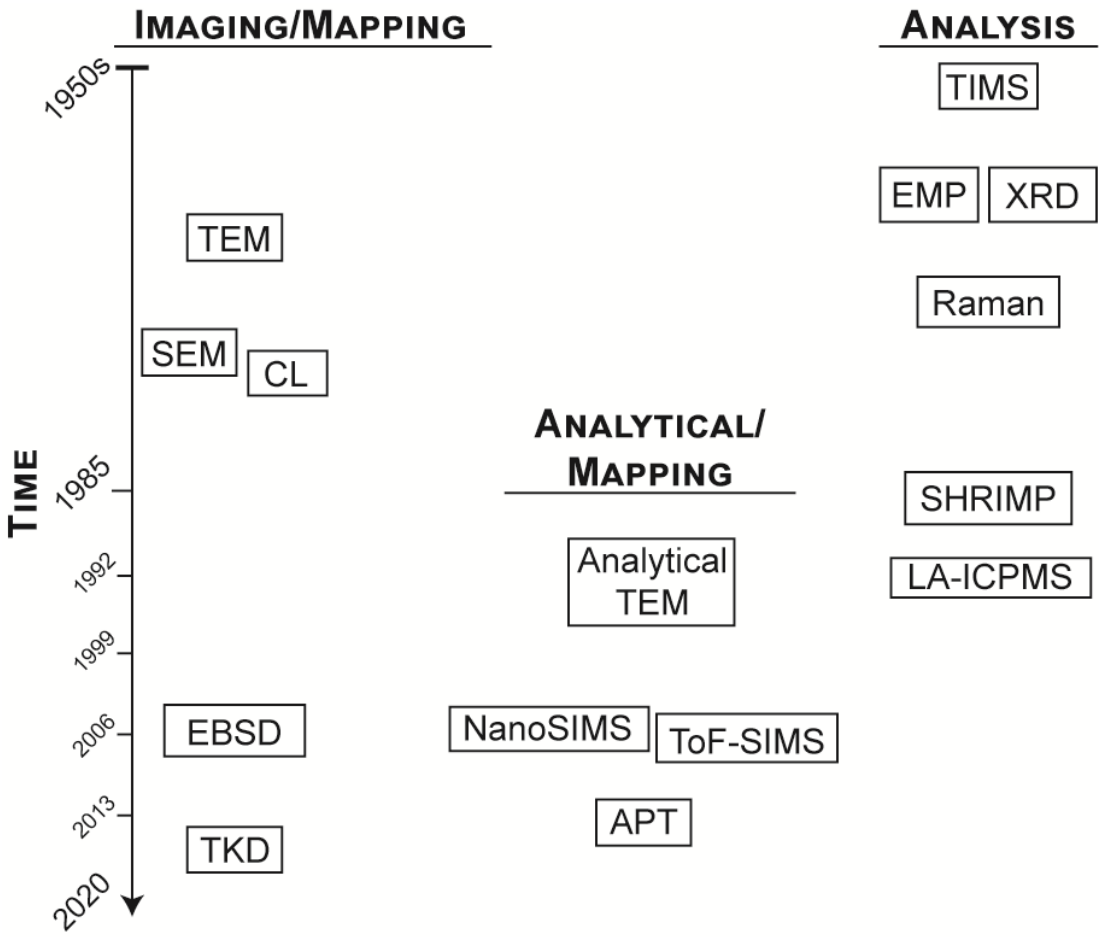

Figure 1.4 Outline of some of the imaging, mapping and analytical techniques commonly used in zircon studies. The techniques are arranged by the approximate time they were first used to study zircon grains. Details are in Table 1.2.

References

Bostel, A., Blavette, D., Menand, A., and Sarrau, J. M., 1989, Toward a tomographic atom-probe: J. Phys. Colloques, v. 50, no. C8, p. C8-501-C508-506.

Bursill, L. A., and McLaren, A. C., 1966, Transmission Electron Microscope Study of Natural Radiation Damage in Zircon (ZrSiO4): physica status solidi (b), v. 13, no. 2, p. 331-343.

Cao, M., Evans, N. J., Reddy, S. M., Fougerouse, D., Hollings, P., Saxey, D. W., McInnes, B. I. A., Cooke, D. R., McDonald, B. J., and Qin, K., 2019, Micro- and nano-scale textural and compositional zonation in plagioclase at the Black Mountain porphyry Cu deposit: Implications for magmatic processes: American Mineralogist, v. 104, no. 3, p. 391-402.

Cerezo, A., Godfrey, T. J., and Smith, G. D. W., 1988, Application of a position-sensitive detector to atom probe microanalysis: Review of Scientific Instruments, v. 59, no. 6, p. 862-866.

Compston, W., and Williams, I. S., 1983, U-Pb Geochronology of Zircons from Breccia 73217 Using a Sensitive High Mass-Resolution Ion Microprobe (shrimp), Lunar and Planetary Science Conference, p. 130.

Dubosq, R., Rogowitz, A., Schweinar, K., Gault, B., and Schneider, D. A., 2019, A 2D and 3D nanostructural study of naturally deformed pyrite: assessing the links between trace element mobility and defect structures: Contributions to Mineralogy and Petrology, v. 174, no. 9, p. 72.

Exertier, F., La Fontaine, A., Corcoran, C., Piazolo, S., Belousova, E., Peng, Z., Gault, B., Saxey, D. W., Fougerouse, D., Reddy, S. M., Pedrazzini, S., Bagot, P. A. J., Moody, M. P., Langelier, B., Moser, D. E., Botton, G. A., Vogel, F., Thompson, G. B., Blanchard, P. T., Chiaramonti, A. N., Reinhard, D. A., Rice, K. P., Schreiber, D. K., Kruska, K., Wang, J., and Cairney, J. M., 2018, Atom probe tomography analysis of the reference zircon gj-1: An interlaboratory study: Chemical Geology, v. 495, p. 27-35.

Feng, R., Machado, N., and Ludden, J., 1993, Lead geochronology of zircon by LaserProbe-inductively coupled plasma mass spectrometry (LP-ICPMS): Geochimica et Cosmochimica Acta, v. 57, no. 14, p. 3479-3486.

Fougerouse, D., Reddy, S. M., Kirkland, C. L., Saxey, D. W., Rickard, W. D., and Hough, R. M., 2019, Time-resolved, defect-hosted, trace element mobility in deformed Witwatersrand pyrite: Geoscience Frontiers, p. 55-63.

Gault, B., Moody, M. P., Cairney, J. M., and Ringer, S. P., 2012, Atom Probe Microscopy: New York, Springer, p. 396.

Gin, S., Jollivet, P., Barba Rossa, G., Tribet, M., Mougnaud, S., Collin, M., Fournier, M., Cadel, E., Cabie, M., and Dupuy, L., 2017, Atom-Probe Tomography, TEM and ToF-SIMS study of borosilicate glass alteration rim: A multiscale approach to investigating rate-limiting mechanisms: Geochimica et Cosmochimica Acta, v. 202, p. 57-76.

Gomer, R., 1994, Field emission, field ionization, and field desorption: Surface Science, v. 299-300, p. 129-152.

Griffith, W. P., 1970, Raman studies on rock-forming minerals. Part II. Minerals containing MO3, MO4, and MO6 groups: Journal of the Chemical Society A: Inorganic, Physical, Theoretical, no. 0, p. 286-291.

Karahka, M., and Kreuzer, H. J., 2015, Field evaporation of insulators and semiconductors: Theoretical insights for ZnO: Ultramicroscopy, v. 159, p. 156-161.

Kellogg, G. L., and Tsong, T. T., 1980, Pulsed-laser atom-probe field-ion microscopy: Journal of Applied Physics, v. 51, no. 2, p. 1184-1193.
Kelly, T. F., Camus, P. P., Larson, D. J., Holzman, L. M., and Bajikar, S. S., 1996, On the many advantages of local-electrode atom probes: Ultramicroscopy, v. 62, no. 1, p. 29-42.
Kelly, T. F., Gribb, T. T., Olson, J. D., Martens, R. L., Shepard, J. D., Wiener, S. A., Kunicki, T. C., Ulfig, R. M., Lenz, D. R., Strennen, E. M., Oltman, E., Bunton, J. H., and Strait, D. R., 2004, First data from a commercial local electrode atom probe (LEAP): Microscopy and Microanalysis, v. 10, no. 3, p. 373-383.
Kelly, T. F., and Larson, D. J., 2012, Atom Probe Tomography 2012: Annual Review of Materials Research, v. 42, no. 1, p. 1-31.
Larson, D. J., Prosa, T. J., Ulfig, R. M., Geiser, B. P., and Kelly, T. F., 2013, Local Electrode Atom Probe Tomography: A user's guide: New York, Springer, p. 318.
Ma, C., and Rossman, G. R., 2005, Microanalysis of Hafnian Zircon: Microscopy and Microanalysis, v. 11, no. S02, p. 1304-1305.
Marvin, U. B., and Klein, C., 1964, Meteoritic Zircon: Science, v. 146, no. 3646, p. 919-920.
McComb, D. W., Brydson, R., Hansen, P. L., and Payne, R. S., 1992, Qualitative interpretation of electron energy-loss near-edge structure in natural zircon: Journal of Physics: Condensed Matter, v. 4, no. 43, p. 8363-8374.
Meredith, P., 2007, An investigation of chemical mobility and variability within a metamict zircon from the Georgeville Granite, Nova Scotia, using ToF-SIMS, Atlantic Universities Geological Conference, Volume 43, Atlantic Geology, p. 117-118.
Miller, M. K., 1986, Atom probe field ion microscopy, Annual joint meeting of the Electron Microscopy Society of America and the Microbeam Analysis Society: Albuquerque, NM (USA)
Miller, M. K., and Forbes, R. G., 2009, Atom probe tomography: Materials Characterization, v. 60, no. 6, p. 461-469.
Miller, M. K., and Forbes, R. G., 2014, Atom-probe tomography: The local electrode atom probe: New York, Springer, p. 423.
Montalvo, S. D., Reddy, S. M., Saxey, D. W., Rickard, W. D. A., Fougerouse, D., Quadir, Z., and Johnson, T. E., 2019, Nanoscale constraints on the shock-induced transformation of zircon to reidite: Chemical Geology, v. 507, p. 85-95.
Moser, D. E., Arcuri, G. A., Reinhard, D. A., White, L. F., Darling, J. R., Barker, I. R., Larson, D. J., Irving, A. J., McCubbin, F. M., Tait, K. T., Roszjar, J., Wittmann, A., and Davis, C., 2019, Decline of giant impacts on Mars by 4.48 billion years ago and an early opportunity for habitability: Nature Geoscience, v. 12, no. 7, p. 522-527.
Müller, E. W., 1956, Field Desorption: Physical Review, v. 102, no. 3, p. 618-624.
Müller, E. W., Panitz, J. A., and McLane, S. B., 1968, The Atom-Probe Field Ion Microscope: Review of Scientific Instruments, v. 39, no. 1, p. 83-86.
Neves, J. M. C., Nunes, J. E. L., and Sahama, T. G., 1974, High hafnium members of the zircon-hafnon series from the granite pegmatites of Zambézia, Mozambique: Contributions to Mineralogy and Petrology, v. 48, no. 1, p. 73-80.

Nishikawa, O., and Kimoto, M., 1994, Toward a scanning atom probe — computer simulation of electric field: Applied Surface Science, v. 76-77, p. 424-430.
Ono, A., 1976, Chemistry and zoning of zircon from some Japanese granitic rocks: The Journal of the Japanese Association of Mineralogists, Petrologists and Economic Geologists, v. 71, no. 1, p. 6-17.
Panitz, J. A., 1973, The 10 cm Atom Probe: Review of Scientific Instruments, v. 44, no. 8, p. 1034-1038.
Peterman, E. M., Reddy, S. M., Saxey, D. W., Fougerouse, D., Snoeyenbos, D. R., and Rickard, W. D. A., 2019, Nanoscale processes of trace element mobility in metamorphosed zircon: Contributions to Mineralogy and Petrology, v. 174, no. 11, p. 92.
Peterman, E. M., Reddy, S. M., Saxey, D. W., Snoeyenbos, D. R., Rickard, W. D. A., Fougerouse, D., and Kylander-Clark, A. R. C., 2016, Nanogeochronology of discordant zircon measured by atom probe microscopy of Pb-enriched dislocation loops: Science Advances, v. 2, p. 9.
Piazolo, S., La Fontaine, A., Trimby, P., Harley, S., Yang, L., Armstrong, R., and Cairney, J. M., 2016, Deformation-induced trace element redistribution in zircon revealed using atom probe tomography: Nature Communications, p. 7.
Reddy, S. M., Johnson, T. E., Fischer, S., Rickard, W. D. A., and Taylor, R. J. M., 2015, Precambrian reidite discovered in shocked zircon from the Stac Fada impactite, Scotland: Geology, v. 43, no. 10, p. 899-902.
Reddy, S. M., Saxey, D. W., Rickard, W. D. A., Fougerouse, D., Montalvo, S. D., Verberne, R., and van Riessen, A., 2020, Atom probe tomography: development and application to the geosciences: Geostandards and Geoanalytical Research, v. 44, no.1, p. 5-50.
Reddy, S. M., van Riessen, A., Saxey, D. W., Johnson, T. E., Rickard, W. D. A., Fougerouse, D., Fischer, S., Prosa, T. J., Rice, K. P., Reinhard, D. A., Chen, Y., and Olson, D., 2016, Mechanisms of deformation-induced trace element migration in zircon resolved by atom probe and correlative microscopy: Geochimica et Cosmochimica Acta, v. 195, p. 158-170.
Rout, S. S., Heck, P. R., Isheim, D., Stephan, T., Zaluzec, N. J., Miller, D. J., Davis, A. M., and Seidman, D. N., 2017, Atom-probe tomography and transmission electron microscopy of the kamacite–taenite interface in the fast-cooled Bristol IVA iron meteorite: Meteoritics & Planetary Science, v. 52, no. 12, p. 2707-2729.
Saxey, D. W., Reddy, S. M., Fougerouse, D., and Rickard, W. D. A., 2018, The Optimization of Zircon Analyses by Laser-Assisted Atom Probe Microscopy: Insights from the 91500 Zircon Standard, *in* Moser, D. E., Corfu, F., Darling, J. R., Reddy, S. M., and Tait, K., eds., Microstructural Geochronology: Planetary Records down to Atom Scale, American Geophysical Union & John Wiley and Sons, Inc., p. 293-313.
Seydoux-Guillaume, A. M., Fougerouse, D., Laurent, A. T., Gardés, E., Reddy, S. M., and Saxey, D. W., 2019, Nanoscale resetting of the Th/Pb system in an isotopically-closed monazite grain: A combined atom probe and transmission electron microscopy study: Geoscience Frontiers, v. 10, no. 1, p. 65-76.
Silver, L. T., and Deutsch, S., 1963, Uranium-Lead Isotopic Variations in Zircons: A Case Study: The Journal of Geology, v. 71, no. 6, p. 721-758.
Stern, R. A., Fletcher, I. R., Rasmussen, B., McNaughton, N. J., and Griffin, B. J., 2005, Ion microprobe (NanoSIMS 50) Pb-isotope geochronology at <5μm scale: International Journal of Mass Spectrometry, v. 244, no. 2, p. 125-134.

Tilton, G. R., Patterson, C., Brown, H., Inghram, M., Hayden, R., Hess, D., and Larsen, A. J., 1955, Isotopic composition and distribution of lead, Uranium, and Thorium in a Precambrian granite: GSA Bulletin, v. 66, no. 9, p. 1131-1148.

Valley, J. W., Cavosie, A. J., Ushikubo, T., Reinhard, D. A., Lawrence, D. F., Larson, D. J., Clifton, P. H., Kelly, T. F., Wilde, S. A., Moser, D. E., and Spicuzza, M. J., 2014, Hadean age for a post-magma-ocean zircon confirmed by atom-probe tomography: Nature Geoscience, v. 7, no. 3, p. 219-223.

Weber, J., Barthel, J., Brandt, F., Klinkenberg, M., Breuer, U., Kruth, M., and Bosbach, D., 2016, Nano-structural features of barite crystals observed by electron microscopy and atom probe tomography: Chemical Geology, v. 424, p. 51-59.

Chapter 2 TRACE ELEMENT ANALYSIS OF MICROMETRE-SCALE ZIRCONS IN BUNBURRA ROCKHOLE METEORITE FROM ATOM PROBE TOMOGRAPHY

This chapter is nearing submission to the Meteoritics and Planetary Science journal.

The principal roles of each co-author are as follows:

Stephanie D. Montalvo: Concept and design of the work; sample preparation; data acquisition, analysis and interpretation (SE, BSE, EBSD, APT); manuscript writing and editing.

Steven M. Reddy: Concept and design of the work; data acquisition, analysis and interpretation (EBSD); manuscript editing.

David W. Saxey: Concept and design of the work; analysis and interpretation of APT data; manuscript editing.

William D.A. Rickard: Data analysis and interpretation; manuscript editing.

Denis Fougerouse: Data analysis and interpretation; manuscript editing.

Gretchen K. Benedix: Concept and design of the work; analysis and interpretation of geochemical data; manuscript editing.

Trace element analysis of micrometre-scale zircons in Bunburra Rockhole meteorite from atom probe tomography

Stephanie D. Montalvo[a,b,*], Steven M. Reddy[a,b], Gretchen K. Benedix[b,c], David W. Saxey[a], William D.A. Rickard[a], and Denis Fougerouse[a,b]

[a] Geoscience Atom Probe, John de Laeter Centre, Curtin University, Perth, Australia.
[b] School of Earth and Planetary Science, Curtin University, Perth, Australia.
[c] Dept. of Earth and Planetary Science, Western Australia Museum, Perth, Australia.
* Email: s.montalvo@postgrad.curtin.edu.au

Abstract

The Bunburra Rockhole meteorite is a brecciated, basaltic achondrite originally classified as a eucrite derived from the asteroid 4 Vesta. It comprises three distinct textural domains defined by grain size variations. The domains have similar mineralogy comprising plagioclase and pyroxene as the major phases, with minor amounts of silica, sulfides, ilmenite, chromite, phosphates and zircon. To date, detailed geochemical analysis of the zircons has been hindered by the difficulty in analysing micrometre-scale size grains with conventional techniques. This study uses atom probe tomography, a technique capable of nanoscale geochemical analyses, to characterise the trace element compositions of individual zircon grains from the meteorite to better understand the formation and evolution of the parent body. The exclusive, high precision chemical analysis of these zircon grains has enabled for the first time their provenance to be studied and compared to other extra-terrestrial bodies. The results suggest the zircon grains from each textural domain came from a similar source melt, with a comparable trace element distribution to eucrite zircon grains. However, the Y/P ratio differed to eucrites, supporting earlier speculations that Bunburra Rockhole was not derived from the asteroid 4 Vesta.

Keywords: zircon, Bunburra Rockhole meteorite, atom probe tomography

Introduction

Zircon ($ZrSiO_4$) is an accessory mineral used in meteoritic studies for retrieving information on the conditions of the early solar system that would otherwise be difficult to obtain. Some examples include calculating formation ages, understanding the evolutionary history of regolith and meteorites, constraining the thermal history of their sources, and further defining the initial isotopic composition of the solar system (e.g. Ireland and Wlotzka, 1992; Misawa et al., 2005; Moser et al., 2013; Haba et al., 2014; Roszjar et al., 2014; Iizuka et al., 2015; Bouvier et al., 2018). However, zircon grains are generally rare in extra-terrestrial materials due to the low concentrations of Zr in the solar system, with chondrites containing on average, less than 8 ppm Zr (Marvin and Klein, 1964; Anders and Grevesse, 1989; Lodders, 2003; Münker et al., 2003). In basaltic eucrites, which have the highest concentration of Zr (up to 65 ppm), the common grain size of zircon grains is only a few microns (e.g. < 10 μm in Roszjar et al., 2014).

The Bunburra Rockhole meteorite was recovered from the Nullarbor Desert in Australia as the first sample recovered by the Desert Fireball Network (Bland et al., 2009). The recovered mass was 324 g, with an estimated original mass of 22 kg (Bland et al., 2009; Weisberg et al., 2009). The meteorite is a brecciated, basaltic achondrite that consists of anorthitic plagioclase and clinopyroxene, with minor amounts of silica, and traces of sulphides, phosphates, ilmenite, chromite and zircon (Bland et al., 2009; Jourdan et al., 2014; Spivak-Birndorf et al., 2015). Previous studies have identified three distinct textural domains based on grain-size and these are referred to as fine-grained (FG), medium-grained (MG), and coarse-grained (CG) domains (Bland et al., 2009; Spivak-Birndorf et al., 2015; Benedix et al., 2017). In general, the MG and CG domains have a subophitic texture, while the FG inclusions can be subophitic or granoblastic in nature (Spivak-Birndorf et al., 2015).

Based on its texture and composition, the Bunburra Rockhole meteorite was originally classified as a eucrite (Weisberg et al., 2009), a Ca-rich pyroxene-plagioclase achondrite that belongs to the howardite, eucrite, and diogenite meteorite grouping (collectively called HED). HED meteorites are considered to originated from the asteroid 4 Vesta (Binzel and Shui, 1993; Takeda, 1997; McSween, 1999; Hutchison, 2006; McSween Jr et al., 2013). However, the inferred orbital trajectory of the Bunburra Rockhole parent body is an Aten-type asteroid orbit with semimajor

axes of < 1 AU (Bland et al., 2009; Spurný et al., 2012). This contrast the 2.15 and 2.57 AU semimajor axes of asteroid 4 Vesta (Rayman and Mase, 2014), placing the entire orbit of 4 Vesta within the main asteroid belt and well outside the Bunburra Rockhole parent body orbit. In addition, the oxygen isotope ratio of Bunburra Rockhole ($\Delta^{17}O = –0.112 \pm 0.042‰$, 2σ) (Bland et al., 2009; Benedix et al., 2017) falls out of the HED parent body fractionation line ($\Delta^{17}O = –0.242 \pm 0.016‰$, 2σ) (Scott et al., 2009), and $\varepsilon^{54}Cr$ values (–0.37 ± 0.11 and –0.35 ± 0.08) (Benedix et al., 2017) also diverge from eucritic compositions (–0.72 ± 0.02) (Trinquier et al., 2007).

A $^{26}Al/^{26}Mg$ age of 4565 ± 0.7 Ma, obtained from pyroxenes and plagioclases within the CG domain is believed to represent the extraction age of the parent melt of Bunburra Rockhole from a chondritic reservoir (Spivak-Birndorf et al., 2015). Disturbances of Mg and Pb isotopes have been interpreted to reflect an impact-related thermal event at 4102 ± 24 Ma (Spivak-Birndorf et al., 2015). Argon isotope data collected from whole rock chip fragments (~250 µm in diameter) of the FG and CG domains record a further range of younger ages (3640 ± 21, 3544 ± 26, and 3419 ± 23 Ma) that have been interpreted to represent the effects of various impacts on the parent rock. These impact events are considered to be responsible for juxtaposing the different textural components of Bunburra Rockhole and welding them together (brecciation event) (Jourdan et al., 2014). A cosmic-ray exposure age of ~22 Ma calculated from ^{38}Ar concentrations in Bunburra Rockhole is inferred to represent the time of launch of the meteoritic material from the parent body (Welten et al., 2012; Jourdan et al., 2014).

Despite the work so far undertaken on Bunburra Rockhole meteorite, zircon grains reported within the different domains of the meteorite have not been studied (Benedix et al., 2017). In part, this reflects the difficulties in analysing micrometre-scale zircon grains with geochemical techniques that typically have much larger analytical volumes than the analysed grains. In this study, atom probe tomography (APT), a technique in which specific sub-μm^3 volumes can be extracted and precisely analysed, is used to analyse the trace element composition of micrometre-scale zircon grains from the different textural domains of the meteorite. The aim of this study is to obtain and compare the chemistry of zircon grains from each textural domain and to determine the differences with zircon compositions derived from eucrite samples reported in the literature. The results provide further constraints on

the formation and evolution of the parent meteorite and illustrate the potential for nanoscale analyses of meteoritic materials by APT.

Methods

The polished petrographic thin section, previously studied by Spivak-Birndorf et al. (2015), and containing the three, previously described textural domains (Fig. 2.1) was used in this study. The thin section was polished 60 nm colloidal silica, cleaned and sputter-coated with a 3 nm layer of carbon. A Tescan MIRA3 Field Emission Scanning Electron Microscope (FESEM) housed at the Microscopy and Microanalysis Facility of the John de Laeter Research Centre, Curtin University was used for sample characterisation prior to atom probe analysis.

Secondary electron (SE) and backscatter electron (BSE) imaging was undertaken using an acceleration voltage of 10-15 kV, a working distance of 15-20 mm and a beam current of ~0.8 nA. Microstructural and compositional analyses were undertaken using Oxford Instruments electron backscatter diffraction (EBSD) and energy dispersive X-ray spectroscopy (EDS) detectors. EBSD data was collected with a Nordlys Nano high resolution detector using an accelerating voltage of 20 kV, 20 mm working distance, 70º specimen tilt, and a beam current of 0.5 nA. EBSD data were acquired and processed using Oxford Instruments AZtec 3.3 and Channel5 software, respectively. The EBSD maps were collected with a range of step sizes (50 nm – 5 µm), with up to 760,000 electron backscatter patterns per map. The post-processed data were noise reduced using standard zero solution and wildspike corrections. EDS data was collected simultaneously with EBSD data using the same acquisition parameters as EBSD.

Zircon grains were located using the Oxford Instruments Feature module within Oxford Instruments INCA Suit 5.05 software housed on the MIRA 3 FESEM. This module thresholds the BSE signal to identify mineral grains with high atomic number contrasts and then utilises EDS to analyse and identify the major element composition of the grains. For each identified zircon grain, feature analysis provided the location and area within the analysed thin section with a spatial resolution of 0.5 µm. The number of zircon grains per domain area was calculated by dividing the number of zircon grains obtained from each domain by the respective domain surface area (number/area) for comparison.

Five zircon grains were selected for APT analysis based on their characteristics and representation of each domain (Table 2.1). To enable reproducibility to be assessed, the largest grains were selected for analysis so that multiple APT specimens could be prepared from the same grain. The five selected zircon grains included three from the FG domain (two from the subophitic region and one from the granoblastic), one from MG, and one from CG domain.

Table 2.1 Summary of the zircon grains analysed for APT.

	Zircon 1	***Zircon 2[a]***	***Zircon 3***	***Zircon 4***	***Zircon 5***
Region	FG (subophitic)	FG (subophitic)	FG (granoblastic)	MG	CG
Grain form	anhedral	anhedral	subhedral	subhedral	anhedral
Surrounded	qz, pl	cpx, pl	cpx, pl, ilm	cpx, pl	qz, pl
Length (µm)[b]	8.5	2.7 - 2.2	11.6	14	7.4
Misorientation (°)	< 5	< 3[c]	< 4	< 10	< 5
#AP specimens [d]	2	4	5	5	3
#AP specimens used [e]	1	1	5	2	1

[a] *Zircon 2 consist of four ~2.5 µm zircon grains.*
[b] *Measured along the longest axis.*
[c] *Misorientation of each individual grain.*
[d] *Total number of specimens manufactured.*
[e] *Total number of specimens that yielded data (> 1.5 M ions).*

A Tescan Lyra3 Ga^+ Focused Ion Beam Scanning Electron Microscope (FIB-SEM) was used to prepare APT specimens from characterised zircon grains. To protect the surface of the sample, a ~200 nm thick platinum strip was ion beam-deposited *in-situ* over the region of interest. Triangular prisms of ~10 µm length and 2.5 µm height were milled from each grain using a Ga^+ ion beam operated at 30 kV. From each grain, the resulting prism was lifted out of the sample using a nanomanipulator and was welded to a prefabricated silicon post. The triangular prism was then cut to leave a specimen of zircon on the silicon post. The welding and cutting process was repeated until the prism was used up. Finally, wedge segments on each of the posts were shaped in the FIB-SEM to obtain needle-shaped specimens of < 100 nm diameter at the tip. This process uses a series of annular milling steps, including a final low voltage polishing stage (5 kV accelerating voltage) to remove the high beam energy damaged region.

APT analysis was undertaken on a Cameca LEAP 4000X HR at the Geoscience Atom Probe Facility at Curtin University. APT utilises field evaporation

of atoms to determine the elemental and isotopic composition of the specimens in three dimension (3D) at sub-nanometre resolutions (Kelly and Larson, 2012). A high voltage is applied to the needle-shaped specimen and an ultraviolet (355 nm in wavelength) short laser pulse (<10 picoseconds) is used to initiate field evaporation of ions from the tip of the specimen. The released ions are accelerated by an electric field towards a position sensitive detector (distance of ~382 mm) recording the position and the timing of each detected ion. The time-of-flight (ToF) of the ion, from the start of the laser pulse to the time of impact with the detector, is used to identify the ion or molecular species being evaporated. In this study, the APT specimens were run at a base temperature of 60 – 80 K, using a laser pulse energy of 300 – 400 pJ, a pulse frequency of 200 – 250 kHz, and an average detection rate of 0.005 – 0.006 ions/pulse. The APT acquisition parameters used for each specimen in this study are summarised in Suppl. Table 2.1, after Blum et al. (2018), and they follow the optimisation parameters for zircon APT analyses by Saxey et al. (2018a). A detailed explanation of the technique and its application to geological materials is given by Reddy et al. (2020).

The reconstruction and analysis of the APT data was undertaken using the Cameca Integrated Visualization & Analysis Software (IVAS) 3.8.0. The APT data was first bowl and voltage corrected for aberrations using the major oxygen peak at 16 dalton (Da). Calibration of each mass spectrum was done using 9 – 12 peaks (14, 16, 22.5, 28, 32, 44, 53, 60, 83, 98, 106 and 121 Da). The mass resolving power (FWHM) based on the O_2^+ peak was typically between 981 – 1055. The background noise recorded was between 23 – 68 ppm/ns. The assumed evaporation field was 32 V/nm (Saxey et al., 2019) with a field factor k = 3.3 and an average atomic volume for zircon of 0.01076 nm^3 (Suppl. Table 2.1).

Given the ToF mass analyser used in APT, one of the outputs is a mass spectrum that contains peaks made from the ion signal and background noise. Manual chemical identification and ranging of the peaks involved associating the peak to a known ion, followed by selecting the lower and upper mass limits of the peaks. The limits of the ranged ions were chosen based on the signal-to-noise ratio with the goal of including most of the signal while minimizing the background noise. In the mass spectrum, the ions were seen in different charge states, as individual, molecular ions or both. Details of these procedures are given in Larson et al. (2013).

To study the chemical composition of the zircon grains, the bulk compositions (and uncertainties) of each specimen were obtained from the ranged mass spectra. This was achieved within the IVAS software by performing a background correction on the counts within each defined range of the entire dataset. The uncertainties were calculated by the software using counting statistics (Poissonian), based on the number of background-corrected counts.

In order to better interpret the zircon grains of the Bunburra Rockhole meteorite in an extra-terrestrial context, the APT results from this study were compared with the results of zircon grains in eucrites from Misawa et al. (2005) (sensitive high-resolution ion microprobe), Haba et al. (2014) (electron microprobe analyser and sensitive high-resolution ion microprobe), and Roszjar et al. (2014) (electron probe micro analyser and secondary ion mass spectrometry). To achieve a comparison between the different techniques, the results from the other studies were converted from oxide weight percent to atomic percent (normalized to the number of oxides).

Results

Petrographic analysis

The Bunburra Rockhole meteorite sample comprises three different textural domains defined by variations in the grain size of the major rock forming minerals (Fig. 2.1 and Suppl. Fig. 2.1). The surface area in the field of view varies between each domain classification, with the FG domain covering 41.6% (9996.3 mm^2/24055.2 mm^2) of the total sample area, the MG covering 34.5% (8304.3 mm^2/24055.2 mm^2), and the CG domain with 23.9% (5754.6 mm^2/24055.2 mm^2). Each domain has a similar mineral assemblage comprising augite, anorthite and enstatite, with minor to trace amounts of quartz, chromite, ilmenite, zircon, pyrrhotite and forsterite (Fig 2.2). The modes of each of the rock-forming minerals, estimated in two dimensions from the grain area in pixels, is similar across the different domains with the highest percentage belonging to augite (FG: 69.8%, MG: 59.8%, CG: 45.5%) followed by anorthite (FG: 24.3%, MG: 28.4%, CG: 32.5%), enstatite (FG: 3.2%, MG: 10.8%, CG: 18.6%) and quartz (FG: 2.3%, MG: 0.5%, CG: 3%). However, the modal distribution in the FG domain differs between the two textures,

where the granoblastic area has more quartz (3.1%) than enstatite (1.2%), while the subophitic has more enstatite (5.9%) than quartz (1.2%).

Texturally, the FG domain comprises regions dominated by subophitic (labelled FGs) or granoblastic (labelled FGg) textures (Figs. 2.2a,b and Suppl. Fig. 2.1). Distinct, large, anhedral to subhedral crystals of pyroxene and plagioclase are present within the FG domain, with pyroxene (opx) being the largest (~1.7 mm) and most identified in the FGs. Both the MG and CG domains record subophitic textures. However, in the 2D thin section, small portions of the FG domain were visible within the other two domains. Maskelynite was identified along some of the domain boundaries and fractures were found crosscutting all domains with no preferred orientation nor through a specific domain or mineral (Figs. 2.1-2.2).

Thresholding of high backscatter signal combined with EDS analysis led to the identification of 628 zircon grains within the sample (Fig. 2.3 and Suppl. Fig. 2.2). The zircon grains sizes (measured along the longest axis) for the FG domain reach up to 12.8 µm with aspect ratios ranging from 1:1 – 1:4. For the MG domain, the largest size measure is 14.1 µm with aspect ratios of 1:1 – 1:4, while for the CG domain is 13 µm with aspect ratios ranging from 1:1 – 1:3. The size distribution is similar within the domains (Fig. 2.3), with an average size of 3.3 µm for FG, 3.7 µm for MG, and 3.2 µm for CG.

From the 628 zircon grains identified, 360 grains were found in the FG domain, 182 in the MG domain and 86 in the CG domain. The FG domain has the highest calculated number of zircon grains per area (0.036 mm^{-2}), followed by the MG domain (0.022 mm^{-2}), and then the CG domain (0.015 mm^{-2}). The zircon grains were found to be randomly distributed in the whole sample with no segregation in the boundaries of the textural domains (Suppl. Fig. 2.2). Inside the three domains, the zircon grains were located within the boundaries of pre-existing grains, with the most common minerals being plagioclase, pyroxene and ilmenite, followed by quartz, fluorapatite minerals and chromite.

From the total number of zircon grains, 59 were confirmed to be zircon using EDS, and imaged with SE and BSE. Subsequent mapping using EBSD was undertaken on 5 of the 59 zircon grains. These zircon grains have anhedral to subhedral forms, and the majority contain or are surrounded by fractures. The EBSD analysis of the 5 zircon grains shows no lattice distortion. The zircon grains were found to not contain any microstructures typically reported in shock-deformed zircon

(e.g. planar features, planar deformation features, twinning, high-P polymorphs) (Fig. 2.4 and Table 2.1).

Geochemical Results

From the 628 zircon grains, five were selected for detailed nanoscale investigation using APT. A total of 19 atom probe specimens were analysed in this study; 9 of these specimens fractured during the early stages of APT analysis and sufficient APT data to quantify the composition of the specimen was only determined from the remaining 10 specimens. Of these specimens, seven came from the FG domain (2 – subophitic, 5 – granoblastic), two from the MG domain, and one from the CG domain (Table 2.1).

The mass-to-charge spectrum of the APT specimens contains both single and molecular ions, with O, Si, and Zr as major elements, Hf as a minor, and Li, Mg, Al, P, Ca, Y and Ce as trace elements (Fig. 2.5). No peak above background noise could be attributed to U or Pb, ruling out the possibility of dating the zircon grains. The 3D reconstructions of the atom probe specimens show a homogeneous distribution of the major, minor and trace elements (Fig. 2.5 and Suppl. Fig. 2.3). The concentration of the elements from each specimen can be found in Table 2.2. The zircon values of Y range from 107 to 293 ppma with an average of 177 ppma, while P range from 118 to 250 ppma with an average of 169 ppma. The Zr/Hf ratio from the specimens are superchrondritic (Suppl. Table 2.2), or higher than the $Zr/Hf_{CI\text{-}chondrite}$ value of 32.9 (Barrat et al., 2012).

The FG domain yield the highest concentration of Li (M18 – 277 ppma), Mg (M16 – 14.2 ppma), P (M18 – 250 ppma) and Y (M14 – 293 ppma), whereas the CG domain has the highest measured concentration of Ca (M3 – 163 ppma), and the lowest concentration of Li (M3 – 34 ppma) (Fig. 2.6). In the MG domain, Al (M10 – 14.4 ppma) and Ce (M10 – 30 ppma) record the highest concentrations, while Y (M4 – 107 ppma) and P (M10 – 118 ppma) record the lowest. Although, there are slight variations of trace elements when comparing between the specimens, no substantial chemical difference was measured between the domains apart from Li in the CG domain (Fig. 2.6).

Table 2.2 Elemental analysis from APT (at.%).

	M3	± (1σ)	M4	± (1σ)	M10	± (1σ)	M12	± (1σ)
	CG		MG		MG		FG granoblastic	
O	62.14	0.01	62.54	0.02	63.47	0.03	64.86	0.02
Si	16.393	0.005	16.736	0.009	16.414	0.011	15.335	0.010
Zr	16.556	0.005	17.771	0.009	17.931	0.012	17.780	0.011
Hf	0.1874	0.0005	0.0432	0.0004	0.1680	0.0010	0.1218	0.0008
Li	0.0034	0.0001	0.0118	0.0002	0.0179	0.0003	0.0133	0.0003
Mg	0.00070	0.00003	0.00024	0.00003	0.00098	0.00008	-	-
Al	0.00096	0.00003	0.00189	0.00009	0.00144	0.00010	0.00154	0.00009
P	0.0192	0.0002	0.0141	0.0002	0.0118	0.0003	0.0132	0.0003
Ca	0.0163	0.0001	0.0085	0.0002	0.0072	0.0002	0.0061	0.0002
Y	0.0137	0.0001	0.0107	0.0002	0.0151	0.0003	0.0146	0.0003
Ce	0.00167	0.00004	0.00161	0.00008	0.00300	0.00014	0.00183	0.00010

	M13	± (1σ)	M14	± (1σ)	M15	± (1σ)	M16	± (1σ)
	FG granoblastic		FG granoblastic		FG granoblastic		FG granoblastic	
O	63.01	0.01	63.09	0.01	62.62	0.01	64.08	0.01
Si	16.210	0.006	16.205	0.005	16.373	0.005	15.966	0.006
Zr	17.818	0.006	17.407	0.006	17.388	0.005	17.095	0.006
Hf	0.1399	0.0005	0.1272	0.0004	0.1407	0.0004	0.2385	0.0006
Li	0.0148	0.0002	0.0187	0.0002	0.0190	0.0002	0.0227	0.0002
Mg	0.00060	0.00003	-	-	-	-	0.00142	0.00005
Al	0.00177	0.00005	0.00060	0.00003	0.00188	0.00005	0.00123	0.00005
P	0.0142	0.0002	0.0226	0.0002	0.0194	0.0002	0.0140	0.0002
Ca	0.0085	0.0001	0.0135	0.0001	0.0141	0.0001	0.0082	0.0001
Y	0.0177	0.0002	0.0293	0.0002	0.0181	0.0002	0.0132	0.0002
Ce	0.00155	0.00005	0.00124	0.00004	0.00176	0.00005	0.00137	0.00005

	M18	± (1σ)	M19	± (1σ)
	FG subophitic		FG subophitic	
O	62.05	0.02	62.60	0.01
Si	16.520	0.007	16.447	0.006
Zr	17.591	0.008	17.189	0.006
Hf	0.1339	0.0006	0.1150	0.0005
Li	0.0277	0.0003	0.0160	0.0002
Mg	0.00068	0.00004	0.00094	0.00004
Al	0.00023	0.00003	0.00115	0.00005
P	0.0250	0.0003	0.0156	0.0002
Ca	0.0148	0.0002	0.0149	0.0002
Y	0.0276	0.0003	0.0167	0.0002
Ce	0.00145	0.00006	0.00153	0.00006

- = below detection limit

Uncertainties are based on counting statistics.

Discussion

Zircon characteristics

A total of 628 microscale zircon grains were found within the three textural domains of the Bunburra Rockhole meteorite sample, with the largest being ~14 µm across the longest axis (Fig. 2.3). Even though the FG domain has the highest number of zircon grains per area, the size distribution is similar between the domains, showing no obvious correlation between grain size and textural domain (Fig. 2.3). In addition, the zircon grains are located within the boundary of pre-existing minerals and do not segregate in the boundaries of the different domains, suggesting they crystallized last within the different domains and prior to the brecciating event (Suppl. Fig. 2.2).

Previous work by Jourdan et al. (2014) on petrographic features from pyroxene and plagioclase grains (fractures, undulatory features and localized cloudiness) established shock metamorphic pressures of 10 – 20 GPa for the Bunburra Rockhole meteorite. These conditions are consistent with our observations of maskelynite (Fig. 2.2) and the absence of diagnostic shock microstructures in the zircon grains.

The geochemical analysis by APT revealed a similar major, minor and trace element composition of zircon grains amongst the three domains, except for Li (Fig. 2.6 and Table 2.2). Li concentrations were lowest in the CG domain, which could be caused by a Li-poor composition of the parent melt, Li diffusion during thermal annealing, or diffusion of Li coupled with the diffusion of other elements (Ushikubo et al., 2008; Sliwinski et al., 2018). Regardless of the low concentration of Li in the CG domain, the chemical homogeneity of zircon grains from the different domains support a common magmatic source.

The zircon grains within Bunburra Rockhole are inferred to be primary magmatic grains that crystallized from a fractionated residual melt, expected to have occurred during the last stage of crystallization within the different domains. This is supported by the morphology of the grains, spatial distribution, superchondritic Zr/Hf ratio value (Figs. 2.4, 2.7), and lack of metamorphic overprint.

Evolution of Bunburra Rockhole

The grain size variation, subophitic and granoblastic textures seen in the Bunburra Rockhole sample suggest a complex history for the meteorite. The meteorite sample comprises texturally distinct clasts surrounded by maskelynite that make up the different domains (Fig. 2.2 and Suppl. Fig. 2.1). The clasts consist mostly of plagioclase (anorthite) and pyroxene (augite and enstatite), minor amounts of quartz, and trace amounts of ilmenite, chromite, forsterite, zircon and pyrrhotite (Fig. 2.2). Although the modal mineralogy is similar between the clasts, the different grain size points to different cooling rates for the different domains. The amalgamation and consolidation of the breccia is overprinted by fractures that crosscut several minerals with no preferred direction, mineralogy or domain (Fig. 2.1). The petrological observations of this meteorite, which reveals FG, MG and CG domains, suggest reclassification as a polymict breccia. This finding is consistent with bulk and trace element chemistry of pyroxene, plagioclase, and Ca phosphate crystals done by Spivak-Birndorf et al. (2015), although these authors classified the Bunburra Rockhole meteorite as a monomict breccia. In this study, the term monomict was not used since it implies the domains of the breccia are all the same and the evidence shows they are texturally different. This difference implies the domains come from different rock types, even if those rocks formed from a similar source.

The formation of the Bunburra Rockhole meteorite parent melt has been interpreted to have occurred at 4565 Ma, 3 Ma after the formation of the solar system (Spivak-Birndorf et al., 2015). An impact-related thermal event re-equilibrated the Mg and Pb isotopic system of the rock around 4102 Ma (Spivak-Birndorf et al., 2015). Several impact events occurring at different times (3640, 3544, 3419 Ma) have been suggested to have struck, formed and excavated the components of the Bunburra Rockhole meteorite (Jourdan et al., 2014). This interpretation assumes that the texturally distinct domains formed at different times.

However, the similar chemical composition and size distribution of the zircon grains found in this study, suggest a similar source melt for the domains. In addition, the zircon grains in the Bunburra Rockhole sample are interpreted to have crystallised from a residual melt based on their location, superchondritic Zr/Hf ratio and their anhedral-subhedral form (Fig. 2.7). This study indicates that the individual

domains are a function of cooling rate of a single melt source. The disruption and consolidation process of the textural domains represents secondary processing associated with impact.

The ages for the domains could not be determined since Pb was not detected within APT analysis of the zircon grains. This could be explained by the low concentration of U (0.10 ppm – FG, 0.10 ppm – MG, 0.09 ppm – CG) and Th (0.39 ppm – FG, 0.35 ppm – MG, 0.36 ppm – CG) within the Bunburra Rockhole meteorite obtained by Spivak-Birndorf et al. (2015). Nevertheless, APT was able to provide important geochemical data that aided in the distinction of the Bunburra Rockhole meteorite source body.

Comparison of Bunburra Rockhole and eucrites

No major difference was identified in the concentrations of Si, Zr and Hf between the zircon grains from the Bunburra Rockhole meteorite and the eucrite zircon from Misawa et al. (2005), Haba et al. (2014) and Roszjar et al. (2014) (Fig. 2.S4). In addition, the Zr/Hf ratio from all of these studies, including this one, are superchondritic (Fig. 2.7 and Suppl. Table 2.2), indicating that the zircon grains in basaltic achondrite crystallized from a residual melt (Misawa et al., 2005; Patzer et al., 2010; Roszjar et al., 2014). In addition, the concentrations of the trace elements from the Bunburra Rockhole meteorite is similar to those found in geochemical studies of eucrite zircon grains (Suppl. Fig. 2.4).

However, when comparing the Y/P ratio between Roszjar et al. (2014) and this study, a difference becomes apparent (Fig. 2.8). The Bunburra Rockhole values of Y range from 0.011 to 0.029 at.% with an average of 0.018 at.%, while P range from 0.012 to 0.025 at.% with an average of 0.017 at.%. The Y values from Roszjar et al. (2014) range from 0 to 0.096 at.% (average of 0.022 at.%), whereas P ranges from 0.017 to 0.149 at.% with an average of 0.049 at.%. The sample suite from Roszjar et al. (2014) consists of eleven different basaltic eucrites for a total of 72 analyses conducted on 69 zircon grains using an electron probe micro analyser and secondary ion mass spectrometry. Misawa et al. (2005) and Haba et al. (2014) did not measure the Y nor P content within the zircon grains.

When using APT data for a chemical analysis, underestimation or overestimation of peak counts must be considered. Such biases can depend on

several variables including, but not limited to peaks overlaps, thermal tails or background noise levels. To verify the accuracy of APT quantification of Y and P in this study, the results have been compared to analyses of zircon standards by APT and other techniques. For the zircon reference material 91500, the Y concentration in the APT data was underestimated when compared to secondary-ion mass spectrometry and laser ablation inductively coupled plasma mass spectrometry (LA-ICP-MS) (Saxey et al., 2018b). In an inter-laboratory analysis of zircon reference material, GJ-1, the Y concentration from the APT data was also underestimated when compared to LA-ICP-MS, while the P concentration were overestimated (Exertier et al., 2018). Hence, a similar bias may be expected in the APT analysis of Y and P concentrations in this study, which if corrected would place the Y/P ratio even further from the eucritic trend line of Roszjar et al. (2014) (Fig. 2.8). Additionally, for the data of this study to plot where Roszjar et al. (2014) data is, the concentration of P from the APT analysis would have to be doubled. This difference is well above any analytical uncertainty caused by peak overlaps, thermal tails or noise levels. Thus, the authors of this study have a high degree of confidence that the higher Y/P ratio measured in the Bunburra Rockhole zircon grains by APT is significant and different from eucrite zircon grains.

The different Y/P ratio, coupled with the previously reported O and Cr isotopic data (Bland et al., 2009; Benedix et al., 2017), and orbital trajectory models (Bland et al., 2009), indicate that the Bunburra Rockhole meteorite is not a eucrite and therefore did not originate from the asteroid 4 Vesta. However, the similarities in texture, mineralogy and general chemistry between the Bunburra Rockhole meteorite and eucrites suggest a similar petrogenesis to that of 4 Vesta and the parent body of the Bunburra Rockhole meteorite.

Conclusion

This study is the first comprehensive analysis of zircon grains from the Bunburra Rockhole meteorite, which have previously not been studied in detail, primarily due to their micrometre size and the limited spatial resolution of conventional analytical techniques. Based on macroscopic and microscopic observations alone, the Bunburra Rockhole meteorite can be classified as a basaltic eucrite. However, with the nanometre characterization by APT the chemical composition of the zircon grains was acquired, proving to be an important tool to

distinguish the composition of the parent body. Considering the morphology, spatial distribution, chemical composition and lack of metamorphic overprint of the zircon grains within the sample, it is established that the Bunburra Rockhole meteorite has a single population of zircon grains. These grains crystallized from a common source melt at the last stage of crystallization within the domains, before the brecciation event. This information indicates the different grain-sizes that define the domains are determined by the cooling rates.

The Bunburra Rockhole meteorite and eucrites have similar textures, mineralogy and general chemistry. However, the nanoscale geochemical analysis of the zircon grains within the Bunburra Rockhole meteorite revealed a difference in the Y/P ratio when compared to that of eucrites. This difference supports previous suggestions that this meteorite is not a eucrite and did not derive from the asteroid 4 Vesta. Despite the differences observed at the nanoscale, the similarities at macro- and microscale scales suggest the origins and formations of the Bunburra Rockhole parent body and the asteroid 4 Vesta are similar.

This study has: (1) demonstrated that the geochemical information from microscale sized grains can be individually analysed to provide insight of the parent body; (2) shown that APT can be applied to detect subtle variations in the trace element concentrations within samples; and (3) provides a foundation for new applications of APT to planetary sciences.

Acknowledgements

The Geoscience Atom Probe Facility, together with the Lyra FIB-SEM are housed within the John de Laeter Centre at Curtin University. These facilities were established with support from the Science and Industry Endowment Fund (RI13-01), under the auspices of the National Resource Sciences Precinct (NRSP), a collaboration between CSIRO, Curtin University, and The University of Western Australia. We acknowledge support from the Curtin International Postgraduate Research Scholarship (CIPRS), Australian Research Council (ARC) Centre of Excellence for Core to Crust Fluid Systems (CE11E0070) and Discovery Early Career Researcher Award (DE190101307) for DF.

Figures

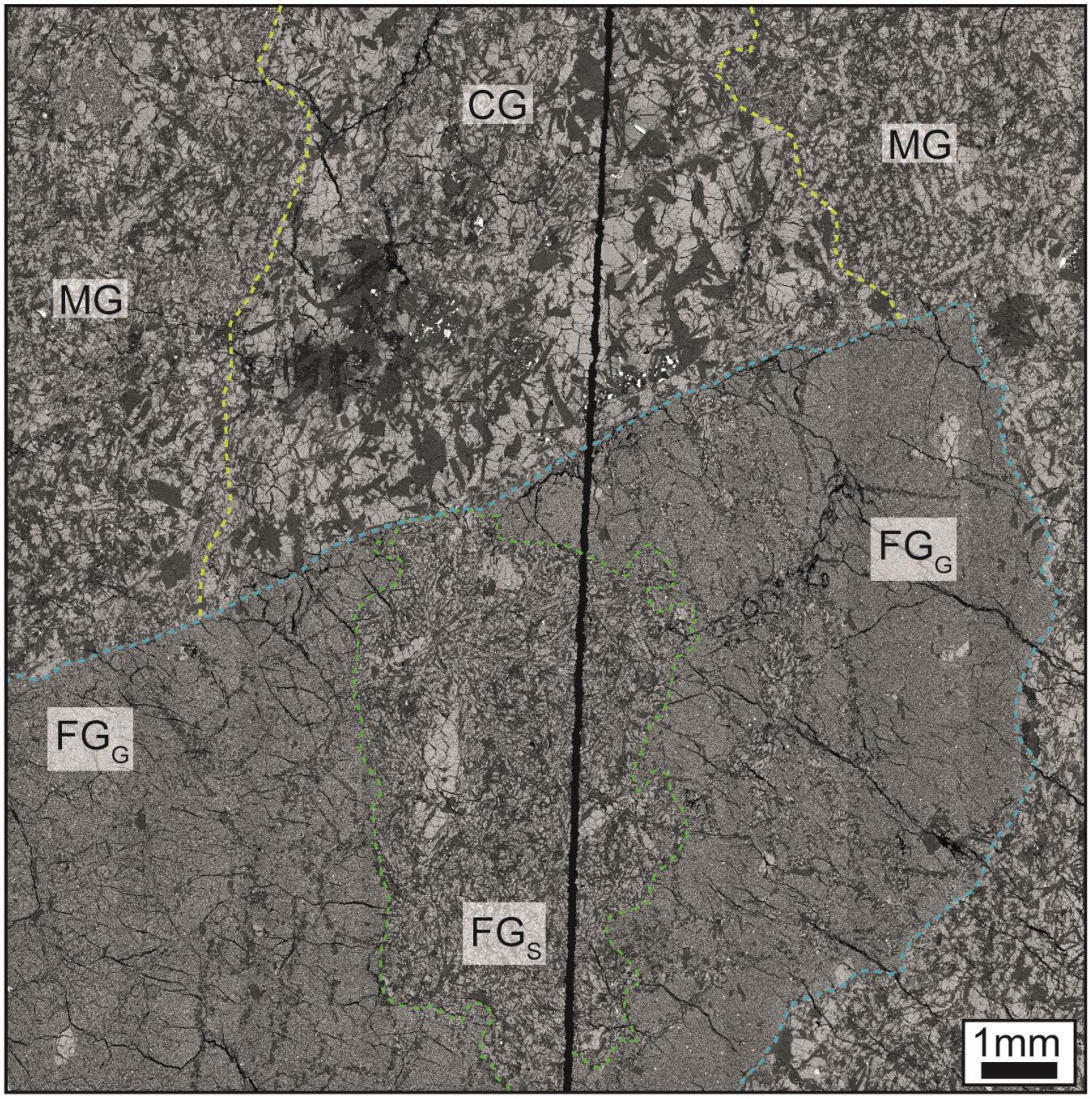

Figure 2.1 A BSE image of the Bunburra Rockhole sample with the three different domains, fine-grained (FG), medium-grained (MG) and coarse-grained (CG). The FG domain is sub-divided by the texture as subophitic (FG_S) and granoblastic (FG_G). Multiple fractures are visible throughout the image, as well as large crystals of pyroxene and plagioclase within the FG domain.

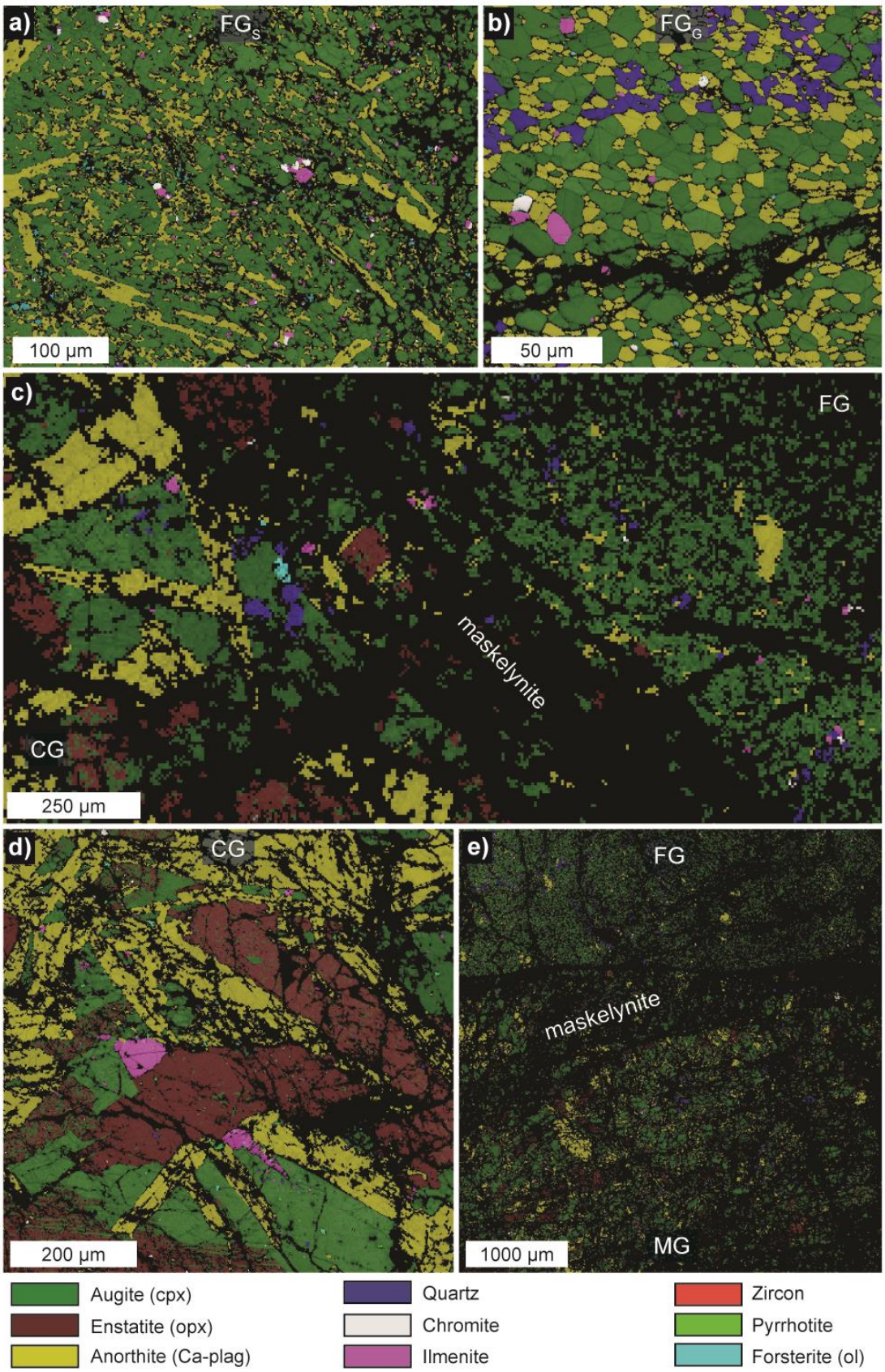

Figure 2.2 EBSD phase maps from **(a)** the FG domain showing the subophitic texture, **(b)** FG domain with the granoblastic texture, **(c)** FG (right) and CG (left) domains with maskelynite along their boundary, **(d)** CG domain, and **(e)** FG (top)

and MG (bottom) domains separated by maskelynite. The minerals identified within the EBSD maps were augite, enstatite, anorthite, quartz, chromite, ilmenite, zircon (too small to see), pyrrhotite (too small to see), and forsterite.

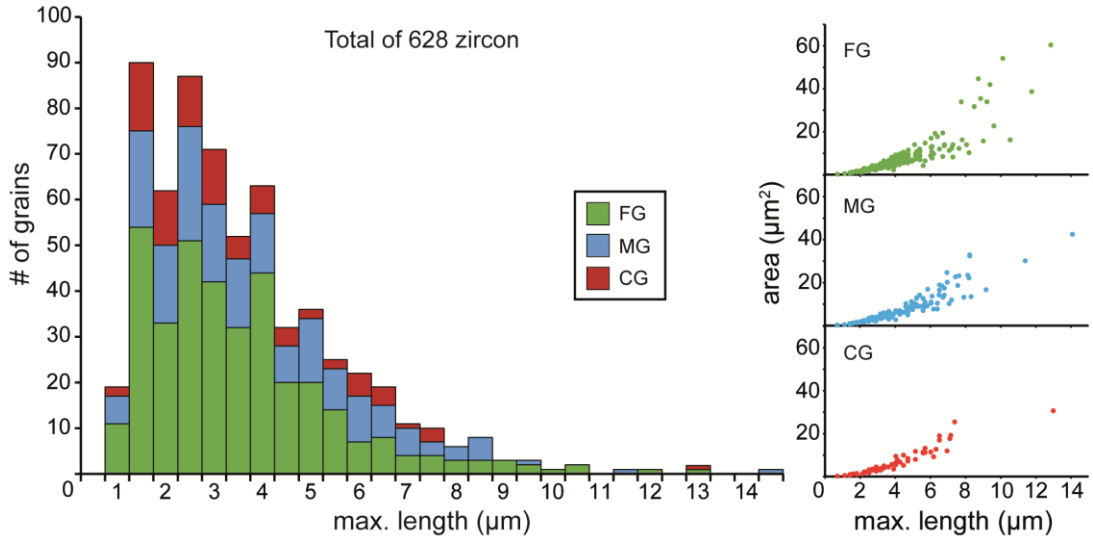

Figure 2.3 Histogram of the size distribution of the zircon grains within the different domains: fine-grained (FG), medium-grained (MG) and coarse-grained (CG). The plots show the number of zircon grains against the maximum length, and the area of the grains against the maximum length. A similar distribution can be seen between the domains. The colours represent the values within each domain (green – FG, blue – MG, and red – CG).

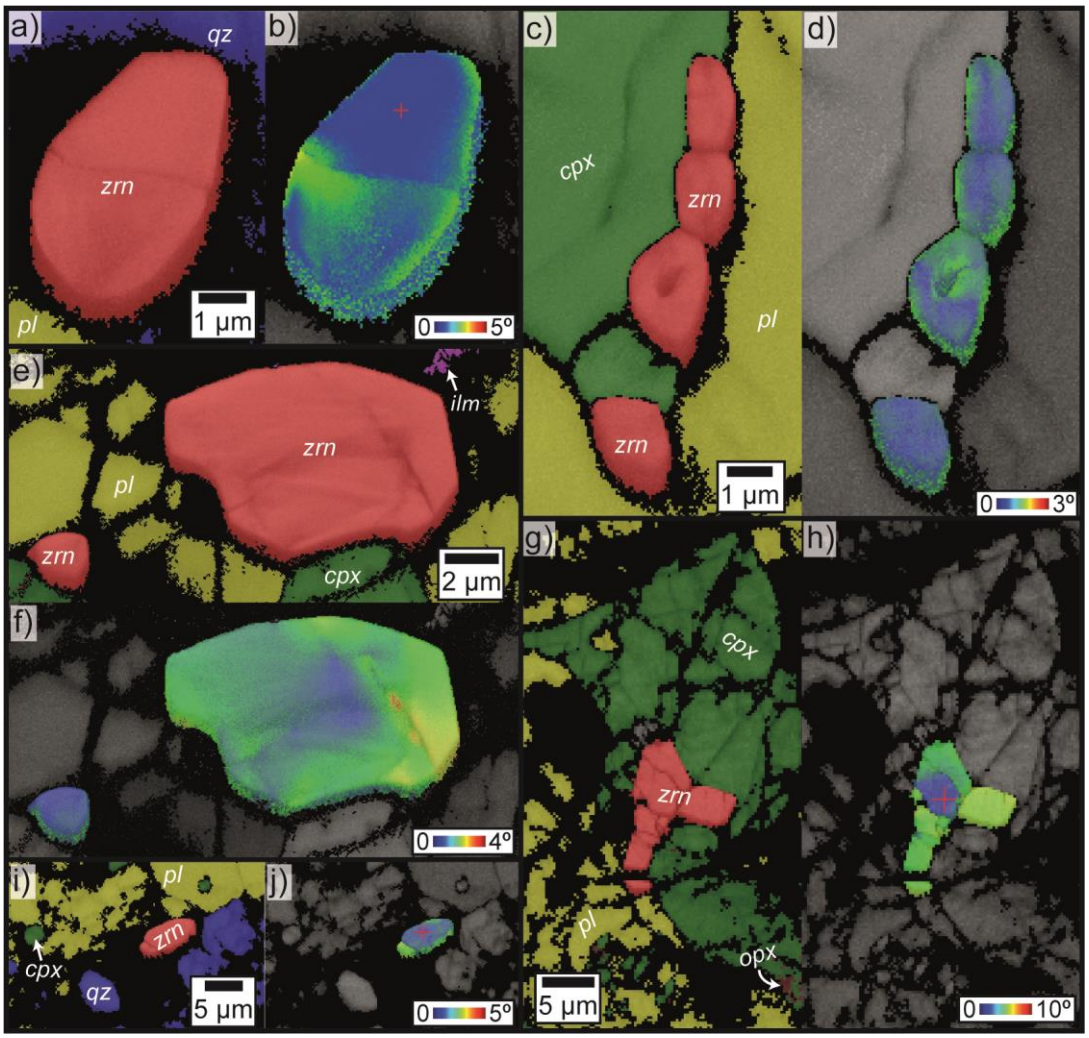

Figure 2.4 EBSD maps of the five zircon grains analysed. Band contrast combined with phase maps of **(a)** zircon 1, **(c)** zircon 2, **(e)** zircon 3, **(g)** zircon 4, and **(i)** zircon 5. The colours in the phase maps represent zircon (zrn – red), clinopyroxene (cpx – green), plagioclase (pl – yellow), quartz (qz – blue), ilmenite (ilm – fuchsia) and orthopyroxene (opx – maroon). Band contrast and texture component (TC) maps of **(b)** zircon 1, **(h)** zircon 4 and **(j)** zircon 5 showing the variation in crystallographic orientation relative to a point of reference in the image (red cross). Band contrast with grain reference orientation deviation (GROD) angle maps of **(d)** zircon 2 and **(f)** zircon 3 showing the misorientation of each individual grain. GROD maps were picked over TC maps for areas that contained more than one zircon grain (zircon 2 and zircon 3).

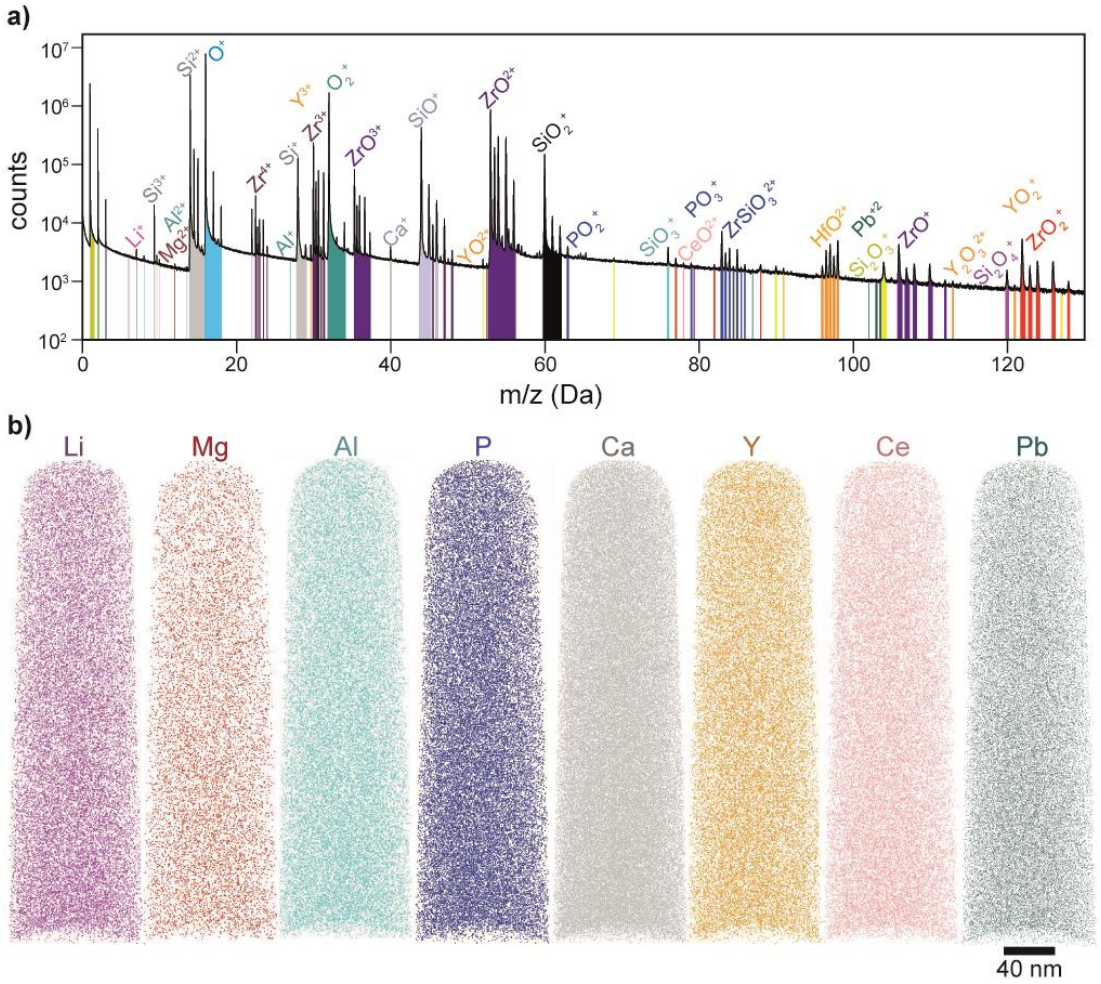

Figure 2.5 APT data for specimen M3 (~91 million ions). **(a)** The mass spectrum from zircon 5 of the CG domain with the ranges of the single ions and molecular ions. **(b)** Atom probe 3D reconstructions showing a homogenous distribution of trace elements, where each sphere represents an atom (Li, Mg, Al, P, Ca, Y, Ce, and Pb). Pb counts were below the detection limit, hence the Pb reconstruction only represent noise.

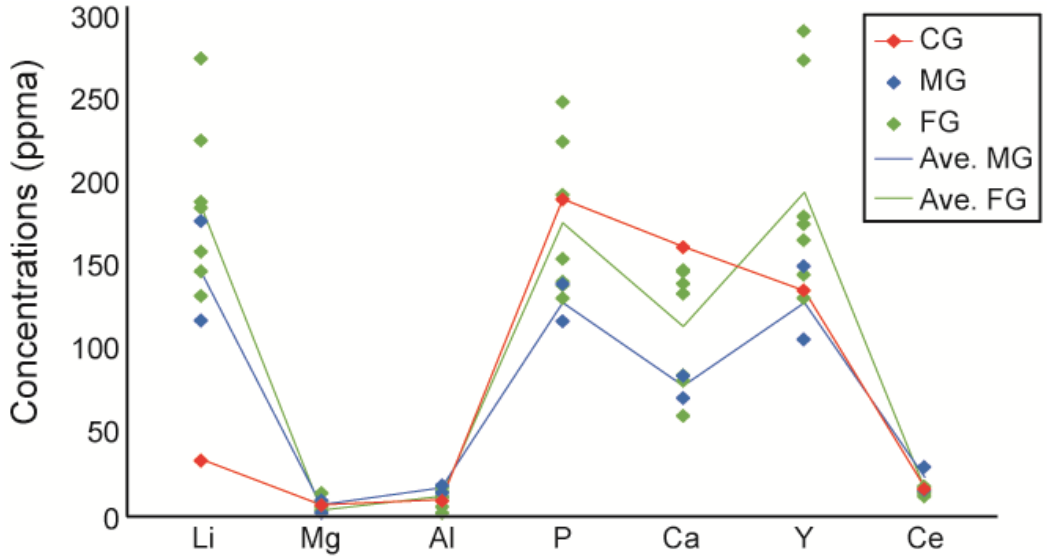

Figure 2.6 A visual representation of the trace element concentration from the APT data of the specimens. The concentrations are given in ppma, and the colours represent the domains (red – CG, blue – MG, and green – FG). The uncertainties are smaller than the marks because they are based only on counting statistics, hence they were not included.

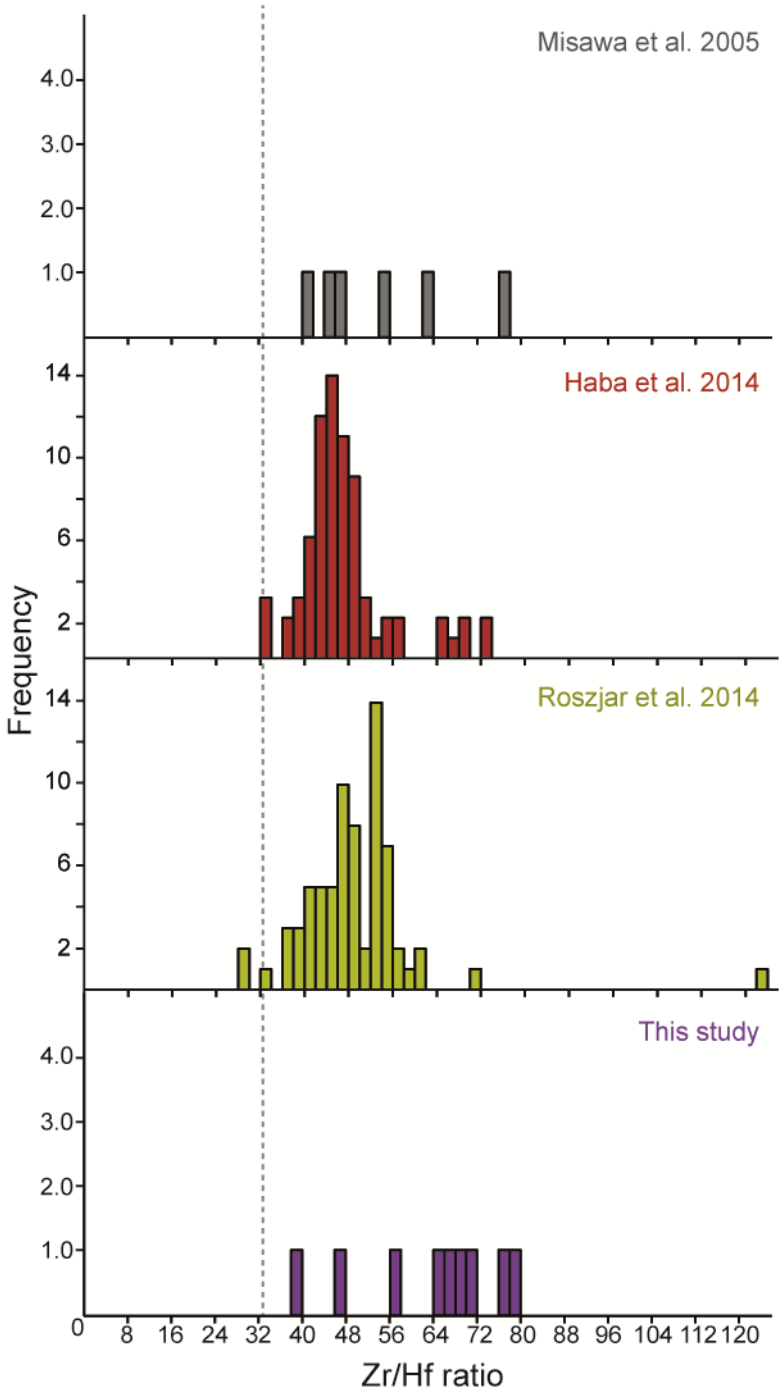

Figure 2.7 Comparison of the Zr/Hf ratio between studies, with the Zr/Hf ratio of CI chondrites added for reference (dashed line = 32.9). Even though the number of zircon grains analysed differ by studies, the Zr/Hf ratio for all of them are superchondritic. One data set from this study (purple) was omitted due to the different parameters used during the APT analysis.

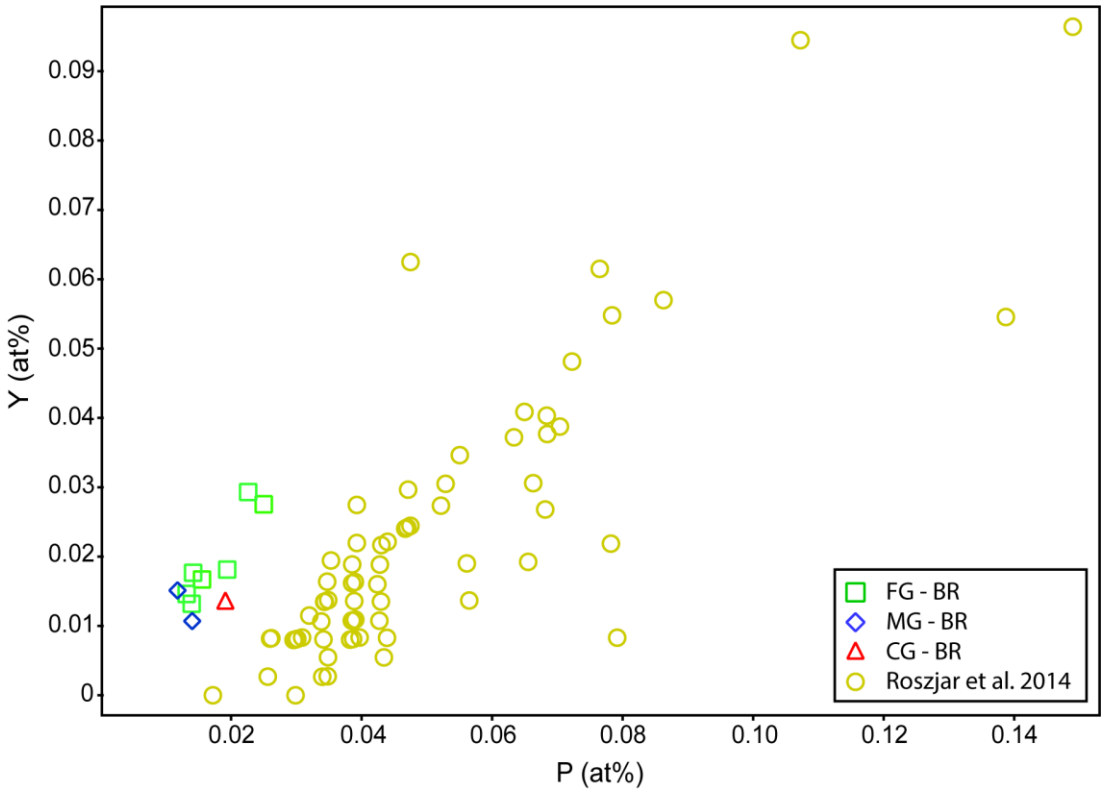

Figure 2.8 Y and P concentrations of zircon grains from this study (Bunburra Rockhole meteorite) and Roszjar et al. (2014) (eucrites). Error bars from this study are smaller than the marks, hence they were not included. Values of the errors can be found in Table 2.2.

Supplementary Material

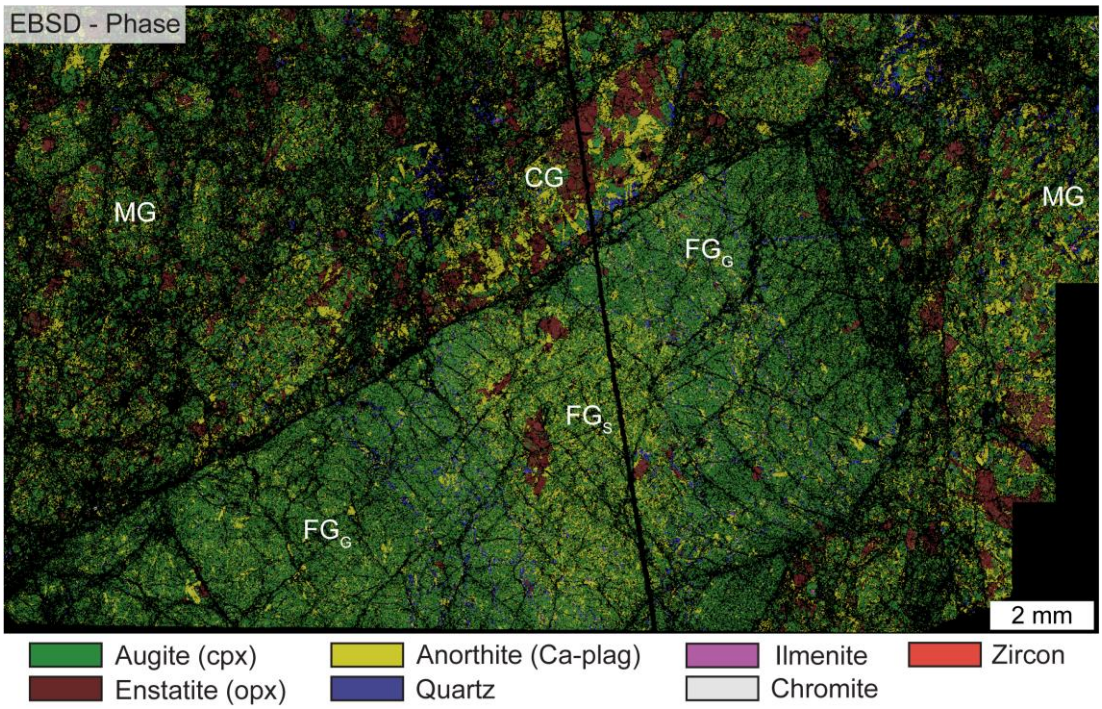

Suppl. Figure 2.1 Large area EBSD map of the Bunburra Rockhole meteorite sample with the different minerals highlighted.

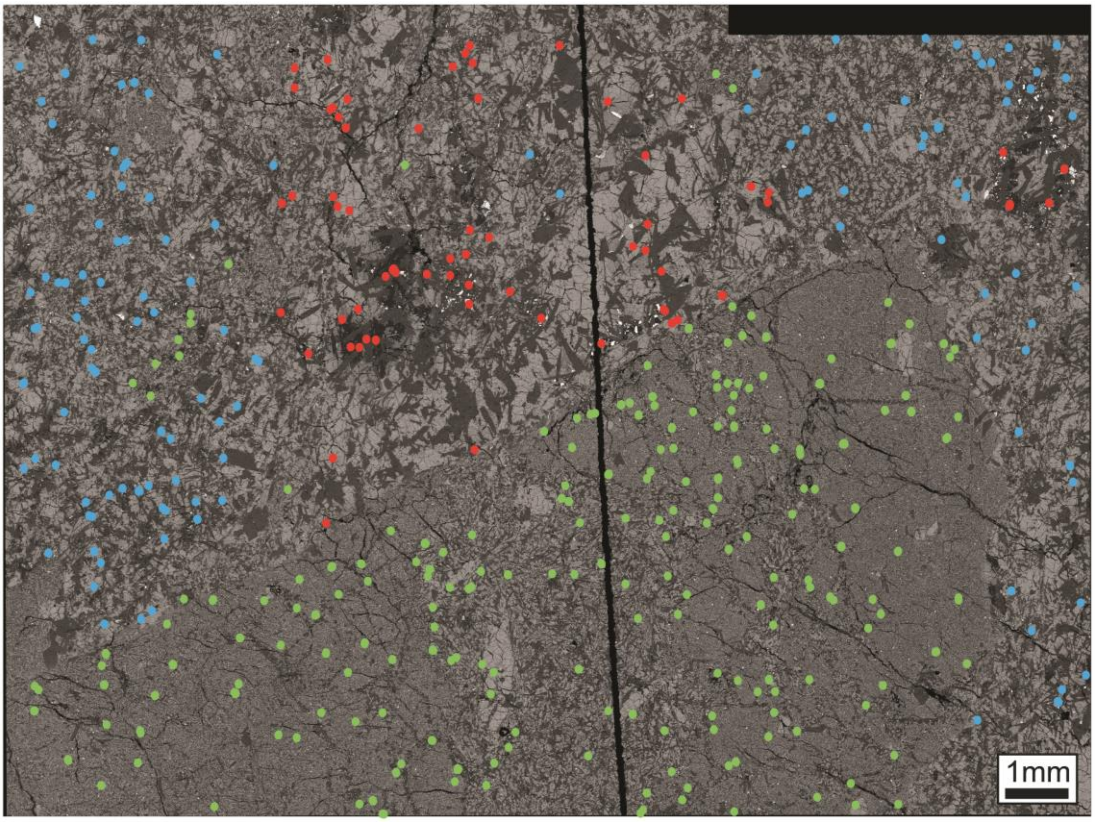

Suppl. Figure 2.2 BSE image of the Bunburra Rockhole sample with the approximate position of the zircon grains identified using feature analysis. The colours represent the grains in the different domains (green – FG, blue – MG, and red – CG).

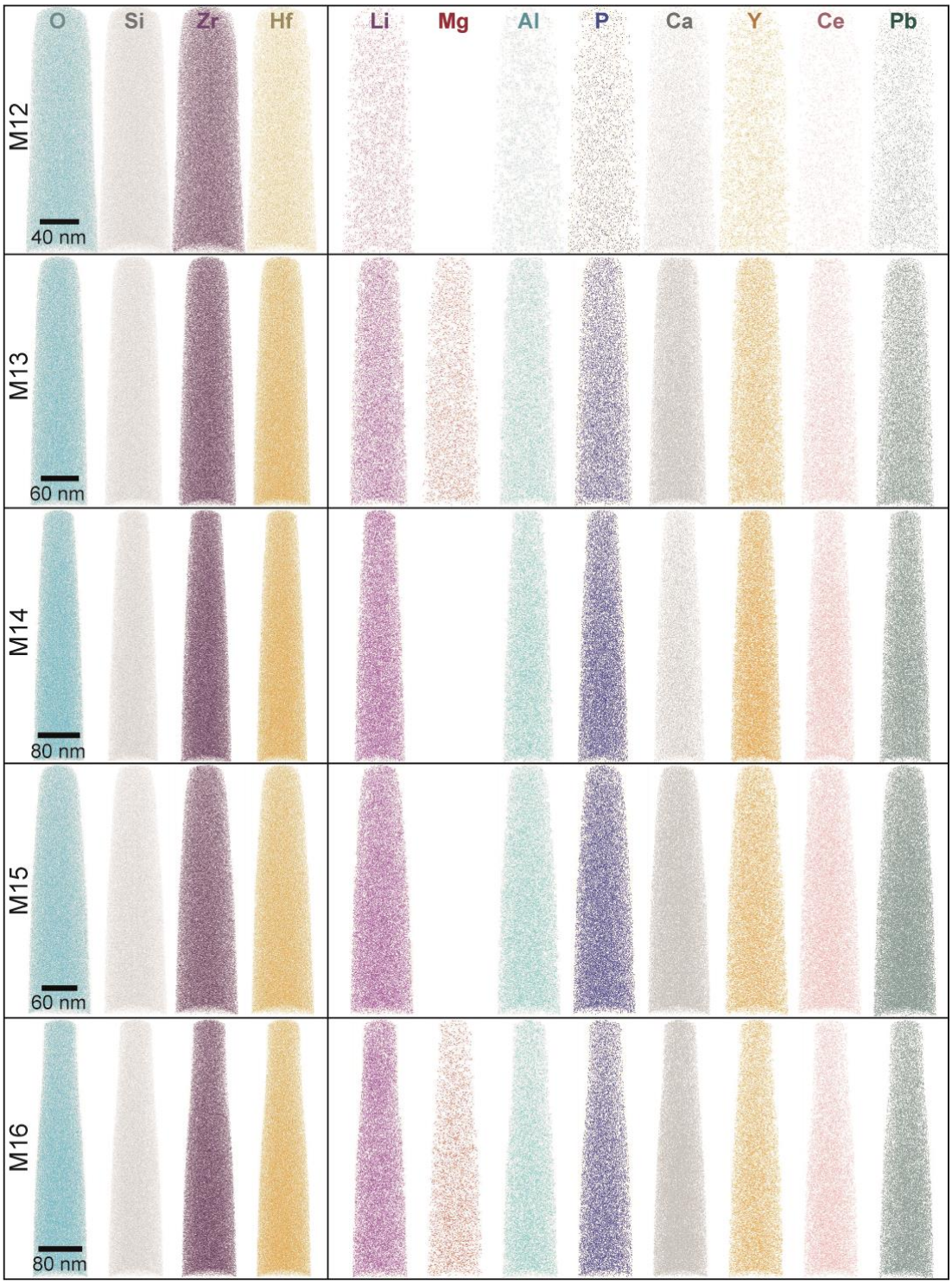
O
Si
Zr
Hf
Li
Mg
Al
P
Ca
Y
Ce
Pb
M12
40 nm
M13
60 nm
M14
80 nm
M15
60 nm
M16
80 nm

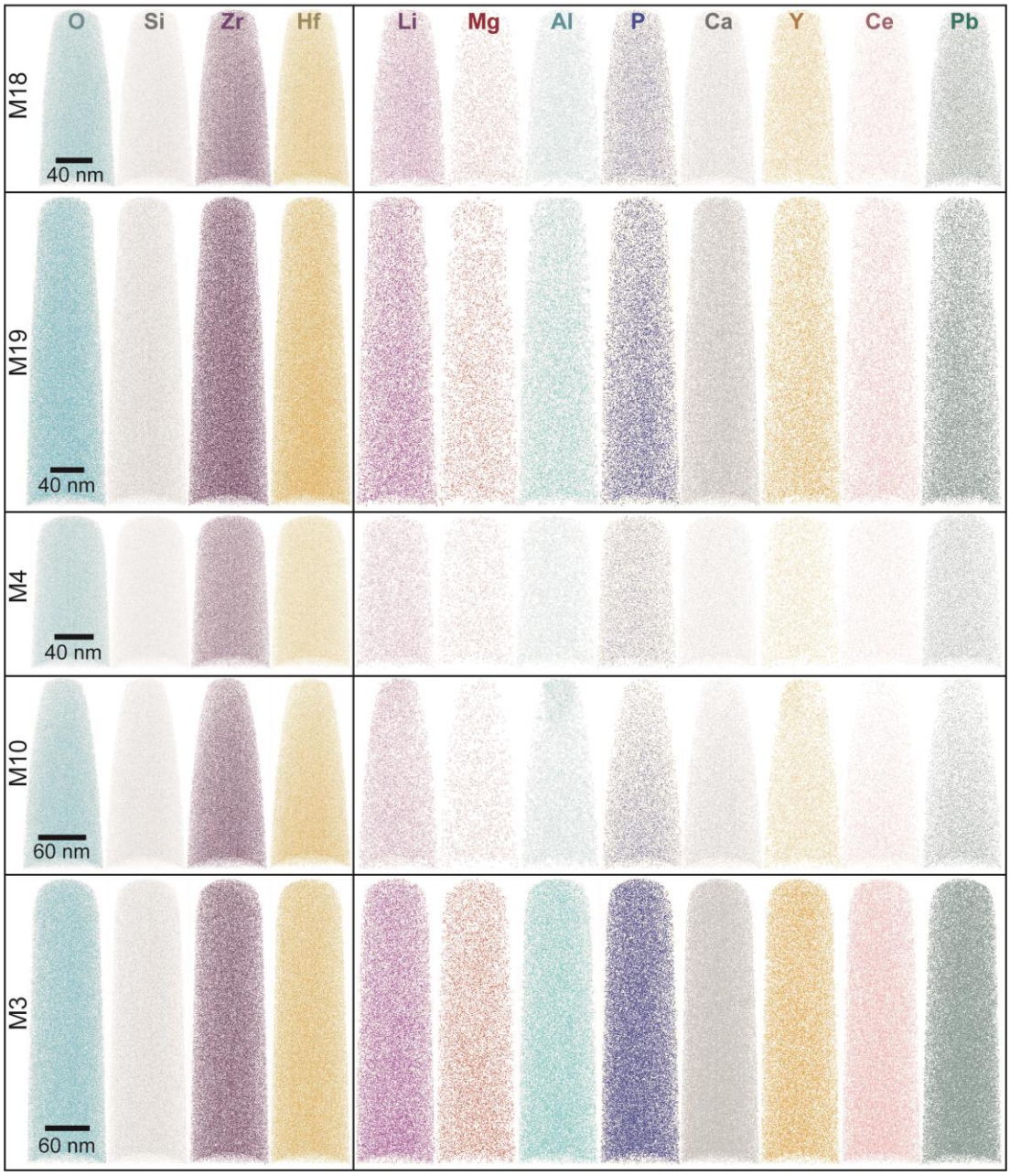

Suppl. Figure 2.3 3D atom probe reconstructions of all the specimens used for the geochemical analysis, showing a homogenous distribution of major, minor and trace elements in each of the specimens. Empty spaces in the Mg column of M12, M14 and M15 indicates the values were below the detection limit. Pb counts were below the detection limit, hence the Pb reconstruction only represent noise.

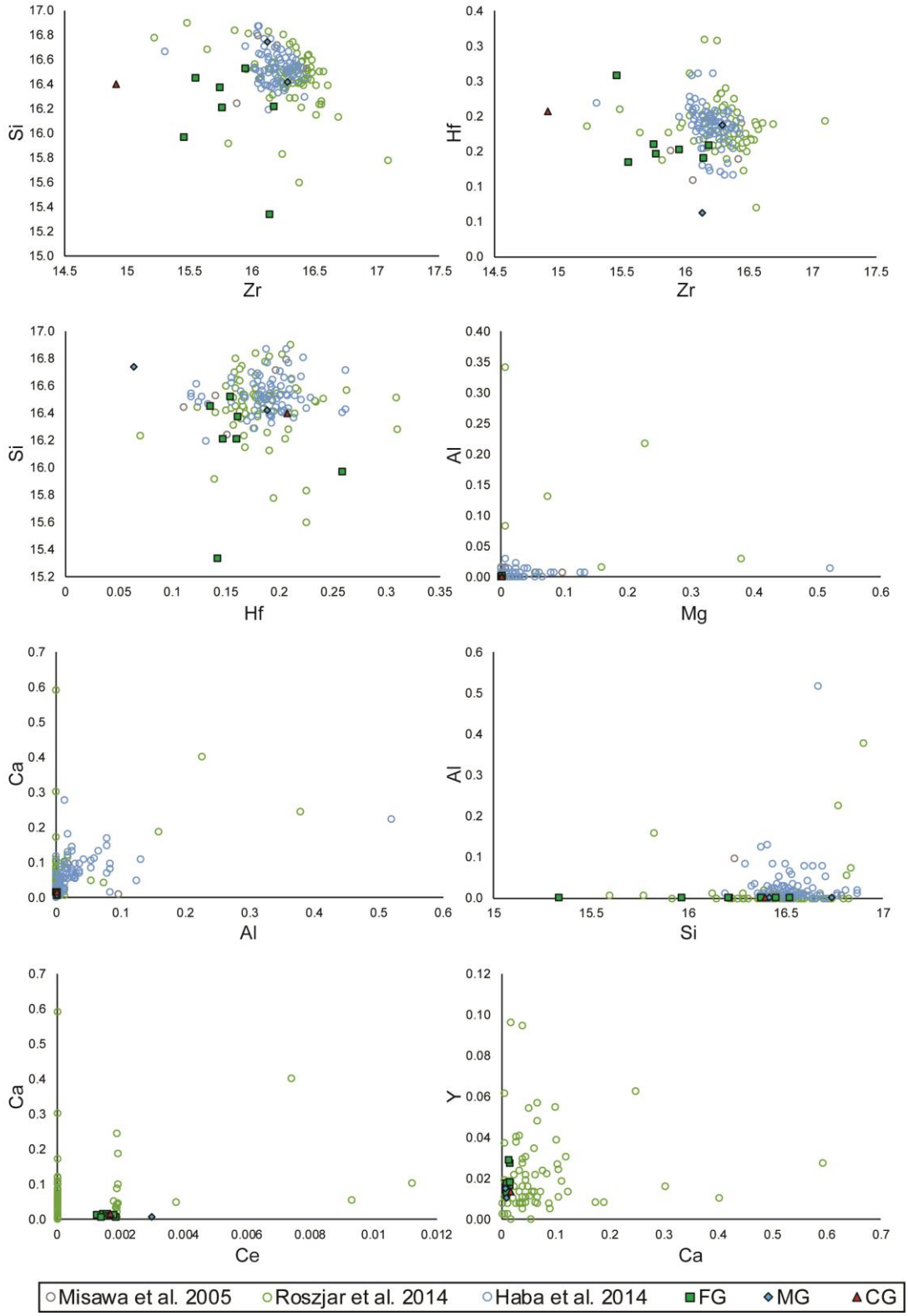

Suppl. Figure 2.4 Chemical comparison (in at.%) between Bunburra Rockhole and the eucrites from Misawa et al. (2005), Haba et al. (2014) and Roszjar et al. (2014). Note the last row only compares this study and Roszjar et al. (2014), since the other two did not measure Y nor Ce.

Suppl. Table 2.1 APT data and acquisition settings.

Grain	**zircon 5**	**zircon 4**			**zircon 3**				**zircon 1**	**zircon 2**
Data set /specimen	**M3**	**M4**	**M10**	**M12**	**M13**	**M14**	**M15**	**M16**	**M18**	**M19**
Instrument Model	LEAP 4000X HR									
Instrument Settings										
Laser wavelength (nm)	355									
Laser pulse energy (pJ)	300	300	400	400	400	400	400	400	400	400
Pulse frequency (kHz)	200	250	250	200	200	200	200	200	200	200
Evaporation control	Detection rate									
Targeted det. rate (ions/pulse)	0.005	0.005	0.006	0.006	0.006	0.006	0.006	0.007	0.005	0.005
Nominal flight path (mm)	382									
Set point temperature (K)	70	70	60	70	70	70	70	70	80	70
Sample temperature (K)	80.7	80.7	69.7	80.9	80.7	80.7	79.9	80.7	91.9	80.7
Chamber pressure ($x10^{-10}$ Torr)	1.9	2.0	1.0	1.9	2.6	1.8	2.6	1.8	2.1	2.6
Data Summary										
LAS Root version	15.41.342l									
CAMECAROOT version	18.44.416									
Analysis Software	IVAS 3.8.0									
Total Ions:	91 M	22 M	31 M	18 M	57 M	68 M	74 M	62 M	35 M	51 M
% Single	79.6	74.9	77.1	70.6	75.7	76.5	73.8	70.9	78.7	77.8
% Multiple	19.7	24.3	22.3	28.6	23.6	22.8	25.6	28.5	20.5	21.5
% Partial	0.8	0.8	0.6	0.8	0.7	0.7	0.7	0.6	0.8	0.7
Volt./bowl corr. peak (Da)	16									
Mass Calib. (peaks/interp.)	9/Lin	10/Lin	9/Lin	9/Lin	9/Lin	10/Lin	9/Lin	12/Lin	11/Lin	9/Lin
*(M/ΔM)	998	1026	1055	1000	1006	1006	981	1025	1002	1000
**(M/ΔM10)	199	201	196	113	191	193	191	184	200	193
Time independent background (ppm/ns)	52.22	67.22	28.73	23.1	28.56	28.76	46.98	29.6	49.18	36.60
Reconstruction										
Final specimen state	NF	F	F	F	F	F	NF	F	F	F
Pre-/post-analysis imaging	SEM									
Radius evolution model	'Voltage'									
Field factor (k)	3.3									
Image compression factor	1.65									
Assumed E-field (V/nm)	32									
Detector efficiency	0.36									
Avg. atomic volume (nm3)	0.01076									
V initial (V)	5530	5721	4071	4165	4887	4999	4863	5127	4954	4777
V final (V)	10031	8239	8976	6563	8473	8916	10024	8991	9265	8810

*ΔM is full width at half maximum of the Volt./bowl corr. peak

** ΔM10 is full width at tenth maximum of the Volt./bowl corr. peak

det. = detection; Volt. = voltage; corr. = correction; Calib. = calibration; interp. = interpolation; Lin = linearization method; Avg. = average; F = fractured, NF = not fractured.

Suppl. Table 2.2 Zr/Hf ratio of the specimens and eucrites

Study	Meteorite	Sample	Zr[a]	Hf[a]	Zr/Hf	Zr/Hf[b]
This study	B.R.	M18	17.59	0.134	131	67
This study	B.R.	M19	17.19	0.115	149	76
This study	B.R.	M12	17.78	0.122	146	75
This study	B.R.	M13	17.82	0.140	127	65
This study	B.R.	M14	17.41	0.127	137	70
This study	B.R.	M15	17.39	0.141	124	63
This study	B.R.	M16	17.09	0.238	72	37
This study	B.R.	M4	17.77	0.043	411	210
This study	B.R.	M10	17.93	0.168	107	55
This study	B.R.	M3	16.56	0.187	88	45
Misawa et al., 2005	Yamato-75011	Y-75011	15.89	0.151	105	54
Misawa et al., 2005	Yamato-792510	Y-792510	16.06	0.110	146	75
Misawa et al., 2005	Asuka-881388	A-881388	16.42	0.140	117	60
Misawa et al., 2005	Asuka-881467	A-881467	16.44	0.190	86	44
Misawa et al., 2005	Padvarninkai	UT1	16.05	0.206	78	40
Misawa et al., 2005	Padvarninkai	UT2	16.20	0.197	82	42
Roszjar et al., 2014	DaG 276	Zrc1*	16.27	0.234	70	36
Roszjar et al., 2014	DaG 391	Zrc1*	17.09	0.194	88	45
Roszjar et al., 2014	Dho 182	Zrc1	16.31	0.163	100	51
Roszjar et al., 2014	Dho 182	Zrc2	16.28	0.232	70	36
Roszjar et al., 2014	Dho 182	Zrc3	16.47	0.176	94	48
Roszjar et al., 2014	Dho 182	Zrc4	16.47	0.166	100	51
Roszjar et al., 2014	Dho 182	Zrc5	16.27	0.163	100	51
Roszjar et al., 2014	HaH 286	Zrc1-1	16.45	0.161	102	52
Roszjar et al., 2014	HaH 286	Zrc1-2	16.33	0.140	117	60
Roszjar et al., 2014	HaH 286	Zrc1-3	16.48	0.150	110	56
Roszjar et al., 2014	HaH 286	Zrc2	16.61	0.191	87	45
Roszjar et al., 2014	HaH 286	Zrc3a	16.48	0.167	99	51
Roszjar et al., 2014	HaH 286	Zrc3b	16.33	0.165	99	51
Roszjar et al., 2014	HaH 286	Zrc3c	16.39	0.159	103	53
Roszjar et al., 2014	HaH 286	Zrc4	16.57	0.183	91	46
Roszjar et al., 2014	HaH 286	Zrc5	16.35	0.197	83	42
Roszjar et al., 2014	HaH 286	Zrc6	16.23	0.150	108	55
Roszjar et al., 2014	HaH 286	Zrc7	16.25	0.309	53	27
Roszjar et al., 2014	HaH 286	Zrc8	16.30	0.178	92	47
Roszjar et al., 2014	Millbillillie	Zrc1	16.40	0.194	84	43
Roszjar et al., 2014	Millbillillie	Zrc2	16.30	0.208	78	40
Roszjar et al., 2014	Millbillillie	Zrc3*	16.51	0.168	98	50
Roszjar et al., 2014	Millbillillie	Zrc8	16.69	0.190	88	45
Roszjar et al., 2014	Millbillillie	Zrc11	16.42	0.184	89	46
Roszjar et al., 2014	Millbillillie	Zrc12*	16.41	0.167	98	50
Roszjar et al., 2014	Millbillillie	Zrc13*	16.42	0.184	89	46
Roszjar et al., 2014	Millbillillie	Zrc14	16.25	0.208	78	40
Roszjar et al., 2014	Millbillillie	Zrc15	16.43	0.155	106	54
Roszjar et al., 2014	NWA 1908	Zrc1	16.45	0.157	105	54
Roszjar et al., 2014	NWA 1908	Zrc2	16.45	0.123	134	69
Roszjar et al., 2014	NWA 2550	Zrc1	16.54	0.193	86	44
Roszjar et al., 2014	NWA 2550	Zrc2	16.45	0.163	101	52
Roszjar et al., 2014	NWA 2550	Zrc3	16.36	0.211	77	40
Roszjar et al., 2014	NWA 2550	Zrc4	16.13	0.202	80	41
Roszjar et al., 2014	NWA 2550	Zrc5	16.31	0.163	100	51
Roszjar et al., 2014	NWA 2550	Zrc6	16.25	0.159	102	52
Roszjar et al., 2014	NWA 2550	Zrc7	16.40	0.177	93	47
Roszjar et al., 2014	NWA 2550	Zrc8	16.36	0.157	104	53
Roszjar et al., 2014	NWA 4523	Zrc1	16.06	0.166	97	50
Roszjar et al., 2014	NWA 4523	Zrc2	16.34	0.175	93	48
Roszjar et al., 2014	NWA 4523	Zrc3	16.35	0.167	98	50

Study	Meteorite	Sample	Zr[a]	Hf[a]	Zr/Hf	Zr/Hf[b]
Roszjar et al., 2014	NWA 4523	Zrc4	16.14	0.168	96	49
Roszjar et al., 2014	NWA 4523	Zrc5	16.21	0.159	102	52
Roszjar et al., 2014	NWA 5073	Zrc1	16.37	0.163	101	51
Roszjar et al., 2014	NWA 5073	Zrc2	16.32	0.241	68	35
Roszjar et al., 2014	NWA 5073	Zrc3	16.15	0.310	52	27
Roszjar et al., 2014	NWA 5073	Zrc4	16.38	0.176	93	48
Roszjar et al., 2014	NWA 5073	Zrc5	16.17	0.157	103	53
Roszjar et al., 2014	NWA 5073	Zrc6	16.03	0.262	61	31
Roszjar et al., 2014	NWA 5073	Zrc7	15.82	0.138	114	58
Roszjar et al., 2014	NWA 5073	Zrc8	16.56	0.070	237	121
Roszjar et al., 2014	NWA 5073	Zrc9	16.54	0.166	99	51
Roszjar et al., 2014	NWA 5073	Zrc10	16.40	0.205	80	41
Roszjar et al., 2014	NWA 5073	Zrc11	16.26	0.179	91	46
Roszjar et al., 2014	NWA 5073	Zrc12	16.51	0.167	99	50
Roszjar et al., 2014	NWA 5073	Zrc13	16.16	0.190	85	44
Roszjar et al., 2014	NWA 5356	Zr1	16.30	0.217	75	38
Roszjar et al., 2014	NWA 5356	Zr2a	16.03	0.201	80	41
Roszjar et al., 2014	NWA 5356	Zr2b	16.19	0.178	91	47
Roszjar et al., 2014	NWA 5356	Zr3	16.39	0.183	89	46
Roszjar et al., 2014	NWA 5356	Zr4	16.29	0.214	76	39
Roszjar et al., 2014	NWA 5356	Zr5	16.48	0.164	100	51
Roszjar et al., 2014	NWA 5356	Zr6	16.55	0.188	88	45
Roszjar et al., 2014	Sah 98110	Zrc1	15.48	0.210	74	38
Roszjar et al., 2014	Sah 98110	Zrc2	15.22	0.186	82	42
Roszjar et al., 2014	Sah 98110	Zrc6*	16.17	0.215	75	38
Roszjar et al., 2014	Sah 98110	Zrc3	15.96	0.185	86	44
Roszjar et al., 2014	Sah 98110	Zrc20*	15.64	0.177	88	45
Roszjar et al., 2014	Sah 98110	Zrc23*	16.38	0.225	73	37
Roszjar et al., 2014	Sah 98110	Zrc4	15.97	0.190	84	43
Roszjar et al., 2014	Sah 98110	ZrcNest1*	16.25	0.225	72	37
Roszjar et al., 2014	Sah 98110	ZrcNest5*	15.87	0.177	90	46
Haba et al., 2014	Y-75011	zircon 1	16.02	0.214	75	38
Haba et al., 2014	Y-75011	zircon 2	16.14	0.201	80	41
Haba et al., 2014	Y-75011	zircon 3	16.28	0.191	85	44
Haba et al., 2014	Y-82082-1	zircon1 clast1b	15.95	0.200	80	41
Haba et al., 2014	Y-82082-1	zircon2 clast1b	16.18	0.127	127	65
Haba et al., 2014	Y-82082-1	zircon3 clast1b	16.10	0.184	88	45
Haba et al., 2014	Y-82082-1	zircon4 clast2	16.15	0.208	78	40
Haba et al., 2014	Y-82082-2	zircon1 clast1	16.06	0.211	76	39
Haba et al., 2014	Y-82082-2	zircon2-1 clast1	16.29	0.179	91	47
Haba et al., 2014	Y-82082-2	zircon2-2 clast1	16.28	0.153	106	54
Haba et al., 2014	Stannern-1	zircon1	16.08	0.202	80	41
Haba et al., 2014	Stannern-1	zircon2	16.15	0.191	85	43
Haba et al., 2014	Stannern-1	zircon3	16.18	0.192	84	43
Haba et al., 2014	Stannern-1	zircon4	16.10	0.261	62	32
Haba et al., 2014	Stannern-1	zircon5	16.23	0.204	80	41
Haba et al., 2014	Stannern-1	zircon6	16.10	0.166	97	50
Haba et al., 2014	Stannern-1	zircon7	16.13	0.220	73	37
Haba et al., 2014	Stannern-1	zircon8	16.04	0.222	72	37
Haba et al., 2014	Stannern-1	zircon9	16.20	0.180	90	46
Haba et al., 2014	Stannern-1	zircon10	16.06	0.206	78	40
Haba et al., 2014	Stannern-1	zircon11	16.13	0.131	124	63
Haba et al., 2014	Stannern-1	zircon12	16.22	0.261	62	32
Haba et al., 2014	Stannern-1	zircon13	16.30	0.204	80	41
Haba et al., 2014	Stannern-1	zircon14	16.16	0.184	88	45
Haba et al., 2014	Stannern-1	zircon15	16.08	0.213	76	39
Haba et al., 2014	Stannern-1	zircon16	16.26	0.169	96	49
Haba et al., 2014	Stannern-2	zircon1	16.33	0.191	86	44
Haba et al., 2014	Stannern-2	zircon2	16.20	0.201	81	41

Study	Meteorite	Sample	Zr[a]	Hf[a]	Zr/Hf	Zr/Hf[b]
Haba et al., 2014	Stannern-2	zircon3	16.03	0.228	70	36
Haba et al., 2014	Stannern-2	zircon4-1	16.37	0.154	106	54
Haba et al., 2014	Stannern-2	zircon4-2	16.18	0.206	78	40
Haba et al., 2014	Stannern-2	zircon5	16.19	0.124	131	67
Haba et al., 2014	Stannern-2	zircon6	15.30	0.220	70	36
Haba et al., 2014	Stannern-2	zircon7	16.05	0.259	62	32
Haba et al., 2014	Stannern-2	zircon8	16.11	0.191	85	43
Haba et al., 2014	Juvinas	zircon1	16.43	0.177	93	48
Haba et al., 2014	Juvinas	zircon2-1	16.27	0.122	133	68
Haba et al., 2014	Juvinas	zircon2-2	16.31	0.118	139	71
Haba et al., 2014	Juvinas	zircon2-3	16.37	0.117	140	72
Haba et al., 2014	Y-792510	zircon1-1	16.23	0.187	87	44
Haba et al., 2014	Y-792510	zircon1-2	16.29	0.186	88	45
Haba et al., 2014	Y-792510	zircon2-1	16.10	0.188	86	44
Haba et al., 2014	Y-792510	zircon2-2	16.32	0.180	91	46
Haba et al., 2014	Y-792510	zircon3	16.19	0.202	80	41
Haba et al., 2014	Y-792510	zircon4	16.05	0.188	86	44
Haba et al., 2014	Y-792510	zircon5-1	16.32	0.208	79	40
Haba et al., 2014	Y-792510	zircon5-2	16.37	0.185	88	45
Haba et al., 2014	Y-792510	zircon6	16.30	0.196	83	42
Haba et al., 2014	Y-792510	zircon7	16.43	0.196	84	43
Haba et al., 2014	Y-792510	zircon8-1	16.07	0.225	71	36
Haba et al., 2014	Y-792510	zircon8-2	16.13	0.179	90	46
Haba et al., 2014	Y-792510	zircon9-1	16.26	0.193	84	43
Haba et al., 2014	Y-792510	zircon9-2	16.21	0.192	84	43
Haba et al., 2014	A-881467-1	zircon1-1	16.14	0.155	104	53
Haba et al., 2014	A-881467-1	zircon1-2	16.12	0.155	104	53
Haba et al., 2014	A-881467-1	zircon2-1	16.34	0.164	100	51
Haba et al., 2014	A-881467-1	zircon2-2	16.23	0.193	84	43
Haba et al., 2014	A-881467-1	zircon3	16.24	0.181	90	46
Haba et al., 2014	A-881467-1	zircon4	16.30	0.168	97	50
Haba et al., 2014	A-881467-1	zircon5	16.23	0.209	78	40
Haba et al., 2014	A-881467-1	zircon6	16.35	0.183	89	46
Haba et al., 2014	A-881467-1	zircon7	16.19	0.174	93	48
Haba et al., 2014	A-881467-2	zircon1	16.40	0.181	91	46
Haba et al., 2014	A-881467-2	zircon2	16.20	0.193	84	43
Haba et al., 2014	A-881467-2	zircon3	16.16	0.173	93	48
Haba et al., 2014	A-881467-2	zircon4	16.37	0.187	87	45
Haba et al., 2014	A-881467-2	zircon5	16.34	0.207	79	40

B.R. = Bunburra Rockhole

[a] = measured (this study) and calculated (other studies) values in atomic percent (at.%).

[b] is the Zr/Hf ratio based on the atomic weight %.

References

Anders, E., and Grevesse, N., 1989, Abundances of the elements: Meteoritic and solar: Geochimica et Cosmochimica Acta, v. 53, no. 1, p. 197-214.

Barrat, J. A., Zanda, B., Moynier, F., Bollinger, C., Liorzou, C., and Bayon, G., 2012, Geochemistry of CI chondrites: Major and trace elements, and Cu and Zn Isotopes: Geochimica et Cosmochimica Acta, v. 83, p. 79-92.

Benedix, G. K., Bland, P. A., Friedrich, J. M., Mittlefehldt, D. W., Sanborn, M. E., Yin, Q. Z., Greenwood, R. C., Franchi, I. A., Bevan, A. W. R., Towner, M. C., Perrotta, G. C., and Mertzman, S. A., 2017, Bunburra Rockhole: Exploring the geology of a new differentiated asteroid: Geochimica et Cosmochimica Acta, v. 208, p. 145-159.

Binzel, R. P., and Shui, X., 1993, Chips off of asteroid 4 Vesta: Evidence for the parent body: Science, v. 260, no. 5105, p. 186.

Bland, P. A., Spurný, P., Towner, M. C., Bevan, A. W. R., Singleton, A. T., Bottke, W. F., Greenwood, R. C., Chesley, S. R., Shrbený, L., Borovička, J., Ceplecha, Z., McClafferty, T. P., Vaughan, D., Benedix, G. K., Deacon, G., Howard, K. T., Franchi, I. A., and Hough, R. M., 2009, An Anomalous Basaltic Meteorite from the Innermost Main Belt: Science, v. 325, no. 5947, p. 1525-1527.

Blum, T. B., Darling, J. R., Kelly, T. F., Larson, D. J., Moser, D. E., Perez-Huerta, A., Prosa, T. J., Reddy, S. M., Reinhard, D. A., Saxey, D. W., Ulfig, R. M., and Valley, J. W., 2018, Best practices for reporting atom probe analysis of geological materials, in Moser, D. E., Corfu, F., Darling, J. R., Reddy, S. M., and Tait, K., eds., Microstructural Geochronology: Planetary Records Down to Atom Scale: USA, American Geophysical Union, p. 416.

Bouvier, L. C., Costa, M. M., Connelly, J. N., Jensen, N. K., Wielandt, D., Storey, M., Nemchin, A. A., Whitehouse, M. J., Snape, J. F., Bellucci, J. J., Moynier, F., Agranier, A., Gueguen, B., Schönbächler, M., and Bizzarro, M., 2018, Evidence for extremely rapid magma ocean crystallization and crust formation on Mars: Nature, v. 558, no. 7711, p. 586-589.

Exertier, F., La Fontaine, A., Corcoran, C., Piazolo, S., Belousova, E., Peng, Z., Gault, B., Saxey, D. W., Fougerouse, D., Reddy, S. M., Pedrazzini, S., Bagot, P. A. J., Moody, M. P., Langelier, B., Moser, D. E., Botton, G. A., Vogel, F., Thompson, G. B., Blanchard, P. T., Chiaramonti, A. N., Reinhard, D. A., Rice, K. P., Schreiber, D. K., Kruska, K., Wang, J., and Cairney, J. M., 2018, Atom probe tomography analysis of the reference zircon gj-1: An interlaboratory study: Chemical Geology, v. 495, p. 27-35.

Haba, M. K., Yamaguchi, A., Horie, K., and Hidaka, H., 2014, Major and trace elements of zircons from basaltic eucrites: Implications for the formation of zircons on the eucrite parent body: Earth and Planetary Science Letters, v. 387, p. 10-21.

Hutchison, R., 2006, Meteorites: a petrologic, chemical, and isotopic synthesis, New York, Cambridge University Press.

Iizuka, T., Yamaguchi, T., Hibiya, Y., and Amelin, Y., 2015, Meteorite zircon constraints on the bulk Lu-Hf isotope composition and early differentiation of the Earth: Proceedings of the National Academy of Sciences of the United States of America, v. 112, no. 17, p. 5331-5336.

Ireland, T. R., and Wlotzka, F., 1992, The oldest zircons in the solar system: Earth and Planetary Science Letters, v. 109, no. 1, p. 1-10.

Jourdan, F., Benedix, G., Eroglu, E., Bland, P. A., and Bouvier, A., 2014, 40Ar/39Ar impact ages and time–temperature argon diffusion history of the Bunburra Rockhole anomalous basaltic achondrite: Geochimica et Cosmochimica Acta, v. 140, p. 391-409.

Kelly, T. F., and Larson, D. J., 2012, Atom Probe Tomography 2012: Annual Review of Materials Research, v. 42, no. 1, p. 1-31.

Larson, D. J., Prosa, T. J., Ulfig, R. M., Geiser, B. P., and Kelly, T. F., 2013, Local Electrode Atom Probe Tomography: A user's guide: New York, Springer, p. 318.

Lodders, K., 2003, Solar system abundances and condensation temperatures of the elements: The Astrophysical Journal, v. 591, no. 2, p. 1220-1247.

Marvin, U. B., and Klein, C., 1964, Meteoritic Zircon: Science, v. 146, no. 3646, p. 919-920.

McSween, H. Y., 1999, Meteorites and their parent planets, New York, Cambridge University Press.

McSween Jr, H. Y., Mittlefehldt, D. W., Russell, C. T., and Raymond, C. A., 2013, Overview of the composition of asteroid 4 Vesta: Constraints from the Dawn spacecraft mission and HEDs: Meteoritics & Planetary Science, v. 48, no. 11, p. 2073-2075.

Misawa, K., Yamaguchi, A., and Kaiden, H., 2005, U-Pb and 207Pb-206Pb ages of zircons from basaltic eucrites: Implications for early basaltic volcanism on the eucrite parent body: Geochimica et Cosmochimica Acta, v. 69, no. 24, p. 5847-5861.

Moser, D. E., Chamberlain, K. R., Tait, K. T., Schmitt, A. K., Darling, J. R., Barker, I. R., and Hyde, B. C., 2013, Solving the Martian meteorite age conundrum using micro-baddeleyite and launch-generated zircon: Nature, v. 499, no. 7459, p. 454.

Münker, C., Pfänder, J. A., Weyer, S., Büchl, A., Kleine, T., and Mezger, K., 2003, Evolution of Planetary Cores and the Earth-Moon System from Nb/Ta Systematics: Science, v. 301, no. 5629, p. 84-87.

Patzer, A., Pack, A., and Gerdes, A., 2010, Zirconium and hafnium in meteorites: Meteoritics & Planetary Science, v. 45, no. 7, p. 1136-1151.

Rayman, M. D., and Mase, R. A., 2014, Dawn′s exploration of Vesta: Acta Astronautica, v. 94, no. 1, p. 159-167.

Reddy, S. M., Saxey, D. W., Rickard, W. D. A., Fougerouse, D., Montalvo, S. D., Verberne, R., and van Riessen, A., 2020, Atom probe tomography: development and application to the geosciences: Geostandards and Geoanalytical Research, v. 44, no.1, p. 5-50.

Roszjar, J., Whitehouse, M. J., and Bischoff, A., 2014, Meteoritic zircon – Occurrence and chemical characteristics: Chemie der Erde - Geochemistry, v. 74, no. 3, p. 453-469.

Saxey, D. W., Moser, D. E., Piazolo, S., Reddy, S. M., and Valley, J. W., 2018a, Atomic worlds: Current state and future of atom probe tomography in geoscience: Scripta Materialia, p. 115-121.

Saxey, D. W., Reddy, S. M., Fougerouse, D., and Rickard, W. D. A., 2018b, The Optimization of Zircon Analyses by Laser-Assisted Atom Probe Microscopy, in Moser, D. E., Corfu, F., Darling, J. R., Reddy, S. M., and Tait, K., eds., Microstructural Geochronology: Planetary Records down to Atom Scale, American Geophysical Union & John Wiley and Sons, Inc., p. 293-313.

Saxey, D. W., Fougerouse, D., Rickard, W. D. A., and Reddy, S., 2019, Spatial Reconstruction of Atom Probe Data from Zircon: Microscopy and Microanalysis, v. 25, p. 2536-2537.
Scott, E. R. D., Greenwood, R. C., Franchi, I. A., and Sanders, I. S., 2009, Oxygen isotopic constraints on the origin and parent bodies of eucrites, diogenites, and howardites: Geochimica et Cosmochimica Acta, v. 73, no. 19, p. 5835-5853.
Sliwinski, J. T., Kueter, N., Marxer, F., Ulmer, P., Guillong, M., and Bachmann, O., 2018, Controls on lithium concentration and diffusion in zircon: Chemical Geology, v. 501, p. 1-11.
Spivak-Birndorf, L. J., Bouvier, A., Benedix, G. K., Hammond, S., Brennecka, G. A., Howard, K., Rogers, N., Wadhwa, M., Bland, P. A., Spurný, P., and Towner, M. C., 2015, Geochemistry and chronology of the Bunburra Rockhole ungrouped achondrite: Meteoritics & Planetary Science, v. 50, no. 5, p. 958-975.
Spurný, P., Bland, P. A., Shrbený, L., Borovička, J., Ceplecha, Z., Singelton, A., Bevan, A. W. R., Vaughan, D., Towner, M. C., McClafferty, T. P., Toumi, R., and Deacon, G., 2012, The Bunburra Rockhole meteorite fall in SW Australia: fireball trajectory, luminosity, dynamics, orbit, and impact position from photographic and photoelectric records: Meteoritics & Planetary Science, v. 47, no. 2, p. 163-185.
Takeda, H., 1997, Mineralogical records of early planetary processes on the howardite, eucrite, diogenite parent body with reference to Vesta: Meteoritics & Planetary Science, v. 32, no. 6, p. 841-853.
Trinquier, A., Birck, J. L., and Allegre, C. J., 2007, Widespread54Cr Heterogeneity in the Inner Solar System: The Astrophysical Journal, v. 655, no. 2, p. 1179-1185.
Ushikubo, T., Kita, N. T., Cavosie, A. J., Wilde, S. A., Rudnick, R. L., and Valley, J. W., 2008, Lithium in Jack Hills zircons: Evidence for extensive weathering of Earth's earliest crust: Earth and Planetary Science Letters, v. 272, no. 3–4, p. 666-676.
Weisberg, M. K., Smith, C., Benedix, G., Folco, L., Righter, K., Zipfel, J., Yamaguchi, A., and Chennaoui Aoudjehane, H., 2009, The Meteoritical Bulletin, No. 95: Meteoritics & Planetary Science, v. 44, no. 3, p. 429-462.
Welten, K. C., Meier, M. M. M., Caffee, M. W., Laubenstein, M., Nishizumi, K., Wieler, R., Bland, P. A., Towner, M. C., and Spurný, P., 2012, Cosmic-ray exposure age and preatmospheric size of the Bunburra Rockhole achondrite: Meteoritics & Planetary Science, v. 47, no. 2, p. 186-196.

Chapter 3 COMPLEX HISTORY OF A DETRITAL ZIRCON OBTAINED BY TEXTURAL AND TRACE ELEMENT ANALYSES

This chapter is nearing submission to the Chemical Geology journal.

The principal roles of each co-author are as follows:

Stephanie D. Montalvo: Concept and design of the work; sample preparation; data acquisition, analysis and interpretation (SE, BSE, CL, EBSD, APT, TEM, Raman); manuscript writing and editing.

Steven M. Reddy: Concept and design of the work; data acquisition, analysis and interpretation (SE, BSE, EBSD); manuscript editing.

David W. Saxey: Analysis and interpretation of the APT data; manuscript editing.

William D.A. Rickard: Data interpretation; manuscript editing.

Denis Fougerouse: Data acquisition, analysis and interpretation (APT, TEM, Raman); manuscript editing.

Chris Kirkland: Geochronological data acquisition, analysis and interpretation (SHRIMP).

Complex history of a detrital zircon obtained by textural and trace element analyses

Stephanie D. Montalvo[a,b,*], Steven M. Reddy[a,b], David W. Saxey[a], William D.A. Rickard[a], Denis Fougerouse[a,b], Thorsten Geisler[c], Tim E. Johnson[b,d], Chris Kirkland[b], and Alexander G. Webb[e]

[a] Geoscience Atom Probe, John de Laeter Centre, Curtin University, Perth, Australia.
[b] School of Earth and Planetary Science, Curtin University, Perth, Australia.
[c] Institute for Geosciences and Meteorology, University of Bonn, Bonn, Germany.
[d] Center for Global Tectonics, State Key laboratory of Geological Processes and Mineral Resources, China University of Geosciences, Wuhan, Hubei Province 430074, China.
[e] Department of Earth Science and laboratory for Space Research, University of Hong Kong, Hong Kong
* Email: s.montalvo@postgrad.curtin.edu.au

Abstract

The coupled trace element composition and U-Th-Pb age of detrital zircon is being increasingly used to constrain the source provenance and evolution of source rocks that are no longer exposed at the Earth's surface. The correct interpretation of such data requires an understanding of the potentially complex processes that may modify the trace element geochemistry of zircon, e.g. metamorphism, hydrothermal alteration and weathering. A metamorphosed detrital zircon grain from the Lalla Rookh Sandstone formation of the Pilbara craton in Western Australia was analysed using atom probe tomography (APT) and transmission electron microscopy (TEM) to develop an understanding of the range of mechanisms that may be responsible for trace element modification of the complex detrital zircon grain.

This grain comprises a partially recrystallised, zoned igneous core and metamorphic rim. The latter has been significantly affected by fluid alteration spatially associated to radial fractures, interpreted to have formed as a response to radiation damage in the core. Geochronological analyses conducted with a sensitive high resolution ion microprobe (SHRIMP) reveal a crystallization age of 3531 ± 12

Ma for the discordant analyses from the core and a 3295 ± 6 Ma metamorphic event age for the rim. The discordancy of the data suggests a recent open system behaviour for the zircon grain.

The APT nanoscale geochemical analysis shows different concentrations of trace elements from the different textural components of the grain, with the metamict regions having the highest concentration. The APT data from the different subdivisions, show large variations in APT specimen yield that suggest the yield is correlated with the chemistry of the sample. However, the specimens from the crystalline region in the core contains nanoscale Pb clusters that formed by an unknown previous mechanism during the metamorphic event that created the core–rim structure of the grain. The TEM analysis shows a trace elements enrichment in the healed fractures and a heterogeneous distribution of nanoscale size voids in the grains structure. The U enrichment in the fractures supports a recent U-gain scenario over a Pb-loss. The complexity of textures in the rim and the U-gain through fractures can be developed by recent hydrothermal alteration or by weathering processes. Establishing a workflow to analyse the trace element composition of the different textural components, the complex history of the metamorphosed detrital zircon grain can be determined.

Keywords: zircon, detrital, hydrothermal, atom probe tomography, nanoscale, geochemistry, trace element, geochronology

Introduction

Zircon ($ZrSiO_4$) is an accessory mineral that is commonly used in geochemical and geochronological studies because of its ability to incorporate trace elements in its structure, especially uranium (U) and thorium (Th). The incorporation of trace elements during crystallization leads to the heterogeneous compositional variations, which can be seen at µm scale (e.g. zoning) (Corfu et al., 2003). The study of trace elements in zircon grains provides fundamental information about the timing and evolution of geological events. Detrital zircon grains have been used to determine their provenance, age of deposition, tectonic reconstruction, in paleogeography studies and to study the early history of Earth and eroded impact structures (e.g. Gray and Zeitler, 1997; Rainbird et al., 2001; Belousova et al., 2002;

Fedo et al., 2003; Cavosie et al., 2010; Thomson et al., 2014). However, multiple studies have shown that the trace element geochemistry of zircon may be modified by a range of different processes (Hoskin and Black, 2000; Ewing et al., 2003; Utsunomiya et al., 2004; Hoskin, 2005; Reddy et al., 2006). Processes that have been shown to disturb the trace element composition of zircon include, but are not limited to, radiation, metamorphism, hydrothermal/fluid alteration, deformation and weathering (e.g. Hoskin and Black, 2000; Geisler et al., 2003; Hoskin, 2005; Geisler et al., 2007; Martin et al., 2008; Pidgeon et al., 2013; Pidgeon et al., 2019).

The processes mentioned above themselves contain a myriad of mechanisms that may affect trace element composition and mobility in different ways. Since zircon grains can incorporate radioactive elements in their structure during crystallization, there is a high probability of self-induced radiation damage for the grain over geological timescales. One of the sources for damage to the structure is α-recoil from the decay of radioactive elements (Romer, 2003), which can result in an open system behaviour and disturb the composition of the grain (Silver and Deutsch, 1963). Murakami et al. (1991) proposed a relationship between the amount of radiation damage, α-decay dose and crystal structure in a zircon grain. It consists of three stages, where in stage 1, isolated point defects start to accumulate in the structure ($< 3x10^{15}$ α-decay events/mg). In stage 2, the structure is distorted creating amorphous regions ($3x10^{15} – 8x10^{15}$ α-decay events/mg), and in stage 3 at $> 8x10^{15}$ α-decay events/mg the structure of the grain becomes irregular. In addition, the process of metamictisation can induce fractures in the grain (Chakoumakos et al., 1987; Lee and Tromp, 1995) that can facilitate trace element mobility and impact the U-Th-Pb system.

Crystal-plastic deformation can also modify the chemical composition of zircon grains by producing microstructures that act as fast-diffusion pathways for trace elements (Reddy et al., 2006; Timms et al., 2006; Reddy et al., 2007; Piazolo et al., 2012). This deformation results from the distortion of the crystal lattice by an external force and has been shown to also modify the cathodoluminescence (CL) response of the zircon grain (Reddy et al., 2006; Timms et al., 2006; Reddy et al., 2007; Timms and Reddy, 2009).

Metamorphic zircon may form by the growth of new zircon, by the recrystallisation of pre-existing zircon or by alteration (Rubatto, 2017), in the presence or absence of fluids (Vonlanthen et al., 2012; Rubatto, 2017). New growth

has a different composition from the pre-existing grain, forms sharp boundaries and it is restricted by the Zr concentration in the system the grain is in (Martin et al., 2008; Kohn et al., 2015; Rubatto, 2017). Commonly, recrystalization involves a change in chemical composition at subsolidus (Vonlanthen et al., 2012; Rubatto, 2017). Alteration is defined as a disturbance to the pre-existing zircon while preserving its chemical composition (Rubatto, 2017).

Recent studies have found that during weathering, areas damaged by radiation in zircon grains can incorporate trace elements into its structure by weathering-fluids (Pidgeon et al., 2013; Pidgeon et al., 2019). The incorporation and deposition of trace elements (Fe, Ca, Al, Y, U and Th) was identified to occur in fractures and mineralized zones within the zircon grains, suggesting a recent U-gain instead of Pb-loss (Pidgeon et al., 2019).

To correctly interpret the geochemical and geochronological data from detrital zircon, the effect of such processes during the complex geological evolution of the grain needs to be understood. This research uses atom probe tomography (APT) and transmission electron microscopy (TEM), in conjunction with conventional techniques, to obtain the nanogeochemistry of several textural subdivisions within a metamorphosed detrital zircon grain from the Lalla Rookh Sandstone of the Pilbara craton. The aim of this research is to isolate and compare the chemistry of the complex textures to understand the formation and evolution of the grain. This research also explores what influence the different textures of the zircon grain have on the yield of the APT specimens.

Geologic settings

To establish the interaction of metamorphism, hydrothermal alteration and weathering on detrital zircon, we undertook a detailed and systematic analysis of a single detrital zircon from the Lalla Rookh Sandstone (LRS), Australia. The LRS is located within the East Pilbara granite-greenstone terrane of the Pilbara craton in Western Australia (Fig. 3.1) and belongs to the De Grey Supergroup (Krapez and Barley, 1987; Van Kranendonk et al., 2002; Van Kranendonk, 2008). This terrane consists of round shaped granitoid complexes, greenstone belts and greenstone complexes (volcano-sedimentary rocks) (Van Kranendonk et al., 2002).

The LRS lies above the Warrawoona Group, Soanesville Group and granitoid batholiths (Fig. 3.1a) and it is unconformably overlain by the Lower Proterozoic Fortescue Group (Geoscience Australia and Australian Stratigraphy Commission, 2017; Stüeken and Buick, 2018). LRS belongs to one of the greenstone complexes and it is bound by unconformities and high-angle faults (Krapez and Barley, 1987; Geoscience Australia and Australian Stratigraphy Commission, 2017; Stüeken and Buick, 2018). The age of the LRS is poorly constrained to ~3000 Ma based on tectonostratigraphic correlations to the 2991 ± 12 Ma Whim Creek Group (Krapez and Barley, 1987; Barley et al., 1994).

The 2-3 km thick Lalla Rookh Sandstone contains sediments from braided streams, lacustrine, fan deltas and alluvial fan deposits (Fig. 3.1b) (Krapez and Barley, 1987; Stüeken and Buick, 2018). Its lithology is mostly sandstones and conglomerates, with up to 85% of the sequence being sandstones (Krapez and Barley, 1987; Geoscience Australia and Australian Stratigraphy Commission, 2017). The environment of the Lalla Rookh Sandstone is interpreted to be a low-strain and low-grade metamorphic (sub-greenschist facies) (Krapez and Barley, 1987; Stüeken and Buick, 2018).

Analytical methodology

The sample used in this study (AW 18-7-15-6), is a coarse pebbly sandstone collected from an alluvial fan deposit of the Lalla Rookh Sandstone. The sample was fragmented using a SelFrag high-voltage pulse, power fragmentation instrument and individual grains were separated with heavy liquids (sodium polytungstate - 2.82 g/cm^3) and a Frantz magnetic separator, all instruments located at Curtin University, Western Australia. Zircon grains were then handpicked and fixed in a 1” round using epoxy. The sample was polished using standard mechanical diamond polishing techniques and was then polished with 60 nm colloidal silica on a Vibromet II polisher. The sample was then coated with a 5 nm layer of carbon. Zircon grains were imaged using secondary electron (SE), backscattered electron (BSE) and CL with a Tescan MIRA3 field emission (FE) scanning electron microscopy (SEM) and a Tescan LYRA3 focused ion beam (FIB) SEM, both housed in the John de Laeter Centre at Curtin University, Western Australia. SE and BSE images were collected using an accelerating voltage of 20 kV and beam current of 0.5 nA at a working

distance of 15 mm, whilst CL imaging was undertaken using 12 kV and at a working distance of 16 mm. From these data, a single zircon grain (002) was selected for further analysis based on its complex textural features (Fig. 3.2).

Microstructural analysis by electron backscatter diffraction (EBSD) was conducted with the Tescan MIRA3 FE-SEM, using an accelerating voltage of 20 kV, beam current of ~0.8 nA, working distance of 20 mm, and 70º sample tilt. Electron backscatter diffraction patterns (EBSPs) were collected using a Nordlys Nano high-resolution detector and Oxford Instruments AZtec 4.0 SP2 software. The EBSD analysis of the zircon grain was collected using a 500 nm step size providing ~150,000 EBSPs. All EBSD maps were processed using the Tango module of the Oxford Instruments Channel5 software (version 5.12.72). The data were noise reduced using typical wild spikes and 6 nearest neighbour zero solutions. Different maps are used to illustrate the microstructures within the grain (Fig. 3.2a,c). Band contrast (BC) maps shows the quality of the EBSPs and texture component (TC) maps are used to display the crystallographic variations within the grain with respect to a user-defined reference point (for more details see Reddy et al., 2007).

Laser-Raman spectroscopy was used to study the internal structure of the zircon grain. The spectra were acquire using a Horiba Scientific LabRam HR800 Raman spectrometer with the 532.18 nm line of a ~30 mW Nd:YAG laser. This instrument is housed at the Institute of Geosciences and Meteorology of the University of Bonn, Germany. A 50X objective with a numerical aperture of 0.7 was used, yielding a lateral spot size at sample surface of about 1 µm. The spectral resolution was 3.5 cm^{-1} and a confocal hole of 300 µm was used. The Raman light was dispersed by a grating of 600 grooves per mm. The Ne line at 1707.06 cm^{-1} was used to correct any spectrometer drift during the mapping procedure. The size of the imaged area was 101 x 101 μm^2 with a pixel spacing of 2 µm. Gauss-Lorentz and a 2nd order polynomial functions were used for fitting the Raman spectra in the frequency range between 700 and 1200 cm-1. The measured band width ($FWHM_{meas}$) was corrected for the finite spectrometer entrance slit (100 µm) using the formula:

$$FWHM_{corr} = FWHM_{meas}(1 - (spectral\ resolution/FWHM_{meas})^2)$$

where FWHM means full width at half maximum (Tanabe and Hiraishi, 1980).

The electron microscopy techniques outlined above were used to identify target areas in zircon grain 002 for APT and TEM analyses. Once regions of interest

had been identified, atom probe specimens were prepared using a 30 kV Ga^+ sourced FIB-SEM. The details of the sample preparation process are given elsewhere (Reddy et al., 2020), and involved electron deposition of Pt buttons at the site selected for atom probe specimen, followed by the FIB deposition of a ~200 nm thick platinum protection layer. The region of interest was milled as a wedge and atom probe specimens were sequentially welded onto the post of prefabricated silicon carrier microtip. Each specimen was then individually sharpened by a series of annular milling steps to shape each specimen into a < 100 nm diameter sharp needle. A final 5 kV annular mill was used to remove the damage caused by the 30 kV Ga^+ ion beam during standard milling. The APT specimens were labelled following a conventional naming protocol, where each specimen is represented by MX, where X represent the number of the specimen. To distinguish between different carriers (also known as coupons), a '*' was added to some of the specimens (e.g. M7 vs. M7*). A total of 31 APT specimens were prepared and analysed in this study.

Laser-assisted APT analyses were performed with a Cameca LEAP 4000X HR at the Geoscience Atom Probe Facility housed in the John de Laeter Centre at Curtin University. APT is a three-dimensional (3D) analytical technique that provides the location and identity of field-evaporated ions using time-of-flight mass spectrometry and a position sensitive detector. A combination of a ultra-high vacuum, cryogenic temperature, an applied voltage, and pulsed laser is used to trigger field evaporation and ionisation of the atoms from the tip of the needle specimen, resulting in positive ions accelerated towards the position sensitive detector. Details of the APT instrumentation and analytical protocols are given by Reddy et al. (2020). The processing and reconstruction of the APT data was undertaken using Cameca Integrated Visualization & Analysis Software (IVAS) version 3.8.2. During these processes, the positions of the ion-hit are converted into 3D spatial coordinates and the chemical identities of the ions are determined. In-depth description of these processes can be found elsewhere (Kelly and Larson, 2012; Larson et al., 2013a; Larson et al., 2013b). Details of the acquisition, processing and reconstruction parameters used in this study are given in Table 3.1.

Table 3.1 APT data acquisition settings for the specimens.

Data set /specimen	**M9***	**M10***	**M11***	**M1**	**M2**	**M3**	**M4**	**M8***
Regions	dark core							interface (dark – light core)
Instrument Model	LEAP 4000X HR							
Instrument Settings								
Laser wavelength (nm)	355							
Laser pulse energy (pJ)	400	400	400	300	250	250	250	400
Pulse frequency (kHz)	200	200	200	250	250	250	250	200
Evaporation control	Detection rate							
Targeted det. rate (ions/pulse)	0.005	0.005	0.005	0.01	0.005	0.004	0.005	0.01
Nominal flight path (mm)	382							
Set point temperature (K)	70	60	70	50	80	80	80	70
Sample temperature (K)	80.7	69.2	80.6	57.3	87.8	-	92	80.7
Chamber pressure (e^{-10} Torr)	1.4	1.3	1.4	1.8	2.2	1.9	1.9	1.4
Data Summary								
LAS Root version	15.41.342l							
CAMECAROOT version	18.46.428							
Analysis Software	IVAS 3.8.2							
Total Ions:	87,229	3 million	1.5 million	219,398	776,821	955,951	257,274	194,976
% Single	60.8	78	76.4	76.4	70.3	71.1	75.9	56.4
% Multiple	37.5	21.2	22.8	20.8	27.9	26.4	21.2	40.9
% Partial	1.7	0.7	0.8	2.8	1.8	2.6	2.9	2.6
Volt./bowl corr. peak (Da)	32	16	16	32	32	32	32	69
Mass Calib. (peaks/interp.)	7/Lin.	12/Lin.	8/Lin.	7/Lin.	8/Lin.	8/Lin.	8/Lin.	6/Lin.
*(M/ΔM)	527.9	1052.7	1127.1	723.6	975.2	920.0	950.4	718.0
**(M/ΔM10)	23.6	204.8	231.2	76.6	167.9	129.6	130.2	152.2
Time independent background (ppm/ns)	218.046	32.814	42.433	85.225	169.235	252.382	162.979	33.019
Reconstruction								
Final specimen state	F	F	F	F	F	F	F	F
Pre-/post-analysis imaging	SEM							
Radius evolution model	'Voltage'							
Field factor (k)	3.3							
Image compression factor	1.65							
Assumed E-field (V/nm)	32							
Detector efficiency	0.36							
Avg. atomic volume (nm^3)	0.01076							
V initial (V)	3787	5559	5516	2133	4635	2818	3443	1000
V final (V)	4014	7456	6531	2164	5425	4360	4430	2457

*ΔM is full width at half maximum of the Volt./bowl corr. peak
**ΔM10 is full width at tenth maximum of the Volt./bowl corr. peak
det. = detection; Volt. = voltage; corr. = correction; Calib. = calibration; interp. = interpolation; Lin. = linearization method; Avg. = average; F = Fractured; NF = not fractured; - = not recorded

Data set /specimen	**M6***	**M7***	**M5**	**M7**	**M8[a]**	**M9**	**M10**	**M19**	**M20**
Regions	light core								
Instrument Model	LEAP 4000X HR								
Instrument Settings									
Laser wavelength (nm)	355								
Laser pulse energy (pJ)	400	400	250	300	300	250	250	250	250
Pulse frequency (kHz)	250	200	250	250	250	250	250	250	250
Evaporation control	Detection rate								
Targeted det. rate (ions/pulse)	0.005	0.005	0.006	0.007	0.006	0.005	0.005	0.005	0.005
Nominal flight path (mm)	382								
Set point temperature (K)	70	70	80	80	80	80	80	80	80
Sample temperature (K)	80.7	80.7	92	92	92	92	91.4	92	92
Chamber pressure (e^{-10} Torr)	1.4	1.4	2.0	1.9	2.1	2.0	2.1	2.4	1.8
Data Summary									
LAS Root version	15.41.342l								
CAMECAROOT version	18.46.428								
Analysis Software	IVAS 3.8.2								
Total Ions:	2.5 million	55 million	72 million	4 million	3.5 million	55 million	63 million	94 million	76 million
% Single	78	77.7	72.3	71.2	82.9	74.1	74.7	73.9	73.4
% Multiple	21.2	21.8	27	27.9	15.9	25.1	24.5	25.3	25.9
% Partial	0.7	0.5	0.7	0.9	1.2	0.8	0.8	0.7	0.7
Volt./bowl corr. peak (Da)	16								
Mass Calib. (peaks/interp.)	12/Lin.	8/Lin.	11/Lin.	10/Lin.	10/Lin.	10/Lin.	10/Lin.	10/Lin.	11/Lin.
*(M/ΔM)	1062.9	1005.3	1030.0	1011.3	1032.2	1026.6	1007.7	1022.6	1024.0
**($M/\Delta M_{10}$)	198.7	199.4	198.9	182.6	197.2	196.9	197.2	194.2	197.8
Time independent background (ppm/ns)	32.403	35.757	53.890	56.053	92.711	66.305	68.514	69.673	64.773
Reconstruction									
Final specimen state	F	NF	NF	F	F	NF	NF	NF	NF
Pre-/post-analysis imaging	SEM								
Radius evolution model	'Voltage'								
Field factor (k)	3.3								
Image compression factor	1.65								
Assumed E-field (V/nm)	32								
Detector efficiency	0.36								
Avg. atomic volume (nm^3)	0.01076								
V initial (V)	5141	6004	5417	6140	5952	5490	5787	6199	5222
V final (V)	7427	10017	10032	7325	6102	10028	10025	9759	9526

[a]APT instrument encountered a noise problem that corrupted the data.
*ΔM is full width at half maximum of the Volt./bowl corr. peak
**ΔM10 is full width at tenth maximum of the Volt./bowl corr. peak
det. = detection; Volt. = voltage; corr. = correction; Calib. = calibration; interp. = interpolation; Lin. = linearization method; Avg. = average; F = Fractured; NF = not fractured

Data set /specimen	**M3***	**M12**	**M16**	**M4***	**M5***	**M14[a]**	**M15**	**M17**	**M18**
Regions	light rim		interface light – grey rim	grey rim					
Instrument Model	LEAP 4000X HR								
Instrument Settings									
Laser wavelength (nm)	355								
Laser pulse energy (pJ)	400	400	300	400	400	400	250	250	250
Pulse frequency (kHz)	250	200	250	200	200	200	250	250	250
Evaporation control	Detection rate								
Targeted det. rate (ions/pulse)	0.008	0.005	0.005	0.005	0.005	0.005	0.005	0.01	0.005
Nominal flight path (mm)	382								
Set point temperature (K)	50	70	80	70	70	60	80	80	80
Sample temperature (K)	57.3	80.7	92	80.7	80.7	69.2	88.5	92	92
Chamber pressure (e^{-10} Torr)	1.3	3.1	1.9	2.0	1.5	1.7	5.2	1.9	1.8
Data Summary									
LAS Root version	15.41.342l								
CAMECAROOT version	18.46.428								
Analysis Software	IVAS 3.8.2								
Total Ions:	6 million	2 million	756,246	25 million	1 million	4 million	6 million	263,060	3 million
% Single	75.7	76.9	75.9	74.5	73.1	80.3	71.5	83.8	70.9
% Multiple	23.7	21.6	22.6	24.9	25.9	16	27.5	13.4	28
% Partial	0.6	1.5	1.5	0.6	1	3.6	1	2.8	1.1
Volt./bowl corr. peak (Da)	16								
Mass Calib. (peaks/interp.)	12/Lin	7/Lin.	9/Lin.	11/Lin	10/Lin	7/Lin.	6/Lin.	9/Lin.	11/Lin.
*(M/ΔM)	1041.5	1013.1	1018.7	999.7	1017.3	1015.4	1005.5	1026.8	1020.8
**($M/\Delta M_{10}$)	208.6	207.5	199.3	178.1	123.4	195.8	186.5	188.5	196.8
Time independent background (ppm/ns)	29.117	51.134	99.324	24.082	28.238	41.048	85.380	180.369	98.490
Reconstruction									
Final specimen state	F	F	F	F	F	F	F	F	F
Pre-/post-analysis imaging	SEM								
Radius evolution model	'Voltage'								
Field factor (k)	3.3								
Image compression factor	1.65								
Assumed E-field (V/nm)	32								
Detector efficiency	0.36								
Avg. atomic volume (nm^3)	0.01076								
V initial (V)	5244	4396	3882	4306	4167	4826	5636	2870	4207
V final (V)	6459	4576	4891	7794	4912	5345	6659	3439	6037

[a]APT instrument encountered a noise problem that corrupted the data.
*ΔM is full width at half maximum of the Volt./bowl corr. peak
**ΔM10 is full width at tenth maximum of the Volt./bowl corr. peak
det. = detection; Volt. = voltage; corr. = correction; Calib. = calibration; interp. = interpolation; Lin. = linearization method; Avg. = average; F = Fractured; NF = not fractured

Data set /specimen	M13	M1*	M2*	M21	M22
Regions			dark rim		
Instrument Model			LEAP 4000X HR		
Instrument Settings					
Laser wavelength (nm)			355		
Laser pulse energy (pJ)	400	300	250	250	250
Pulse frequency (kHz)	200	250	200	250	250
Evaporation control			Detection rate		
Targeted det. rate (ions/pulse)	0.005	0.01	0.005	0.01	0.008
Nominal flight path (mm)			382		
Set point temperature (K)	70	50	50	80	80
Sample temperature (K)	80.7	56.5	57.3	91.8	92
Chamber pressure (e^{-10} Torr)	2.0	2.1	1.3	3.0	1.7
Data Summary					
LAS Root version			15.41.342l		
CAMECAROOT version			18.46.428		
Analysis Software			IVAS 3.8.2		
Total Ions:	1.5 million	844,755	430,287	223,377	173,871
% Single	77.7	73.8	68	79.8	81.3
% Multiple	21	24.6	30.7	16.3	13.3
% Partial	1.3	1.6	1.4	3.9	5.5
Volt./bowl corr. peak (Da)	16	32	32	32	12
Mass Calib. (peaks/interp.)	9/Lin.	10/Lin.	10/Lin.	10/Lin.	4/Lin.
*(M/ΔM)	1020.1	972.6	940.5	1054.6	719.3
**($M/\Delta M_{10}$)	207.4	169.6	172.6	177.7	69.8
Time independent background (ppm/ns)	64.217	85.897	88.175	157.410	147.428
Reconstruction					
Final specimen state	F	F	F	F	F
Pre-/post-analysis imaging			SEM		
Radius evolution model			'Voltage'		
Field factor (k)			3.3		
Image compression factor			1.65		
Assumed E-field (V/nm)			32		
Detector efficiency			0.36		
Avg. atomic volume (nm^3)			0.01076		
V initial (V)	4588	4414	4091	4113	3658
V final (V)	5051	9003	5145	4775	3739

*ΔM is full width at half maximum of the Volt./bowl corr. peak
**ΔM10 is full width at tenth maximum of the Volt./bowl corr. peak
det. = detection; Volt. = voltage; corr. = correction; Calib. = calibration; interp. = interpolation; Lin. = linearization method; Avg. = average; F = Fractured; NF = not fractured

From the resulting APT reconstruction, the bulk composition was obtained from the mass spectrum of each of the specimens (of the entire dataset), covering the different textural regions within the zircon grain. IVAS was used to calculate the standard deviation of the bulk composition values by obtaining the square root of the number of background-corrected counts. User-defined chemical isoconcentration surfaces were used to delineate high solute contents (clusters) within the reconstructed data to estimate their morphology and chemical composition. Each isotopic Pb count within the clusters was background corrected along with its uncertainties.

The TEM foil was manufactured with the FIB-SEM using 30kV Ga^+ ion beam. A Pt layer of ~2.5 µm was deposited onto the region of interest to protect it

from the beam damage. The extracted foil was mounted into a copper half-grid, thinned down to ≤ 100 nm and cleaned up with 2 kV ion beam. The 80 nm thick and 12 µm long TEM foil made contained parts of the core, the rim and a fracture that cut across both parts. Bright field (BF), dark field (DF) and high-angle annular dark-field (HAADF) scanning transmission electron microscopy (STEM) images were collected with a FEI Talos FS200X FEG TEM, housed in the John de Laeter Centre at Curtin University. Diffraction images and TEM-EDS data were also acquired to characterise the structure of the material and obtain elemental maps. The TEM instrument was operated at 200 kV.

U-Th-Pb geochronology data was acquired using sensitive high resolution ion microprobe (SHRIMP) II housed in the John de Laeter Centre at Curtin University. Four analyses were performed on the grain using a 30 µm diameter spot with ~2.0 nA primary beam. The raw data was calibrated against zircon standards CUYZ ($^{238}U/^{206}Pb$ age = 569 Ma, $^{207}Pb/^{206}Pb$ age = 570 Ma, U = 583 ppm and Th = 83 ppm) and OGC ($^{207}Pb/^{206}Pb$ age = 3465 Ma). Twenty analyses of the CUYZ standard were obtained during the session, of which 19 indicated an external spot-to-spot (reproducibility) uncertainty of 1.8% (1σ) and a $^{238}U/^{206}Pb^*$ calibration uncertainty of 0.5% (1σ) (* indicates a ^{204}Pb corrected Pb value). Common Pb corrections were applied to all analyses using contemporaneous isotopic compositions determined according to the model of Stacey and Kramers (1975). OCG yielded a $^{207}Pb/^{206}Pb$ age =3462 ± 4 Ma with a mean square weighted deviation (MSWD) of 1.57, which is within the accepted range of uncertainty (3465 Ma) (Stern et al., 2009) and therefore no correction for fractionation on the $^{207}Pb/^{206}Pb$ ratio was necessary. Data reduction and age calculations were done using SQUID 2 and Isoplot 3.75 software (Ludwig, 2009, 2012).

Results

Textural variations

CL imaging reveals complex compositional variations within zircon grain 002. These variations define a clear core and rim structure, but these two features are also compositionally heterogeneous (Fig. 3.2a-b). The core comprises a CL-dark, lower BC region that shows alternating bands of darker, low BC zircon and lighter, higher BC zircon that has the general appearance of growth zoning (dark core in Fig.

3.2b). This is surrounded by a CL-light, higher BC, homogenous core region (light core in Fig. 3.2b). The interface between the two core regions is irregular (Fig. 3.2a-b).

The zircon rim reveals far more complex CL variations. A zone in the upper right of the grain (Fig. 3.2a-b) has higher BC and CL characteristics that have the appearance of growth zoning. However, the most obvious feature of the rim is the patchy CL pattern that by enlarge radiate from fractures that transect the rim (Fig. 3.2b). These fractures crosscut both the core and rim of the zircon grain and appear to radiate outwards (Fig. 3.2), but they only appear to modify CL in the rim. The patchy CL comprises an intermediate CL-grey zircon closest to the fractures that texturally overprints a dark CL zircon that represents the primary CL signal of the rim zircon. The interface between the dark and intermediate CL rim zircon is CL-bright (Fig. 3.2b). The dark CL of the rim corresponds to regions of very low BC (c.f. Fig. 3.2a and b), that do not index during EBSD analysis (Fig. 3.2c). Regions of the zircon that do index include the dark CL regions of the core and rim (Fig. 3.2c). The well indexed regions of the grain show no significant orientation with a variation accumulated misorientation of 5º, indicating that the grain is not internally deformed by crystal plastic deformation processes (Fig. 3.2c).

From the Raman data, colour-coded Raman images were made for the intensity, frequency and width of the $v_3(SiO_4)$ band of zircon (Fig. 3.3a-c), as well as the intensity of the 637 cm^{-1} band (Fig. 3.3d). These images were made to show the degree of structural disorder in the grain. The intensity of the $v_3(SiO_4)$ and the 637 cm-1 bands is the highest in the light core region and parts of the rim (Fig. 3.3a,d), which correspond to regions with a low width of the $v_3(SiO_4)$ band of zircon. The dark core region has low intensity and high width of the $v_3(SiO_4)$ band. The frequency of the $v_3(SiO_4)$ band is irregular with the boundaries of the grain and the growth zoning in the dark core having the highest values (Fig. 3.3b). Two Raman spectra were taken from the grain for comparison, one from the light core region and the other from the rim region (Fig. 3.3c,e). The spectrum from the light core region has a higher intensity and narrower width than the spectrum from the rim region.

Nanoscale analyses

HAADF imaging of the TEM foil reveals differences in intensities in both the core and rim, although more variation was seen in the rim region (Fig. 3.4). At higher resolution BF images, voids of ~50 nm were identified in the core–rim interface and the darker region in the rim from the HAADF image (Fig. 3.4b-d). Electron diffraction taken from two regions in the rim revealed a crystalline pattern for both regions (Suppl. Fig. 3.1).

TEM-EDS maps show a heterogeneous distribution of element within the core and rim (Fig. 3.4d,3.5). These include higher concentrations of trace elements (Ca, Fe, Y) in darker areas from the HAADF image of the rim and core (Fig. 3.4d), a higher concentration of Fe in the rim than the core, and higher concentration of Ca, Fe and Y in the core–rim interface (Fig. 3.5). However, the chemical variation in the core occurs only next to the fracture, while in the rim it was found all around. This variation included an increase of Si, Zr and Hf in the light areas of the HAADF image in Fig. 3.4d, while in the darker areas the concentration of Y, Fe and Ca appeared enhanced. In addition, the concentration of Fe was found to be much higher in the rim region than the core (Fig. 3.5).

The fracture in the foil that cuts across the core and the rim, show enrichment in Ca, Fe, Y, Ce, Th and U, indicating that the fracture is a site of chemical modification (Suppl. Fig. 3.2). Higher resolution STEM images and EDS maps of the fracture revealed a chemical variation along the fracture (Fig. 3.5). The trace element enhancement along the fracture appears to be more enriched on the core side of the fracture, except for Fe. Trace amounts of Nd and Yb were also identified in the EDS mass spectra of the fracture at the interface.

From the five regions of interest targeted for APT (Fig. 3.2d), a total of 31 specimens were made, covering all the compositional and textural variations within the grain, as identified from the CL and BC imaging. All 31 samples were analysed by APT. Of these, 25 specimens fractured during the analysis and only 6 specimens remained intact at the end of the analysis (Table 3.1). Despite this failure rate, 16 specimens yielded sufficient counts (>1.5 M ions) to be used for geochemical analysis (Table 3.2).

Table 3.2 APT chemical data in at.%

	M6*	±	M7*	±	M5	±	M7	±	M9	±	M10	±
						Light core						
O	61.90	0.12	61.20	0.03	62.94	0.02	63.60	0.10	62.24	0.03	61.99	0.03
Si	14.91	0.05	16.76	0.01	16.31	0.01	15.98	0.04	16.43	0.01	16.48	0.01
Zr	19.30	0.06	17.80	0.01	17.74	0.01	18.14	0.05	17.78	0.01	17.72	0.01
Hf	0.163	0.005	0.151	0.001	0.149	0.001	0.165	0.004	0.155	0.001	0.154	0.001
Li	0.0086	0.0011	0.0138	0.0003	0.0091	0.0002	0.0096	0.0010	0.0127	0.0003	0.0141	0.0003
Be	-	-	-	-	-	-	-	-	-	-	-	-
Mg	-	-	-	-	-	-	-	-	-	-	-	-
Al	0.0055	0.0009	-	-	-	-	-	-	-	-	-	-
P	0.0311	0.0021	0.0140	0.0003	0.0143	0.0003	0.0138	0.0012	0.0137	0.0003	0.0153	0.0003
Ca	0.0086	0.0011	0.0133	0.0003	0.0084	0.0002	0.0040	0.0006	0.0106	0.0003	0.0110	0.0003
Mn	-	-	-	-	-	-	-	-	-	-	-	-
Fe	-	-	-	-	-	-	-	-	-	-	-	-
Y	0.0322	0.0021	0.0192	0.0004	0.0170	0.0003	0.0267	0.0017	0.0204	0.0004	0.0175	0.0003
Pb	0.0050	0.0008	0.0050	0.0002	0.0046	0.0002	0.0085	0.0009	0.0046	0.0002	0.0055	0.0002
Ce	0.0020	0.0005	0.0035	0.0002	0.0028	0.0001	0.0055	0.0008	0.0030	0.0001	0.0028	0.0001
Yb	-	-	-	-	-	-	-	-	-	-	-	-
U	0.0028	0.0006	0.0043	0.0002	0.0011	0.0001	0.0039	0.0006	0.0020	0.0001	0.0034	0.0001

	M19	±	M20	±	M10*	±	M11*	±	M3*	±	M12	±
			Light core				Dark core				Light rim	
O	62.72	0.02	63.02	0.02	60.74	0.11	61.20	0.17	61.95	0.08	63.17	0.15
Si	16.36	0.01	16.30	0.01	15.88	0.05	11.99	0.06	15.18	0.03	16.65	0.07
Zr	17.67	0.01	17.76	0.01	18.39	0.05	18.81	0.079	18.80	0.04	18.79	0.07
Hf	0.154	0.001	0.155	0.001	0.176	0.005	0.198	0.008	0.179	0.003	0.171	0.006
Li	0.0093	0.0002	0.0224	0.0003	0.0189	0.0015	0.0040	0.0011	0.0300	0.0013	0.0208	0.0022
Be	-	-	-	-	0.0056	0.0008	0.0077	0.0015	-	-	-	-
Mg	-	-	-	-	0.0031	0.0006	0.0032	0.0010	-	-	-	-
Al	-	-	-	-	0.0111	0.0012	0.2449	0.0083	-	-	-	-
P	0.0127	0.0002	0.0128	0.0003	0.0263	0.0018	0.3236	0.0096	0.0407	0.0015	0.0195	0.0021
Ca	0.0090	0.0002	0.0079	0.0002	0.0256	0.0018	0.1049	0.0054	0.0056	0.0006	0.0148	0.0018
Mn	-	-	-	-	0.0124	0.0012	0.0219	0.0025	-	-	-	-
Fe	-	-	-	-	0.0114	0.0012	0.0484	0.0037	-	-	-	-
Y	0.0192	0.0003	0.0193	0.0003	0.0358	0.0021	0.2628	0.0086	0.0315	0.0014	0.0318	0.0027
Pb	0.0045	0.0001	0.0043	0.0001	0.0173	0.0015	0.0339	0.0031	0.0124	0.0009	0.0158	0.0019
Ce	0.0028	0.0001	0.0029	0.0001	0.0229	0.0017	0.1104	0.0056	0.0386	0.0015	0.0092	0.0015
Yb	-	-	-	-	0.0036	0.0007	0.0119	0.0018	-	-	-	-
U	0.0030	0.0001	0.0032	0.0001	0.0223	0.0017	0.0568	0.0040	0.0178	0.0010	0.0173	0.0020

	M4*	±	M15	±	M18	±	M13	±
			Grey rim				Dark rim	
O	61.95	0.04	63.33	0.08	63.50	0.12	62.54	0.17
Si	15.14	0.02	15.41	0.03	15.11	0.05	16.72	0.07
Zr	17.64	0.02	17.54	0.04	17.75	0.06	18.70	0.08
Hf	0.141	0.001	0.173	0.003	0.167	0.005	0.189	0.007
Li	0.0053	0.0003	0.0151	0.0010	0.0230	0.0018	0.0187	0.0023
Be	-	-	-	-	-	-	-	-
Mg	-	-	-	-	-	-	-	-
Al	0.0129	0.0004	0.0121	0.0009	-	-	-	-
P	0.0436	0.0008	0.0351	0.0015	0.0343	0.0022	0.0231	0.0025
Ca	0.0120	0.0004	0.0089	0.0008	0.0027	0.0006	0.0099	0.0016
Mn	0.0073	0.0003	0.0054	0.0006	-	-	-	-
Fe	0.0200	0.0005	0.0178	0.0011	-	-	-	-
Y	0.0357	0.0007	0.0415	0.0016	0.0308	0.0021	0.0422	0.0034
Pb	0.0103	0.0004	0.0121	0.0009	0.0153	0.0015	0.0178	0.0034
Ce	0.0518	0.0009	0.0356	0.0015	0.0277	0.0019	0.0098	0.0016
Yb	0.0005	0.0001	-	-	-	-	-	-
U	0.0143	0.0005	0.0129	0.0009	0.0024	0.0006	0.0079	0.0015

- Below detection limit

Uncertainties are based on counting statistics and are shown in 2σ

From these specimens around 480 million ions were detected in total. Representative examples of the APT spectra from the different regions are shown in Fig. 3.6 and Suppl. Fig. 3.3. These mass spectra show a variety of trace elements that are commonly associated with primary substitutions in the zircon lattice (e.g. Hf, Y, P, U), radiogenic decay of U (Pb) and chemical alteration of zircon (e.g. Fe, Ca). However, the data also reveal interstitial trace elements (Be, Li, Mg and Al), whose geochemical significance is largely unclear. The major, minor and most of the trace elements show a homogenous distribution in each of the 16 specimens, with Pb being the only element to show evidence of segregation. The highest concentration of trace elements is found in the dark core region, except for Li which is highest in the light rim (Fig. 3.7). The elements U and Pb were the lowest in the light core specimens. Apart from Ce and Yb, the other REE were not identified in the data set.

Three of the atom probe specimens from the light core region contained a total of five Pb clusters, each ~10 nm in diameter (Fig. 3.8). No other element was enriched in the clusters. The concentration of ^{207}Pb and ^{206}Pb within the clusters yields ^{207}Pb/^{206}Pb isotopic ratio ranging from ~0.660 to 0.992 (Table 3.3). Although the clusters are broadly spherical, two of the clusters (III and IV in Fig. 3.8) show a flattened upper surface. This represents an artefact associated with either the different evaporation fields of the host zircon and the Pb cluster or the reconstruction. Such artefacts do not influence the calculation of Pb ratios (Peterman et al., 2016). Using the ^{207}Pb/^{206}Pb ratio of all the Pb clusters yields a model age of 3435 ± 372 Ma (2σ). This age was based on the total corrected ^{207}Pb/^{206}Pb ratio and the crystallization age obtain from the SHRIMP data (see below).

Table 3.3 APT chemical data from Pb clusters

Specimen	Cluster	Pb counts		Corr. ^{207}Pb/^{206}Pb
		^{206}Pb	^{207}Pb	
M5	I	97	64	0.660 ± 0.216
M5	II	112	82	0.732 ± 0.215
M5	III	43	33	0.766 ± 0.359
M10	IV	120	119	0.992 ± 0.260
M19	V	71	69	0.972 ± 0.334
Total		**443**	**367**	**0.828 ± 0.118**
Calculated reservoir age				**4972 ± 204 Ma (2σ)**
Correct reservoir age*				**3435 ± 372 Ma (2σ)**

Corr. = background corrected.
*=corrected using SHRIMP crystallization age (3531 ± 12 Ma)

U-Pb geochronology

Four analyses were conducted on the zircon grain using the SHRIMP (Table 3.4 and Figs. 3.2d and 3.9). Two analyses focused on the core (1.2 and 1.4) and two on the rim (1.1 and 1.3). One concordant analysis gave a $^{207}Pb/^{206}Pb$ age of 3295 ± 6 Ma (2σ), and the weighted average $^{207}Pb/^{206}Pb$ age of the analyses from the core gave an age of 3531 ± 12 Ma (n=2, MSWD = 1.5, 2σ). The Concordia diagram made from the SHRIMP data also points to a recent event that caused either Pb-loss or U-gain (Fig. 3.9).

Table 3.4 Zircon U-Th-Pb isotopic SHRIMP data

spot	U (ppm)	Th (ppm)	Th/U	% comm ^{206}Pb*	$^{204}Pb/^{206}Pb$	$^{208}Pb^{*}/^{232}Th$	$^{207}Pb^{*}/^{235}U$	$^{206}Pb^{*}/^{238}U$	$^{207}Pb^{*}/^{206}Pb^{*}$	$^{206}Pb^{*}/^{238}U$ age	$^{207}Pb^{*}/^{206}Pb^{*}$ age	% disc
1.1	778	2911	3.86	0.09	0.0001	0.0041± 0.0002	23.55± 0.87	0.637± 0.023	0.2681± 0.0010	3177±92	3295±6	5
1.2	752	1653	2.27	0.83	0.0007	0.0067± 0.0005	7.74± 0.38	0.180± 0.009	0.3116± 0.0026	1067±48	3529±12	75
1.3	5826	15674	2.78	8.46	0.0070	0.0013± 0.0003	1.04± 0.06	0.027± 0.001	0.2825± 0.0100	171±6	3377±56	96
1.4	2486	14278	5.93	4.96	0.0043	0.0027± 0.0002	2.49± 0.12	0.057± 0.002	0.3167± 0.0082	358±14	3554±40	92

Ages are listed in Ma and the uncertainties are listed at 2σ.
comm = common; disc = discordance
* Indicates a ^{204}Pb corrected Pb value taken after Stacey and Kramers (1975)

Discussion

Textural characterization

Zircon grain 002 displays a complexity of textures visible by the different CL intensities: a dark metamict core surrounded by a lighter homogenous core, followed by a rim with complex zoning (Fig. 3.2). The remanets of growth zoning in the CL-dark core (Fig. 3.2b) indicate an igneous origin for the zircon grain. Faded or weak zoning in zircon is generally considered a secondary texture that indicates a metamorphic disturbance to the grain (Hoskin and Schaltegger, 2003). The weak primary growth zoning in the CL-dark core (Fig. 3.2b) suggests the structure of zircon grain 002 was disturbed by a metamorphic event. The light core region of the grain is more crystalline than the surrounding regions, it has a sharp boundary with the CL-dark core and lacks growth textures. Based on these observations, the light core region formed by recrystallization of the grain.

The complex structure of the core and rim conflicts with the possibility of the core being detrital and the rim resulting from new growth caused by a younger metamorphic event. As previously mentioned, new growth forms sharp boundaries and it is restricted by the Zr concentration in the system the grain is in. Since the longest part of the rim is ~87 μm, it is difficult understand where did the Zr budget originate from if the grain was detrital.

A more likely scenario is that the rim formed by the recrystallization of the pre-existing grain. In addition, the presence of a brighter CL core–rim interface indicates that the recrystallization process that formed the rim is the interface-coupled dissolution-reprecipitation reaction. This mechanism has been described as the dissolution of elements along with the reprecipitation of new zircon as the interface migrates inward, mediated by a fluid or melt (Geisler et al., 2007). These core–rim interfaces have also been seen in zircon grains from ultrahigh pressure and temperature metamorphic rocks (Peterman et al., 2019).

The Raman spectrum from the rim (spectrum 1 in Fig. 3.3e) is less intense and broader than the spectrum from the light core (spectrum 2), indicating the rim is more metamict than the light core (Nasdala et al., 1995). This interpretation is reinforced by the BC map and CL image of the grain (Fig. 3.2a-b). Fractures within the CL-light core of the grain have a radial appearance. This pattern of fractures has been previously interpreted to form due to lattice expansion associated with metamictisation (Chakoumakos et al., 1987; Lee and Williams, 1993). Since the fractures appear to nucleate from the CL and BC dark region of the core (dark core in Fig. 3.2b), it is inferred that the radial fractures in zircon grain 002 are consistent with these previous models.

The complex zoning seen in the rim (Fig. 3.2b) appears to be the result of an interaction of the zircon grain with fluids. In addition, the variation of the CL intensities in the rim appear to be related to the fractures, pointing to either hydrothermal alteration or contact with weathering solutions via fractures. Fractures formed by metamictisation can create fast pathways for trace elements to diffuse in and out of zircon grains (Fig. 3.5) (Chakoumakos et al., 1987; Lee, 1995).

Evolutional history of the zircon grain

The integration of a range of analytical techniques has been used to establish the geological evolution of a complex, detrital zircon grain that incorporates an igneous, metamorphic and alteration history. From the four SHRIMP analyses conducted on zircon grain 002, two were from the core and two from the rim (Fig. 3.2d). The 3531 ± 12 Ma $^{207}Pb/^{206}Pb$ weighted average age of the analyses from the core was interpreted to be the crystallization age of the zircon grain. It is possible that the zircon grain originated from the ~3.5 Ga tholeiitic basalts and intermediate–felsic volcanic rocks from the Coonterunah Group in the East Pilbara granite-greenstone terrane (Van Kranendonk et al., 2002).

A concordant $^{207}Pb/^{206}Pb$ age of 3295 ± 6 Ma was obtained from one of the SHRIMP analyses from the rim (1.1 in Fig. 3.9), which is inferred to be the age of the metamorphic event that recrystallized the grain by the interface-coupled dissolution-reprecipitation replacement process. In other words, ~236 Ma after crystallization, the zircon grain was metamorphosed, resulting in the core–rim structure. In the East Pilbara granite-greenstone terrane, the formation and uplift of the granitoids induced metamorphism to the greenstone belts and complexes around 3.3 Ga (Van Kranendonk et al., 2002). This event could be the event that metamorphosed zircon grain 002.

From the Pb clusters in the APT specimens, the age of cluster formation was calculated by counting the number of ^{206}Pb and ^{207}Pb isotopes within the clusters (Table 3.3). With the total Pb isotopic ratio of the clusters (0.828 ± 0.118), a $^{207}Pb/^{206}Pb$ age of 4972 ± 204 Ma was obtained. However, this erroneous cluster formation age assumes the Pb atoms originated within that space and have not migrated since. To correctly calculate the clusters formation age, the Pb isotopic ratio and the crystallization age from the SHRIMP data were used, resulting in a corrected Pb reservoir age of 3435 ± 372 Ma. This age is interpreted to be the age of a metamorphic event that created the core–rim structure and it is within the acceptable error range of the SHRIMP concordant age (3295 ± 6 Ma). Hence, it is assumed that the metamorphic event that created the core–rim structure also caused Pb to migrate and segregate into clusters in the light core.

After the metamorphic event, the decay of the radioactive elements incorporated in the grain as its crystallized damaged sections of the core, resulting in

the CL-dark core. Subsequently, the radiation damage created fractures that radiate outward, which resulted in fast diffusion pathways for trace elements into and out of the zircon grain (Fig. 3.5). This is supported by the discordant points of the SHRIMP data (Fig. 3.9), meaning the zircon grain acted as an open system resulting in Pb-loss or U-gain. Based on the SHRIMP and TEM-EDS data, it is interpreted that the zircon grain had recent U-gain facilitated by the defects within its structure, which produced the patchy zoning seen in the rim. Two possible processes that can account for the recent U-gain and the patchy textures in the rim are hydrothermal alterations and interactions with weathering solutions. The interactions of weathering fluids with the radiation damaged regions of zircon grains has been previously shown to decouple the U-Pb system (Pidgeon et al., 2013). Based on the results of this research, it is challenging to determine which of the processes apply to zircon grain 002.

APT analytical aspects

APT data was collected from each of component of the zircon grain 002 textural framework. APT specimen yields from the different textural domains show systematic patterns that suggest the yield is correlated with the chemistry. The specimens from the light core yielded the highest number of ions and had the lowest concentration of P, Y, Pb, Ce and U (Figs. 3.9-3.10). The specimens from the CL-dark metamict core produced a low number of ions but had the highest concentration of all trace elements, except for Li. The specimens from the rim produced less ions than the specimens from the light core but more ions than the specimens from the CL-dark core. Besides the concentration of Li being the highest in the light rim, there is no other correlation for the rim.

The field-induced stress APT specimens are subjected to during the analytical process can sometimes cause the specimens to prematurely fracture or melt down to the silicon carrier microtip they are fixed to (Suppl. Fig. 3.4) (Larson et al., 2013b). The specimens obtained from zircon grain 002 that did not fracture during the APT analysis belong to the light core, which is the crystalline area with low radiation damage as well as with the lowest concentration of U (Fig. 3.10). The APT specimens from the CL-dark metamict core region fracture prematurely resulting in low yield. Despite this, the dark core specimens had the highest concentration of U, which was used as a proxy for amount of radiation damage and was backed by the

CL, EBSD and Raman data. In other words, it was found that the amount of radiation damage could influence the yield of the APT specimens.

What is more, the TEM analysis revealed the presence of defects (e.g. nano-voids) in the structure of the zircon grain (Fig. 3.4b-c) with a lesser number of the defects in the light core region when compared to the rim. Defects in the structure can alter the mechanical properties of the zircon grain, affecting the yield of the APT specimen (refer to Chapter 5 for further discussion).

Nano-features and trace element distribution

The CL, BC and Raman imaging used to establish the textural evolution of the zircon grain are proxies for different compositions. However, the scale of compositional complexity is so fine that traditional analytical techniques can not readily provide quantitative compositional data, particularly for nanoscale features and the trace element variations.

Nanoscale size voids were identified in the core, rim and the core–rim interface of the grain (Fig. 3.4). The nano-voids had a heterogeneous distribution in the grain, occurring in the darker regions of the HAADF image (atomic number contrast) (Fig. 3.4d). These darker regions were more common in the rim and interface than in the core. In the core, the darker regions were as related to the fracture (Fig. 3.4a). These features are interpreted to have formed because of the radiation damage the grain experienced based on the location of the voids. Similar features have been found in other studies (micro- and nano-pores), which are attribute to chemical modifications of the grains (Tomaschek et al., 2003; Schwartz et al., 2010; Courtney-Davies et al., 2019).

The HAADF images of zircon grain 002 revealed a heterogeneous distribution of trace elements in the core, rim and core–rim interface of the grain (Figs. 3.4-3.5). The fracture in the TEM foil appears to be sealed and it is enriched in Ca, Fe, Y, Ce, Th, U, Nd and Yb, with a higher concentration of those trace elements within the core (Fig. 3.5). It is possible that the sealed fractured was healed by a reaction between fluids and the fracture, which could explain the trace element enhancement along the fracture. The trace element enrichment seen inside the fracture is evidence of the fractures in the grain acts as pathway for element diffusion.

The core–rim interface appears enriched in trace elements, especially Fe and Y, also acting as pathway for diffusion through the interface (see Y in Fig. 3.5). Since the TEM-EDS (Fig. 3.5) shows there has been U gain in the zircon grain, the Th/U ratio obtained from the SHRIMP data (Table 3.4) is not a reliable characteristic to identify whether the grain is metamorphic or igneous.

The elemental analysis results from the APT specimens show different concentrations of trace elements from the subdivisions of the grain (Fig. 3.8 and Suppl. Fig. 3.5). Trace elements commonly associated with fluid alterations and weathering were found in all the APT specimens (e.g. Ca, Al, Fe, Mn and Ce). However, the highest concentration of those elements occurs in the metamict dark core (Fig. 3.8). Furthermore, the specimens from the dark core had the highest concentration of most trace elements, including U and Pb. A possible explanation for the high concentration of trace elements in the dark core could be fluid interactions with the radiation damage area (Geisler et al., 2003a) facilitated by fractures, defects within the core or both (Murakami et al., 1991).

The specimens from the CL-dark core region had the lowest value for Li. An initial a low concentration of Li in the dark core region could explain this. Another explanation can be the diffusion of Li. Since Li diffuses much faster than other elements in zircon grains (Cherniak and Watson, 2010), it is possible that Li diffused out of the metamict core through fractures and defects into the rim, which resulted in a low concentration of Li in the APT data set from the dark core. This interpretation is supported by the connection between the alteration of the CL intensities observed in the rim and the fractures that radiate from the core (Fig. 3.2b), along with a high concentration of Li in the light rim area.

Clusters of Pb were identified in 3 specimens from the light core (Fig. 3.8), which is the area that had the lowest concentration of U and Pb from the APT data. The presence of the Pb clusters implies there was an event that triggered the migration and segregation of Pb in the light core. The known mechanisms proposed for Pb clustering at the nanoscale are: diffusion to amorphous domains caused by radiation damage (Valley et al., 2014; Valley et al., 2015), dislocation loops formed by the annealing of radiation damage (Peterman et al., 2016; Peterman et al., 2019), spinodal decomposition within planar features (Peterman et al., 2019), migration of dislocations (Piazolo et al., 2016), thermal annealing resulting in metallic Pb to separate from other phases (Kusiak et al., 2015), trapping into other clusters formed

by exsolution (Seydoux-Guillaume et al., 2019), intersection of dislocations (Fougerouse et al., 2019), phase exsolution (Fougerouse et al., 2018) and high-angle boundaries (Fougerouse et al., 2019). In addition, Pb clustering has been identified in zircon standards annealed by humans to produce a gem-like quality material (Reinhard et al., 2018).

However, the above-mentioned mechanisms cannot explain the Pb clusters observed in this research. First, the clusters have an ellipsoidal shape, not the toroidal shaped seen in Peterman et al. (2016) and Peterman et al. (2019), which discounts the dislocation loops mechanism. There was no other feature identified in the APT specimens, ruling out spinodal decomposition within planar features, intersection of dislocations and high-angle boundaries (Fougerouse et al., 2019; Peterman et al., 2019). The clusters are identified as zircon (no absence of Zr, Si and O atoms) enriched only in Pb, removing the thermal annealing, trapping into other clusters and phase exsolution mechanisms as possibilities (Kusiak et al., 2015; Fougerouse et al., 2018; Seydoux-Guillaume et al., 2019).

That leaves the diffusion of Pb to amorphous domains, Pb getting trapped by the migration of dislocations and human-induced annealing. The first two are possible, although less likely since the Pb clusters were found in the light core, which is the more crystalline area (Fig. 3.3c,e), and dislocation should have captured other trace elements while migrating, especially interstitial ones. Human-induced annealing is not possible since the Pb ratio within the clusters produced an age of 3435 Ma.

Apart from thermal annealing and human-induced annealing, all the proposed mechanisms for Pb clustering include other trace elements in the clusters. The clusters in this research only contain Pb and cannot be explained by any of the previously proposed mechanism. Hence, a new mechanism that has not been considered previously may be attributed to the clustering of Pb seen in this research.

Conclusion

APT and TEM were used in conjunction with conventional analytical techniques, to analyse a complex zircon grain from the Lalla Rookh Sandstone to understand its formation and evolution. The results from the geochronological analyses provide a crystallization age of 3.5 Ga for the zircon grain, followed by a

3.3 Ga metamorphic event that created the core–rim structure and caused the radiogenic Pb to segregate and cluster in the crystalline core. The complex, patchy textures in zircon rim are consistent with a relatively young hydrothermal or weathering event that introduced a recent U component to the grain through fractures. This U addition is responsible for the gross discordance of U-Pb data recovered by SHRIMP analysis. The nanoscale geochemical analyses revealed a heterogeneous distribution of trace elements within the zircon grain representative of the different processes that have acted on the grain.

When looking at the APT specimen yield from the different textural subdivisions of the grain, it was found that the amount of radiation damage and defects (e.g. nano-voids and fractures) caused by the decay of radioactive elements disturbs the yield of the APT specimens. Regions with a high amount of radiation damage and defects can potentially make the process of acquiring the nano-geochemical data challenging. This new information can help researchers assess their sample prior a nanoscale analysis to determine the best region to investigate.

Acknowledgements

We recognize the support from the Australian Research Council (ARC) Centre of Excellence for Core to Crust Fluid Systems (CE11E0070). We also thank Rick Verberne for his assistance with the production of figures.

Figures

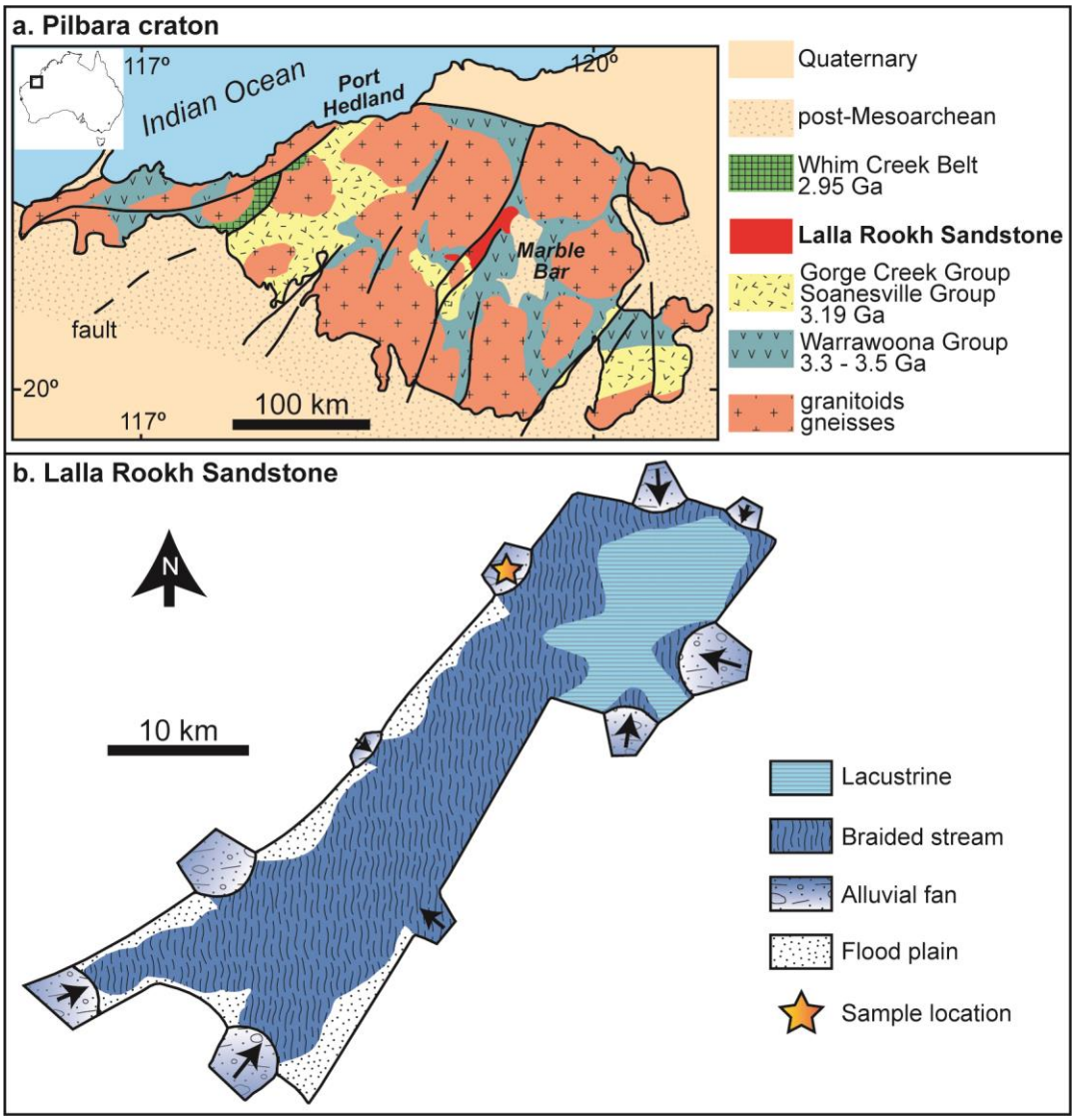

Figure 3.1 **(a)** Simplified geological map of the Pilbara Craton and its location in Australia. The towns of Port Hedland and Marble Bar were added for orientation. **(b)** Sedimentary units within the Lalla Rookh Sandstone and sample location (star). Modified from Stüeken and Buick (2018) and Krapez and Barley (1987). Figure incorporates Adobe Illustrator swatches from U.S. Geological Survey (2006).

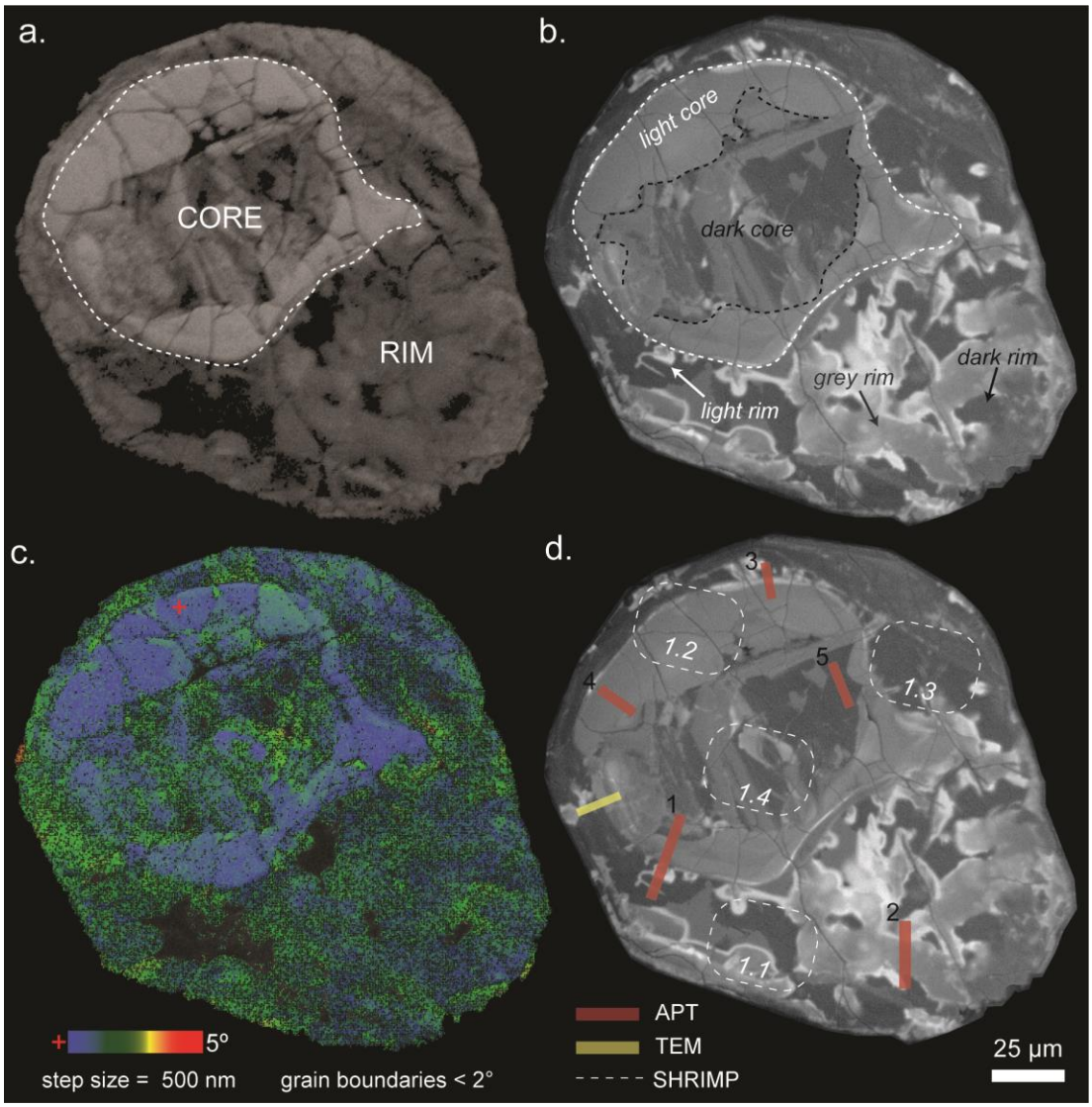

Figure 3.2 EBSD and CL images of the interior of zircon grain 002. **(a)** EBSD – BC map showing the structure of the grain. The white dash line represents the boundary between the core and the rim. **(b)** CL image with the different subdivisions of the core and rim. The black dashed line represents the division of the dark and light core. **(c)** EBSD – TC map showing the misorientation of the grain, plus that the majority of the accumulated misorientation is < 3º. **(d)** Same CL image as b but with the location of the spots analysed with the different techniques (TEM, APT and SHRIMP).

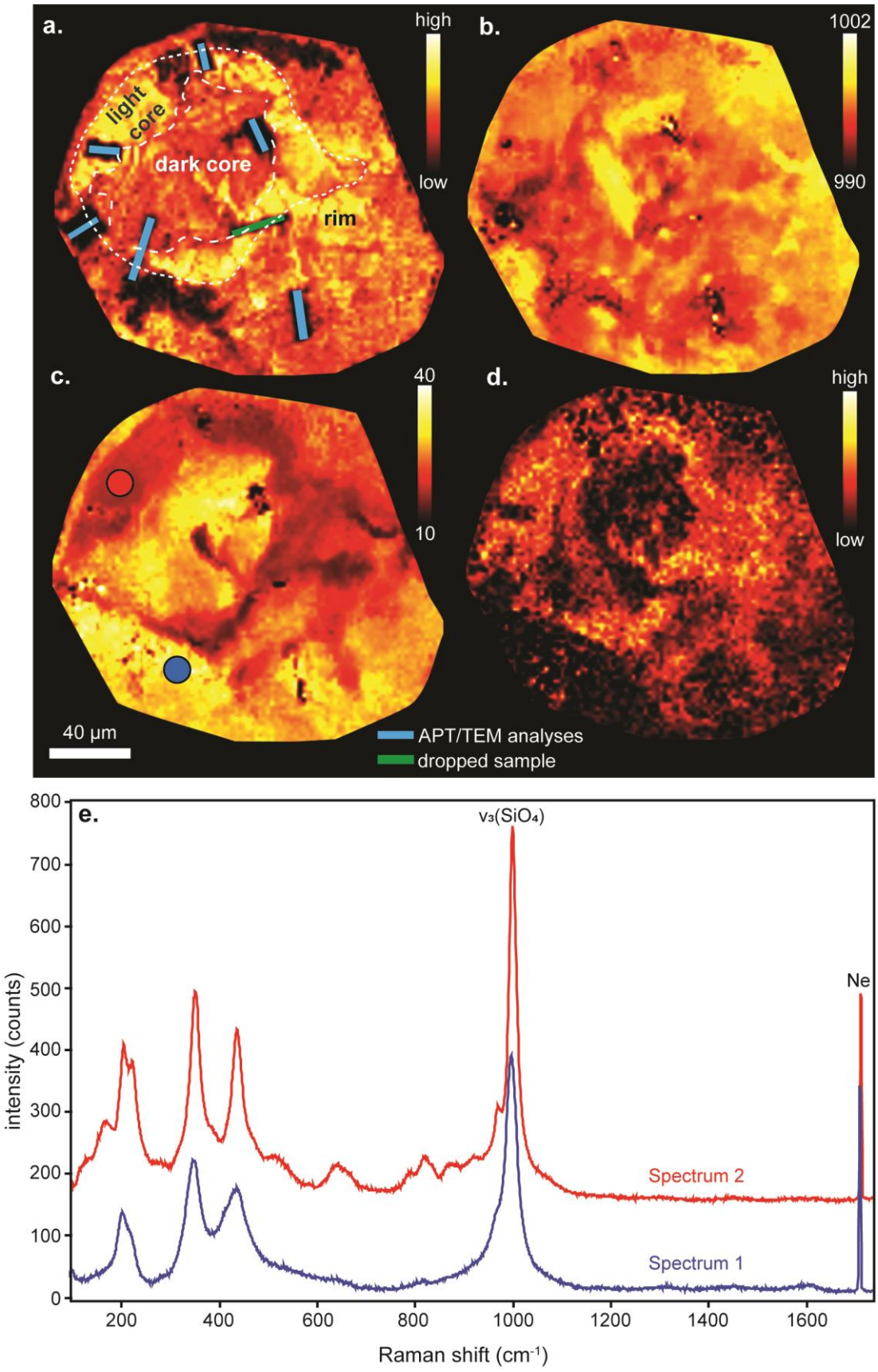

Figure 3.3 Colour-coded, hyperspectral Raman images and Raman spectra with the subdivisions of the core and the location of the APT and TEM analyses (blue

rectangles), including the location of a sample that was dropped during transport (green rectangle). **(a)** Integrated intensity, **(b)** frequency, **(c)** width (FWHM) of the $v_3(SiO_4)$ band of zircon and **(d)** the integrated intensity of a Raman band observed near 637 cm^{-1}. **(e)** The representative Raman spectra extracted from the hyperspectral data set shown in **(c)**

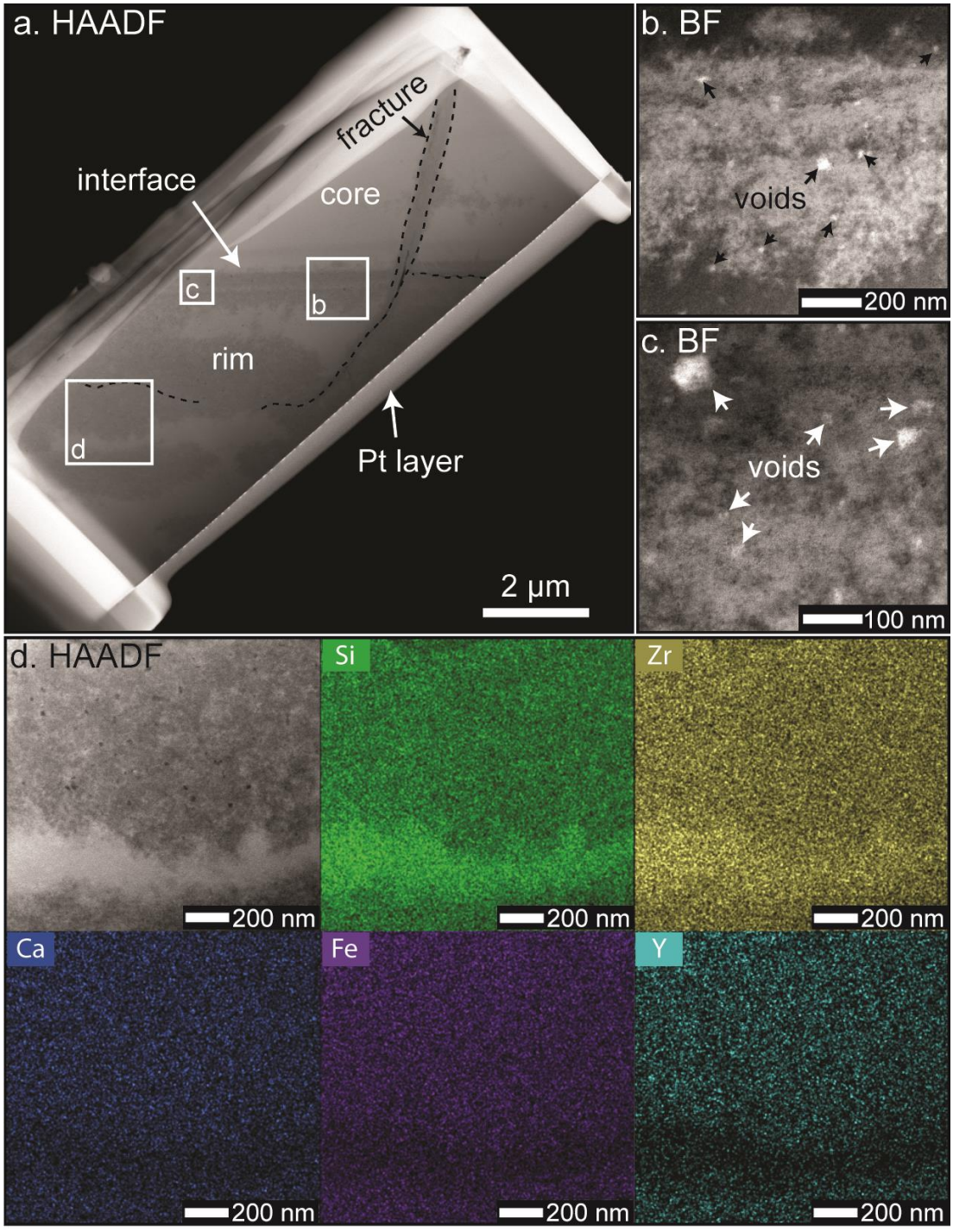

Figure 3.4 STEM images of a TEM foil. **(a)** HAADF image of the foil comprising parts of the core, rim, interface and a fracture that cross both regions. **(b-**

c) BF images of the interface with voids pointed by the arrows. **(d)** HAADF image and EDS maps showing chemical variation within the rim.

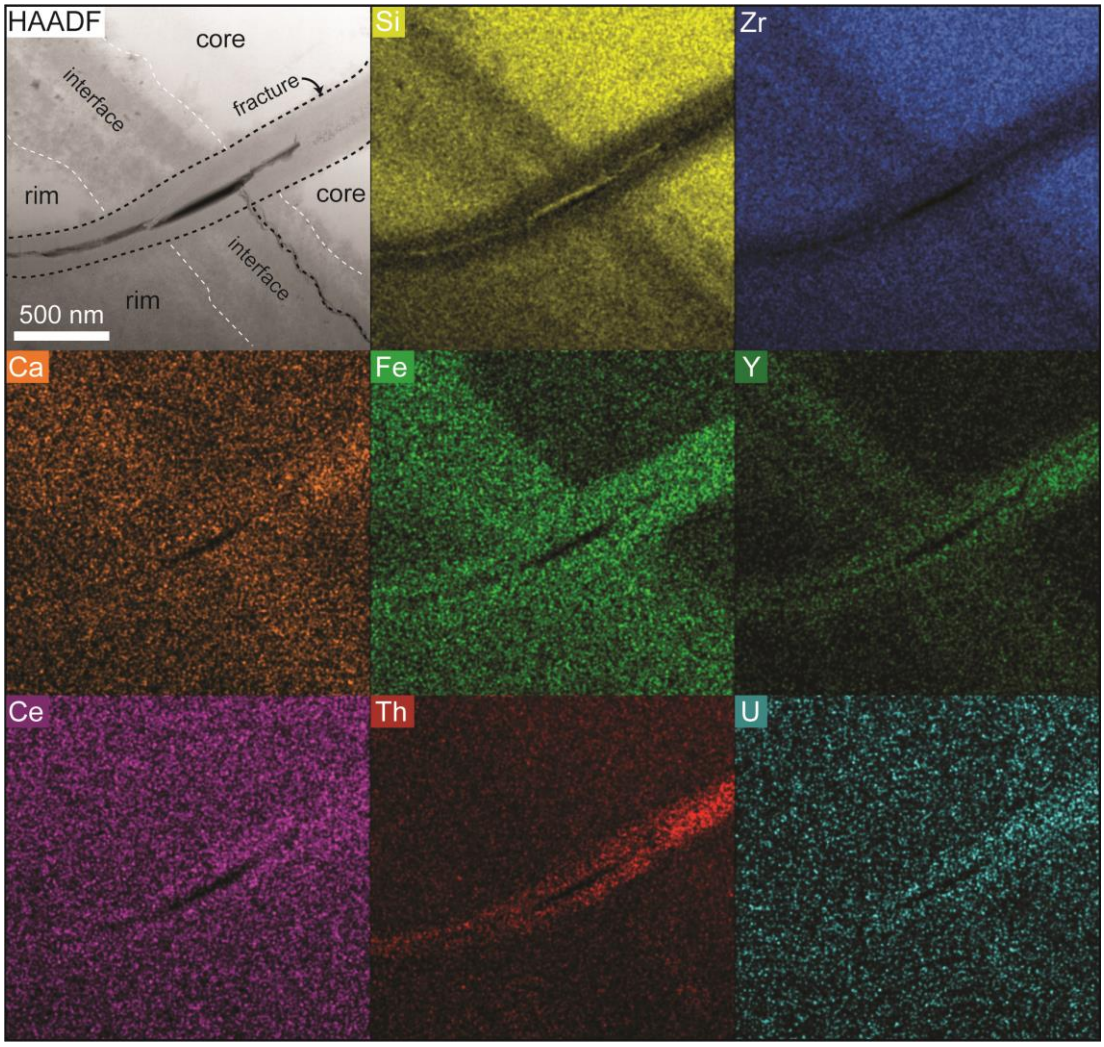

Figure 3.5 HAADF image and EDS maps of the core–rim interface and a fracture seen in Figure 3.4. A chemical variation is highlighted by the different intensities of the colours in the maps. Note the higher concentration of trace elements, as well as radioactive elements, in the fracture when compared to the surroundings. Notice the high concentration of Si in the middle of the fracture.

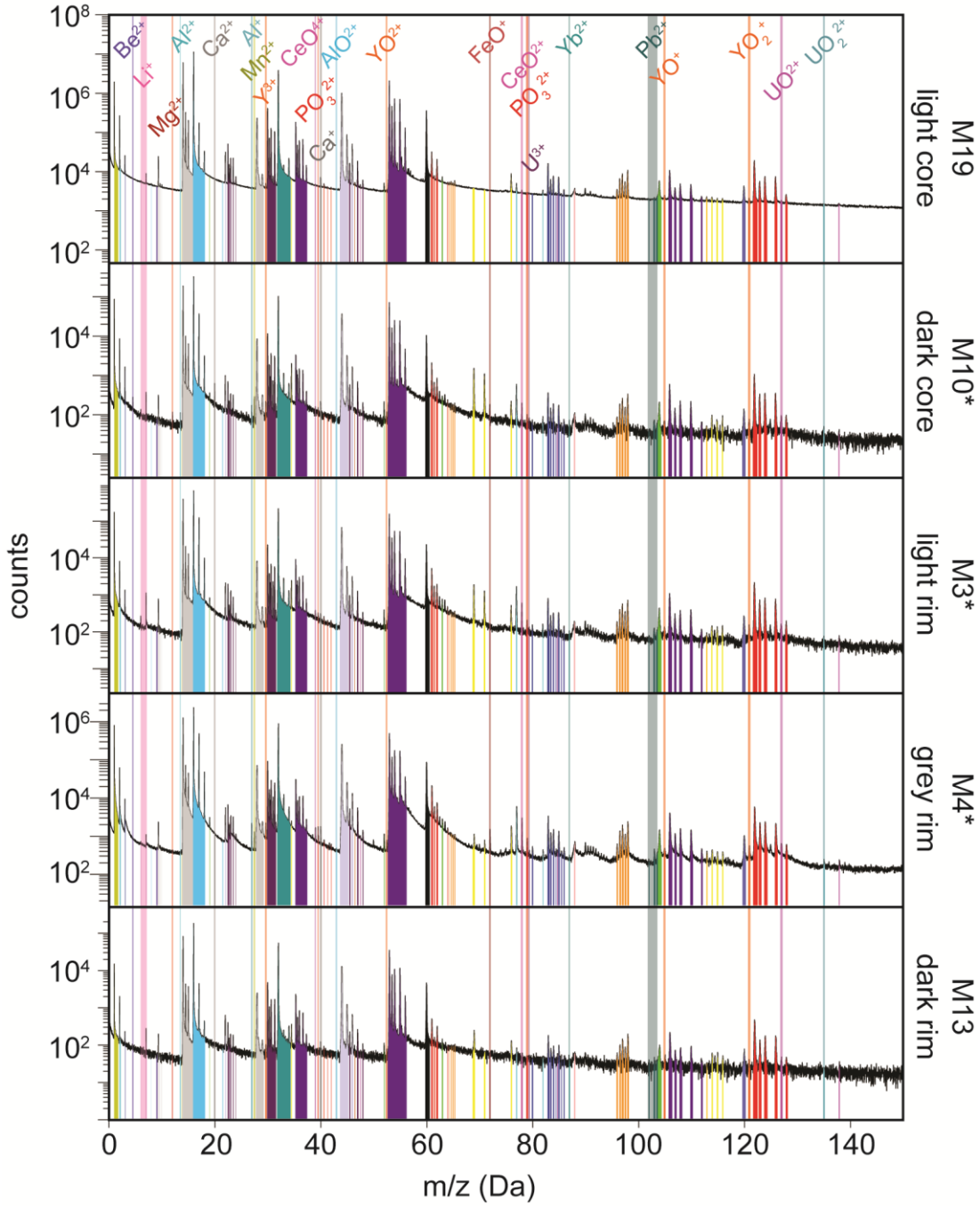

Figure 3.6 Examples of the APT mass spectrums from specimens of different regions with zircon grain 002. The trace elements identified with the specimens are highlighted for easy comparison.

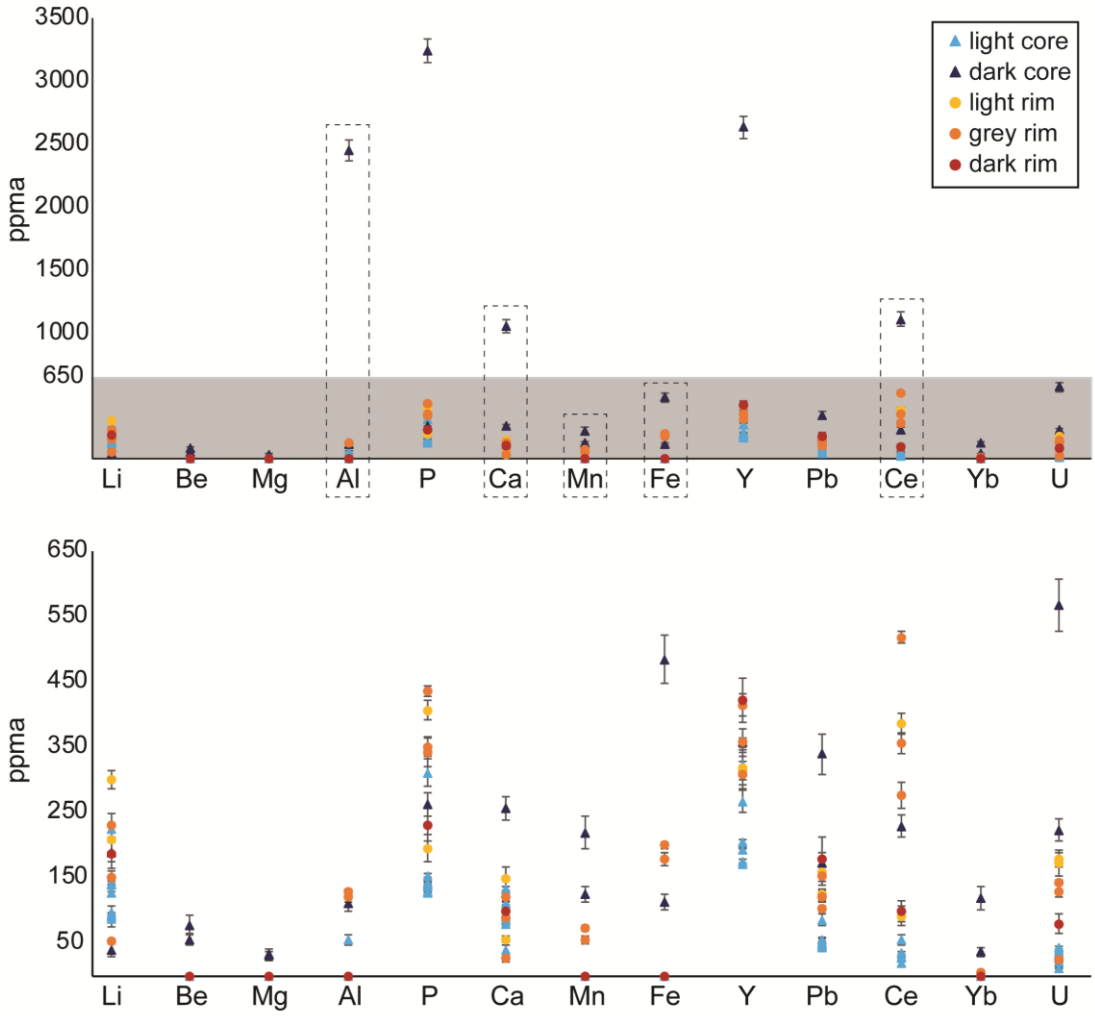

Figure 3.7 Trace elements composition (ppma) from the APT specimens. The data is classified into light core (light blue triangle), dark core (purple triangle), light rim (yellow circle), grey rim (orange circle) and dark rim (red circle). The dashed black rectangles highlight trace elements commonly seen in metamorphic zircon grains. The grey area from the upper graph is showed in detail in the lower graph.

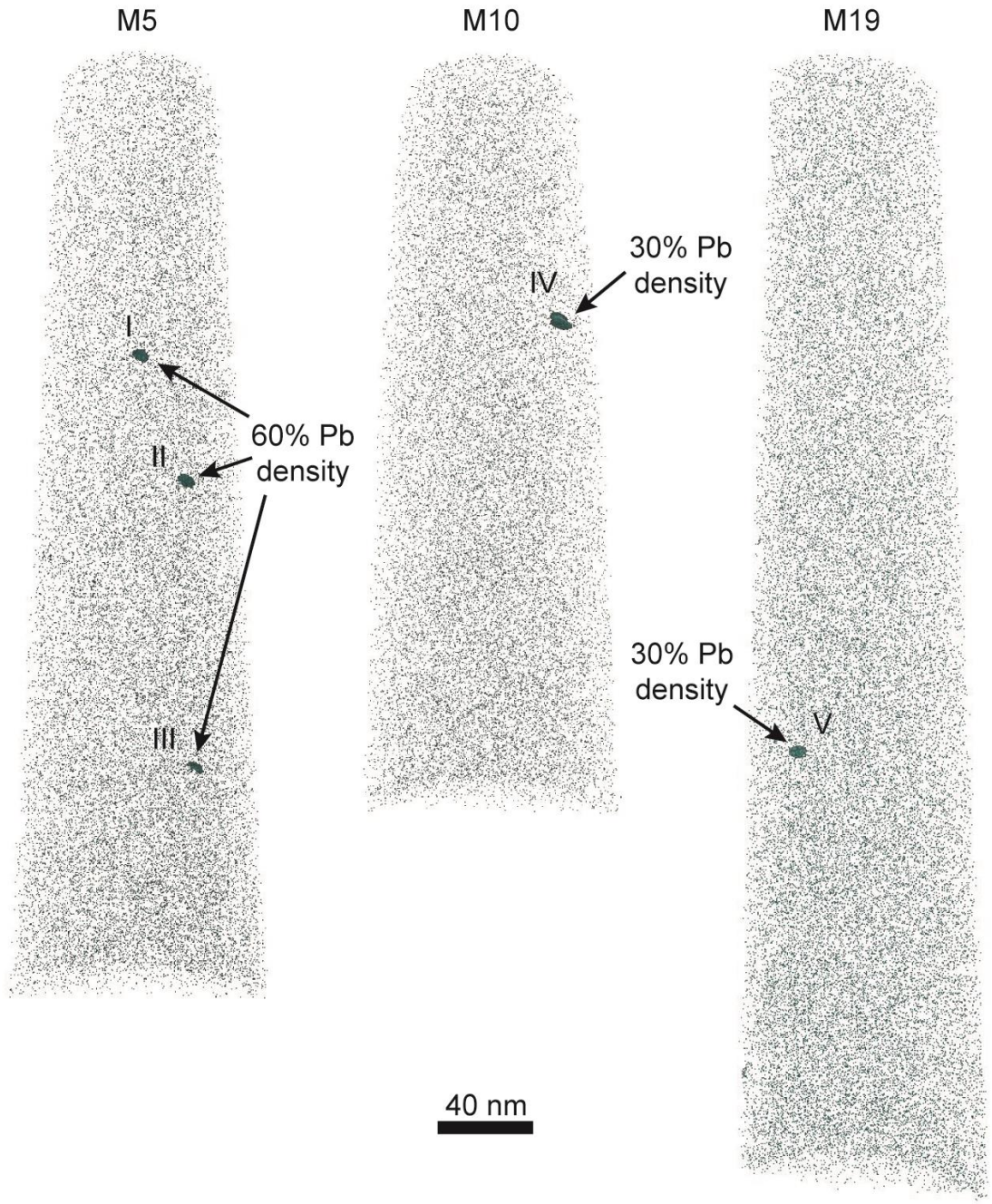

Figure 3.8 3D reconstruction of the APT specimens that contain Pb clusters. Each sphere in the reconstruction represent a single Pb atom. The isoconcentration surfaces of each specimen are included and they are based on Pb density compared to the rest of the specimen.

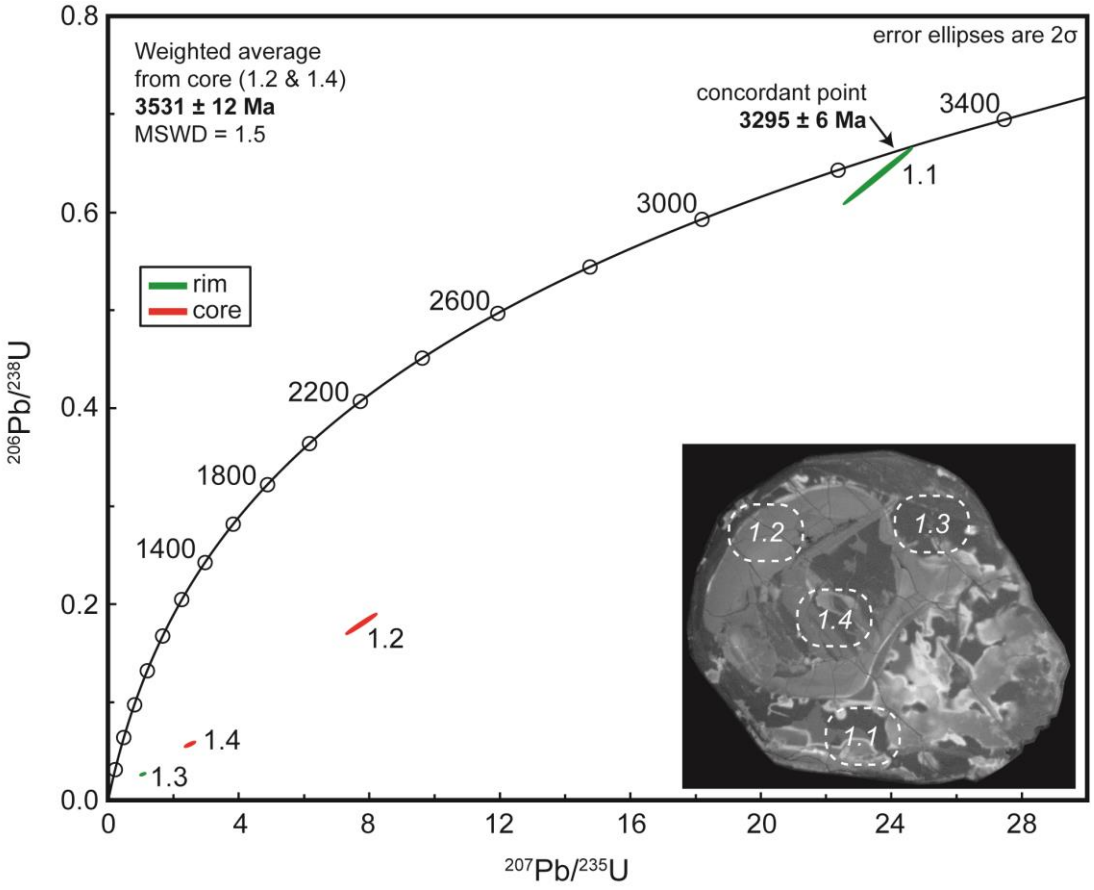

Figure 3.9 Geochronological SHRIMP data of the zircon grain 002 with a concordant age of an analysis, the weighted average from the core analyses, and the CL image with the location of each analyses.

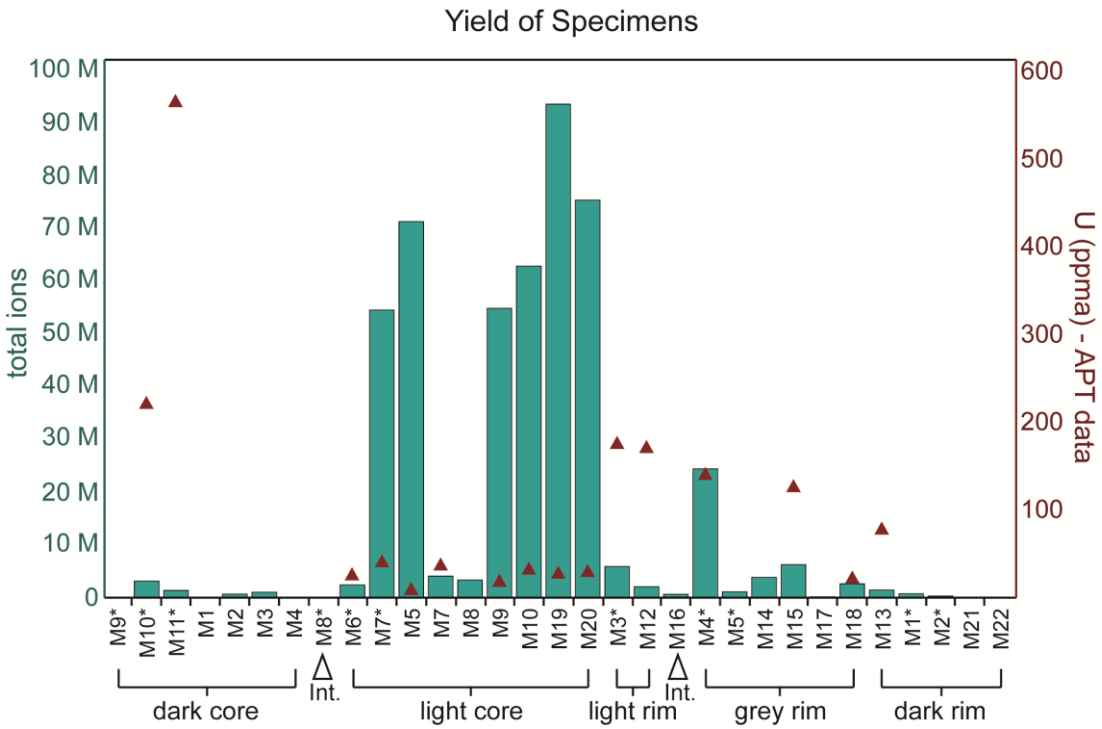

Figure 3.10 APT specimen yield plot from the different subdivisions, including two specimens that were acquired from interfaces (Int.). The concentration of U (in ppma) from the APT data was added (red triangles) to show its relationship to the yield of the specimens. Notice the connection between the high number of ions, the low concentration of U, and the subdivision (light core).

Supplementary Material

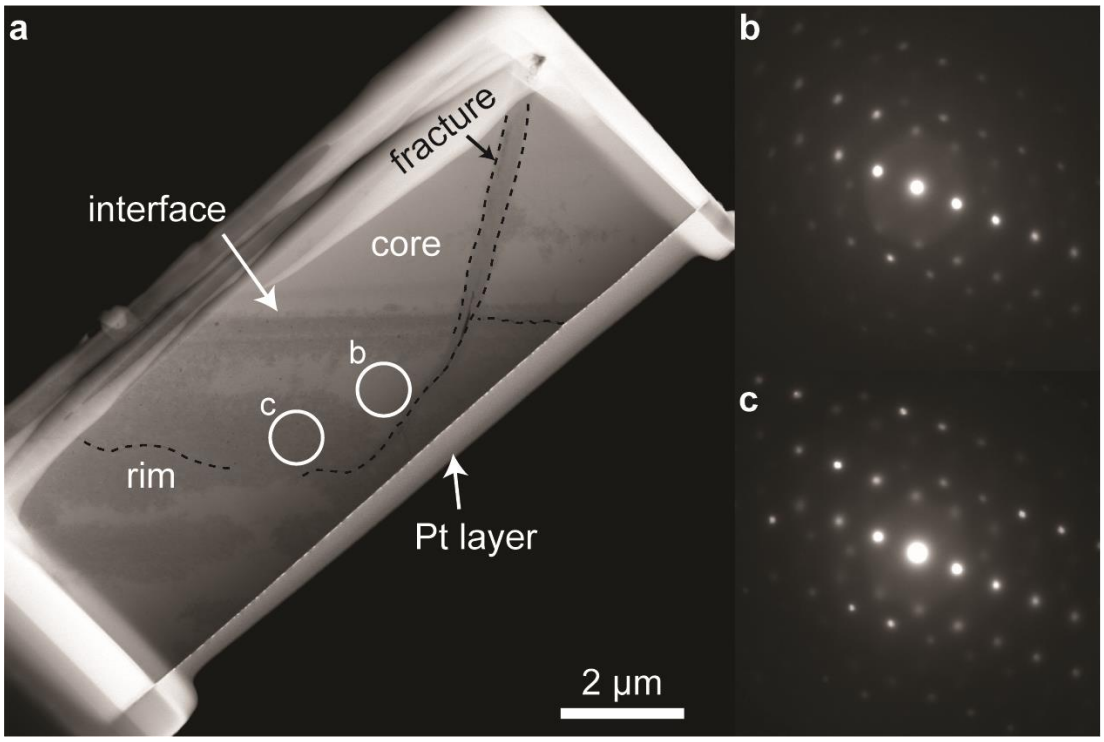

Suppl. Figure 3.1 **(a)** HAADF image and **(b-c)** diffraction patterns from two locations withing the rim region. The electron diffraction patterns were found to be crystalline with no amorphous pattern seen.

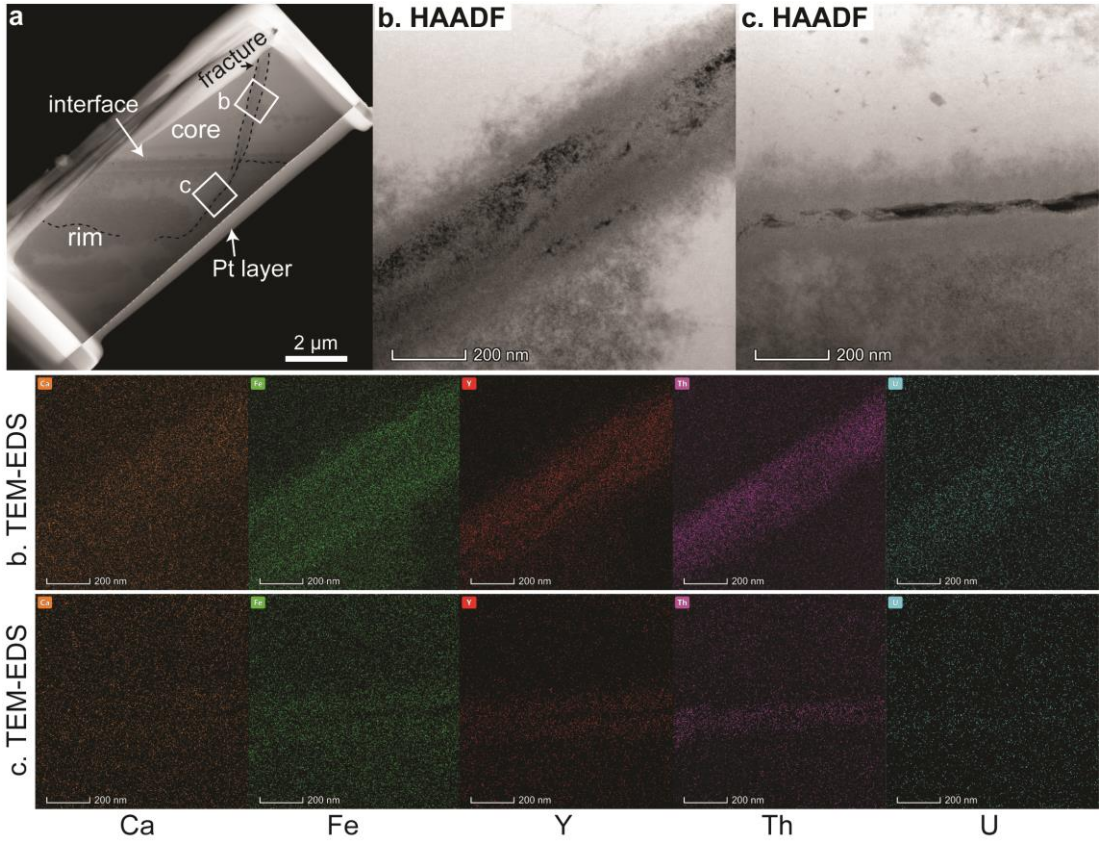

Suppl. Figure 3.2 **(a)** HAADF and TEM-EDS maps of the healed fracture in the **(b)** core and the **(c)** rim.

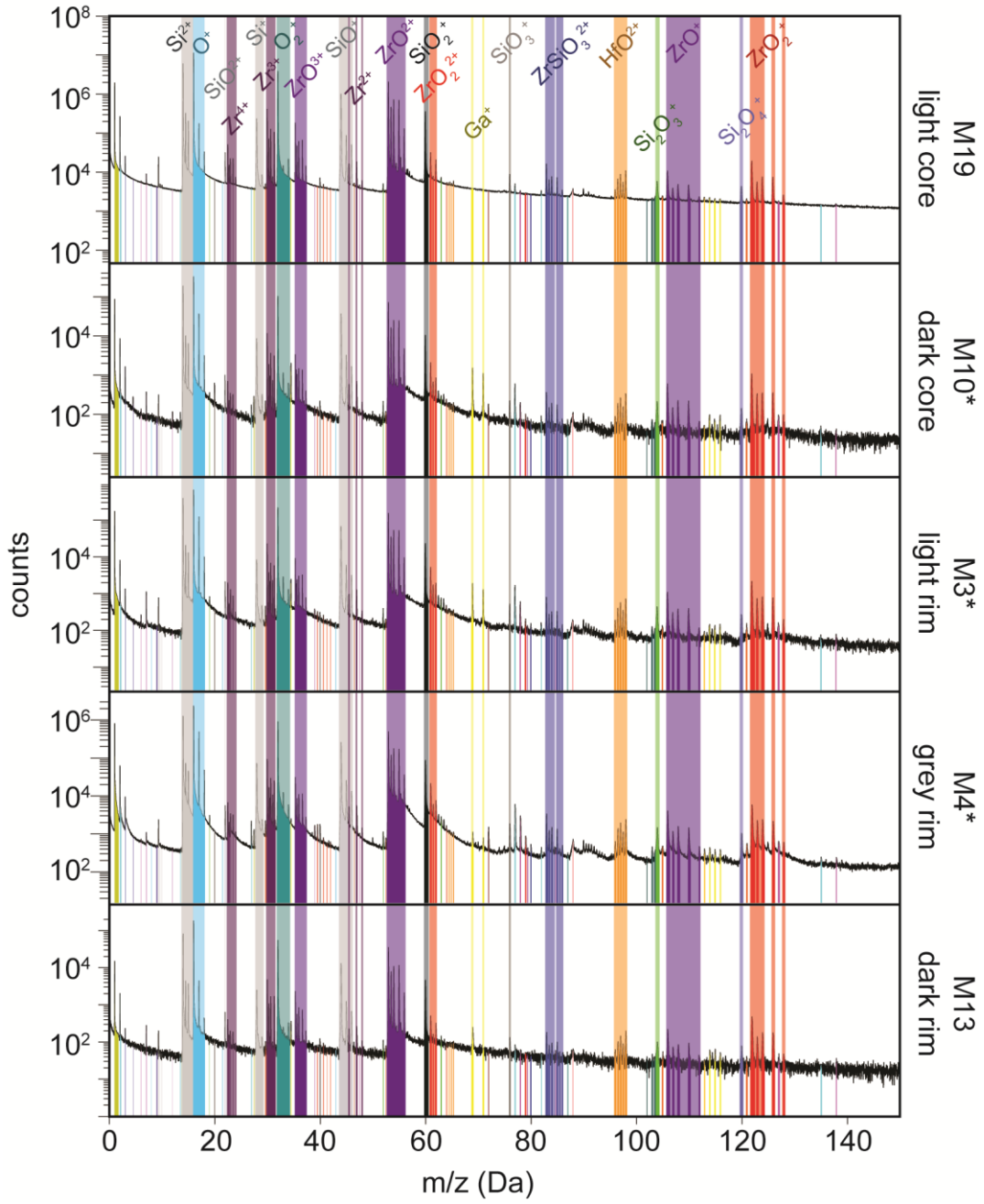

Suppl. Figure 3.3 Examples of APT mass spectrums of the different regions with the ranges of the major elements.

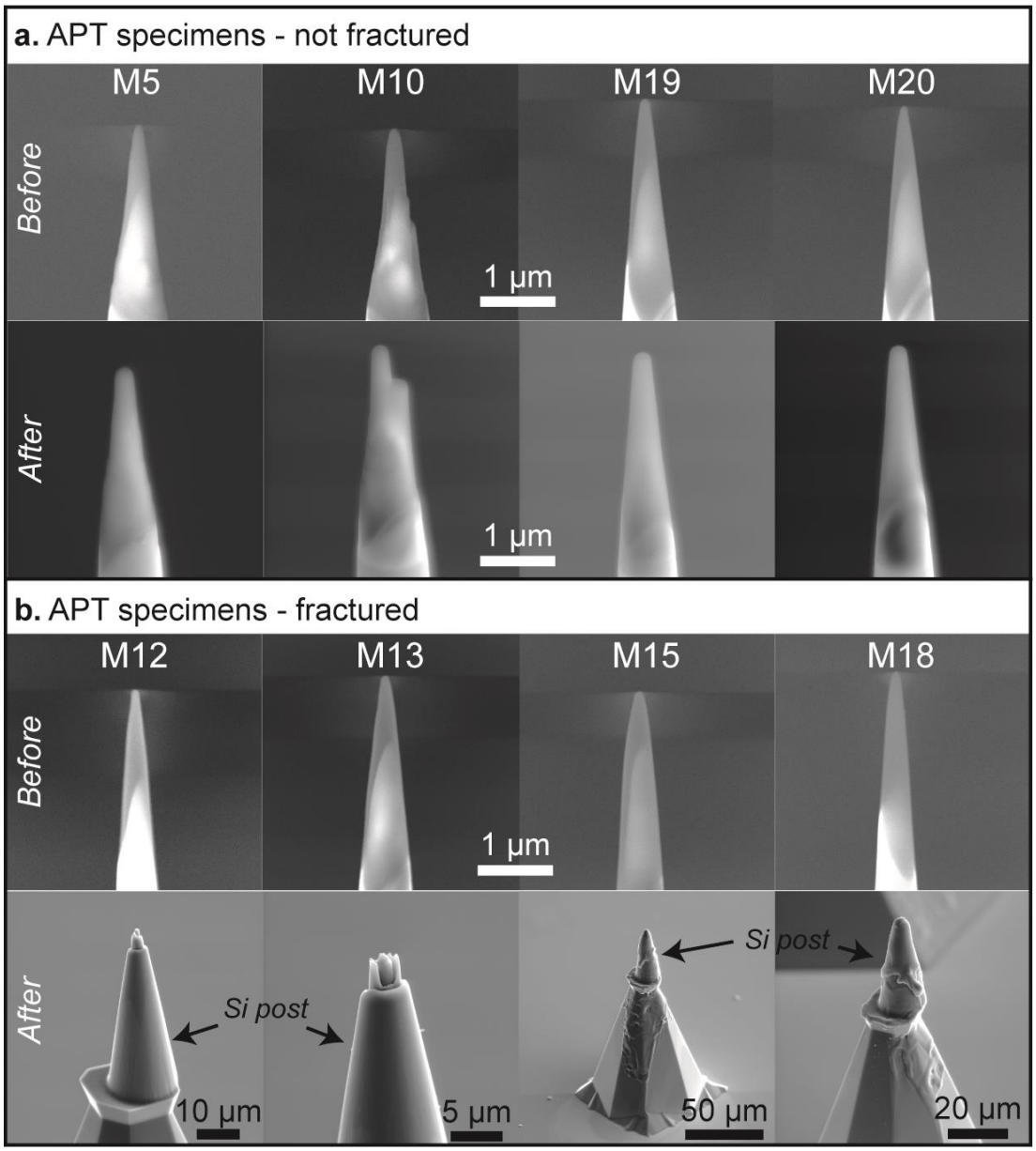

Suppl. Figure 3.4 Examples of the APT specimens before (In-beam SE) and after (SE) the APT analysis. **(a)** Shows APT specimens that did not fracture and produced a high yield, while **(b)** shows a few specimens that fractured. Notice in **(b)** the fracturing events reached down the Si post of the carrier microtip.

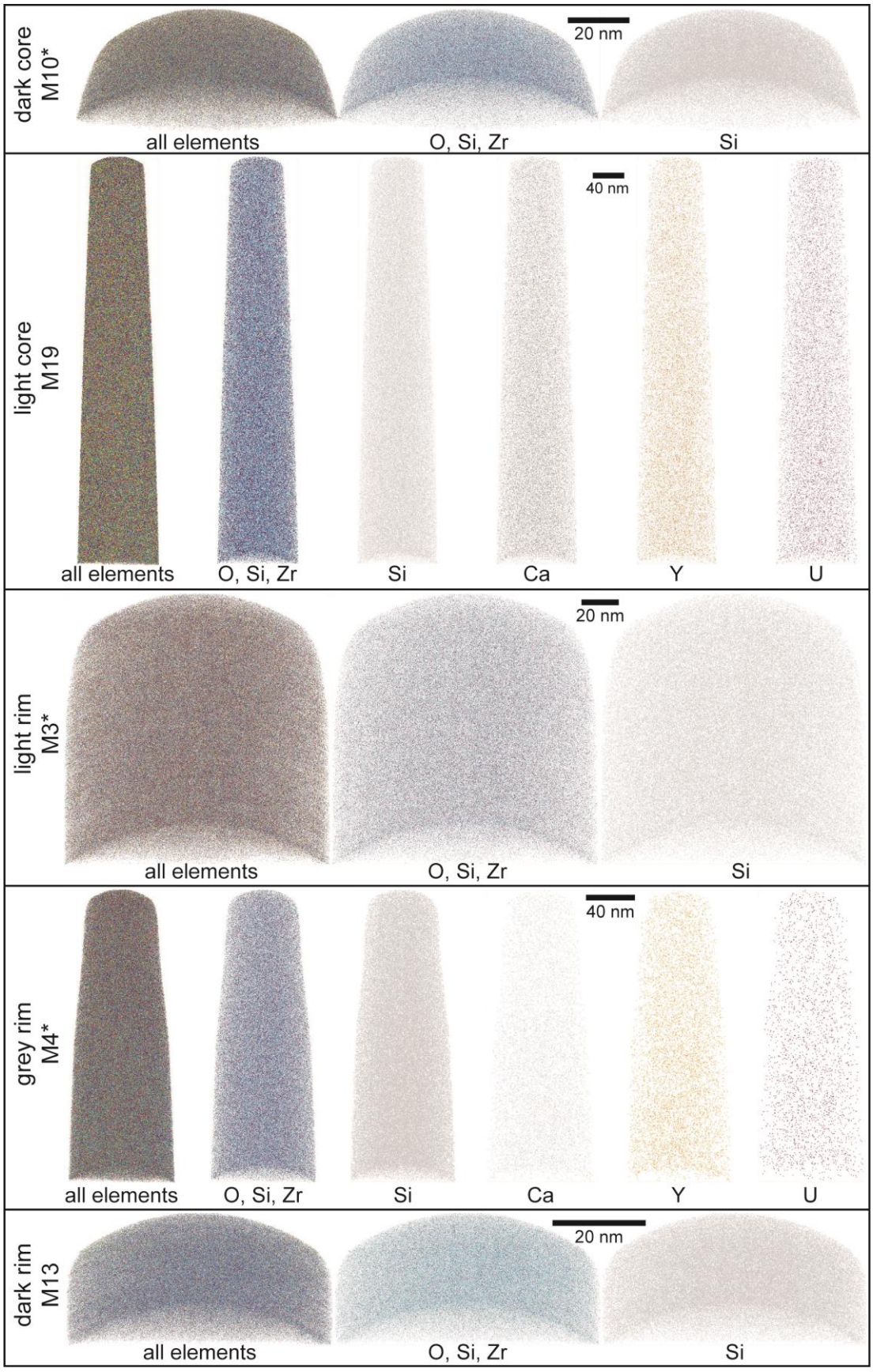

Suppl. Figure 3.5 Examples of APT 3D reconstructions for several specimens of different textural regions. The reconstructions include all elements, the major

elements, Si, and, in two cases, the trace elements Ca, Y and U. Besides the specimens from the light core region, the reconstructions of the trace elements were complicated to illustrate due to the low ion counts, hence they were not included in the figure. Only a few were selected for the 3D reconstruction (Ca, Y and U).

References

Barley, M. E., McNaughton, N. J., Williams, I. S., and Compston, W., 1994, Geologic Note: Age of Archaean volcanism and sulphide mineralization in the Whim Creek Belt, west Pilbara: Australian Journal of Earth Sciences, v. 41, no. 2, p. 175-177.

Belousova, E., Griffin, W., O'Reilly, S. Y., and Fisher, N., 2002, Igneous zircon: trace element composition as an indicator of source rock type: Contributions to Mineralogy and Petrology, v. 143, no. 5, p. 602-622.

Cavosie, A. J., Quintero, R. R., Radovan, H. A., and Moser, D. E., 2010, A record of ancient cataclysm in modern sand shock microstructures in detrital minerals from the Vaal River, Vredefort Dome, South Africa: Geological Society of America Bulletin, v. 122, no. 11, p. 1968-1980.

Chakoumakos, B. C., Murakami, T., Lumpkin, G. R., and Ewing, R. C., 1987, Alpha-Decay—Induced Fracturing in Zircon: The Transition from the Crystalline to the Metamict State: Science, v. 236, no. 4808, p. 1556-1559.

Cherniak, D. J., and Watson, E. B., 2010, Li diffusion in zircon: Contributions to Mineralogy and Petrology, v. 160, no. 3, p. 383-390.

Corfu, F., Hanchar, J. M., Hoskin, P. W. O., and Kinny, P., 2003, Atlas of zircon textures, *in* Hanchar, J. M., and Hoskin, P. W. O., eds., Reviews in Mineralogy and Geochemistry: Zircon, Volume 53.

Courtney-Davies, L., Ciobanu, C. L., Verdugo-Ihl, M. R., Slattery, A., Cook, N. J., Dmitrijeva, M., Keyser, W., Wade, B. P., Domnick, U. I., Ehrig, K., Xu, J., and Kontonikas-Charos, A., 2019, Zircon at the Nanoscale Records Metasomatic Processes Leading to Large Magmatic–Hydrothermal Ore Systems: Minerals, v. 9, no. 6.

Ewing, R. C., Meldrum, A., Wang, L., Weber, W. J., and Corrales, L. R., 2003, Radiation Effects in Zircon, *in* Hanchar, J. M., and Hoskin, P. W. O., eds., Zircon, Volume 53: Wagington, DC., The Mineralogical Society of America, p. 387-425.

Fedo, C. M., Sircombe, K. N., and Rainbird, R. H., 2003, Detrital Zircon Analysis of the Sedimentary Record: Reviews in Mineralogy and Geochemistry, v. 53, p. 277-303.

Fougerouse, D., Reddy, S. M., Kirkland, C. L., Saxey, D. W., Rickard, W. D., and Hough, R. M., 2019, Time-resolved, defect-hosted, trace element mobility in deformed Witwatersrand pyrite: Geoscience Frontiers, p. 55-63.

Fougerouse, D., Reddy, S. M., Saxey, D. W., Erickson, T. M., Kirkland, C. L., Rickard, W. D. A., Seydoux-Guillaume, A. M., Clark, C., and Buick, I. S., 2018, Nanoscale distribution of Pb in monazite revealed by atom probe microscopy: Chemical Geology, v. 479, p. 251-258.

Geisler, T., Pidgeon, R. T., Kurtz, R., van Bronswijk, W., and Schleicher, H., 2003, Experimental hydrothermal alteration of partially metamict zircon: American Mineralogist, v. 88, no. 10, p. 1496-1513.
Geisler, T., Schaltegger, U., and Tomaschek, F., 2007, Re-equilibration of Zircon in Aqueous Fluids and Melts: Elements, v. 3, no. 1, p. 43-50.
Geoscience Australia and Australian Stratigraphy Commission, 2017, Australian Stratigraphic Units Database. (accessed February 2020).
Gray, M. B., and Zeitler, P. K., 1997, Comparison of clastic wedge provenance in the Appalachian foreland using U/Pb ages of detrital zircons: Tectonics, v. 16, no. 1, p. 151-160.
Hoskin, P. W. O., 2005, Trace-element composition of hydrothermal zircon and the alteration of Hadean zircon from the Jack Hills, Australia: Geochimica et Cosmochimica Acta, v. 69, no. 3, p. 637-648.
Hoskin, P. W. O., and Black, L. P., 2000, Metamorphic zircon formation by solid-state recrystallization of protolith igneous zircon: Journal of Metamorphic Geology, v. 18, no. 4, p. 423-439.
Hoskin, P. W. O., and Schaltegger, U., 2003, The composition of zircon and igneous and metamorphic petrogenesis, *in* Hanchar, J. M., and Hoskin, P. W. O., eds., Zircon, Volume 53: Washington, DC, The Mineralogical Society of America, p. 27-62.
Kelly, T. F., and Larson, D. J., 2012, Atom Probe Tomography 2012: Annual Review of Materials Research, v. 42, no. 1, p. 1-31.
Kohn, M. J., Corrie, S. L., and Markley, C., 2015, The fall and rise of metamorphic zircon: American Mineralogist, v. 100, no. 4, p. 897-908.
Krapez, B., and Barley, M. E., 1987, Archaean strike-slip faulting and related ensialic basins: Evidence from the Pilbara Block, Australia: Geological Magazine, v. 124, no. 6, p. 555-567.
Kusiak, M. A., Dunkley, D. J., Wirth, R., Whitehouse, M. J., Wilde, S. A., and Marquardt, K., 2015, Metallic lead nanospheres discovered in ancient zircons: Proceedings of the National Academy of Sciences, v. 112, no. 16, p. 4958-4963.
Larson, D. J., Gault, B., Geiser, B. P., De Geuser, F., and Vurpillot, F., 2013a, Atom probe tomography spatial reconstruction: Status and directions: Current Opinion in Solid State and Materials Science, v. 17, no. 5, p. 236-247.
Larson, D. J., Prosa, T. J., Ulfig, R. M., Geiser, B. P., and Kelly, T. F., 2013b, Local Electrode Atom Probe Tomography: A user's guide: New York, Springer, p. 318.
Lee, J. K. W., 1995, Multipath diffusion in geochronology: Contributions to Mineralogy and Petrology, v. 120, no. 1, p. 60-82.
Lee, J. K. W., and Tromp, J., 1995, Self-induced fracture generation in zircon: Journal of Geophysical Research: Solid Earth, v. 100, no. B9, p. 17753-17770.
Lee, J. K. W., and Williams, I. S., 1993, Microstructural controls on U-Pb mobility in zircons, Volume 74: Washington, DC, Washington, DC, United States: American Geophysical Union, p. 650-651.
Ludwig, K., 2009, SQUID 2: A user's manual: Berkeley Geochronology Center Special Publication No. 5, p. 110.
-, 2012, User's manual for Isoplot 3.75: A geochronological toolkit for microsoft excel: Berkeley Geochronology Center Special Publication No. 5, p. 75.

Martin, L. A. J., Duchêne, S., Deloule, E., and Vanderhaeghe, O., 2008, Mobility of trace elements and oxygen in zircon during metamorphism: Consequences for geochemical tracing: Earth and Planetary Science Letters, v. 267, no. 1–2, p. 161-174.

Murakami, T., Chakoumakos, B. C., Ewing, R. C., Lumpkin, G. R., and Weber, W. J., 1991, Alpha-decay event damage in zircon: American Mineralogist, v. 76, p. 1510-1532.

Nasdala, L., Irmer, G., and Wolf, D., 1995, The degree of metamictization in zircon: a Raman spectroscopic study: European Journal of Mineralogy, v. 7, no. 3, p. 471-478.

Peterman, E. M., Reddy, S. M., Saxey, D. W., Fougerouse, D., Snoeyenbos, D. R., and Rickard, W. D. A., 2019, Nanoscale processes of trace element mobility in metamorphosed zircon: Contributions to Mineralogy and Petrology, v. 174, no. 11, p. 92.

Peterman, E. M., Reddy, S. M., Saxey, D. W., Snoeyenbos, D. R., Rickard, W. D. A., Fougerouse, D., and Kylander-Clark, A. R. C., 2016, Nanogeochronology of discordant zircon measured by atom probe microscopy of Pb-enriched dislocation loops: Science Advances, v. 2, p. 9.

Piazolo, S., Austrheim, H., and Whitehouse, M., 2012, Brittle-ductile microfabrics in naturally deformed zircon: Deformation mechanisms and consequences for U-Pb dating: American Mineralogist, v. 97, no. 10, p. 1544-1563.

Piazolo, S., La Fontaine, A., Trimby, P., Harley, S., Yang, L., Armstrong, R., and Cairney, J. M., 2016, Deformation-induced trace element redistribution in zircon revealed using atom probe tomography: Nature Communications, p. 7.

Pidgeon, R. T., Nemchin, A. A., and Cliff, J., 2013, Interaction of weathering solutions with oxygen and U–Pb isotopic systems of radiation-damaged zircon from an Archean granite, Darling Range Batholith, Western Australia: Contributions to Mineralogy and Petrology, v. 166, no. 2, p. 511-523.

Pidgeon, R. T., Nemchin, A. A., Roberts, M. P., Whitehouse, M. J., and Bellucci, J. J., 2019, The accumulation of non-formula elements in zircons during weathering: Ancient zircons from the Jack Hills, Western Australia: Chemical Geology, v. 530, p. 119310.

Rainbird, R. H., Hamilton, M. A., and Young, G. M., 2001, Detrital zircon geochronology and provenance of the Torridonian, NW Scotland: Journal of the Geological Society, v. 158, no. 1, p. 15-27.

Reddy, S. M., Saxey, D. W., Rickard, W. D. A., Fougerouse, D., Montalvo, S. D., Verberne, R., and van Riessen, A., 2020, Atom probe tomography: development and application to the geosciences: Geostandards and Geoanalytical Research, v. 44, no. 1, p. 5-50.

Reddy, S. M., Timms, N. E., Pantleon, W., and Trimby, P., 2007, Quantitative characterization of plastic deformation of zircon and geological implications: Contributions to Mineralogy and Petrology, v. 153, no. 6, p. 625-645.

Reddy, S. M., Timms, N. E., Trimby, P., Kinny, P. D., Buchan, C., and Blake, K., 2006, Crystal-plastic deformation of zircon: A defect in the assumption of chemical robustness: Geology, v. 34, no. 4, p. 257-260.

Reinhard, D. A., Moser, D. E., Martin, I., Rice, K. P., Chen, Y., Olson, D., Lawrence, D., Prosa, T. J., and Larson, D. J., 2018, Atom Probe Tomography of Phalaborwa Baddeleyite and Reference Zircon BR266, *in* Moser, D. E., Corfu, F., Darling, J. R., Reddy, S. M., and Tait, K., eds., Microstructural

Geochronology: Planetary Records Down to Atom Scale, American Geophysical Union & John Wiley and Sons, Inc., p. 315-326.
Romer, R. L., 2003, Alpha-recoil in U–Pb geochronology: effective sample size matters: Contributions to Mineralogy and Petrology, v. 145, no. 4, p. 481-491.
Rubatto, D., 2017, Zircon: The Metamorphic Mineral: Reviews in Mineralogy and Geochemistry, v. 83, no. 1, p. 261-295.
Schwartz, J. J., John, B. E., Cheadle, M. J., Wooden, J. L., Mazdab, F., Swapp, S., and Grimes, C. B., 2010, Dissolution–reprecipitation of igneous zircon in mid-ocean ridge gabbro, Atlantis Bank, Southwest Indian Ridge: Chemical Geology, v. 274, no. 1–2, p. 68-81.
Seydoux-Guillaume, A. M., Fougerouse, D., Laurent, A. T., Gardés, E., Reddy, S. M., and Saxey, D. W., 2019, Nanoscale resetting of the Th/Pb system in an isotopically-closed monazite grain: A combined atom probe and transmission electron microscopy study: Geoscience Frontiers, v. 10, no. 1, p. 65-76.
Silver, L. T., and Deutsch, S., 1963, Uranium-Lead Isotopic Variations in Zircons: A Case Study: The Journal of Geology, v. 71, no. 6, p. 721-758.
Stacey, J. S., and Kramers, J. D., 1975, Approximation of terrestrial lead isotope evolution by a two-stage model: Earth and Planetary Science Letters, v. 26, no. 2, p. 207-221.
Stern, R. A., Bodorkos, S., Kamo, S. L., Hickman, A. H., and Corfu, F., 2009, Measurement of SIMS Instrumental Mass Fractionation of Pb Isotopes During Zircon Dating: Geostandards and Geoanalytical Research, v. 33, no. 2, p. 145-168.
Stüeken, E. E., and Buick, R., 2018, Environmental control on microbial diversification and methane production in the Mesoarchean: Precambrian Research, v. 304, p. 64-72.
Tanabe, K., and Hiraishi, J., 1980, Correction of finite slit width effects on Raman line widths: Spectrochimica Acta Part A: Molecular Spectroscopy, v. 36, no. 4, p. 341-344.
Thomson, O. A., Cavosie, A. J., Moser, D. E., Barker, I., Radovan, H. A., and French, B. M., 2014, Preservation of detrital shocked minerals derived from the 1.85 Ga Sudbury impact structure in modern alluvium and Holocene glacial deposits: GSA Bulletin, v. 126, no. 5-6, p. 720-737.
Timms, N. E., Kinny, P. D., and Reddy, S. M., 2006, Enhanced diffusion of Uranium and Thorium linked to crystal plasticity in zircon: Geochemical Transactions, v. 7, no. 1, p. 10.
Timms, N. E., and Reddy, S. M., 2009, Response of cathodoluminescence to crystal-plastic deformation in zircon: Chemical Geology, v. 261, no. 1–2, p. 12-24.
Tomaschek, F., Kennedy, A. K., Villa, I. M., Lagos, M., and Ballhaus, C., 2003, Zircons from Syros, Cyclades, Greece—Recrystallization and Mobilization of Zircon During High-Pressure Metamorphism: Journal of Petrology, v. 44, no. 11, p. 1977-2002.
U.S. Geological Survey, 2006, GDC Digital Cartographic Standard for Geologic Map Symbolization (available at http://pubs.usgs.gov/tm/2006/11A02/).
Utsunomiya, S., Palenik, C. S., Valley, J. W., Cavosie, A. J., Wilde, S. A., and Ewing, R. C., 2004, Nanoscale occurrence of Pb in an Archean zircon: Geochimica et Cosmochimica Acta, v. 68, no. 22, p. 4679-4686.
Valley, J. W., Cavosie, A. J., Ushikubo, T., Reinhard, D. A., Lawrence, D. F., Larson, D. J., Clifton, P. H., Kelly, T. F., Wilde, S. A., Moser, D. E., and

Spicuzza, M. J., 2014, Hadean age for a post-magma-ocean zircon confirmed by atom-probe tomography: Nature Geoscience, v. 7, no. 3, p. 219-223.
Valley, J. W., Reinhard, D. A., Cavosie, A. J., Ushikubo, T., Lawrence, D. F., Larson, D. J., Kelly, T. F., Snoeyenbos, D. R., and Strickland, A., 2015, Nano- and micro-geochronology in Hadean and Archean zircons by atom-probe tomography and SIMS: New tools for old minerals: American Mineralogist, v. 100, no. 7, p. 1355-1377.
Van Kranendonk, M., 2008, Structural geology of the central part of the Lalla Rookh - Western Shaw structural corridor, Pilbara Craton, Western Australia Geological Survey of Western Australia, p. 29.
Van Kranendonk, M. J., Hickman, A. H., Smithies, R. H., Nelson, D. R., and Pike, G., 2002, Geology and Tectonic Evolution of the Archean North Pilbara Terrain, Pilbara Craton, Western Australia: Economic Geology, v. 97, no. 4, p. 695-732.
Vonlanthen, P., Fitz Gerald, J. D., Rubatto, D., and Hermann, J., 2012, Recrystallization rims in zircon (Valle d'Arbedo, Switzerland): An integrated cathodoluminescence, LA-ICP-MS, SHRIMP, and TEM study: American Mineralogist, v. 97, no. 2-3, p. 369-377.

Chapter 4 NANOSCALE CONSTRAINTS ON THE SHOCK-INDUCED TRANSFORMATION OF ZIRCON TO REIDITE

This chapter is published in Chemical Geology 507, (doi.org/10.1016/j.chemgeo.2018.12.039).

The principal roles of each co-author are as follows:

Stephanie D. Montalvo: Concept and design of the work; sample preparation; data acquisition, analysis and interpretation (EBSD, SE, BSE, CL, ToF-SIMS, TKD, APT, TEM); manuscript writing and editing.

Steven M. Reddy: Concept and design; data analysis and interpretation (EBSD, SE, BSE, CL); manuscript editing.

David W. Saxey: Concept and design; acquisition, analysis and interpretation of APT data; manuscript editing.

William D.A. Rickard: Data acquisition, analysis and interpretation (ToF-SIMS, TKD); manuscript editing.

Denis Fougerouse: Data acquisition, analysis and interpretation (APT, TEM), and manuscript editing.

Zakaria Quadir: Acquisition, analysis and interpretation of TEM data, and manuscript editing.

Tim E. Johnson: Contributions to the conception and design of the work, field data acquisition; manuscript editing.

Chemical Geology 507 (2019) 85–95

Contents lists available at ScienceDirect

Chemical Geology

journal homepage: www.elsevier.com/locate/chemgeo

Nanoscale constraints on the shock-induced transformation of zircon to reidite

Stephanie D. Montalvo[a,b,*], Steven M. Reddy[a,b], David W. Saxey[a], William D.A. Rickard[a], Denis Fougerouse[a,b], Zakaria Quadir[c], Tim E. Johnson[b,d]

[a] Geoscience Atom Probe, Advanced Resource Characterisation Facility, John de Laeter Centre, Curtin University, Perth, Australia
[b] School of Earth and Planetary Science, Curtin University, Perth, Australia
[c] Microscopy and Microanalysis Facility, Curtin University, John de Laeter Centre, Perth, Australia
[d] Center for Global Tectonics, State Key Laboratory of Geological Processes and Mineral Resources, China University of Geosciences, Wuhan, Hubei Province 430074, China

ARTICLE INFO

Editor: Balz Kamber

Keywords:
Reidite
Shocked zircon
Trace element mobility
Phase transformation
Atom probe tomography

ABSTRACT

In a hypervelocity impact event, the temperatures and pressures generated by the shock waves far exceed the values produced by endogenic processes. The shock-induced processes can modify the distribution of trace elements in zircon grains located in target rocks, potentially affecting the geochemical reliability of zircon, but also providing an opportunity to better understand the mechanisms of shock deformation. The formation of reidite lamellae by the shock-induced phase change of zircon has previously been proposed to be a diffusionless, martensitic transformation, with no associated atomic mobility over nanometre length scales. However, nanoscale characterization of the zircon–reidite interface and a low-angle boundary within the reidite by atom probe tomography, transmission electron microscopy and correlative analytical techniques, shows localised enrichment of particular trace elements (Y, Al, Ca, Be, Mg, Mn, and Ti). These observations indicate the presence of additional short-range diffusional components to explain the local compositional variations observed at the nanoscale for the high-pressure transformation of zircon to reidite lamellae. A new model for this transformation is proposed that consists of two stages: 1) the early stage of the impact event where the shock waves induce defects in the zircon grain and trigger a phase transformation, resulting in trace element segregation by interface migration; and 2) the recovery stage where the trace elements and shock induced defects migrate to areas of lower energy.

1. Introduction

The trace element composition of zircon ($ZrSiO_4$) have been widely used to place constraints on the processes of crustal evolution as far back as the Hadean eon (e.g. Wilde et al., 2001; Valley et al., 2014). For instance, the isotopic systems U–Th–Pb, Sm–Nd, and Lu–Hf are used to constrain absolute and model ages, Ti is used as a thermometer, and the rare earth elements (REE) can be used to study the composition and history of Earth's crust (Kinny and Maas, 2003; Watson et al., 2006; Hanchar and van Westrenen, 2007; Harley and Kelly, 2007). The successful application of trace element geochemistry requires a thorough understanding of the mechanisms by which trace elements are incorporated into the zircon lattice and how these compositions can be subsequently modified. The incorporation of trace elements into zircon is now generally well understood, with either direct substitution into the lattice or integration via interstitial sites or vacancies (Hinton and Upton, 1991; Hoskin et al., 2000; Cherniak and Watson, 2003; Hoskin and Schaltegger, 2003; Cherniak, 2010; Reddy et al., 2016). However, the mechanisms by which trace elements may be modified remain poorly understood. Volume diffusion, diffusion through radiation-induced defects, and diffusion through deformation microstructures have been suggested as possible mechanisms for element migration (e.g. Cherniak and Watson, 2001; Cherniak and Watson, 2003; Reddy et al., 2006; Timms et al., 2006; Nasdala et al., 2010; Piazolo et al., 2016). Significantly, there is little known about trace element mobility associated with shock deformation.

The physical, structural and chemical composition of zircon grains can be altered by the extreme temperatures and pressures associated with hypervelocity impact events (Melosh, 1989; Leroux et al., 1999; Reddy et al., 2016; Timms et al., 2017b). One of the ways zircon may

* Corresponding author at: Geoscience Atom Probe, Advanced Resource Characterisation Facility, John de Laeter Centre, Curtin University, Perth, Australia.
E-mail address: s.montalvo@postgrad.curtin.edu.au (S.D. Montalvo).

https://doi.org/10.1016/j.chemgeo.2018.12.039
Received 22 August 2018; Received in revised form 19 December 2018; Accepted 29 December 2018
Available online 16 January 2019

respond to these extreme conditions is to transform into reidite, a high-pressure polymorph with a scheelite-type crystal structure (Reid and Ringwood, 1969; Glass et al., 2002). In laboratory shock experiments, the transformation from zircon to reidite occurs at pressures ranging from ~30 to 60 GPa (Kusaba et al., 1985; Kusaba et al., 1986; Leroux et al., 1999; Timms et al., 2017a). Even though it has been suggested that reidite can form in subducted crust deep within the mantle (Reid and Ringwood, 1969; Tange and Takahashi, 2004), the presence of reidite is commonly considered a diagnostic feature of impacts.

In nature, reidite has been found in shocked zircon grains in two forms, as lamellae and in granular form, both of which occur within impact structures and ejecta deposits (Glass et al., 2002; Gucsik et al., 2004; Wittmann et al., 2006; Chen et al., 2013; Cavosie et al., 2015; Reddy et al., 2015; Drake et al., 2017; Cox et al., 2018). The form taken by reidite is thought to be dependent on the crystallinity of the zircon host and the mechanism of transformation (Erickson et al., 2017). Granular reidite forms by a reconstructive mechanism in metamict regions within the zircon, whereas reidite lamellae are thought to form by a martensitic mechanism in areas of crystalline zircon (Erickson et al., 2017).

Martensitic transformations are considered to be non-diffusional displacive transformations, which reflect shear along specific crystallographic planes, and results in the formation of a new phase (polymorph) with the same chemical composition as the host (Balluffi et al., 2005; Aaronson et al., 2010). The near-instantaneous transformation of zircon to reidite lamellae during an impact event limits the time available for diffusion and supports formation by a martensitic transformation (Kusaba et al., 1985; Kusaba et al., 1986), involving modification of the SiO_4 tetrahedron, accompanied by a component of rotation of the oxygen atoms (Kusaba et al., 1985; Kusaba et al., 1986; Leroux et al., 1999; Turner et al., 2014; Erickson et al., 2017).

One prediction of a martensitic transformation is that a consistent crystallographic relationship between the host mineral and the martensitic phase should exist. For zircon (z) and reidite (r), a range of studies have confirmed a consistent relationship, such that $\{100\}_z$ is parallel to $\{112\}_r$, $\langle 001\rangle_z$ is parallel to $\langle 110\rangle_r$, $\{112\}_z$ is parallel to $\{112\}_r$, and $(001)_r$ is coincident with $\{110\}_z$, (Kusaba et al., 1986; Leroux et al., 1999; Cavosie et al., 2015; Reddy et al., 2015; Erickson et al., 2017). In the past, such relationships have been used to infer that the zircon–reidite interface (or habit plane) is crystallographically controlled and lies parallel to $\{100\}_z$ and $\{112\}$ (Kusaba et al., 1986; Leroux et al., 1999). However, recent three-dimensional analysis of the orientation of reidite lamellae has shown that the habit plane between the zircon host and the reidite lamellae can have a range of different orientations and is generally not the plane of lattice coincidence (Reddy et al., 2015; Erickson et al., 2017). This inconsistency suggests that the phase transformation mechanism associated with the formation of reidite lamellae is still not completely understood.

To better understand the mechanisms of transformation of zircon to reidite lamellae, a detailed crystallographic and geochemical analysis of reidite from the Stac Fada ejecta deposit of NW Scotland has been undertaken (Amor et al., 2008). The analytical workflow spans a range of scales and includes nanometre characterization by atom probe tomography (APT). This nanoscale approach provides fundamentally new insights into the mechanisms of the zircon to reidite phase transformation and associated trace element mobility.

2. Geological background

The analysed zircon grain comes from a sample (14-SF-01) from the Stac Fada Member of the Mesoproterozoic Stoer Group, in northwest Scotland (Ordnance Survey National Grid coordinate reference NC 03348 28515) (Fig. 1). The Stoer Group, part of the Torridonian Supergroup, mainly consists of sedimentary rocks from fluvial, lacustrine, playa, and alluvial fan environments (Johnstone and Mykura, 1989), which have been weakly metamorphosed at low temperatures (Stewart, 2002; Parnell et al., 2011). The Stac Fada Member is unique within the Stoer Group in comprising brecciated materials containing accretionary lapilli. Although previously considered to be volcaniclastic in origin (Lawson, 1972; Stewart, 1988; Sanders and Johnston, 1989; Young, 2002), recent geochemical and microstructural data have led to the Stac Fada Member being interpreted as an ejecta deposit associated with a ~1177 Ma meteorite impact event (Amor et al., 2008; Branney and Brown, 2011; Parnell et al., 2011; Reddy et al., 2015), possibly represented by the Lairg Gravity Low located approximately 50 km to the east (Simms, 2015). The Stac Fada Member comprises three main facies. A massive suevite (impact breccia) is overlain by a mixed unit of suevite and accretionary lapilli, and an uppermost, thin layer of dust pellets that likely originated from an impactoclastic density current that was deposited onto water-saturated sediments (Branney and Brown, 2011). The unit shows local evidence for soft-sediment deformation, but there is little evidence for subsequent tectonic deformation or significant metamorphic overprinting following its original deposition (Stewart, 2002; Simms, 2015). However, the Stac Fada Member is cut by mineralized vesicular zones inferred to have formed by degassing of the pre-lithified sediments upon which the ejecta was deposited (Sanders and Johnston, 1989; Parnell et al., 2011).

3. Methods

The shocked zircon analysed in this research (grain 86) was previously studied by Reddy et al. (2015) and Reddy et al. (2016) using electron backscatter diffraction (EBSD), transmission Kikuchi diffraction (TKD), and by APT on a low-angle boundary in the host zircon grain. In this research, we focus on the reidite lamellae in grain 86.

Individual grains were extracted from the sample (14-SF-01) using SelFrag high-voltage pulse, power fragmentation at Curtin University and zircon grains were separated and concentrated using heavy liquids (sodium polytungstate - NaPT) and a Frantz magnetic separator. From the zircon-rich fraction, 200 zircon grains were handpicked, mounted on SEM stubs, polished and coated with a thin layer of carbon (~3 nm). All zircon grains were imaged by backscattered electron (BSE), secondary electron (SE) and cathodoluminescence (CL) imaging using a Tescan MIRA3 field emission scanning electron microscope (FESEM) housed at the Microstructure and Microanalysis Facility (MMF) of the John de Laeter Centre, Curtin University. SE, BSE and CL imaging were undertaken using an accelerating voltage of 10 kV and working distance of ~17 mm, with a spectral range of 185–850 nm for the CL imaging. Details of these procedures are reported in Reddy et al. (2015).

Microstructural analysis by EBSD mapping was undertaken on a Tescan MIRA3 FESEM using an accelerating voltage of 20 kV, 70° sample tilt, a working distance of 20 mm, and a beam current of 18 nA. EBSD patterns were collected with a Nordlys Nano high-resolution detector. The EBSD data were acquired with Oxford Instruments AZtec 2.3 software. The whole grain map was collected with a 200 nm step size with approximately 530,000 electron backscatter patterns collected, with a mean angular deviation value of 0.55°. The acquired data was processed with the Oxford Instruments Channel5 software. A more detailed description of the EBSD procedure can be found in Reddy et al. (2015) and Reddy et al. (2016). Combined EBSD maps, such as band contrast (BC), phase component, and inverse pole figures (IPF), were produced to show the distribution of the phases in the grains and microstructural characterization of the zircon.

High spatial resolution maps of trace elements were acquired using a Ga^+ Tescan Lyra Focused Ion Beam Scanning Electron Microscope (FIB-SEM) equipped with a Tofwerk Time-of-Flight Secondary Ion Mass Spectrometry (ToF-SIMS) detector that provided high spatial resolution elemental maps and isotopic information. This instrument is part of the Advanced Resource Characterisation Facility (ARCF) and is housed within the John de Laeter Centre at Curtin University. The Ga^+ primary ion beam was operated with a current of 200 pA and an accelerating voltage of 20 kV. A total of 200 frames (~500 nm of depth) were

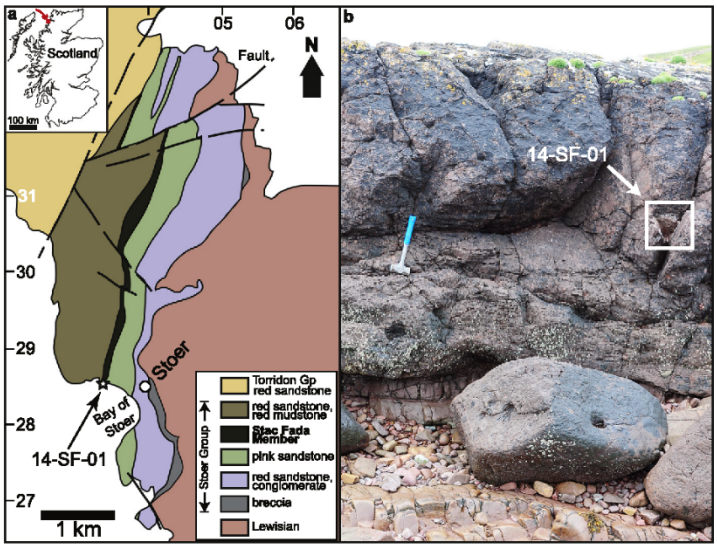

Fig. 1. (a) Simplified geological map with the location of the sample (14-SF-01) and the location of the area in Scotland. (b) Photograph of the sample location in the outcrop. Ordnance Survey National Grid coordinate reference NC 03348 28515 (latitude 58.2014N & longitude 5.3482W). Modified from Reddy et al. (2016).

collected from the analysed region.

ToF-SIMS works by detecting all the secondary ions of one polarity released by the interaction of a pulsed primary ion beam with the sample (Stephan, 2001). Once the ions are released from the sample, they are accelerated and separated by their mass/charge ratio (Stephan, 2001). By measuring the time differential between the primary ion pulse and the impact of secondary ions on the detector (time-of-flight), the mass/charge ratio of the ions can be obtained and from this the ionic species identified.

The acquisition and processing of the ToF-SIMS data was undertaken using the Tof-Sims Explorer version 1.3 software made by Tofwerk. A 7.5 × 7.5 μm region with a pixel resolution of 60 nm was analysed.

A Zeiss Neon 40EsB FIB-SEM housed within the John de Laeter Centre at Curtin University was also used for milling cross sections in the grains to obtain 3D orientation of the features of interest. The Ga^+ primary ion beam was operated with a current of 8 nA and an accelerating voltage of 30 kV.

Regions of interest were targeted for site-specific atom probe specimen preparation using the Tescan Lyra FIB-SEM. An ion beam deposition platinum strip of ~200 nm in thickness was applied over the regions of interest to protect them from ion beam damage during the lift-out process. The specimen preparation involves using a 30 kV Ga^+ ion beam to mill a wedge that was subsequently attached to a prefabricated silicon post, and then shaped for APT. The sharpening process consisted of several stages of annular milling to form atom probe tips with < 100 nm diameter at the tip. To reduce high beam energy Ga^+ implantation, a final milling stage at 5 kV was performed. Nine specimens were manufactured from the regions of interest. The orientation of each specimens is perpendicular to the polished grain surface, with the tip facing the surface. TKD was carried out on the tips of the specimens to identify the phases present. This technique offers crystallographic and compositional information that can be correlated to the atom probe needles (Babinsky et al., 2014). The TKD analyses were conducted using a 30 kV electron beam with a 30 nm step size using the Tescan Lyra FIB-SEM and an Oxford EBSD system.

Laser-assisted APT was conducted on a Cameca LEAP 4000X HR at the Geoscience Atom Probe Facility, part of the ARCF housed in the John de Laeter Centre in Curtin University. APT is a three-dimensional analytical technique that provides the elemental composition of materials at sub-nanometre resolution (Gault et al., 2012; Larson et al., 2013a). This technique is based on the field evaporation of ions, from a nanoscale needle-shaped sample. The acquisition process starts with an applied voltage that creates an electrical field at the surface of the tip, which is a little less than the electrical field needed for field evaporation. A laser-pulse applied to the specimen is used to momentarily heat the apex, thereby initiating the field evaporation of ions from the tip of the needle. Once liberated, the ions are accelerated towards a position sensitive detector that records the X and Y coordinates. This information is used to locate the original atoms within the 3-dimensional spatial reconstruction. Their Z location is obtained from the evaporation sequence of the atoms. The atom probe instrument is a ToF mass spectrometer, thus it measures the ions time-of-flight to identify them (Larson et al., 2013b). The APT acquisition parameters used follow the optimisation parameters established by Saxey et al. (2018) and are summarised in the online Supplementary Material 1, following recommendations of Blum et al. (2018).

In APT, the electrical field required to evaporate atoms from the needle apex results in high stress on the specimen. This can often cause the specimens to fracture and can result in low data yield. Shocked zircon grain 86 has a high density of defects, making the needles more fragile than those from an undeformed zircon grain. From nine APT prepared specimens, only two needles are reported in this paper since the other needles either didn't contain the region of interest (e.g. reidite phase) or fractured during data acquisition before significant data could be acquired.

The atom probe data was processed for reconstruction and analysis with a Cameca Integrated Visualization & Analysis Software (IVAS) version 3.6.14. This process includes selecting a range of ions, choosing the spatial region of interest from the detector, correcting the ToF spectrum (voltage and bowl corrections), conversion from ToF to mass/charge ratio (mass calibration), mass spectrum ranging (chemical identification of peaks), and mass spectrum reconstruction (Larson et al., 2013b). The result from IVAS is a 3D reconstruction of the

position of each detected ion identified by the user. To study the trace elements in the specimens, 1D concentration profiles and the bulk composition of the mass spectrum were made from isolated regions. The errors presented in the atom probe data are estimates of the standard deviation calculated by the IVAS software. It is based on the number of background-corrected counts and Poissonian statistics.

A foil for transmission electron microscopy (TEM) analysis was extracted from the region near the atom probe needles using a Tescan Lyra FIB-SEM. The foil was mounted into a copper half-grid and thinned to ≤100 nm, followed by a low kV (2 kV) clean-up procedure. Bright field (BF) scanning transmission electron microscopy (STEM) images, high-angle annular dark-field (HAADF) STEM images, high-resolution (HR) TEM images, and energy-dispersive X-ray spectroscopy (EDS) maps of the foil were acquired with a FEI Talos FS200X FEG TEM operated at 200 kV and equipped with a Super-X EDS detector. This instrument is housed in MMF of the John de Laeter Centre at Curtin University.

4. Results

4.1. Microstructural characterization

From the 4048 zircon grains handpicked from sample 14-SF-01, six contained reidite lamellae but only grain 86 was chosen for this study. EBSD analysis confirms that grain 86 comprises zircon with three distinct orientations of reidite lamellae (Fig. 2a–b, Reddy et al., 2015). The lamellae extend through the rim of the zircon but not the core. Several crystallographic relationships between the zircon host and the reidite lamellae were found: $\{100\}_z \,||\, \{112\}_r$, $\{112\}_z \,||\, \{112\}_r$, $\langle 001\rangle_z \,||\, \langle 110\rangle_r$, and $\{110\}_z \,||\, (001)_r$ (coincidal planes in Fig. 2c). However, the orientation of the habit plane from the three lamellae did not match the planes of lattice coincidence between the reidite and zircon host.

TEM analysis of a foil extracted from an area denoted in Fig. 2b revealed the presence of a ~500 nm thick reidite lamella that dips at 55° from the polished surface of the grain (Fig. 3). The lamella contains an amorphous (no lattice fringes present) linear feature that show signs of recrystallization in the form of crystal lattices along its borders (Fig. 3a–c). The interfacial domain between the amorphous feature and the host zircon, displays a quasi-periodic structure of dislocations a few nm apart (Fig. 3b). TEM-EDS maps indicated an Y and Al enrichment in the reidite-zircon interfaces, especially in the interfacial domain between the amorphous feature and the host zircon (Fig. 3e–f). In contrast, none of the major elements (Zr, Si and O) are enriched in this area.

4.2. High resolution compositional analysis

ToF-SIMS analysis of a region containing reidite lamellae in two different orientations shows enhancement of trace elements through the thinner lamella and along the reidite-zircon interface in the thickest lamellae (Fig. 4). The distribution of trace elements is heterogeneous within the lamellae and higher concentrations are found at the intersection of different lamellae orientations (Fig. 4). No significant compositional variation was identified in any of the major elements or other trace elements.

The two specimens (M1 and M4) from zircon grain 86 illustrate a compositional variation of trace elements in the vicinity of the reidite lamellae. The specimens were obtained from an area that contained two different orientations of reidite lamellae (Fig. 2b). TKD analysis confirmed that each specimen contained reidite (Fig. 5a) and that they are in the same crystallographic orientation of the targeted lamella (Fig. 5b). The TKD analysis had a relatively low percentage of indexing because the analytical conditions were set to minimise beam damage and improve APT yield. The samples are also expected to have a high defect concentration from the shock event which further limited the successful indexing.

The mass spectrum of both specimens shows single ions and molecular ions, with Zr, Si and O detected as the major elements. An example of mass-to-charge ratio spectrum for reidite is provided in Fig. 6, and it appear similar to previously reported atom probe analyses of zircon (Valley et al., 2015; Peterman et al., 2016). The 3D

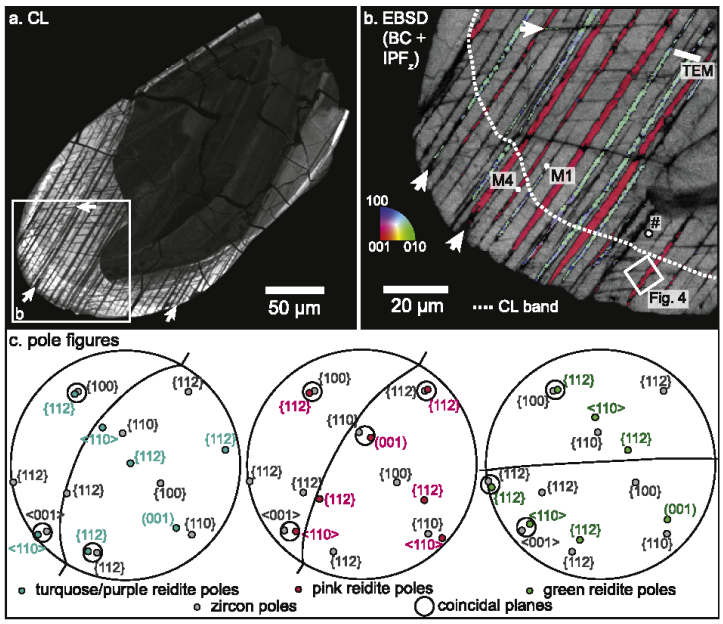

Fig. 2. Images of grain 86 with reidite lamellae (pointed by the white arrows). (a) Panchromatic CL image of grain 86, where there is a dark core surrounded by an intermediate rim, followed by a brighter outer rim. (b) Detailed band contrast (BC) plus inverse pole figure (IPF_z) map of grain 86 highlighting three different orientations of reidite lamellae (pointed by the white arrows), the location of the two atom probe specimens (M1 and M4), the division of different CL bands (white dashed line), the location of the TEM analysis, and the position of the APT specimen (#) previously analysed by Reddy et al. (2016). (c) Pole figures (lower hemisphere and equal area projection) of the each individual reidite lamellae plotted with the zircon host; data colour coded with (b). The curved line represents the habit plane and the straight small black lines outside the circle represent the trend of the lamellae. Data re-plotted from Reddy et al. (2015). (For interpretation of the references to colour in this figure legend, the reader is referred to the web version of this article.)

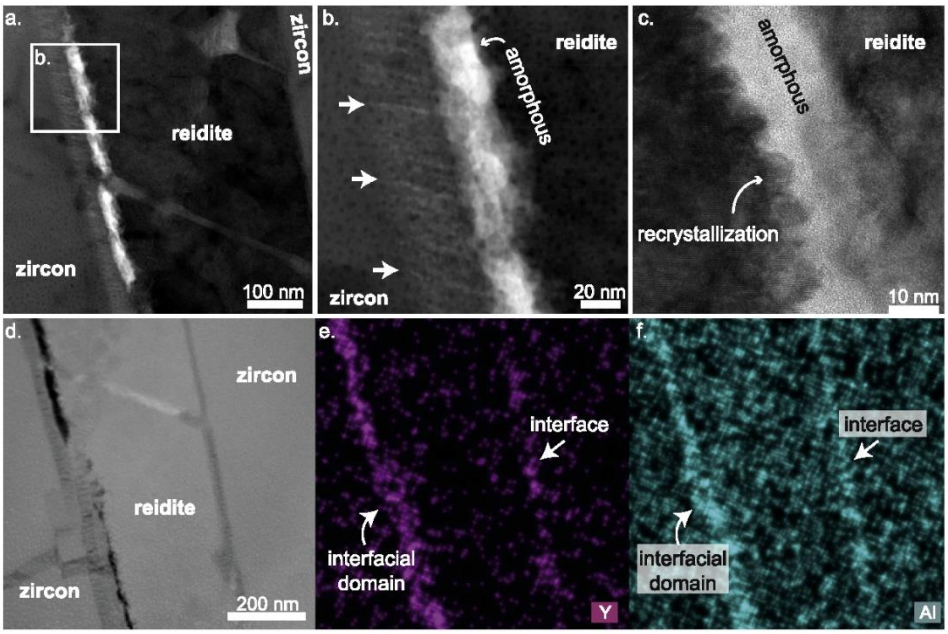

Fig. 3. TEM analysis of foil extracted from grain 86. (a) BF STEM image showing reidite lamella and the amorphous feature. (b) Detailed BF STEM image of the amorphous domain showing a quasi-periodic structure (white arrows) adjacent to the amorphous feature. (c) HR TEM image of the amorphous feature and the lobate recrystallised domains along its borders. (d) HAADF STEM image of the lower section of the reidite lamella. (e–f) TEM-EDS maps of Y (purple) and Al (blue) atoms from area (d). (For interpretation of the references to colour in this figure legend, the reader is referred to the web version of this article.)

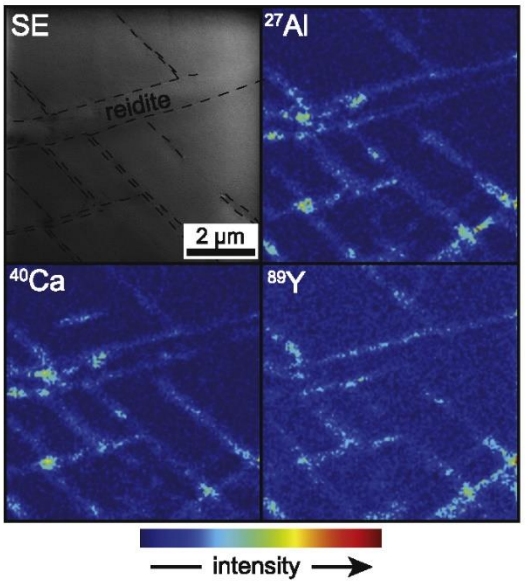

Fig. 4. SE image with reidite lamellae highlighted and ToF-SIMS isotopic maps showing spatial relationship between reidite lamellae and enrichments of ^{27}Al, ^{40}Ca and ^{89}Y atoms.

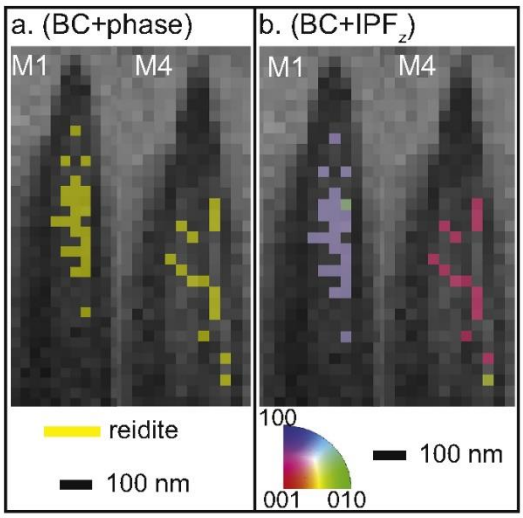

Fig. 5. TKD maps of specimens M1 and M4. (a) Combined BC plus phase, and (b) BC plus IPF$_z$ maps of the atom probe specimens.

reconstruction of the APT data reveals trace element variation that define planar features (Fig. 7a).

The feature in M1 is 16 nm thick and dips at 60° with respect to the polished surface of the grain. From the known orientation of the needle

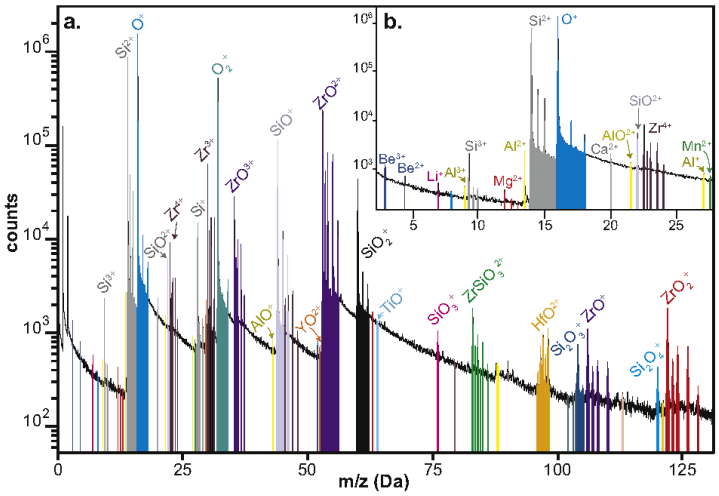

Fig. 6. (a) The atom probe tomography mass spectrum of the whole specimen M4 with the ranges of the major and trace elements. (b) Inset is a closer view of the first 30 mass/charge ratio (Da) of the mass spectrum in (a) with a clearer view of the trace elements.

with respect to the sample surface, and the geometric relationship of the reidite lamellae to the surface of the grain, it was determined that the feature in M1 is a zircon–reidite interface. A 1D concentration profile was created from an area containing both reidite and the interface (Fig. 7b). A clear enhancement of trace elements (Al, Ca, Mn, Be and Mg) was detected at the interface. Also, the Zr/Si ratio is higher in the reidite region than in the interface (transition represented by dashed lines in Fig. 7b). A compositional difference between the average concentration of the reidite phase and the average concentration of the interface region was also identified within the specimen M1 (Table 1). This difference was manifest by enhanced Si, Al, Be, Mn, Mg, and Ca at the interface, with higher concentrations of O, Zr and Hf in the reidite phase.

The feature in M4 dips at ~20° to the sample polished surface, negating the possibility of it being the zircon–reidite interface. TKD analysis of the atom probe needle was unable to constrain the nature of the feature due to poor indexing. However, EBSD analysis of the area where this specimen was extracted, indicates that the feature in M4 is a low-angle boundary (LAB) within the reidite. The 1D concentration profile of the LAB in M4 shows an enhancement of Al, Ca, Mn, Be, Mg, Y and Ti (Fig. 7b). Just like in the other specimen, the Zr/Si ratio appears higher in the reidite phase. Compositional analysis of M4 shows a high segregation of Y atoms in the LAB, different to M1. Ti atoms were only identified in the LAB of M4. Zr and Hf atoms were more abundant in the reidite phase. Another observation is that the LAB in M4 has the highest concentration of trace elements when compared to the other three areas: reidite phase in M4, the interface in M1, and the reidite phase in M1 (Table 1).

No atoms of phosphorous were detected in either specimen, suggesting that the concentration of P is below background levels, resulting in a ratio of REE to P > 1.

5. Discussion

5.1. Microstructures in reidite and the host zircon

The CL imaging shows three different CL signatures, a metamict core that is surrounded by an intermediate rim, followed by a brighter outer rim. These features indicate a complex igneous and metamorphic history. The growth zoning indicates a compositional variation of substitutional trace elements and a crystallization from a magmatic source (Mattinson et al., 1996; Corfu et al., 2003). The core of the zircon grain has U and Th concentrations of ~460 and 210 ppm respectively and were sourced from 2.7 to 2.9 Ga Lewisian Complex basement (Wheeler et al., 2010). These concentrations are sufficiently large for the zircon core to have been metamict at the time of impact (~1.2 Ga), which may explain the absence of reidite lamellae in the zircon core (Reddy et al., 2015; Erickson et al., 2017).

The zircon grain shows ubiquitous intragranular defects, associated with crystal plastic distortion of the zircon lattice and the formation of LABs. Although, such features can form by tectonic deformation, the presence of reidite, itself containing a LAB, is convincing evidence that the grain has undergone impact-related shock metamorphism and deformation (Reddy et al., 2015; Reddy et al., 2016) at pressures > 30 GPa (Kusaba et al., 1985). These LABs are believed to have formed by the migration of shock-induced defects (e.g. dislocations) to lower-energy configurations during recovery (Reddy et al., 2016).

Three orientations of reidite lamellae were identified in zircon grain 86 (Fig. 2). Their crystallographic relationships with the host zircon are consistent with previous studies, where $\{100\}_z$ is parallel to $\{112\}_r$, $\{112\}_z$ is parallel to $\{112\}_r$, and $\langle 001\rangle_z$ is parallel to $\langle 110\rangle_r$ (Leroux et al., 1999; Reddy et al., 2015; Erickson et al., 2017). Only one lamella (pink in Fig. 2c) displayed the $\{110\}_z$ parallel to $\{001\}_r$ relationship reported by Cavosie et al. (2015). However, none of the habit planes overlaps with the orientation of the planes of lattice coincidence between zircon and reidite lamellae (Fig. 2c).

Nanoscale structural investigations by TEM of the interfacial domain between zircon and reidite reveals a ~40 nm wide quasi-periodic structure of dislocations nearly perpendicular to the boundary (Fig. 3b). This structure is similar to features typically observed in manufactured and mineral specimens and is interpreted to be an interface-localised dislocation network formed during deformation (Skrotzki, 1994; Priester, 2001). Next to the interfacial domain is a sub-parallel amorphous feature where recrystallization seems to have commenced along its borders (Fig. 3c). Since the amorphous feature is truncated between reidite and the interface, it is interpreted to post-date the reidite transformation.

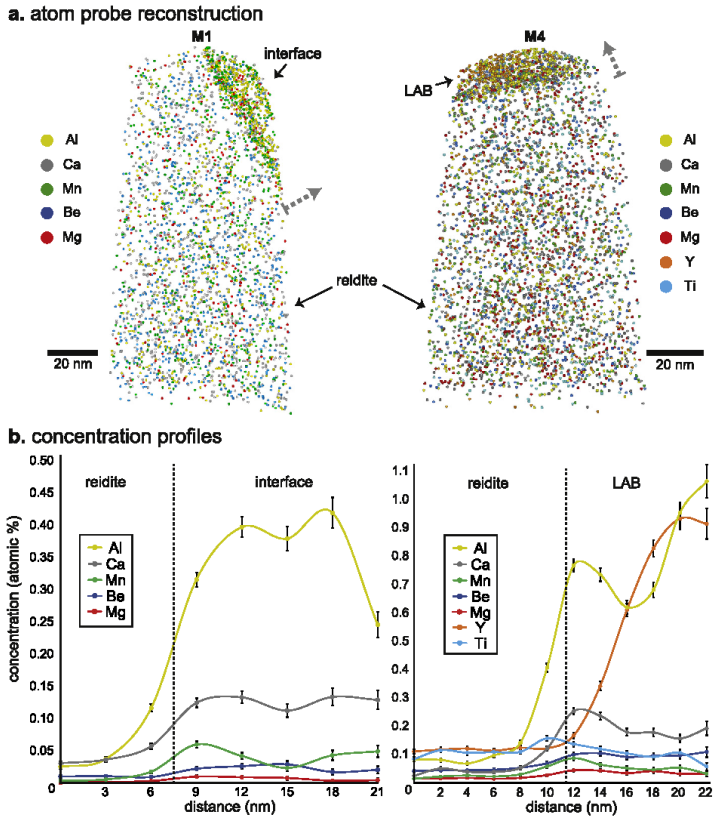

Fig. 7. (a) Atom probe 3D reconstruction of specimens M1 and M4. Each sphere represents an Al, Ca, Mn, Be, Mg, Y or Ti atom. The interface between reidite and zircon and a low-angle boundary (LAB) displays an enrichment of trace elements with respect to the rest of the reidite. The grey dashed arrow represents the direction of the 1D concentration profiles. (b) 1D concentration profiles from reidite to the interface of M1 and from reidite to the LAB of M4. Curved lines are drawn as a guide to the eye. Dashed line corresponds to a Zr/Si ratio of 1.

Table 1
Element analysis derived from APT. Concentrations and uncertainties are in at.%.

Elements	M1				M4			
	Reidite	± (1σ)	Interface	± (1σ)	Reidite	± (1σ)	LAB	± (1σ)
O	65.546	0.060	65.05	0.14	63.419	0.050	63.49	0.15
Si	17.449	0.026	18.981	0.065	16.897	0.022	17.643	0.066
Zr	15.665	0.025	14.227	0.055	18.036	0.023	15.774	0.062
Hf	0.1340	0.0021	0.0890	0.0041	0.1813	0.0021	0.0798	0.0041
Y	0.0294	0.0010	0.0231	0.0021	0.0369	0.0010	0.497	0.010
Al	–	–	0.4251	0.0090	–	–	0.811	0.013
Be	0.00506	0.00041	0.0129	0.0016	0.00811	0.00045	0.0699	0.0038
Mn	–	–	0.0495	0.0031	–	–	0.0515	0.0033
Mg	–	–	0.0077	0.0012	–	–	0.0311	0.0025
Ca	–	–	0.1244	0.0048	–	–	0.2148	0.0067
Ti	–	–	–	–	–	–	0.0551	0.0034

– Below detection limit.
Values correspond to the average concentration of each region as a whole.

5.2. Trace element distribution and mobility

In zircon grains, the CL emission is controlled by the crystallinity of the grain and the concentration of trace elements in the structure (Nasdala et al., 2002). The CL data (Fig. 2a) is consistent with differences in composition of the two rims, which is supported by the APT data since the specimens were derived from different CL-zones within the host zircon (Fig. 2b). In addition, Y segregation along the interface appears heterogeneous in the ToF-SIMS data (Fig. 4), with a higher concentration of trace elements where lamellae of different

orientations coalesce.

If charge neutrality is retained, trace elements can be incorporated into the structure of zircon by occupying interstitial sites or oxygen vacancies, as well as by substitution of Si and Zr (Speer, 1980; Hinton and Upton, 1991; Hoskin et al., 2000; Cherniak, 2010). When considering the APT elemental data, simple substitution and charge balance coupled substitutions are probable for the incorporation of trace elements. Simple substitution is appropriate for 4+ ions [$Ti^{4+} = Zr^{4+}$] (Hoskin and Schaltegger, 2003). In the case of coupling substitutions, for the 2+ ions [$(Mg, Mn, Be)^{2+}_{(int)} + 3Y^{3+} + P^{5+} = 3Zr^{4+} + Si^{4+}$] and for the 3+ ions [$Al^{3+}_{(int)} + 4Y^{3+} + P^{5+} = 4Zr^{4+} + Si^{4+}$] (Hoskin et al., 2000). Ca^{2+} has an ionic radii of 99 pm (Tennent, 1976), which is similar in size to the substitutional elements. Consequently, it is not clear whether Ca^{2+} is interstitial or substitutional. However, due to its ionic radii, Ca^{2+} has been categorized as a substitutional element. The common xenotime substitution proposed by Speer (1980) was not considered as a mechanism for the substitution because it requires the REE/P ratio to be 1 (Hoskin et al., 2000) and the average ratio obtained from this research is > 1, given the low concentration (below background noise levels) of P atoms in the APT analysis.

TEM EDS, ToF-SIMS and APT shows enrichment of interstitial (Al) and substitutional elements (Y) in zircon–reidite interfaces (Figs. 3–4, 7). ToF-SIMS analysis revealed the presence of an additional trace element (Ca) in the interfaces (Fig. 4). Using APT, several other interstitial elements were found (Mn, Be, Mg & Ti), as well as an additional region (LAB inside reidite) where there is trace element enhancement (Fig. 7). In the APT data, only interstitial elements were found to segregate in the interface (M1 in Fig. 7). However, there is evidence from the TEM EDS and ToF-SIMS data that supports the segregation of the substitutional element Y in the zircon–reidite interfaces (Figs. 3–4). The inconsistency in the identification of substitutional and interstitial elements across the data sets can be related to the heterogeneous and fine scale nature of compositional variations in the zircon grain and the inability to analyse exactly the same material with these techniques (Fig. 2).

In the research presented here, a LAB within a reidite lamella was found to be enriched in trace elements (Y, Ca, Al, Be, Mg, Mn, Ti) (Table 1 and Fig. 7). In zircon grains that are plastically deformed, LABs accommodate the misorientation of the crystal lattice and affect the diffusional properties of the zircon grain (Reddy et al., 2006; Timms et al., 2006; Piazolo et al., 2012). Reddy et al. (2016) found evidence of element mobility in grain 86, with interstitials (Al, Be, Mg) and substitutional (Y) elements segregated into a LAB in the host zircon grain (# in Fig. 2b indicates the location of previous specimen).

When comparing the APT data from the interface and LAB with their respective reidite phases (Table 1), an increase in the concentration of trace elements, as well as a decrease in the Zr/Si ratio is observed. These chemical changes can be explained using the previously mentioned coupling substitutions, where for every Si atom lost, 3 to 4 Zr atoms are also lost. In other words, the Zr/Si ratio after the substitutions should be less than the previous Zr/Si ratio, which correlates with the APT data (Table 1).

5.3. Mechanisms of reidite formation

The martensitic models previously proposed for the transformation of zircon to reidite lamellae do not account for trace element enrichment and habit plane variations seen in this study. The results from this research confirm trace element enrichment associated with the formation of reidite lamellae during a meteorite impact event. The possible mechanisms for trace element mobility in deformed zircon grains includes pipe diffusion along static or mobile dislocation cores, diffusion associated with the migration of shock-related vacancy, and the migration of Cottrell atmospheres around mobile dislocations (e.g. Cherniak, 2010; Piazolo et al., 2016; Reddy et al., 2016). The enrichment of both substitutional and interstitial elements within reidite lamellae suggests that there is more than one mechanism responsible for their migration. Given that trace element segregation appears to be constrained to the vicinity of the reidite lamellae, short-range diffusion can be considered a plausible mechanism.

In phase transformations, the habit plane is frequently depicted as a unique invariant plane between the phases (e.g. Balluffi et al., 2005; Zhang and Weatherly, 2005). Pond et al. (2003) proposed a model for martensitic transformations where the habit plane is perceived as terraces interrupted by disconnections (defects that have dislocation and ledge properties). The idea of terraces of ledges was also mentioned by Spanos and Aaronson (1990) to explain why there are habit planes that don't have a unique orientation. They attributed the variation of orientations to be related to the difference between the atomic habit plane (atomic level habit plane of the terraces) and the apparent habit plane (determined by microscopic techniques). The concept of the habit plane as an array of terraces containing defects and the different apparent and atomic habit plane could explain the inconsistency between the observations from this research and previous interpretations of the orientation of the habit planes in zircon to reidite lamellae transformations.

Martensitic transformations are commonly defined as shear-induced, diffusionless and displacive transformations that do not require thermal activation to occur (Balluffi et al., 2005; Aaronson et al., 2010). Based on this information, and the findings of this study, the phase transformation of zircon to reidite lamellae is not consistent with a simple martensitic model. An additional short-range diffusional component associated with the transformation must take place to be able to explain the local compositional variation observed at the nanoscale.

During a phase transformation, the migration and energy of the interface influences the nucleation and the growth of the new phase (Aaronson, 1975; Gouné et al., 2015). The energy from a transformation can dissipate in several ways: by diffusion of trace elements within the interface, by the friction at the interface (which acts against the migration of the interface), and by the segregation and physical incorporation of trace elements within the migrating interface (Svoboda et al., 2002; Gamsjäger et al., 2006; Gouné et al., 2015). When considering the movement of trace elements associated with the zircon to reidite transformation, the expected trace element enrichment associated with the reidite formation can be determined once the direction of the interface migration is known. There are three possible ways the newly formed interface can grow/expand: (Case I, Fig. 8) the interface migrates in one direction, ending with a higher segregation of trace elements in one of the interfaces of the lamella, (Case II) the interface migrates in two directions, producing a similar amount of trace elements in each interface of the lamella, and (Case III) two opposite migrating interfaces combine causing the trace elements to segregate in the middle of the lamellae. These cases are similar to the planar growth of ferrite plates in austenite-ferrite phase transformation, where diffusion of substitutional elements through the interface happens at the same time as the migration of the interface (Gamsjäger et al., 2006).

A possible model that can explain these and previous observations consists of short-ranged diffusion and segregation of the incompatible elements due to the migration of the zircon–reidite interface (Fig. 9). The model proposed consists of 2 stages: (1) During the early stage of the impact event, the shock wave induces defects in the crystal structure (e.g. dislocations and vacancies) and initiates the phase transformation of zircon to reidite lamellae in the non-metamict regions. The segregation of trace elements in the zircon–reidite interface is determined by the direction of interface migration. In metals, diffusion of substitutional elements within the interface occurs simultaneously to the migration of the interface (Gamsjäger et al., 2006). Based on the trace element segregation along the zircon–reidite interface, Case II is a better choice for this study (Figs. 3–4). Case I and Case III are improbable since the segregation of trace element is not higher in one of the interfaces and does not occur in the middle of the reidite lamella (Figs. 3–4).

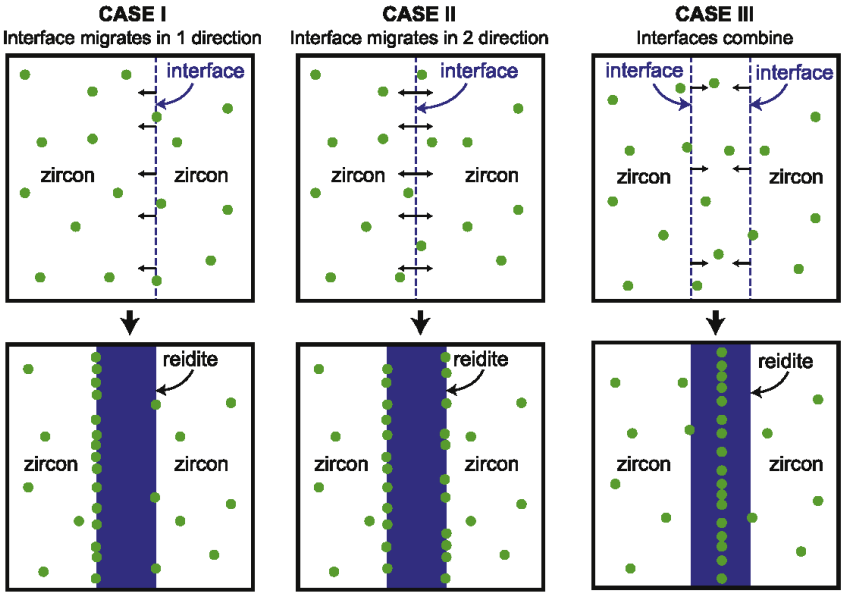

Fig. 8. Simplified model for the zircon–reidite interface migration and the possible trace element (green circles) outcome based on the way the interface migrates. (For interpretation of the references to colour in this figure legend, the reader is referred to the web version of this article.)

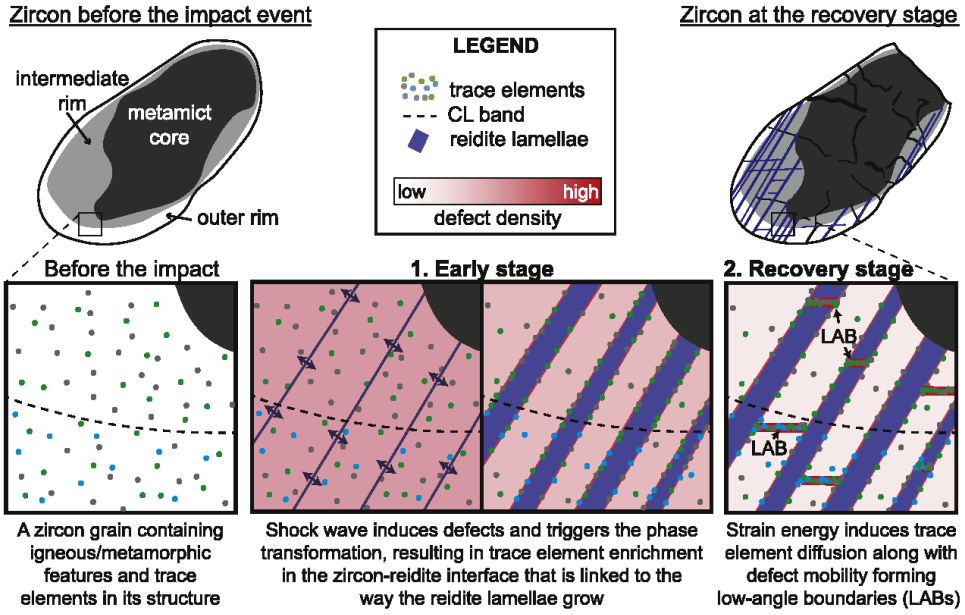

Fig. 9. Schematic diagram of the proposed model for the phase transformation of zircon to reidite lamellae. For simplicity, the model assumes a metamict core pre-impact. It is divided into two stages: (**1**) during the early stage of impact with the formation of defect and starting of the phase transformation, as well as the diffusion of trace elements through the interface, and (**2**) the recovery stage with the diffusion of trace elements coupled with defect mobility to low-energy areas forming low-angle boundaries (LABs).

The recovery stage (2) is where the strain energy of the grain induces short-ranged diffusion of trace elements to areas of low-energy, forming LABs in both phases (Fig. 9). Reddy et al. (2016) proposed that the mechanism for trace element mobility in shocked zircon grains consists of the migration of trace elements and shock-induced defects to low-energy areas during the recovery phase, around the last stages of the Stac Fada impact event. More specifically, the migration of oxygen vacancies along with substitutional ions, and the migration of interstitial ions trapped in Cottrell atmospheres underpin this interpretation. Although these two mechanisms were described for element mobility to LABs in the host shocked zircon, it is to be expected given the relationships of the phases involved, that these mechanisms also apply to trace element (Al^{3+}, Mg^{2+}, Be^{2+}, Y^{3+}) segregation to LABs within reidite lamellae, including the additional interstitials (Mn^{2+}) and substitutional elements (Ca^{2+}, Ti^{4+}).

6. Conclusions

This study presents a detailed investigation into the high-pressure $ZrSiO_4$ polymorph reidite, which occurs as lamellae within a shocked zircon grain from the Stac Fada impact, NW Scotland. Previous EBSD analysis revealed three orientations of lamellae, which were targeted for nanoscale analysis by ToF-SIMS, APT and TEM. The non-uniqueness of the habit plane and the enhancement of trace element concentrations in a LAB within reidite and at zircon–reidite interfaces requires a new model for the zircon to reidite transformation. This new data reveals that the mechanism for the phase transition of zircon to reidite lamella involves a martensitic transformation accompanied by additional short-range diffusional components that are responsible for the segregation of trace elements along the interfaces and to areas of low energy. The mechanisms believed to be responsible for element mobility are: (i) migration of the growing interface along with dragging and segregation of trace elements to the zircon–reidite interface; (ii) local diffusion of trace elements through the migrating interface, and (iii) migration of shock-induced defects, coupled with trace elements, in the formation of LABs in both phases during the post-shock recovery phase.

Supplementary data to this article can be found online at https://doi.org/10.1016/j.chemgeo.2018.12.039.

Acknowledgments

The Geoscience Atom Probe Facility, together with the FIB-SEM and ToF-SIMS instrumentation at Curtin University is housed within the John de Laeter Centre and forms part of the Advanced Resource Characterization Facility (ARCF). The ARCF, under the auspices of the National Resource Sciences Precinct (NRSP), a collaboration between CSIRO, Curtin University, and The University of Western Australia, is supported by the Science and Industry Endowment Fund (RI13-01). SEM, EBSD and TEM analyses were performed within the John de Laeter Centre's Microscopy and Microanalysis Facility. We acknowledge support from the Centre of Excellence for Core to Crust Fluid Systems, Australian Research Council (CE11E0070). We also thank Sebastian Fischer for collecting the Stac Fada sample, and two anonymous reviewers and editor, Balz Kamber, for valuable comments that helped improve the final version.

References

Aaronson, H.I., 1975. Lectures on the Theory of Phase Transformations. American Institute of Mining, Metallurgical and Petroleum Engineers, New York, pp. 178.
Aaronson, H.I., Enomoto, M., Lee, J.K., 2010. Mechanisms of Diffusional Phase Transformations in Metals and Alloys. CRC Press, USA, pp. 667.
Amor, K., Hesselbo, S.P., Porcelli, D., Thackrey, S., Parnell, J., 2008. A Precambrian proximal ejecta blanket from Scotland. Geology 36 (4), 303–306.
Babinsky, K., De Kloe, R., Clemens, H., Primig, S., 2014. A novel approach for site-specific atom probe specimen preparation by focused ion beam and transmission electron backscatter diffraction. Ultramicroscopy 144, 9–18.
Balluffi, R.W., Allen, S.M., Carter, W.C., 2005. Kinetics of Materials. Wiley-Interscience, Hoboken, N.J, pp. 645.
Blum, T.B., Darling, J.R., Kelly, T.F., Larson, D.J., Moser, D.E., Perez-Huerta, A., Prosa, T.J., Reddy, S.M., Reinhard, D.A., Saxey, D.W., Ulfig, R.M., Valley, J.W., 2018. Best practices for reporting atom probe analysis of geological materials. In: Moser, D.E., Corfu, F., Darling, J.R., Reddy, S.M., Tait, K. (Eds.), Microstructural Geochronology: Planetary Records Down to Atom Scale. American Geophysical Union, USA, pp. 416.
Branney, M.J., Brown, R.J., 2011. Impactoclastic density current emplacement of terrestrial meteorite-impact ejecta and the formation of dust pellets and accretionary lapilli: evidence from Stac Fada, Scotland. J. Geol. 119 (3), 275–292.
Cavosie, A.J., Erickson, T.M., Timms, N.E., 2015. Nanoscale records of ancient shock deformation: reidite ($ZrSiO_4$) in sandstone at the Ordovician Rock Elm impact crater. Geology 43 (4), 315–318.
Chen, M., Yin, F., Li, X., Xie, X., Xiao, W., Tan, D., 2013. Natural occurrence of reidite in the Xiuyan crater of China. Meteorit. Planet. Sci. 48 (5), 796–805.
Cherniak, D.J., 2010. Diffusion in accessory minerals: zircon, titanite, apatite, monazite and xenotime. In: Zhang, Y., Cherniak, D.J. (Eds.), Diffusion in Minerals and Melts. Vol. 72. The Mineralogical Society of America, Virginia, pp. 827–869.
Cherniak, D.J., Watson, E.B., 2001. Pb diffusion in zircon. Chem. Geol. 172 (1–2), 5–24.
Cherniak, D.J., Watson, E.B., 2003. Diffusion in Zircon. In: Hanchar, J.M., Hoskin, P.W.O. (Eds.), Zircon. vol. 53. Mineralogical Society of America, Washington, DC, pp. 113–143.
Corfu, F., Hanchar, J.M., Hoskin, P.W.O., Kinny, P., 2003. Atlas of zircon textures. In: Hanchar, J.M., Hoskin, P.W.O. (Eds.), Reviews in Mineralogy and Geochemistry: Zircon. vol. 53.
Cox, M.A., Cavosie, A.J., Bland, P.A., Miljković, K., Wingate, M.T.D., 2018. Microstructural dynamics of central uplifts: reidite offset by zircon twins at the Woodleigh impact structure, Australia. Geology 46 (11), 983–986.
Drake, S.M., Beard, A.D., Jones, A.P., Brown, D.J., Fortes, A.D., Millar, I.L., Carter, A., Baca, J., Downes, H., 2017. Discovery of a meteoritic ejecta layer containing unmelted impactor fragments at the base of Paleocene lavas, Isle of Skye, Scotland. Geology 46 (2), 171–174.
Erickson, T.M., Pearce, M.A., Reddy, S.M., Timms, N.E., Cavosie, A.J., Bourdet, J., Rickard, W.D.A., Nemchin, A.A., 2017. Microstructural constraints on the mechanisms of the transformation to reidite in naturally shocked zircon. Contrib. Mineral. Petrol. 172 (1), 6.
Gamsjäger, E., Militzer, M., Fazeli, F., Svoboda, J., Fischer, F.D., 2006. Interface mobility in case of the austenite-to-ferrite phase transformation. Comput. Mater. Sci. 37 (1), 94–100.
Gault, B., Moody, M.P., Cairney, J.M., Ringer, S.P., 2012. Atom Probe Microscopy. Springer, New York, pp. 396.
Glass, B.P., Liu, S., Leavens, P.B., 2002. Reidite: an impact-produced high-pressure polymorph of zircon found in marine sediments. Am. Mineral. 87 (4), 562–565.
Goué, M., Danoix, F., Ågren, J., Bréchet, Y., Hutchinson, C.R., Militzer, M., Purdy, G., van der Zwaag, S., Zurob, H., 2015. Overview of the current issues in austenite to ferrite transformation and the role of migrating interfaces therein for low alloyed steels. Mater. Sci. Eng. R. Rep. 92, 1–38.
Gucsik, A., Koeberl, C., Brandstätter, F., Libowitzky, E., Reimold, W.U., 2004. Cathodoluminescence, electron microscopy, and Raman spectroscopy of experimentally shock metamorphosed zircon crystals and naturally shocked zircon from the Ries impact crater. In: Dypvik, H., Burchell, M.J., Claeys, P. (Eds.), Cratering in Marine Environments and on Ice. Springer, Berlin, pp. 281–322.
Hanchar, J.M., van Westrenen, W., 2007. Rare earth element behavior in zircon-melt systems. Elements 3 (1), 37–42.
Harley, S.L., Kelly, N.M., 2007. Zircon tiny but timely. Elements 3 (1), 13–18.
Hinton, R.W., Upton, B.G.J., 1991. The chemistry of zircon: variations within and between large crystals from syenite and alkali basalt xenoliths. Geochim. Cosmochim. Acta 55 (11), 3287–3302.
Hoskin, P.W.O., Schaltegger, U., 2003. The composition of zircon and igneous and metamorphic petrogenesis. In: Hanchar, J.M., Hoskin, P.W.O. (Eds.), Zircon. vol. 53. The Mineralogical Society of America, Washington, DC, pp. 27–62.
Hoskin, P.W.O., Kinny, P.D., Wyborn, D., Chappell, B.W., 2000. Identifying accessory mineral saturation during differentiation in granitoid magmas: an integrated approach. J. Petrol. 41 (9), 1365–1396.
Johnstone, G.S., Mykura, W., 1989. British Regional Geology. 219 Northern Highlands of Scotland, London, UK.
Kinny, P.D., Maas, R., 2003. Lu-Hf and Sm-Nd isotope systems in zircon. In: Hanchar, J.M., Hoskin, P.W.O. (Eds.), Zircon. vol. 53. The Mineralogical Society of America, Washington, DC, pp. 327–341.
Kusaba, K., Syono, Y., Kikuchi, M., Fukuoka, K., 1985. Shock behavior of zircon: phase transition to scheelite structure and decomposition. Earth Planet. Sci. Lett. 72 (4), 433–439.
Kusaba, K., Yagi, T., Kikuchi, M., Syono, Y., 1986. Structural considerations on the mechanism of the shock-induced zircon-scheelite transition in ZrSiO4. J. Phys. Chem. Solids 47 (7), 675–679.
Larson, D.J., Gault, B., Geiser, B.P., De Geuser, F., Vurpillot, F., 2013a. Atom probe tomography spatial reconstruction: status and directions. Curr. Opinion Solid State Mater. Sci. 17 (5), 236–247.
Larson, D.J., Prosa, T.J., Ulfig, R.M., Geiser, B.P., Kelly, T.F., 2013b. Local Electrode Atom Probe Tomography: A User's Guide. Springer, New York, pp. 318.
Lawson, D.E., 1972. Torridonian volcanic sediments. Scott. J. Geol. 8 (4), 345–362.
Leroux, H., Reimold, W.U., Koeberl, C., Hornemann, U., Doukhan, J.C., 1999. Experimental shock deformation in zircon: a transmission electron microscopic study. Earth Planet. Sci. Lett. 169 (3), 291–301.
Mattinson, J.M., Graubard, C.M., Parkinson, D.L., McClelland, W.C., 1996. U-Pb reverse discordance in zircons: the role of fine-scale oscillatory zoning and sub-micron transport of Pb. In: Basu, A., Hart, S. (Eds.), Earth Processes: Reading the Isotopic

Code. American Geophysical Union, USA, pp. 437.
Melosh, H.J., 1989. Impact Cratering: A Geologic Process. Oxford University Press, New York, USA, pp. 245.
Nasdala, L., Lengauer, C.L., Hanchar, J.M., Kronz, A., Wirth, R., Blanc, P., Kennedy, A.K., Seydoux-Guillaume, A.-M., 2002. Annealing radiation damage and the recovery of cathodoluminescence. Chem. Geol. 191 (1), 121–140.
Nasdala, L., Hanchar, J.M., Rhede, D., Kennedy, A.K., Váczi, T., 2010. Retention of uranium in complexly altered zircon: an example from Bancroft, Ontario. Chem. Geol. 269 (3–4), 290–300.
Parnell, J., Mark, D., Fallick, A.E., Boyce, A., Thackrey, S., 2011. The age of the Mesoproterozoic Stoer Group sedimentary and impact deposits, NW Scotland. J. Geol. Soc. 168 (2), 349–358.
Peterman, E.M., Reddy, S.M., Saxey, D.W., Snoeyenbos, D.R., Rickard, W.D.A., Fougerouse, D., Kylander-Clark, A.R.C., 2016. Nanogeochronology of discordant zircon measured by atom probe microscopy of Pb-enriched dislocation loops. Sci. Adv. 2, 9.
Piazolo, S., Austrheim, H., Whitehouse, M., 2012. Brittle-ductile microfabrics in naturally deformed zircon: Deformation mechanisms and consequences for U-Pb dating. Am. Mineral. 97 (10), 1544–1563.
Piazolo, S., La Fontaine, A., Trimby, P., Harley, S., Yang, L., Armstrong, R., Cairney, J.M., 2016. Deformation-induced trace element redistribution in zircon revealed using atom probe tomography. Nat. Commun. 7.
Pond, R.C., Celotto, S., Hirth, J.P., 2003. A comparison of the phenomenological theory of martensitic transformations with a model based on interfacial defects. Acta Mater. 51 (18), 5385–5398.
Priester, L., 2001. "Dislocation–interface" interaction — stress accommodation processes at interfaces. Mater. Sci. Eng. A 309-310, 430–439.
Reddy, S.M., Timms, N.E., Trimby, P., Kinny, P.D., Buchan, C., Blake, K., 2006. Crystal-plastic deformation of zircon: a defect in the assumption of chemical robustness. Geology 34 (4), 257–260.
Reddy, S.M., Johnson, T.E., Fischer, S., Rickard, W.D.A., Taylor, R.J.M., 2015. Precambrian reidite discovered in shocked zircon from the Stac Fada impactite, Scotland. Geology 43 (10), 899–902.
Reddy, S.M., van Riessen, A., Saxey, D.W., Johnson, T.E., Rickard, W.D.A., Fougerouse, D., Fischer, S., Prosa, T.J., Rice, K.P., Reinhard, D.A., Chen, Y., Olson, D., 2016. Mechanisms of deformation-induced trace element migration in zircon resolved by atom probe and correlative microscopy. Geochim. Cosmochim. Acta 195, 158–170.
Reid, A.F., Ringwood, A.E., 1969. Newly observed high pressure transformations in Mn3O4, CaAl2O4, and ZrSiO4. Earth Planet. Sci. Lett. 6 (3), 205–208.
Sanders, I.S., Johnston, J.D., 1989. The Torridonian Stac Fada Member: an extrusion of fluidised peperite? Trans. R. Soc. Edinb. Earth Sci. 80 (1), 1–4.
Saxey, D.W., Moser, D.E., Piazolo, S., Reddy, S.M., Valley, J.W., 2018. Atomic worlds: current state and future of atom probe tomography in geoscience. Scr. Mater. 115–121.
Simms, M.J., 2015. The Stac Fada impact ejecta deposit and the Lairg Gravity Low: evidence for a buried Precambrian impact crater in Scotland? Proc. Geol. Assoc. 126 (6), 742–761.
Skrotzki, W., 1994. Dislocation-interface interactions in exsolved augite. Mater. Sci. Eng. A 175 (1), 149–158.
Spanos, G., Aaronson, H.I., 1990. The interfacial structure and habit plane of proeutectoid cementite plates. Acta Metall. Mater. 38 (12), 2721–2732.
Speer, J.A., 1980. Zircon. Rev. Mineral. Geochem. 5 (1), 67–112.
Stephan, T., 2001. TOF-SIMS in cosmochemistry. Planet. Space Sci. 49 (9), 859–906.
Stewart, A.D., 1988. The Stoer group, Scotland. In: Winchester, J.A. (Ed.), Later Proterozoic Stratigraphy of the Northern Atlantic Regions. Blackie and Son Ltd., Glasgow, pp. 97–103.
Stewart, A.D., 2002. The Later Proterozoic Torridonian Rocks of Scotland: their sedimentology, geochemistry and origin. Geol. Soc. Mem. 130.
Svoboda, J., Fischer, F.D., Gamsjäger, E., 2002. Influence of solute segregation and drag on properties of migrating interfaces. Acta Mater. 50 (5), 967–977.
Tange, Y., Takahashi, E., 2004. Stability of the high-pressure polymorph of zircon (ZrSiO4) in the deep mantle. Phys. Earth Planet. Inter. 143–144, 223–229.
Tennent, R.M., 1976. Science Data Book. Oliver & Boyd, UK, pp. 104.
Timms, N.E., Kinny, P.D., Reddy, S.M., 2006. Enhanced diffusion of uranium and thorium linked to crystal plasticity in zircon. Geochem. Trans. 7 (1), 10.
Timms, N.E., Erickson, T.M., Pearce, M.A., Cavosie, A.J., Schmieder, M., Tohver, E., Reddy, S.M., Zanetti, M.R., Nemchin, A.A., Wittmann, A., 2017a. A pressure-temperature phase diagram for zircon at extreme conditions. Earth Sci. Rev. 165, 185–202.
Timms, N.E., Erickson, T.M., Zanetti, M.R., Pearce, M.A., Cayron, C., Cavosie, A.J., Reddy, S.M., Wittmann, A., Carpenter, P.K., 2017b. Cubic zirconia in > 2370 °C impact melt records Earth's hottest crust. Earth Planet. Sci. Lett. 477, 52–58.
Turner, D., Langenhorst, F., Pollok, K., 2014. Martensitic mechanism of the zircon-to-reidite transformation. In: 77th Annual Metting of the Meteoritical Society: Casablanca, Morocco. 5411.
Valley, J.W., Cavosie, A.J., Ushikubo, T., Reinhard, D.A., Lawrence, D.F., Larson, D.J., Clifton, P.H., Kelly, T.F., Wilde, S.A., Moser, D.E., Spicuzza, M.J., 2014. Hadean age for a post-magma-ocean zircon confirmed by atom-probe tomography. Nat. Geosci. 7 (3), 219–223.
Valley, J.W., Reinhard, D.A., Cavosie, A.J., Ushikubo, T., Lawrence, D.F., Larson, D.J., Kelly, T.F., Snoeyenbos, D.R., Strickland, A., 2015. Nano- and micro-geochronology in Hadean and Archean zircons by atom-probe tomography and SIMS: new tools for old minerals. Am. Mineral. 100 (7), 1355–1377.
Watson, E.B., Wark, D.A., Thomas, J.B., 2006. Crystallization thermometers for zircon and rutile. Contrib. Mineral. Petrol. 151 (4), 413.
Wheeler, J., Park, R.G., Rollinson, H.R., Beach, A., 2010. The Lewisian complex: insights into deep crustal evolution. Geol. Soc. Lond., Spec. Publ. 335 (1), 51–79.
Wilde, S.A., Valley, J.W., Peck, W.H., Graham, C.M., 2001. Evidence from detrital zircons for the existence of continental crust and oceans on the Earth 4.4 Gyr ago. Nature 409, 175.
Wittmann, A., Kenkmann, T., Schmitt, R.T., Stöffler, D., 2006. Shock-metamorphosed zircon in terrestrial impact craters. Meteorit. Planet. Sci. 41 (3), 433–454.
Young, G.M., 2002. Stratigraphy and geochemistry of volcanic mass flows in the Stac Fada Member of the Stoer Group, Torridonian, NW Scotland. Trans. R. Soc. Edinb. Earth Sci. 93 (1), 1–16.
Zhang, W.Z., Weatherly, G.C., 2005. On the crystallography of precipitation. Prog. Mater. Sci. 50 (2), 181–292.

Chapter 5 STRATEGIES FOR NANOSCALE ANALYSIS OF SHOCKED ZIRCON GRAINS

The principal roles of each co-author are as follows:

Stephanie D. Montalvo: Concept and design of the work; sample preparation; data acquisition, analysis and interpretation (SE, BSE, CL, EBSD, ToF-SIMS, NanoSIMS, APT, TEM, SHRIMP); manuscript writing and editing.

Steven M. Reddy: Concept and design; EBSD acquisition, analysis and interpretation.

David W. Saxey: Analysis and interpretation of APT data.

William D.A. Rickard: Data analysis and interpretation (NanoSIMS, ToF-SIMS).

Denis Fougerouse: Concept and design, data acquisition, analysis and interpretation (APT, TEM), and chapter editing.

Introduction

The trace element composition of zircon has been studied extensively because it can be used to understand geological processes of rock formation, metamorphism and sedimentation (e.g. Finch and Hanchar, 2003; Harley and Kelly, 2007; Rubatto, 2017). Nevertheless, there are several processes that can modify the trace element composition of zircon (e.g. radiation damage, tectonic deformation, and metamorphism) (Cherniak and Watson, 2003; Martin et al., 2008; Piazolo et al., 2016; Peterman et al., 2019). If not recognized and understood, these modifications can affect the reliability of the geochemical and geochronological data.

Recent studies have shown that during tectonic deformation (crystal plastic deformations), resulting microstructures can alter the composition of trace elements in the grain (Reddy et al., 2006; Timms et al., 2006; Piazolo et al., 2012). In contrast, the effect of shock metamorphism on the distribution of trace elements within zircon has not been studied in detail. This disparity could be attributed to the complexity of the textures resulting from shock metamorphism that are typically smaller than the analytical volume or conventional geochemical microbeam techniques.

To fill this this gap in knowledge, this chapter explores the suitability of several correlative techniques to provide a multiscale structural and geochemical analysis. A special emphasis is given for emerging techniques, such as atom probe tomography (APT), because it can provide geochemical and isotopic data for volumes < 0.02μm^3 suitable for the fine shock metamorphism textures (Reddy et al., 2020). This study also explores the potential of APT to determine the geochronology of hypervelocity impact events.

Implementing a workflow that spans from the microscale to the nanoscale is essential in order to gain a statistically robust interpretation of the processes at operation. The analytical workflow used within this study includes scanning electron microscopy (SEM), cathodoluminescence (CL), electron backscatter diffraction (EBSD), sensitive high-resolution ion micro probe (SHRIMP), focused ion bean based time-of-flight secondary ion mass spectrometry (FIB-ToF-SIMS), nanoscale secondary ion mass spectrometer (NanoSIMS), transmission electron microscopy (TEM) and APT. Examining the limitations of these techniques for shocked mineral studies can also provide a guide for future research.

Shock metamorphism

Shock metamorphism is described as the conditions of rocks and minerals experienced by the extreme conditions of a hypervelocity impact event (Reimold and Gibson, 2009). The energy associated to a hypervelocity impact event propagates through the target area as a high pressure shock wave (Melosh, 1989). The high pressures, temperatures, strain and strain-rate associated with the hypervelocity impact event surpass the normal values of endogenic processes in Earth's crust (Melosh, 1989; Langenhorst and Deutsch, 2012). These extreme conditions can vaporize, melt, deform, decompose or transform the target rocks and minerals (Langenhorst and Deutsch, 2012). Shocked mineral grains can provide valuable information about the impactor, impact event and the processes associated with the event (e.g. Wittmann et al., 2006; Cavosie et al., 2015; Reddy et al., 2015; Erickson et al., 2016; Timms et al., 2017; Montalvo et al., 2019; White et al., 2019). This information can assist the understanding of the formation and evolution of Earth, the planets and our solar system.

Geological setting

The suite of samples chosen for this research originates from the Stac Fada Member of the Stoer Group in Scotland, and it represents an ejecta deposit associated with a 1.18 Ga hypervelocity impact event (Branney and Brown, 2011; Parnell et al., 2011). The Stac Fada Member consist of three facies, which are a massive suevite (impact breccia) at the base, a mixture of suevite and lapilli (pyroclastic rocks) and a topmost layer of dust pellets (Branney and Brown, 2011). The Stac Fada Member deposited on top of pre-lithified sediments that were saturated in water, degassing and forming vesicular zones in the ejecta deposit (Sanders and Johnston, 1989; Branney and Brown, 2011). Other than soft-sediment deformation, there is no evidence for metamorphic overprints or tectonic deformation after its emplacement (Stewart, 2002; Simms, 2015).

Methodology

From non-magnetic fractions of the three facies that were previously separated and concentrated by Reddy et al. (2015), 4048 grains were handpicked to

look for diagnostic features of shock metamorphism in zircon grains. These grains were placed on epoxy mounts, polished and coated with a ~3 nm layer of carbon. All the grains were imaged using secondary electrons (SE), backscattered electrons (BSE) and EBSD mapping from a Tescan MIRA3 field emission scanning electron microscope (FESEM) with a Nordlys Nano high resolution detector located at the John de Laeter Centre, Curtin University.

Large area EBSD maps (Fig. 5.1) produced an effective visual means of identifying shocked grains. These large area maps (LAM) were acquired using 2, 2.5 and 5 µm step size, for a duration of 2, 11.5, 14.5, 19 hrs. The LAMs were used to identify the minerals and evidence of shock deformation, such as planar fractures (PF), twins or the presence of reidite ($ZrSiO_4$ high pressure polymorph).

Once the zircon grains of interest were identified, they were characterised with SE, BSE, CL imaging, and higher resolution EBSD mapping. From the 4048 handpicked grains, 25 zircon grains, including two reidite bearing zircon, were selected for SHRIMP U-Th-Pb geochronological study. A total of 64 analyses were conducted using SHRIMP II from Curtin University. These grains were selected to represent a collection of diverse complex structures (Suppl. Fig. 5.1).

From the 25 zircon grains selected for SHRIMP analysis, 8 of those grains were analysed with FIB-ToF-SIMS to identify possible targeting areas for APT and TEM. The zircon grains selected for analysis included 4 reidite bearing grains and 4 metamict grains to provide a variety of different textures seen in the sample suite. FIB-ToF-SIMS provided elemental and isotopic maps of the different regions within the analysed grains. This detector is housed in a Ga^+ Tescan LYRA FIB SEM at Curtin University. Further chemical analysis on a reidite bearing zircon grain consisted of the used of NanoSIMS. The NanoSIMS investigation was conducted using a Cameca NanoSIMS 50L, housed in the Ion probe Facility at The University of Western Australia. The analytical parameters for FIB-ToF-SIMS and NanoSIMS are summarized in Table 5.1.

Further chemical and structural analysis included a FEI Talos FS200X FEG TEM for the TEM analysis and a Cameca LEAP 4000X HR for the APT analysis. These instruments are housed within the John de Laeter Research Centre, at Curtin University. Both the TEM foils and the APT specimens were extracted using the Tescan LYRA FIB SEM. Two TEM foils (~12 µm) (Fig. 5.2) were produced from reidite bearing zircon grain 86. The process included a protection layer on top of the

regions of interest and subsequent milling to form the foils. Once extracted, the foils were attached to a copper half grid for thinning to near electron transparency (< 100 nm). A final cleaning run was conducted at 2 kV. The TEM instrument worked at 200 kV and produced several bright field (BF) and high-angle annular dark-field (HAADF) scanning transmission electron microscopy (STEM) images from the foils, as well as energy-dispersive X-ray spectroscopy (EDS) maps and electron diffraction patterns. The acquisition parameters of the TEM instrument are summarised in Table 5.1.

The manufacturing process for APT specimens involved adding a protection layer to the regions of interest, milling a wedge, attaching the wedges to a silicon post from a microtip carrier, sharpening the wedges to form needle-shape specimens with a tip of < 100 nm in diameter, and a final cleaning at low voltage (5 kV). The acquisition parameters of the APT instrument are summarised in Table 5.2 and were chosen with the goal of maximising the yield of the specimen. More details of these procedures are described in Montalvo et al. (2019) (chapter 4). A total of 45 APT specimens were manufactured from 4 zircon grains (zircon grains 001, 66, 86 and 211) covering various textures (Fig. 5.2). These grains were chosen to represent the variety of textures seen across all grains. The APT specimens were labelled MX, where X indicated the number of the specimen (e.g. M6).

To compare the APT number of successful analyses and the size of the datasets from Stac Fada, results from four APT specimens of a zircon grain from the Indian Ocean have been included. This grain, labelled the Indian Ocean zircon (IOZ), was studied at the commencement of this project to develop the techniques used with the APT to apply to all subsequent analyses. The IOZ was previously collected from an olive gabbro sample (Reddy et al., 2006). This sample originated from a drilled core of the “Atlantis II Fracture Zone” located in the Indian Ocean (32º43.392’S, 57º15.960’E) (Reddy et al., 2006; Reddy et al., 2007). The IOZ grain is a ~11 Ma crystalline, low U and Th, zircon that only has evidence of crystal-plastic deformation (Reddy et al., 2006; Timms et al., 2006).

The α-decay radiation dose (events/mg) was calculated for the zircon grains analysed with APT. The amount of radiation damage can provide information about the current crystallinity state of the grain. The calculation was based on Murakami et al. (1991) equation and the chemical analyses were populated from the SHRIMP data.

Table 5.1 Simplify instruments acquisition parameters (all but APT).

	Acquisition parameters	Instrument	Notes
SE, BSE	AV: 10 – 15 kV WD: 10 – 15 mm BI:14	MIRA3 FESEM	--
CL	AV: 10 – 12 kV WD: 16 – 17mm BI:14	MIRA3 FESEM	Spectral range 185–850 nm
EBSD	AV: 20 kV WD: 20 mm BI:18 70° tilt	MIRA3 FESEM	Step size (LAM): 2 – 5 µm Step size 500 – 200 nm Duration: 2 – 19 hrs
ToF-SIMS	AV: 20 kV WD: 9 mm BI: 10 BC: 200 – 500 pA	LYRA FIB-SEM	Positive ion mode ROI: 20x20, 10x10, 8x8 µm Dwell time: 10-14 µs Frames: 100-100 Duration: minutes
NanoSIMS	BC: 15, 50, 100 pA O- primary ion beam RF plasma source	NanoSIMS 50L	ROI: 20x20, 30x30, 50x50, 100x100 µm Dwell time: 2.5 – 100ms/pixel Durartion:3 – 15 hrs
SHRIMP	BC: ~2.5 nA 6 scans	SHRIMP II	Dwell time: 25 ns Standard: BR266 (zircon)
TEM	AV: 200 kV	FS200X FEG TEM	Super-X EDS detector BF and HAADF STEM images

AV=accelerating voltage; WD=working distance; BI=beam intensity; BC=beam current; ROI=region of interest; BF=bright field; HAADF= High-angle annular dark-field

Table 5.2 APT data acquisition parameters for all specimens.

Grain	**zircon 001**							
Specimen	**M12**	**M13**	**M14**	**M15**	**M16**	**M17**	**M18**	**M19**
Instrument Model	LEAP 4000X HR							
Instrument Settings								
Laser wavelength (nm)	355							
Laser pulse energy (pJ)	300	300	300	300	250	400	400	500
Pulse frequency (kHz)	200	250	200	200	250	200	200	200
Evaporation control	Detection rate							
Targeted det. rate (ions/pulse)	0.007	0.007	0.007	0.007	0.02	0.007	0.005	0.007
Nominal flight path (mm)	382							
Set point temperature (K)	50	50	50	50	50	60	70	70
Sample temperature (K)	57.3	57.4	57.3	57.3	57.2	69.1	80.7	80.7
Chamber pressure (e^{-11} Torr)	9.9	10	11	11	11	12	14	22
Data Summary								
LAS Root version	15.41.342l							
CAMECAROOT version	18.46.428							
Analysis Software	IVAS 3.8.2							
Total Ions:	32 m	199146	67 m	88 m	77469	380357	4.6 m	685009
% Single	71.9	79.6	75.9	72.9	89.5	74.3	73.7	58
% Multiple	27.7	18.5	23.7	26.8	8	24.2	25.7	35.3
% Partial	0.4	1.9	0.4	0.4	2.5	1.5	0.5	6.7
Volt./bowl corr. peak (Da)	16	16	16	16	1	16	16	27
Mass Calib. (peaks/interp.)	10/Lin	4/Lin	11/Lin	10/Lin	4/Lin	10/Lin	7/Lin	4/Lin
*(M/ΔM)	1002.6	1031.4	1028.5	1014.3	557.1	1011.5	1010.5	755.5
**(M/ΔM10)	157.6	213	195.4	195.9	72.4	169.7	194.9	136.7
Time independent background (ppm/ns)	18.06	120.86	23.39	23.46	270.14	28.67	30.87	64.26
Reconstruction								
Final specimen state	F	F	F	F	F	F	F	F
Pre-/post-analysis imaging	SEM							
Radius evolution model	'Voltage'							
Field factor (k)	3.3							
Image compression factor	1.65							
Assumed E-field (V/nm)	32							
Detector efficiency	0.36							
Avg. atomic volume (nm^3)	0.01076							
V initial (V)	5186	1980	6174	4258	4530	3745	4855	1224
V final (V)	6637	4015	9608	9801	5725	4817	7474	2494

*ΔM is full width at half maximum of the Volt./bowl corr. peak
**ΔM10 is full width at tenth maximum of the Volt./bowl corr. peak
m = million; det. = detection; Volt. = voltage; corr. = correction; Calib. = calibration; interp. = interpolation; Lin = linearization method; Avg. = average; F = Fractured; NF = not fractured

Grain	**zircon 001**					**zircon 66**		
Specimen	**M20**	**M21**	**M22**	**M1**	**M2**	**M3**	**M4**	**M5**
Instrument Model	LEAP 4000X HR							
Instrument Settings								
Laser wavelength (nm)	355							
Laser pulse energy (pJ)	400	400	400	300	300	300	300	300
Pulse frequency (kHz)	250	250	250	250	200	200	250	200
Evaporation control	Detection rate							
Targeted det. rate (ions/pulse)	0.005	0.02	0.007	0.005	0.007	0.005	0.005	0.007
Nominal flight path (mm)	382							
Set point temperature (K)	70	70	70	60	60	60	60	60
Sample temperature (K)	80.7	80.7	80.7	68.5	65.6	65.7	65.5	65.5
Chamber pressure (e^{-11} Torr)	13	12	1.2	8.2	7.7	7.7	7.5	7.3
Data Summary								
LAS Root version	15.41.342l					15.41.342j		
CAMECAROOT version	18.46.428							
Analysis Software	IVAS 3.8.2							
Total Ions:	8.9 m	239636	302004	96476	22 m	66156	578638	11 m
% Single	74.5	82.7	78.1	63.8	71.2	30.8	64.5	68.6
% Multiple	24.9	10.4	20.3	32.3	28.5	66.1	33.2	31
% Partial	0.6	7	1.6	4	0.4	3.1	2.3	0.4
Volt./bowl corr. peak (Da)	16	28	16	28	16	14	12	16
Mass Calib. (peaks/interp.)	7/Lin	3/Lin	8/Lin	5/Lin	10/Lin	6/Lin	9/Lin	7/Lin
*(M/ΔM)	994.7	968.4	989.8	809.4	1023	396	531.5	997.1
**(M/ΔM10)	206.1	139.7	33.8	181.8	188.1	83	102.8	183.5
Time independent background (ppm/ns)	28.10	63.85	24.93	75.51	38.49	33.62	8.60	33.04
Reconstruction								
Final specimen state	F	F	F	F	F	F	F	F
Pre-/post-analysis imaging	SEM							
Radius evolution model	'Voltage'							
Field factor (k)	3.3							
Image compression factor	1.65							
Assumed E-field (V/nm)	32							
Detector efficiency	0.36							
Avg. atomic volume (nm^3)	0.01076							
V initial (V)	4700	1609	3972	1685	5410	1178	2926	4308
V final (V)	7251	5133	4950	1685	8976	1811	4433	6672

*ΔM is full width at half maximum of the Volt./bowl corr. peak
**ΔM10 is full width at tenth maximum of the Volt./bowl corr. peak
m = million; det. = detection; Volt. = voltage; corr. = correction; Calib. = calibration; interp. = interpolation; Lin = linearization method; Avg. = average; F = Fractured; NF = not fractured

Grain	**zircon 66**			**zircon 86 - reidite**				
Specimen	**M6**	**M1**	**M2**	**M3**	**M4**	**M5**	**M6**	**M7**
Instrument Model	LEAP 4000X HR							
Instrument Settings								
Laser wavelength (nm)	355							
Laser pulse energy (pJ)	300	250	300	300	300	300	300	350
Pulse frequency (kHz)	125	200	250	125	200	125	100	250
Evaporation control	Detection rate							
Targeted det. rate (ions/pulse)	0.005	0.008	0.005	0.007	0.007	0.007	0.005	0.004
Nominal flight path (mm)	382							
Set point temperature (K)	60	50	70	50	50	50	50	50
Sample temperature (K)	65.4	54.7	77	54.7	54.7	54.7	54.7	54.7
Chamber pressure (e^{-11} Torr)	7.1	5.2	7.0	5.4	5.7	5.4	5.6	5.6
Data Summary								
LAS Root version	15.41.342j							
CAMECAROOT version	18.46.428							
Analysis Software	IVAS 3.8.2							
Total Ions:	55182	14 m	1.5 m	150 m	13 m	6 m	109005	1.5 m
% Single	89.7	67.7	74.4	73.8	71	69.8	40.2	57.9
% Multiple	7.7	32	25	25.9	28.7	29.8	55.6	40.6
% Partial	2.5	0.3	0.6	0.3	0.3	0.4	4.2	1.6
Volt./bowl corr. peak (Da)	1	16	16	16	16	16	14	28
Mass Calib. (peaks/interp.)	4/Lin	9/Lin	14/Lin	11/Lin	6/Lin	5/Lin	6/Lin	6/Lin
*(M/ΔM)	525.8	1044.6	1025.6	1020.5	1044.8	1017	284.4	510.6
**(M/ΔM10)	96.2	157.2	189.9	181.3	193.2	191.7	86.2	138.5
Time independent background (ppm/ns)	142.24	19.82	60.34	20.61	11.25	16.99	28.89	13.27
Reconstruction								
Final specimen state	F	F	F	F	F	F	F	F
Pre-/post-analysis imaging	SEM							
Radius evolution model	'Voltage'							
Field factor (k)	3.3							
Image compression factor	1.65							
Assumed E-field (V/nm)	32							
Detector efficiency	0.36							
Avg. atomic volume (nm^3)	0.01076							
V initial (V)	2343	5141	4887	4436	4735	3673	815	1858
V final (V)	3331	6763	5692	9499	7383	6412	954	2642

*ΔM is full width at half maximum of the Volt./bowl corr. peak
**ΔM10 is full width at tenth maximum of the Volt./bowl corr. peak
m = million; det. = detection; Volt. = voltage; corr. = correction; Calib. = calibration; interp. = interpolation; Lin = linearization method; Avg. = average; F = Fractured; NF = not fractured

Grain	**zircon 86 - reidite**			**zircon 86 - core**				
Specimen	**M8**	**M9**	**M1**	**M2**	**M5**	**M6**	**M7**	**M8**
Instrument Model	LEAP 4000X HR							
Instrument Settings								
Laser wavelength (nm)	355							
Laser pulse energy (pJ)	350	350	250	300	300	140	300	300
Pulse frequency (kHz)	200	125	200	250	250	200	250	250
Evaporation control	Detection rate							
Targeted det. rate (ions/pulse)	0.006	0.007	0.006	0.005	0.006	0.006	0.005	0.006
Nominal flight path (mm)	382							
Set point temperature (K)	50	50	60	60	60	60	60	60
Sample temperature (K)	54.6	54.6	65.5	65.5	65.4	67.1	65.4	66.7
Chamber pressure (e^{-11} Torr)	5.6	5.4	7.1	7.1	7.0	7.6	7.1	7.2
Data Summary								
LAS Root version	15.41.342j							
CAMECAROOT version	18.46.428							
Analysis Software	IVAS 3.8.2							
Total Ions:	13 m	2.7 m	1.5 m	8 m	11 m	4 m	21 m	19 m
% Single	73.2	70.6	63.9	72	70.4	62.7	74.5	73.9
% Multiple	26.4	29	35.1	27.4	29.1	36.7	25	25.6
% Partial	0.3	0.4	1	0.6	0.5	0.6	0.5	0.5
Volt./bowl corr. peak (Da)	16	16	16	16	16	16	16	16
Mass Calib. (peaks/interp.)	6/Lin	9/Lin	7/Lin	5/Lin	8/Lin	7/Lin	5/Lin	8/Lin
*(M/ΔM)	1043.6	1032.6	466.3	1013.4	1023.2	950.9	1047.6	1033
**(M/ΔM10)	195.2	191	23.1	170.7	173.9	168.9	190.2	178.4
Time independent background (ppm/ns)	28.21	16.28	17.9	39.14	46.18	29.66	62.10	59.00
Reconstruction								
Final specimen state	F	F	F	F	F	F	F	F
Pre-/post-analysis imaging	SEM							
Radius evolution model	'Voltage'							
Field factor (k)	3.3							
Image compression factor	1.65							
Assumed E-field (V/nm)	32							
Detector efficiency	0.36							
Avg. atomic volume (nm^3)	0.01076							
V initial (V)	5392	4805	3219	5508	5510	2685	5651	5575
V final (V)	7333	6001	4437	6161	6959	5822	7952	7353

*ΔM is full width at half maximum of the Volt./bowl corr. peak
**ΔM10 is full width at tenth maximum of the Volt./bowl corr. peak
m = million; det. = detection; Volt. = voltage; corr. = correction; Calib. = calibration; interp. = interpolation; Lin = linearization method; Avg. = average; F = Fractured; NF = not fractured

Grain	**zircon 86 - core**		**zircon 211**					
Specimen	**M9**	**M10**	**M12**	**M13**	**M14**	**M15**	**M16**	**M17**
Instrument Model	LEAP 4000X HR							
Instrument Settings								
Laser wavelength (nm)	355							
Laser pulse energy (pJ)	300	300	250	400	400	400	600	400
Pulse frequency (kHz)	250	250	200	200	125	200	200	200
Evaporation control	Detection rate							
Targeted det. rate (ions/pulse)	0.005	0.005	0.008	0.008	0.01	0.004	0.004	0.004
Nominal flight path (mm)	382							
Set point temperature (K)	60	60	60	60	60	60	100	70
Sample temperature (K)	65.4	70.1	69.2	69.2	69.2	69.2	111.9	80.7
Chamber pressure (e^{-11} Torr)	8	8.6	15	15	15	15	15	14
Data Summary								
LAS Root version	15.41.342j				15.41.342l			
CAMECAROOT version	18.46.428							
Analysis Software	IVAS 3.8.2							
Total Ions:	17 m	5 m	430786	1.4 m	148319	581654	450420	1.6 m
% Single	75.5	71	68.6	72.2	45.5	76.2	73.2	77.5
% Multiple	24.1	28.4	30	26.9	52.3	22.4	24.9	21.2
% Partial	0.4	0.6	1.4	0.8	2.3	1.4	1.8	1.3
Volt./bowl corr. peak (Da)	16	16	32	16	69	16	16	16
Mass Calib. (peaks/interp.)	10/Lin	11/Lin	12/Lin	9/Lin	6/Lin	10/Lin	8/Lin	10/Lin
*(M/ΔM)	1052.6	1023.2	910.4	1018.1	519.9	974.5	982	1031.5
**(M/ΔM10)	196.1	199.5	90.4	195.3	114.6	195.9	208.9	203.7
Time independent background (ppm/ns)	56.05	86.16	46.74	29.86	25.07	40.18	53.87	37.04
Reconstruction								
Final specimen state	F	F	F	F	F	F	F	F
Pre-/post-analysis imaging	SEM							
Radius evolution model	'Voltage'							
Field factor (k)	3.3							
Image compression factor	1.65							
Assumed E-field (V/nm)	32							
Detector efficiency	0.36							
Avg. atomic volume (nm^3)	0.01076							
V initial (V)	6298	5152	2448	3772	2761	3738	2998	3212
V final (V)	8039	6534	455	5298	3008	10008	3104	5076

*ΔM is full width at half maximum of the Volt./bowl corr. peak
**ΔM10 is full width at tenth maximum of the Volt./bowl corr. peak
m = million; det. = detection; Volt. = voltage; corr. = correction; Calib. = calibration; interp. = interpolation; Lin = linearization method; Avg. = average; F = Fractured; NF = not fractured

Grain	zircon 211				
Specimen	**M18**	**M19**	**M20**	**M21**	**M22**
Instrument Model	LEAP 4000X HR				
Instrument Settings					
Laser wavelength (nm)	355				
Laser pulse energy (pJ)	400	400	400	400	400
Pulse frequency (kHz)	200	200	250	200	200
Evaporation control	Detection rate				
Targeted det. rate (ions/pulse)	0.01	0.002	0.003	0.01	0.002
Nominal flight path (mm)	382				
Set point temperature (K)	70	70	70	80	80
Sample temperature (K)	80.7	80.7	80.7	90.9	91.9
Chamber pressure (e^{-11} Torr)	14	16	16	26	22
Data Summary					
LAS Root version	15.41.342l				
CAMECAROOT version	18.46.428				
Analysis Software	IVAS 3.8.2				
Total Ions:	629397	376935	653951	157796	220440
% Single	65.9	80.5	80.2	66.9	88.3
% Multiple	31.7	17	18.1	29.6	7.8
% Partial	2.4	2.5	1.7	3.5	3.8
Volt./bowl corr. peak (Da)	69	16	16	14	32
Mass Calib. (peaks/interp.)	11/Lin	9/Lin	9/Lin	7/Lin	6/Lin
*(M/ΔM)	426.9	1088.5	1029.7	293	434.7
**(M/ΔM10)	118.7	216.6	209.8	27.2	6.2
Time independent background (ppm/ns)	40.96	93.27	82.96	102.40	312.40
Reconstruction					
Final specimen state	F	F	F	F	F
Pre-/post-analysis imaging	SEM				
Radius evolution model	'Voltage'				
Field factor (k)	3.3				
Image compression factor	1.65				
Assumed E-field (V/nm)	32				
Detector efficiency	0.36				
Avg. atomic volume (nm^3)	0.01076				
V initial (V)	2870	3141	3958	1042	3441
V final (V)	2870	4273	8004	1097	4600

*ΔM is full width at half maximum of the Volt./bowl corr. peak
**ΔM10 is full width at tenth maximum of the Volt./bowl corr. peak
m = million; det. = detection; Volt. = voltage; corr. = correction;
Calib. = calibration; interp. = interpolation; Lin = linearization method; Avg. = average; F = Fractured; NF = not fractured

Results

Of the 4048 zircon grains picked, the majority presented evidence of shock metamorphism related structures including: fractures, fragmentation, or the presence of reidite. Although the single reliable indicator to confirm shock metamorphism in the sample suite is the presence of reidite (Fig. 5.3) (Leroux et al., 1999; Glass et al., 2002), it is believed that the other grains experience similar extreme conditions based on the complex internal textures. From 4048, only 5 grains contained reidite for an abundance of 0.12% (5/4048). Three of these grains were found in the massive suevite unit with an abundance of 0.12% (3/2435), one in the suevite and lapilli mix

unit with an abundance of 0.12% (1/816), and one in the pellet unit with an abundance of 0.13% (1/797). Reidite was identified in the grains in the form of lamellae with up to 3 different orientations. EBSD maps of the zircon grains showed that most of the grains have a < 20° misorientation and the reidite lamellae have < 90° misorientation (Fig. 5.4).

The Tera-Wasserburg ($^{207}Pb/^{206}Pb$ vs $^{238}U/^{206}Pb$ - SHRIMP) shows that most of the zircon grains are discordant and spread of spot analyses define an apparent field between the crystallization age and the age of the hypervelocity impact event (Fig. 5.5). An additional component of recent Pb-loss (or U-gain) was also identified in the Tera-Wasserburg diagram. The SHRIMP measurements indicate a wide range of uranium compositions, from 33 to 3199 ppm (Table 5.3) and a broad correlation between Pb-loss and U content (Fig. 5.5). The FIB-ToF-SIMS analysis conducted on the grains showed a higher concentration of Li, Al, Ca and Y in dark CL-bands at the core, fractures and around clasts within metamict regions. Reidite lamellae were also seen to be enriched in Al, Ca and Y inside and along interfaces (Fig. 5.6). From the NanoSIMS analysis of zircon grain 001, an enhancement of Mg, Al, Y, and Yb was also seen along the reidite lamellae, as well as a heterogeneous distribution of Y, Yb, U and Pb (although minor) in the grain (Fig. 5.7).

The TEM analysis of zircon grain 86, showed three reidite lamellae in TEM foil 1 (Fig. 5.8a-b) and one reidite lamella in TEM foil 2 (Suppl. Fig. 5.2). Amorphous features were identified at the zircon–reidite interface (Fig. 5.8c-d) and nanocrystalline domains were seen within the reidite lamellae. These nanocrystalline domains were identified using HAADF STEM images and by obtaining the electron diffraction (ring pattern) of the area (Suppl. Fig. 5.3).

Table 5.3 U-Th-Pb isotopic data from SHRIMP.

Spot	$^{204}Pb/^{206}Pb$	±%	$^{207}Pb/^{206}Pb$	±%	$^{208}Pb/^{206}Pb$	±%	$^{206}Pb/^{238}U$	±%	% $^{206}Pb_c$	U (ppm)	Th (ppm)
SF-214.2	5.2E-5	39	0.201	0.69	0.055	1.3	1.37	3.6	0.07	138	27
SF-214.1	1.7E-4	33	0.186	1.12	0.166	1.8	1.31	5.1	0.24	57	33
SF-211.1	1.6E-3	7	0.139	1.98	0.066	5.8	0.49	4.0	2.78	3199	42
SF-202.7	5.1E-4	5	0.144	0.64	0.059	2.1	0.63	4.4	0.82	1825	274
SF-202.6	7.5E-4	5	0.147	0.38	0.056	0.6	0.48	6.8	1.25	1762	188
SF-202.5	9.7E-4	7	0.150	0.48	0.061	0.5	0.61	3.1	1.59	1664	166
SF-202.4	1.1E-3	5	0.156	2.27	0.071	1.7	0.47	2.0	1.80	1567	149
SF-202.3	1.2E-4	15	0.172	2.32	0.068	4.0	0.88	3.2	0.18	701	173
SF-202.2	2.4E-3	7	0.197	2.99	0.408	2.2	0.92	4.3	3.31	135	163
SF-202.2	2.9E-3	8	0.203	0.58	0.576	0.6	1.11	3.7	4.10	77	133
SF-202.1	1.3E-3	16	0.192	0.81	0.386	1.0	0.81	2.1	1.85	136	164
SF-202.1	5.7E-4	5	0.149	2.18	0.057	1.5	0.75	6.8	0.93	1360	176
SF-164.5	6.4E-4	7	0.123	1.02	0.087	7.1	0.63	3.5	1.06	1356	303
SF-164.4	1.4E-3	4	0.133	1.71	0.130	2.5	0.74	3.1	2.32	2149	567
SF-164.3	1.4E-3	3	0.117	0.41	0.106	0.6	0.55	4.8	2.28	2182	432
SF-164.2	7.8E-4	4	0.124	0.42	0.081	1.2	0.56	5.7	1.27	2010	399
SF-164.1	5.8E-4	4	0.121	0.19	0.079	0.4	0.65	6.6	0.93	2126	451
SF-129.2	7.7E-4	8	0.173	1.10	0.159	0.5	0.79	7.1	1.20	402	203
SF-129.1	5.1E-4	9	0.161	0.32	0.151	1.3	0.70	6.3	0.81	451	372
SF-122.1	2.5E-4	18	0.187	0.50	0.206	2.6	1.34	4.1	0.35	138	103
SF-121.1	-3.6E-5	100	0.179	1.85	0.296	1.2	1.23	4.3	--	33	35
SF-109.1	2.4E-4	20	0.191	0.47	0.256	0.7	1.29	4.7	0.33	125	111
SF-105.1	1.4E-4	20	0.192	0.56	0.152	1.7	1.28	2.5	0.20	265	132
SF-100.1	1.9E-4	24	0.207	0.49	0.100	2.0	1.49	3.4	0.26	92	33
SF-099.4	8.6E-4	6	0.129	0.61	0.046	0.9	0.44	3.8	1.43	1813	83
SF-099.3	8.2E-4	7	0.112	0.90	0.048	1.0	0.42	2.0	1.38	1365	60
SF-099.2	8.9E-4	5	0.110	0.30	0.041	3.1	0.65	4.4	1.46	1994	103
SF-099.1	1.2E-3	7	0.104	0.44	0.051	1.0	0.40	1.9	2.03	1131	38
SF-086.1	1.5E-4	16	0.182	0.59	0.131	0.9	0.90	4.2	0.23	466	215
SF-083.2	2.4E-4	27	0.188	0.64	0.264	1.4	1.29	3.9	0.34	68	66
SF-083.1	1.0E-3	5	0.152	0.91	0.109	0.5	0.64	4.9	1.67	1259	317
SF-078.1	7.0E-5	35	0.111	0.57	0.146	0.8	0.80	3.6	0.11	224	110
SF-074.1	2.3E-3	3	0.142	0.23	0.093	0.5	0.44	4.4	3.90	1955	74
SF-066.5	7.9E-4	6	0.119	0.50	0.102	0.5	0.59	5.9	1.32	1106	315
SF-066.4	9.3E-4	5	0.117	0.26	0.098	2.3	0.60	7.1	1.55	1378	328
SF-066.3	7.8E-4	9	0.107	0.74	0.088	0.8	0.59	5.9	1.31	1283	270
SF-066.2	8.1E-4	6	0.129	0.69	0.109	0.5	0.63	5.4	1.33	840	256
SF-066.1	1.0E-3	5	0.135	0.42	0.126	1.5	0.65	5.8	1.65	937	328
SF-062.2	9.7E-5	23	0.192	0.34	0.151	0.6	1.24	4.6	0.13	237	131
SF-062.1	2.2E-4	19	0.190	0.39	0.215	0.6	1.12	3.9	0.31	201	169
SF-036.1	2.4E-3	8	0.175	0.25	0.133	3.2	0.55	3.4	4.01	1327	311
SF-186.6	6.1E-4	8	0.161	0.31	0.057	0.9	0.60	3.1	0.98	1096	113
SF-186.5	4.4E-4	9	0.171	0.48	0.040	1.0	0.76	3.0	0.68	1029	102
SF-186.4	2.6E-4	11	0.168	0.26	0.055	1.5	0.86	1.8	0.40	927	138
SF-186.3	6.5E-4	12	0.152	0.51	0.055	1.3	0.55	3.8	1.07	1194	166

SF-186.2	1.8E-3	5	0.150	0.33	0.177	0.5	0.44	2.6	3.07	1408	561
SF-186.1	1.1E-3	6	0.160	0.60	0.092	1.8	0.52	4.5	1.77	1296	286
SF-018.2	3.6E-4	15	0.194	0.59	0.131	0.5	1.05	4.9	0.53	593	291
SF-018.1	5.1E-4	7	0.167	0.64	0.101	0.8	0.91	3.2	0.79	723	217
SF-015.2	3.3E-4	10	0.164	0.61	0.034	4.2	0.79	5.2	0.50	615	104
SF-015.1	7.3E-5	22	0.185	0.45	0.042	0.8	1.33	4.2	0.10	461	66
SF-009.1	2.3E-4	29	0.185	1.53	0.319	1.7	1.36	3.6	0.32	59	69
SF-005.1	2.4E-4	11	0.175	0.25	0.033	2.2	0.76	4.8	0.38	767	67
SF-004.5	5.9E-4	8	0.161	0.30	0.044	0.9	0.64	2.5	0.95	996	156
SF-004.4	1.6E-4	14	0.178	0.24	0.024	3.3	1.03	4.0	0.23	639	121
SF-004.4	6.8E-4	8	0.175	0.35	0.045	2.8	0.79	5.1	1.04	742	117
SF-004.3	1.4E-3	9	0.137	0.63	0.091	3.5	0.54	5.0	2.31	1784	323
SF-004.3	7.6E-4	8	0.123	0.75	0.081	2.2	0.57	5.6	1.26	1958	559
SF-004.2	1.8E-3	5	0.132	1.54	0.124	5.4	0.60	6.1	3.01	1897	458
SF-004.2	2.0E-3	14	0.154	0.77	0.130	4.0	0.56	5.0	3.25	1488	492
SF-004.1	7.1E-4	6	0.158	0.73	0.055	1.3	0.82	4.1	1.10	1006	180
SF-004.1	5.3E-4	8	0.136	0.46	0.031	1.9	0.59	3.5	0.90	968	39
SF-001.3	1.9E-3	19	0.195	2.01	0.626	1.0	0.59	4.0	2.99	42	70
SF-001.2	1.6E-3	13	0.194	2.20	0.638	2.5	0.65	6.0	2.58	85	147
SF-001.1	1.2E-3	19	0.189	0.88	0.455	1.0	0.78	3.9	1.91	47	70

Spot	4-corr $^{206}Pb^*$ (ppm)	$^{232}Th/^{238}U$	±%	$^{238}U/^{206}Pb^*$	±%	$^{207}Pb^*/^{206}Pb^*$	±%	$^{207}Pb^*/^{235}U$	±%	$^{206}Pb^*/^{238}U$	±%
SF-214.2	65	0.20	0.55	1.8	1.6	0.201	0.70	15.1	1.7	0.55	1.6
SF-214.1	26	0.60	0.55	1.9	1.5	0.183	1.20	13.2	1.9	0.52	1.5
SF-211.1	512	0.014	2.1	5.4	5.2	0.117	2.8	3.0	5.9	0.186	5.2
SF-202.7	414	0.155	2.0	3.8	2.3	0.137	0.7	5.0	2.5	0.264	2.3
SF-202.6	331	0.110	1.0	4.6	3.5	0.138	0.5	4.1	3.6	0.219	3.5
SF-202.5	345	0.103	0.2	4.1	1.7	0.137	0.8	4.6	1.9	0.241	1.7
SF-202.4	274	0.098	3.7	4.9	3.2	0.142	2.6	4.0	4.1	0.203	3.2
SF-202.3	253	0.256	3.0	2.4	1.5	0.171	2.3	9.9	2.8	0.420	1.5
SF-202.2	58	1.244	2.1	2.0	4.0	0.167	3.9	11.4	5.5	0.496	4.0
SF-202.2	30	1.77	0.34	2.2	1.4	0.167	1.98	10.4	2.4	0.45	1.4
SF-202.1	52	1.248	1.4	2.2	1.8	0.176	1.8	10.8	2.5	0.445	1.8
SF-202.1	302	0.13	1.81	3.9	3.4	0.141	2.33	5.0	4.1	0.26	3.4
SF-164.5	273	0.231	4.1	4.3	2.5	0.114	1.2	3.7	2.8	0.234	2.5
SF-164.4	485	0.272	0.5	3.8	2.3	0.113	2.2	4.1	3.2	0.262	2.3
SF-164.3	409	0.204	1.5	4.6	2.4	0.098	0.8	2.9	2.6	0.218	2.4
SF-164.2	419	0.205	1.7	4.1	3.6	0.113	0.6	3.8	3.6	0.242	3.6
SF-164.1	506	0.219	0.8	3.6	3.2	0.113	0.4	4.3	3.2	0.277	3.2
SF-129.2	111	0.52	1.04	3.1	2.2	0.163	1.28	7.2	2.6	0.32	2.2
SF-129.1	111	0.85	0.49	3.5	2.8	0.155	0.52	6.1	2.8	0.29	2.8
SF-122.1	60	0.77	1.86	2.0	2.2	0.184	0.59	12.8	2.3	0.50	2.2
SF-121.1	14	1.09	0.61	2.0	1.8	0.179	1.86	12.2	2.6	0.50	1.8
SF-109.1	55	0.92	0.88	1.9	1.2	0.188	0.57	13.4	1.3	0.51	1.2
SF-105.1	106	0.51	0.65	2.2	1.7	0.190	0.59	12.2	1.8	0.46	1.7
SF-100.1	43	0.36	0.52	1.9	2.2	0.205	0.56	15.2	2.2	0.54	2.2
SF-099.4	325	0.047	2.5	4.8	3.3	0.117	0.9	3.4	3.5	0.209	3.3
SF-099.3	216	0.045	0.4	5.4	1.5	0.100	1.3	2.5	2.0	0.184	1.5
SF-099.2	407	0.053	3.2	4.2	2.1	0.097	0.8	3.2	2.2	0.238	2.1
SF-099.1	160	0.035	1.3	6.1	3.8	0.087	1.5	2.0	4.1	0.165	3.8
SF-086.1	144	0.48	0.21	2.8	3.4	0.180	0.62	9.0	3.4	0.36	3.4
SF-083.2	29	1.00	1.16	2.0	1.4	0.185	0.79	12.8	1.6	0.50	1.4
SF-083.1	255	0.26	1.05	4.2	2.6	0.139	1.11	4.5	2.8	0.24	2.6
SF-078.1	60	0.51	0.30	3.2	2.2	0.110	0.65	4.7	2.3	0.31	2.2
SF-074.1	241	0.04	1.62	7.0	2.0	0.112	0.90	2.2	2.2	0.14	2.0
SF-066.5	203	0.29	1.77	4.7	1.8	0.108	0.80	3.2	2.0	0.21	1.8
SF-066.4	246	0.25	0.73	4.8	2.2	0.105	0.69	3.0	2.3	0.21	2.2
SF-066.3	216	0.22	1.02	5.1	1.5	0.096	1.33	2.6	2.0	0.20	1.5
SF-066.2	169	0.32	0.55	4.3	1.9	0.118	0.96	3.8	2.1	0.23	1.9
SF-066.1	191	0.36	1.29	4.2	1.8	0.121	0.74	4.0	2.0	0.24	1.8
SF-062.2	104	0.57	0.28	2.0	2.1	0.191	0.37	13.4	2.2	0.51	2.1
SF-062.1	79	0.87	0.42	2.2	1.7	0.187	0.49	11.8	1.8	0.46	1.7
SF-036.1	205	0.24	1.43	5.6	1.5	0.144	1.77	3.6	2.3	0.18	1.5
SF-186.6	245	0.107	1.2	3.8	2.7	0.153	0.5	5.5	2.8	0.261	2.7
SF-186.5	288	0.103	0.4	3.1	2.0	0.165	0.6	7.4	2.1	0.325	2.0
SF-186.4	275	0.154	1.1	2.9	1.5	0.164	0.4	7.8	1.6	0.345	1.5
SF-186.3	242	0.143	0.8	4.2	2.8	0.144	0.9	4.7	2.9	0.236	2.8
SF-186.2	226	0.412	0.2	5.4	1.9	0.126	1.0	3.3	2.2	0.187	1.9

SF-186.1	252	0.228	2.5	4.4	2.7	0.146	0.9	4.5	2.8	0.226	2.7
SF-018.2	201	0.51	0.18	2.5	1.3	0.189	0.70	10.3	1.5	0.39	1.3
SF-018.1	199	0.31	0.32	3.1	1.7	0.161	0.73	7.1	1.9	0.32	1.7
SF-015.2	177	0.18	5.35	3.0	1.6	0.159	0.69	7.4	1.7	0.34	1.6
SF-015.1	190	0.15	1.38	2.1	1.7	0.184	0.47	12.2	1.8	0.48	1.7
SF-009.1	26	1.21	1.11	1.9	2.5	0.182	1.62	13.1	3.0	0.52	2.5
SF-005.1	195	0.09	0.90	3.4	1.9	0.172	0.32	7.0	1.9	0.30	1.9
SF-004.5	240	0.162	1.0	3.6	2.1	0.154	0.5	5.9	2.1	0.280	2.1
SF-004.4	219	0.20	1.68	2.5	1.3	0.176	0.28	9.7	1.3	0.40	1.3
SF-004.4	226	0.163	2.6	2.8	4.9	0.166	0.6	8.1	5.0	0.354	4.9
SF-004.3	355	0.187	1.0	4.3	3.4	0.118	1.7	3.8	3.8	0.232	3.4
SF-004.3	356	0.29	1.62	4.7	1.2	0.113	1.12	3.3	1.6	0.21	1.2
SF-004.2	336	0.25	2.70	4.8	1.7	0.107	2.30	3.1	2.8	0.21	1.7
SF-004.2	305	0.342	1.7	4.2	2.9	0.128	3.1	4.2	4.2	0.239	2.9
SF-004.1	285	0.185	1.4	3.0	2.9	0.149	0.9	6.8	3.0	0.330	2.9
SF-004.1	163	0.04	1.96	5.1	1.3	0.129	0.66	3.5	1.5	0.20	1.3
SF-001.3	10	1.74	1.04	3.7	1.7	0.171	3.53	6.3	3.9	0.27	1.7
SF-001.2	21	1.78	1.73	3.4	4.4	0.174	2.94	7.0	5.3	0.29	4.4
SF-001.1	12	1.55	0.70	3.2	1.5	0.174	1.96	7.4	2.5	0.31	1.5

Spot	err corr	$^{206}Pb/^{238}U$ Age		$^{207}Pb/^{206}Pb$ Age		% discordant
SF-214.2	0.91	2816	±36	2831	±11	+1
SF-214.1	0.78	2700	±33	2685	±20	-1
SF-211.1	0.88	1101	±53	1911	±51	+46
SF-202.7	0.96	1512	±32	2195	±12	+35
SF-202.6	0.99	1275	±41	2197	±9	+46
SF-202.5	0.90	1393	±22	2192	±15	+40
SF-202.4	0.78	1193	±35	2253	±45	+51
SF-202.3	0.53	2261	±28	2565	±39	+14
SF-202.2	0.72	2596	±85	2529	±65	-3
SF-202.2	0.56	2411	±27	2524	±33	+5
SF-202.1	0.72	2371	±37	2616	±29	+11
SF-202.1	0.82	1480	±45	2245	±40	+38
SF-164.5	0.90	1356	±31	1864	±22	+30
SF-164.4	0.73	1502	±31	1850	±39	+21
SF-164.3	0.95	1272	±28	1582	±15	+22
SF-164.2	0.99	1399	±45	1848	±11	+27
SF-164.1	0.99	1577	±45	1853	±7	+17
SF-129.2	0.87	1801	±35	2483	±22	+31
SF-129.1	0.98	1625	±40	2400	±9	+36
SF-122.1	0.97	2623	±47	2691	±10	+3
SF-121.1	0.70	2598	±39	2644	±31	+2
SF-109.1	0.90	2677	±26	2729	±9	+2
SF-105.1	0.94	2461	±35	2742	±10	+12
SF-100.1	0.97	2785	±49	2863	±9	+3
SF-099.4	0.96	1221	±37	1913	±17	+40
SF-099.3	0.74	1091	±15	1629	±25	+36
SF-099.2	0.94	1375	±26	1574	±14	+14
SF-099.1	0.93	984	±35	1361	±28	+30
SF-086.1	0.98	1984	±58	2657	±10	+29
SF-083.2	0.88	2617	±31	2697	±13	+4
SF-083.1	0.92	1364	±32	2210	±19	+42
SF-078.1	0.96	1751	±33	1795	±12	+3
SF-074.1	0.91	866	±16	1824	±16	+56
SF-066.5	0.91	1250	±20	1764	±15	+32
SF-066.4	0.96	1217	±25	1707	±13	+31
SF-066.3	0.75	1154	±16	1551	±25	+28
SF-066.2	0.89	1360	±23	1931	±17	+33
SF-066.1	0.93	1373	±23	1975	±13	+34
SF-062.2	0.99	2657	±46	2750	±6	+4
SF-062.1	0.96	2435	±35	2717	±8	+12
SF-036.1	0.65	1065	±15	2278	±31	+58
SF-186.6	0.98	1494	±36	2384	±9	+42
SF-186.5	0.96	1815	±32	2508	±10	+32
SF-186.4	0.97	1910	±25	2502	±6	+27
SF-186.3	0.95	1366	±34	2273	±16	+44
SF-186.2	0.88	1104	±20	2045	±18	+50

SF-0186.1	0.95	1313	±32	2295	±15	+47
SF-018.2	0.88	2144	±23	2736	±12	+25
SF-018.1	0.92	1791	±27	2464	±12	+31
SF-015.2	0.92	1867	±26	2450	±12	+27
SF-015.1	0.96	2523	±36	2692	±8	+8
SF-009.1	0.84	2699	±55	2673	±27	-1
SF-005.1	0.99	1672	±28	2575	±5	+40
SF-004.5	0.97	1592	±29	2385	±9	+37
SF-004.4	0.98	2162	±24	2617	±5	+20
SF-004.4	0.99	1954	±83	2520	±9	+26
SF-004.3	0.90	1344	±41	1930	±30	+34
SF-004.3	0.73	1238	±13	1850	±20	+36
SF-004.2	0.59	1209	±18	1756	±42	+34
SF-004.2	0.68	1381	±36	2067	±54	+37
SF-004.1	0.96	1839	±46	2332	±15	+24
SF-004.1	0.89	1156	±14	2086	±12	+49
SF-001.3	0.43	1531	±23	2568	±59	+45
SF-001.2	0.83	1643	±63	2595	±49	+41
SF-001.1	0.62	1738	±23	2598	±33	+38

Errors are 1-sigma; Pb_c=common Pb; Pb*=radiogenic Pb

Other features identified included quasi-periodic structures of dislocations in the interfacial domain (chapter 4), fractures and dislocations within the host zircon grain. TEM-EDS of foil 1 revealed trace element enhancement (Ca, Al, and Y) along the zircon–reidite interfaces, including the one with the quasi-periodic structure, and in the nanocrystalline domains within the reidite lamellae (Fig. 5.9).

Microstructures identified within the Stac Fada APT specimens included zircon–reidite interfaces (chapter 4), low-angle boundaries within reidite (chapter 4) and dislocation loops enriched in trace elements (Fig. 5.10). The dislocation loops were identified within a specimen of the metamict area of zircon grain 66 (label M2). The loops have a toroidal shape, ~50 nm in diameter and they are enriched with Al, Ca, Y and U. No segregation of Pb or any other element was identified within the loops. In addition, a heterogeneous distribution of trace elements was seen in two specimens (M2 and M5) from the metamict area of zircon grain 66, including the specimen with the dislocation loops. Specimen M2 displayed a heterogenous distribution of Be, Mg and Mn (Fig. 5.11) with a region of low concentration of Be, Mg and Mn that is surrounded by two regions of higher concentration. In the one-dimensional (1D) concentration profile of the APT specimen, Mn was identified as the element with the highest concentration. In contrast, the heterogenous distribution in M5 can be divided into two regions, one with a low concentration of Be, Ca, Al,

Mn, Fe, and Y (top of specimen) and the other with a high concentration of the trace elements (Fig. 5.12). In the 1D profile, the elements with the highest concentration are Mn, Ca and Al.

From the chemical data, a relationship between U concentration, calculated radiation damage dose (α-decay dose) and the yield of the APT specimens is apparent (Fig. 5.13). The APT specimens from the crystalline regions of the reidite bearing zircon grains (001 and 86) provided the highest number of ions. In addition, these two grains had the lowest concentration of U (U_{zircon} 001 = 42–85 ppm, U_{core}-zircon 86 = 466 ppm) with respect to the other grains analysed with APT. Zircon grain 211, which had the highest concentration of U (3199 ppm) and the highest amount of radiation damage, produced APT specimens that yielded less than 2 million ions (Table 5.2). Zircon 66 (U = 840–1378 ppm) produced 2 APT specimens that yielded > 1 million ions, whereas the other 4 specimens yielded < 1million ions.

When comparing the yield of all 45 Stac Fada APT specimens, it was found that 46% of the samples yielded < 1 million ions, 20% produced 1–5 million ions, 7% yielded 5–10 million ions, ~11% produced 10–15 million ions, 5% had 15–20 million ions, and ~11% produced >20 million ions (Fig. 5.14). In other words, 89% of the total APT specimens yielded < 20 million ions, while only 11% yielded >20 million ions. The specimens from the crystalline areas of the reidite bearing zircon grains were the ones that produced the highest number of ions.

The APT specimens from the IOZ produced a high number of ions (> 80 million ions). The acquisition process was stopped at 10 kV for all IOZ specimens. None of the specimens from the IOZ fractured. Major, minor and most trace elements showed a homogenous distribution in the APT specimens. The only variation identified was in the form of planes enriched in Y (Fig. 5.15). No other elements were identified to be enriched within the planes.

Discussion

Indian Ocean zircon - control sample

The IOZ was included in this research as a control sample for comparison of APT yield. The IOZ has already been studied considerably with different techniques (Reddy et al., 2006; Reddy et al., 2007; Timms and Reddy, 2009). This grain was chosen because it is young (~11 Ma), with minor amount of radiation damage and

has undergone some degree of crystal-plastically deformation. Both samples (IOZ and Stac Fada) are deformed, although the Stac Fada grains experienced much higher strain deformation. The planes enriched in Y in the IOZ specimens correspond to low-angle boundaries that formed from the crystal-plastic deformation. Piazolo et al. (2016) and La Fontaine et al. (2017) found similar Y-enriched planes in zircon grains hosted in high-temperature metamorphism terranes. The high APT specimen yield from the IOZ indicate that grains subject to deformation can be suitable for APT analyses.

Distribution of trace elements in Stac Fada

The zircon grains from the Stac Fada suite show a variety of textures and shock related microstructures (e.g. reidite lamellae and fractures) (Suppl. Figs. 5.4-5.5). Enrichment of trace elements within the zircon grains was identified as heterogenous distributions and segregations into microstructures. APT specimens from metamict regions in zircon grains (M2 and M5 from zircon 66) displayed a clear heterogenous distribution of trace elements (e.g. Be, Ca, Mg, Al, Mn, Fe and Y) (Figs. 5.11-5.12). The greatest difference in trace element concentration (e.g. Mn) from the different regions was seven to eight times that of the region with the lowest concentration. A similar distribution was seen in FIB-ToF-SIMS maps from other metamict zircon grains (Suppl. Figs. 5.6-5.9). These results suggest that areas affected by radiation lack a regular trace element distribution, which is indicative of enhanced element diffusion through metamict areas (e.g. Cherniak, 2010).

In the Stac Fada samples, the identified microstructures enhanced in trace elements are dislocation loops, low-angle boundaries and zircon–reidite interfaces. The characterisation of the low-angle boundaries within reidite lamella and zircon–reidite interfaces are explained in detail within chapter 4 (Montalvo et al., 2019) and only a brief summary is provided here for context. Using APT, low-angle boundaries enriched in substitutional and interstitial elements (Al, Ca, Mn, Be, Mg, Y and Ti) were identified. These boundaries were proposed to form at the recovery stage of the impact event (Reddy et al., 2016; Montalvo et al., 2019). During this stage, the strain energy on the grain causes defects and trace elements to migrate to low-energy areas, resulting in the formation of low-angle boundaries in the reidite and the host zircon grain (Reddy et al., 2016; Montalvo et al., 2019).

The trace element enrichment was identified at zircon-reidite interfaces using FIB-ToF-SIMS (Suppl. Figs. 5.10-5.11), TEM and APT. The interfacial domains are distinct from the zircon and the reidite, with one interface showing quasi-periodic structures (dislocation network) that formed during deformation (Montalvo et al., 2019). During the growth of the reidite lamellae and the migration of the interphases, it is suggested that the moving boundary dragged and segregated trace elements, at the same time as local diffusion of trace elements along the interface. This resulted in different concentration of trace elements in the different interfaces.

The ~50 nm wide dislocation loops are enriched in Al, Ca, Y and U, with no Pb segregation detected in the data set (Fig. 5.10). This research is understood to be one of the first reports of U segregation in dislocation loops observed from APT specimens. Previous studies conducted in deformed and metamict zircon grains attribute the U migration to the presence of high-diffusion pathways in the grains (e.g. amorphous/metamict areas, low-angle boundaries and high-angle boundaries) (Geisler et al., 2002; Timms et al., 2006; Piazolo et al., 2016). Dislocation loops have been seen in other zircon studies (Bursill and McLaren, 1966; Peterman et al., 2016; Peterman et al., 2019). The ~10 nm wide dislocation loops in Peterman et al. (2016) were enriched only in Y and Pb, whereas Bursill and McLaren (1966) recorded dislocation loops widths of 10–100 nm with no chemical information from the TEM study provided. Peterman et al. (2019) found dislocation loops of various sizes (10-150 nm in diameter) that were enriched in Pb. In these studies, the proposed mechanism responsible for the formation of dislocation loops is believed to be the annealing of the radiation damaged areas during metamorphism, coupled with the migration of trace elements into them (Bursill and McLaren, 1966; Peterman et al., 2016). Given that the concentrations of U and Th (Table 5.3) in the Stac Fada grains are high enough for the zircon grains to have been metamict prior to the hypervelocity impact event, it is possible for the dislocation loops to have been formed by the annealing of radiation damage that came immediately after the impact event. However, the lack of Pb within the loops is not well understood. A possible explanation is that the Pb diffused out of the grain through other defects. The likelihood of Pb diffusing out of the grain is supported by the fact that these grains experienced shock metamorphism, which created a high density of defects in the structure.

Geochronological analysis

From the SHRIMP data of the zircon grains from Stac Fada, a crystallization age that ranges from 2.7 to 2.9 Ga was calculated (Fig. 5.5, Suppl. Fig. 5.12). These ages correlate with the age of the rocks from the Lewisian Complex basement in Scotland. The Concordia diagram also shows multiple events for either Pb-loss or U-gain, one recent and another around 1 Ga. The ~1 Ga is interpreted to be the age of the hypervelocity impact event, which is recognised to be 1.18 Ga (Parnell et al., 2011). However, the SHRIMP analyses could not directly date the impact event with concordant analyses at 1.18 Ga.

One of the motivations of this research was to use APT to obtain the age of the impact event from the shocked zircon grains. This nanogeochronology approach was successful in other studies (e.g. Valley et al., 2014; Peterman et al., 2016; White et al., 2017; Fougerouse et al., 2019; White et al., 2019). Even though the microstructures are enriched in trace elements, no Pb signal above background could be quantified and no segregation of Pb was identified. Therefore, the calculation of the age of the hypervelocity impact event could not be resolved from the data obtained from this study. This shows that APT geochronology requires the presence of relatively high concentrations of radioactive and radiogenic elements and a high signal-to-noise ratio for effective quantification.

Advantages and limitations of analytical techniques

LAM EBSD mapping provided a convenient and effective way to search for specific signs of shock metamorphism (e.g. reidite) in a sample that contained around 4,000 grains. Depending on the step size and the number of grains in a row, the acquisition time could last from 2 to 19 hrs. If the step size chosen was greater than the shock features, there was the possibility of overlooking the feature. The optimal conditions for detecting shock features is to minimize the number of grains in a row (to speed up the process) and have a small step size (≤ 2 μm). Technical advances (e.g. Symmetry EBSD detector) could provide faster acquisition time for LAM.

Both the FIB-ToF-SIMS and NanoSIMS offer elemental and isotopic maps (Figs. 5.6-5.7). The data was used to provide the context for other analytical methods, in particular for the nanoscale analyses (TEM and APT) that have a much more restrained field of view. The larger scale maps were also used to identify target

areas for further analyses. Despite a spatial resolution of ~50 nm, the resolution of FIB-ToF-SIMS and NanoSIMS was not high enough for differentiating the trace element distributions in thin lamellae (~500 nm). When using these techniques, it was difficult to identify whether the distribution of trace elements occurred inside the reidite lamellae or along the zircon–reidite interface. Although, according to the instrument specification NanoSIMS is more sensitive to Pb and U using the O- primary source than FIB-ToF-SIMS, both techniques identified Pb within the sample. However, neither technique could quantify spatially the Pb/Pb or Pb/U composition of the zircon grains (Yang et al., 2012; Lyon et al., 2019) (see Fig. 5.7 for NanoSIMS). The NanoSIMS instrument has multiple detectors that allow for seven ions to be detected, while the FIB-ToF-SIMS does not have an ion limit. In contrast, with the FIB-ToF-SIMS, Al, Ca and Y were identified in the reidite lamellae, while the NanoSIMS also identified Mg and Yb within the lamellae. Nevertheless, both techniques provided chemical information to determine the regions of interest for the following analyses.

The SHRIMP was another essential technique for this research. It provided the geochemical and geochronological data needed to confirm the geological evolution of the Stac Fada grains (Parnell et al., 2011; Reddy et al., 2016). The geochemical data (radioactive element composition) and the crystallization age obtained were used to calculate the amount of radiation damage the zircon grains had endured. This information was used to find its correlation with the yield of the APT specimen. The limitations of this technique were related to the acquisition time and its spatial resolution (~25 µm). Just like the NanoSIMS, the SHRIMP data can take hours (up to days) to collect. In addition, the features of interest from these grains were reidite lamellae of < 5µm. When the SHRIMP was used to analyse a shocked zircon grain, the spot size of the technique covered several lamellae as well as the host zircon (Suppl. Fig. 5.13) resulting in a mix of ages. This restrained the possibility of obtaining geochronological data from the reidite lamellae.

TEM was used for the nanoscale geochemical and structural analysis of reidite lamellae. This technique offered the necessary resolution to study the reidite lamellae, interfaces, microstructures, defects and crystallinity, as well as the trace element composition of the zircon grain (Fig. 5.8-5.9, Suppl. Fig. 5.2-5.3). The main limitation of this technique is that even though it can provide chemical information (EDS), it cannot offer the isotopic data. In addition, it has a detection limit of ~1-0.5

wt.%, meaning that trace elements below that concentration would not be detected. However, incorporating APT analysis with TEM studies can solve the problems of isotopic information and detection limit.

The effectiveness of APT relies heavily on the specimen yield (number of ions per APT specimen). The yield of the specimen depends on several factors such as: sample preparation, acquisition parameters and sample integrity. For example, sample integrity includes the degree of crystallinity, grain boundaries, defects, porosity, interfaces, multiple phases, the amount of radiation damage and deformation of the grains. These can influence the yield of the specimen, i.e. the more damaged the grain is, the less likely it is to generate a high APT specimen yield.

The preparation of the Stac Fada specimens was similar between the samples to produce stable specimens. The APT running conditions (e.g. laser pulse energy, pulse frequency, set point temperature, and detection rate) were chosen independently of each other (Table 5.2 and Suppl. Fig. 5.13) with the purpose of obtaining a high yield from the APT specimens. Unlike the previous two factors (sample preparation and running conditions), the integrity of the sample varied greatly between grains and target areas.

From the results of the Stac Fada zircon grains, a link between sample integrity and the APT specimen yield is evident, especially with respect to crystallinity, amount of radiation damage and density of defects. The crystallinity of the zircon grains, which is related to the radiation damage (an outcome of the concentration of radioactive elements in the lattice with time), contributes to the yield of the APT specimens. The APT specimens derived from the crystalline areas of the zircon grains (zircon 001 and 86) produced the highest number of detected ions (Figs. 5.13-5.14).

Likewise, the amount of radiation damage of the grains influenced the yield of the APT specimens. It was found that the higher the amount of radiation damage, the less likely the specimens would produce sufficient ions (e.g. zircon 211) to allow the chemistry of the specimen to be captured (Fig. 5.13). In contrast, the APT specimens from the IOZ produced a high number of ions, even though the grain was deformed. This indicates that deformation alone is not the sole cause of a low yield.

The zircon grains from Stac Fada were under shock metamorphic conditions, which induced defects into the crystals (Reddy et al., 2015). Even though, at the

recovery phase, defects and trace elements migrated to low-energy areas (Reddy et al., 2016; Montalvo et al., 2019), it is possible that many defects remained in the crystal structure of the grains. The high-density of defects in the structure (e.g. dislocations and vacancies) could explain the recent Pb-loss (or U-gain) seen in the SHRIMP data (Fig. 5.5) and can also affect the yield of the APT specimens. In addition, the presence of interfaces, which is an intrinsic feature of shocked grains, can also contribute to the yield of the specimens due to premature fracturing of the specimen (Reddy et al., 2020).

In summary, the degree of crystallinity, defects, amount of radiation damage of the grain and the presence of interfaces was found to have an impact on the yield of the APT specimens. In this study, the APT yield for each sample varied significantly and ranged from <1 million to 150 million ions (Fig. 5.14). However, the minimum number of ions to obtain the necessary chemical data for this study was ~1.5 million ions.

Conclusion

Microstructures enriched in trace elements from Stac Fada zircon grains were analysed to understand the distribution of trace element associated to a hypervelocity impact event. Trace element segregation into dislocation loops and the heterogenous distributions seen in the grains was attributed to element diffusion through metamict areas and annealing of radiation damaged areas associated to the impact event. The segregation of trace elements into zircon–reidite interfaces was attributed to the migration of the growing interface while incorporating trace elements. Low-angle boundaries enriched in trace elements were formed from the migration of defects and trace elements into low-energy areas by the strain energy of the grain.

The SHRIMP geochronological analysis provided a crystallization age for the zircon grains and an imprecise age for the hypervelocity impact event. It also showed evidence for recent Pb-loss or U-gain for the grains. Unfortunately, APT could not be used to obtain the age of the hypervelocity impact event that created the Stac Fada deposit due to the lack of Pb segregation in the APT specimens, which impedes the age calculation based on the Pb isotopes.

Several techniques were combined in this research in order to understand the effect of shock metamorphism on the distribution of trace elements. This research

explored the limitations of each analytical technique and the suitability for this study. It was found that by combining the techniques and creating an appropriate workflow, the respective limitations of individual techniques were overcome. This research also demonstrates a correlation between the APT specimen yield and sample integrity, meaning the amount of radiation damage, crystallinity and defects in the analysed sample result in a lower APT yield. Obtaining an in-depth characterization of the sample prior to the APT analysis provides valuable information to help the researcher assess which analytical technique may be most appropriate and where to target for a higher APT specimen yield.

Figures

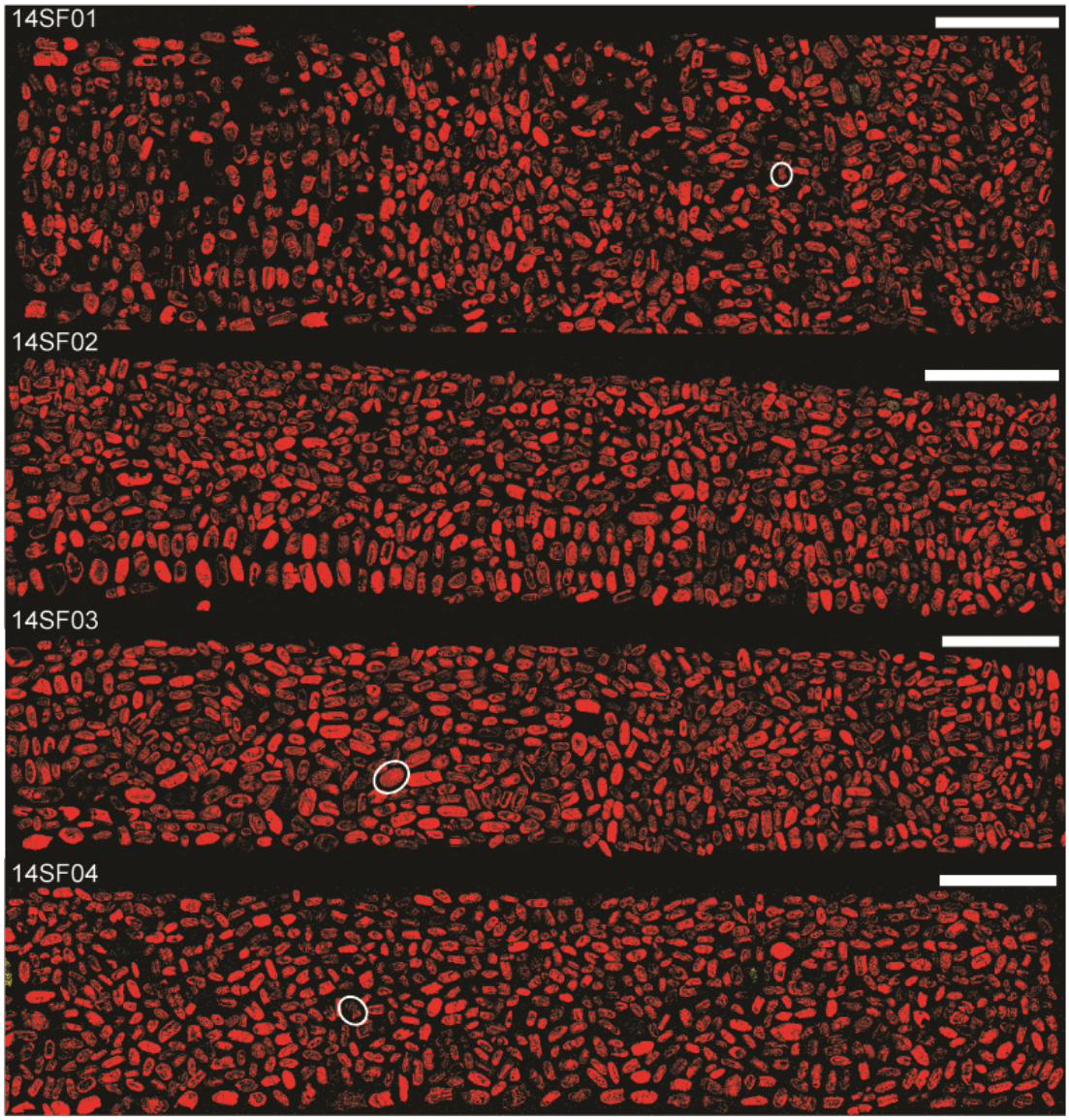

Figure 5.1 Large area EBSD phase map of the Stac Fada samples (red = zircon, yellow = quartz, blue = reidite). The sample labels represent year, name of location and number of sample (e.g. 14SF01 = 2014, Stac Fada, sample 01). Samples 14SF01 and 14SF02 come from the massive suevite unit, 14SF03 derives from the mixture of suevite and lapilli, and sample 14SF04 comes from the upper layer of dust pellets. The reidite bearing zircon grains are encircled in white and the scale bars represent 1000 µm.

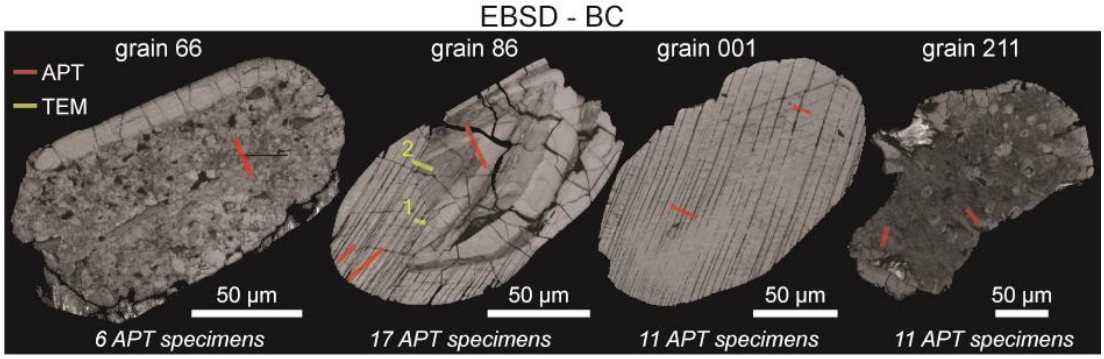

Figure 5.2 Band contrast (BC) EBSD maps of the shocked zircon grains examined for the APT and TEM analyses. The location of the APT specimens is highlighted in red and the location of the TEM foils are highlighted in yellow. The total number of APT specimens manufactured for each of the grains is located below the BC images.

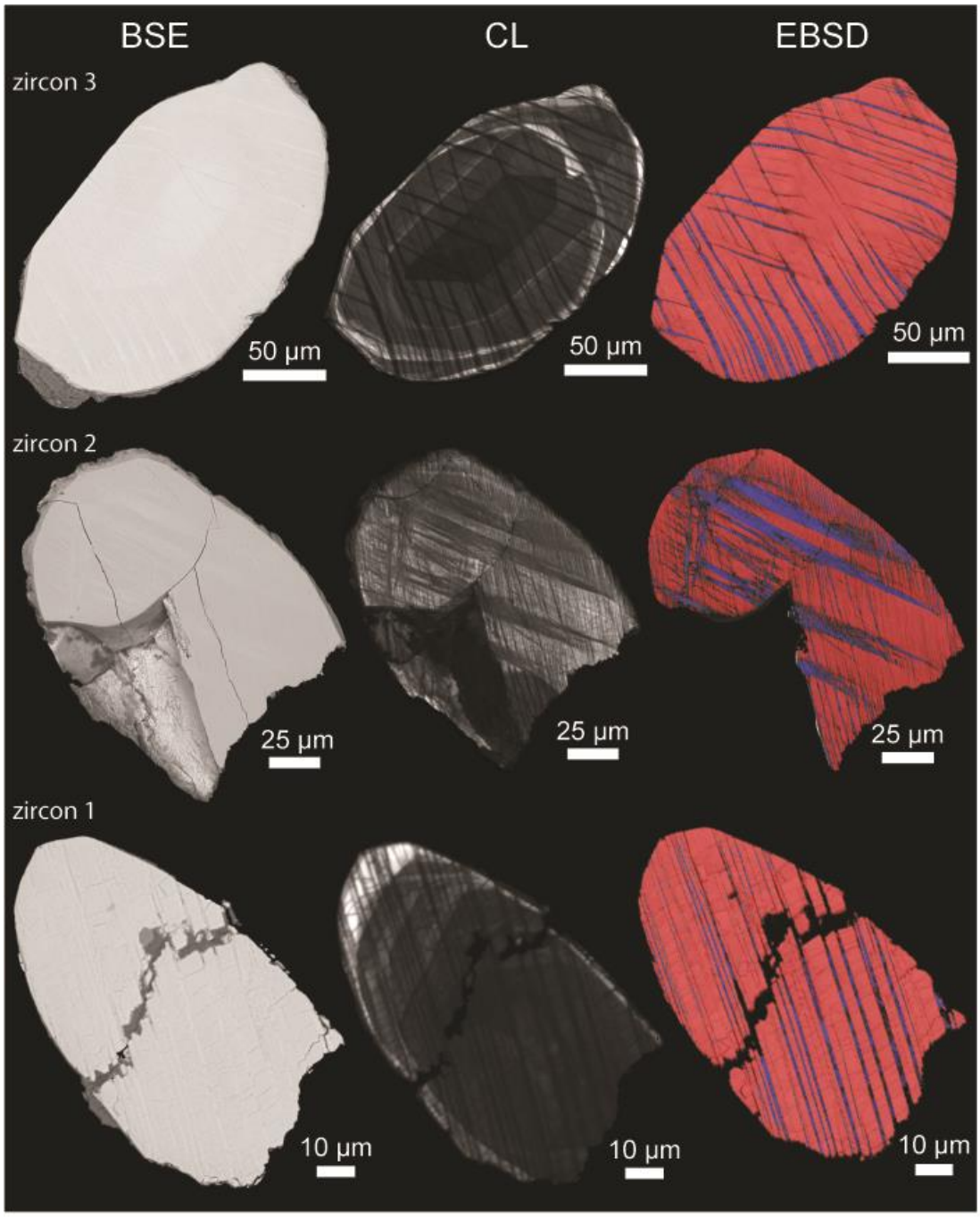

Figure 5.3 Interior images of zircon grains with reidite lamellae, including BSE imaging, CL imaging and EBSD phase maps. Reidite lamellae are evident in CL and EBSD maps, although barely visible in BSE. Colours of the EBSD map indicate zircon in red and reidite in blue.

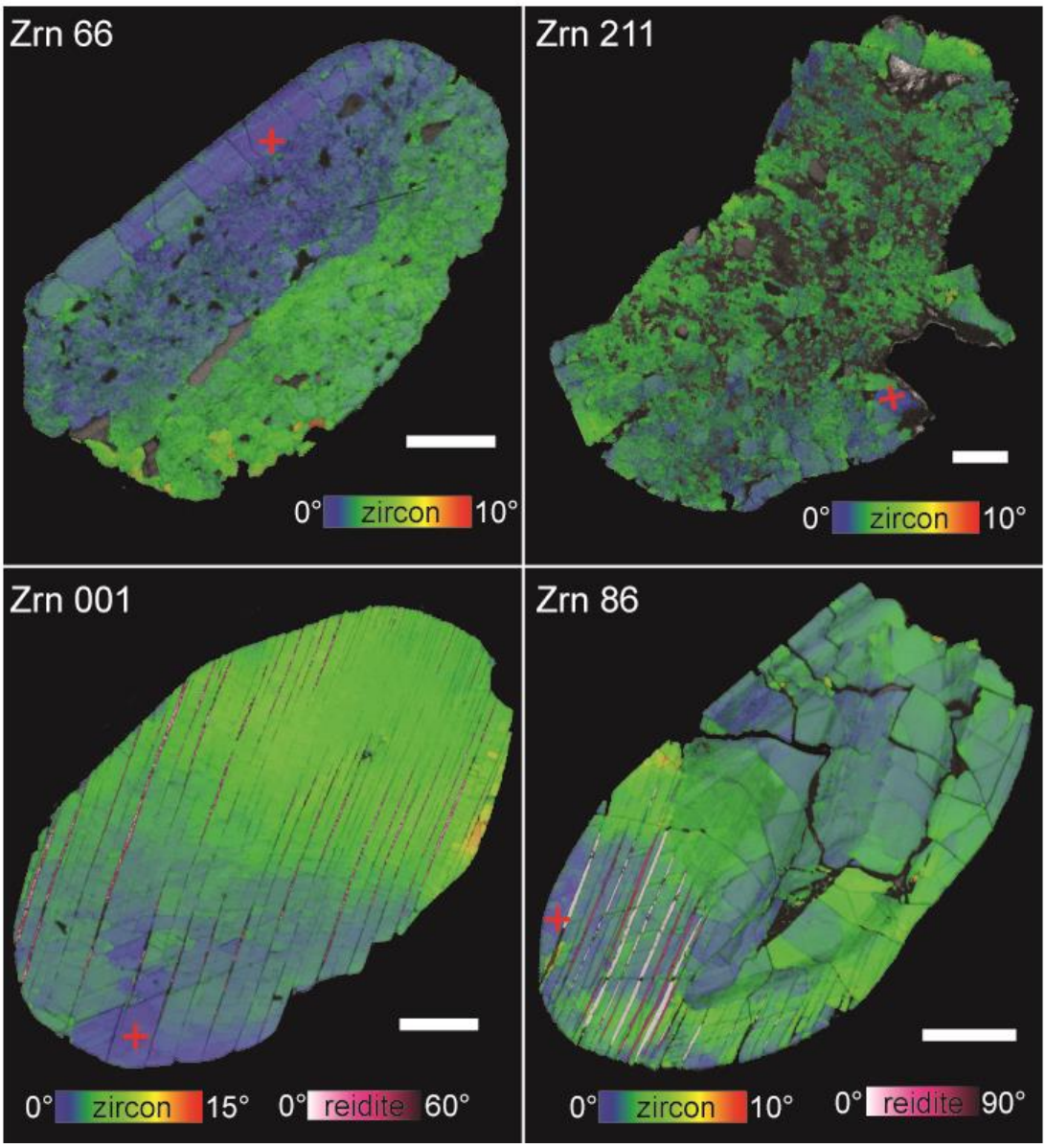

Figure 5.4 EBSD maps showing the misorientation of zircon grains (rainbow scale) with respect to a point of reference (red cross) and the misorientation of the reidite lamellae (fuchsia scale). The scale bar represents 25 µm.

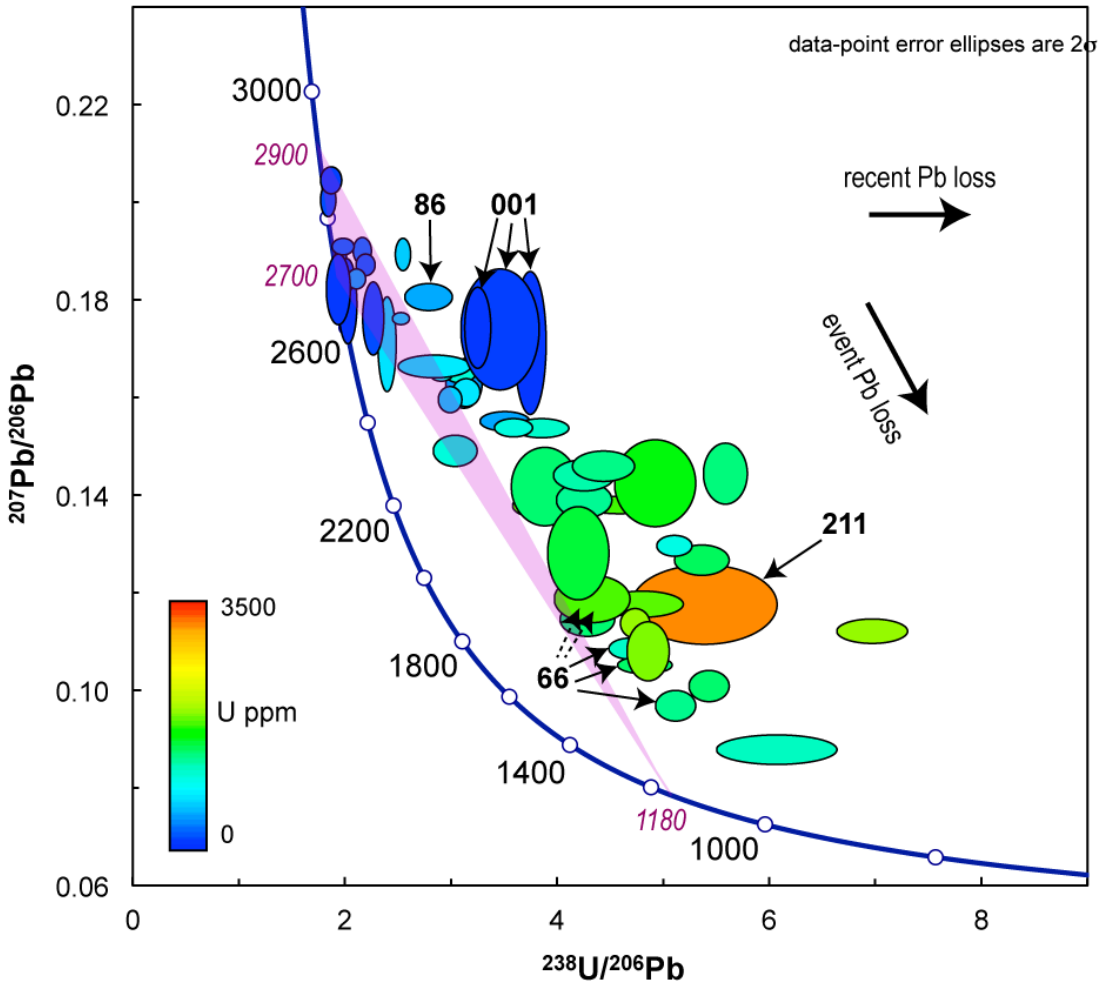

Figure 5.5 A Tera-Wasserburg diagram showing a discordant trend and the concentration of U in ppm. The trend of the data set point to the age of the meteorite event (1180 Ma) (Parnell et al., 2011) and the age of Lewisian Complex basement (2.7 – 2.9 Ga) (Wheeler et al., 2010) where the zircon grains from Stac Fada are believed to derive from. The data also shows recent Pb-loss (or U-gain). The data for the four zircon grains (001, 66, 86 and 211) that were analysed with APT and TEM are shown by the black arrows. Dashed arrows indicate the ellipses of the grain are at the back of other ellipses.

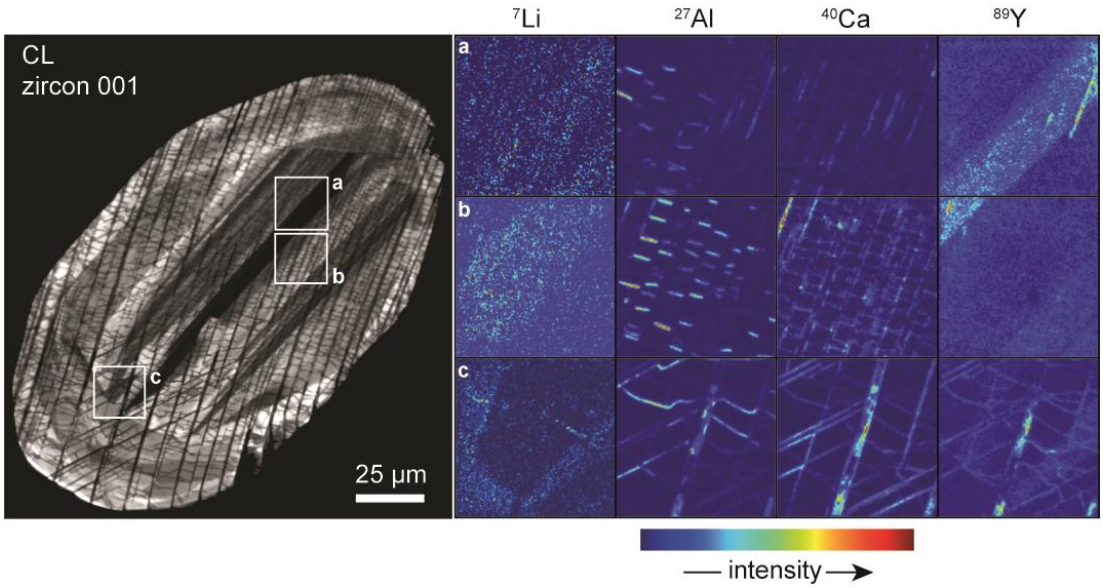

Figure 5.6 CL images and ToF-SIMS isotopic maps of reidite bearing zircon grain 001 showing the distribution of ^{7}Li, ^{27}Al, ^{40}Ca and ^{89}Y in the grain. Notice the enrichment of ^{27}Al, ^{40}Ca and ^{89}Y atoms along the reidite lamellae, and the trace element distribution in the different CL bands.

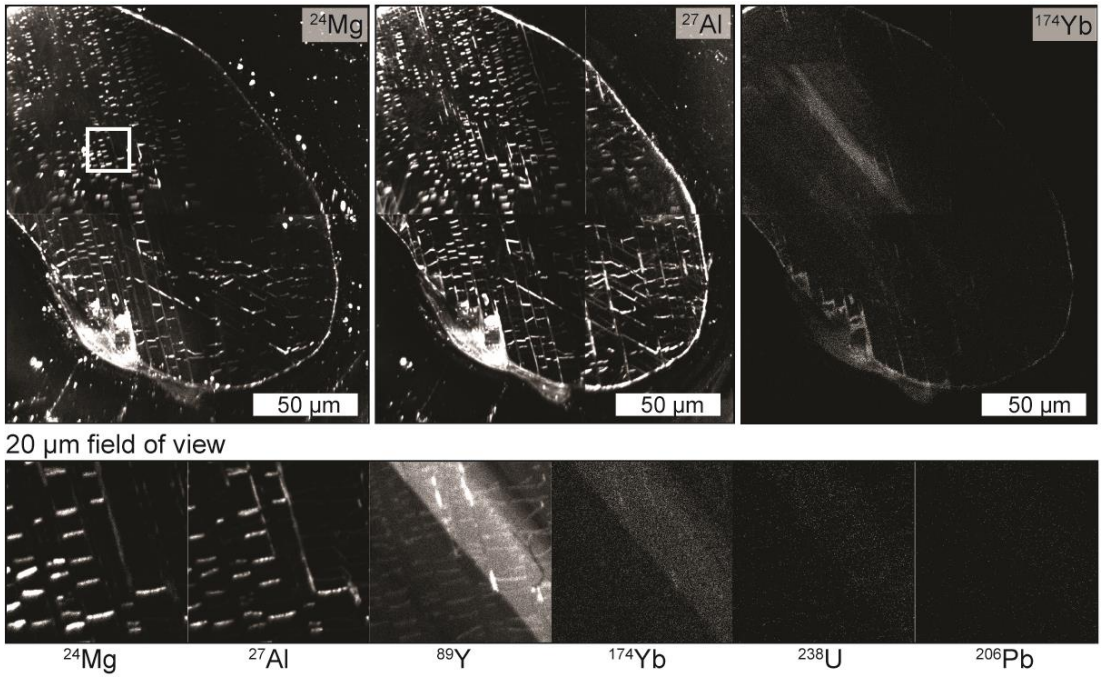

Figure 5.7 NanoSIMS data from reidite bearing zircon 001. The top three images are mosaic images of ^{24}Mg, ^{27}Al and ^{174}Yb. The bottom ones are ^{24}Mg, ^{27}Al, ^{89}Y, ^{174}Yb, ^{238}U and ^{206}Pb detailed images of the grain with a 20 µm field of view from the area inside the white square. Although barely visible, a heterogenous distribution of ^{238}U and ^{206}Pb is present and follows the CL zoning (see Fig. 5.6).

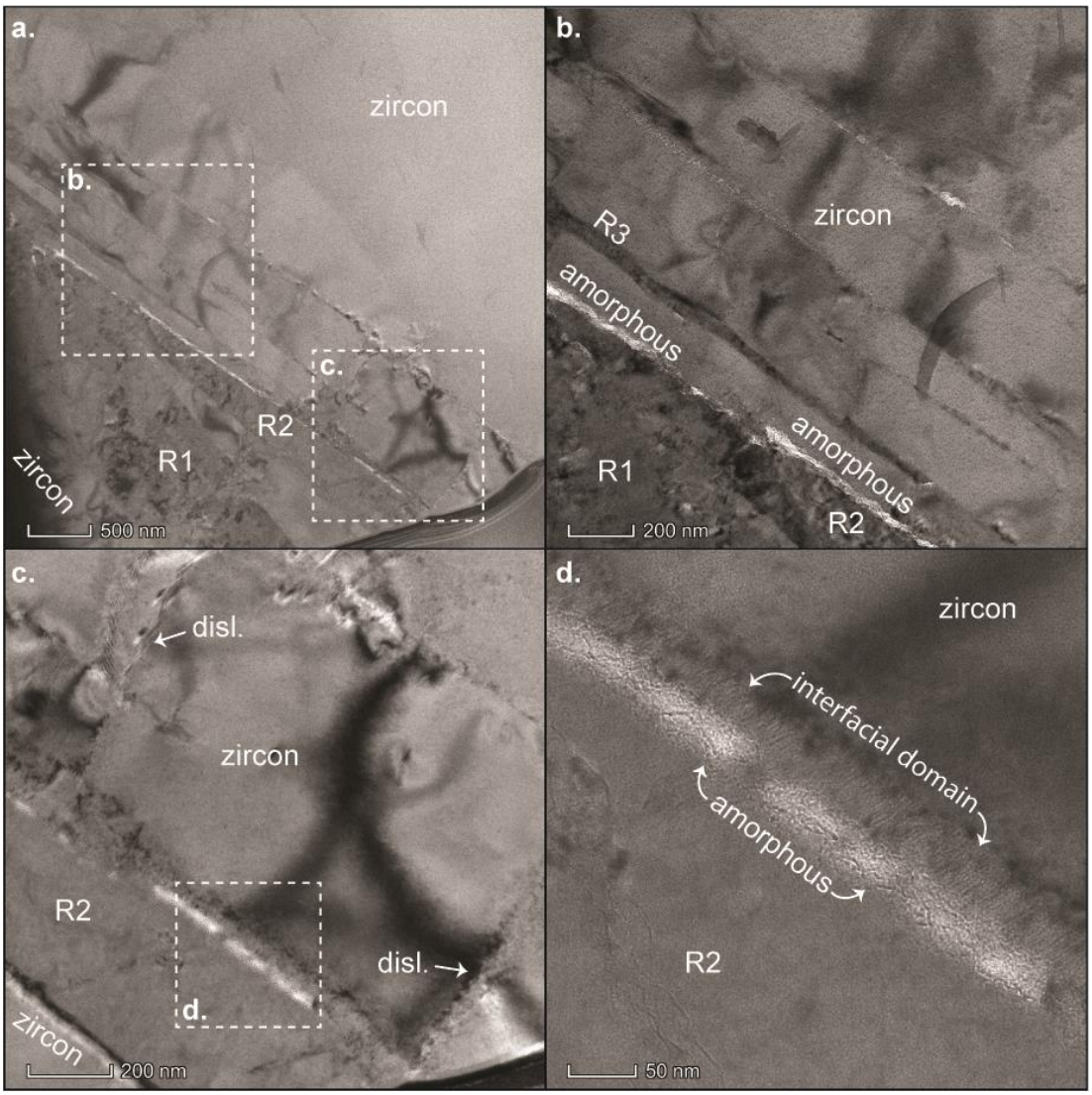

Figure 5.8 **(a)** BF STEM image of TEM foil 1, showing three reidite lamellae (R1 – R3) and the location of the next detailed images. **(b)** BF STEM image of the three reidite lamellae and the amorphous feature next to R2. **(c)** BF STEM image of the lower part of R2 showing dislocations in the zircon grain. Notice the bend of the zircon host is illustrated by the dark curve. **(d)** Detailed BF STEM image of the amorphous feature and the interfacial domain with a quasi-periodic structure between R2 and zircon.

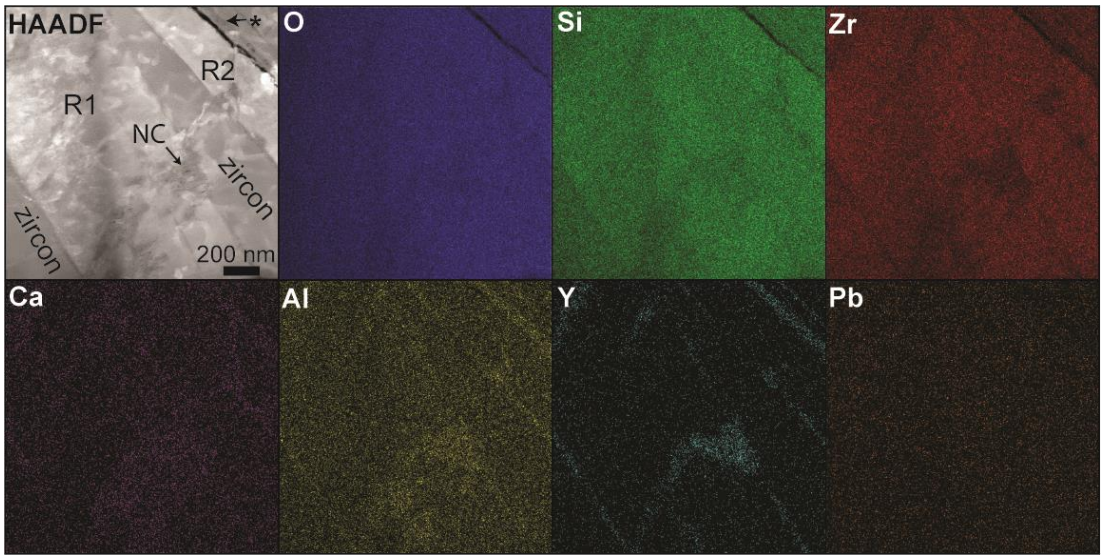

Figure 5.9 HAADF STEM image and TEM EDS maps of TEM foil 1. The HAADF image shows two reidite lamellae (R1 and R2), nanocrystalline (NC) domains, an amorphous feature (*) next to the interfacial domain with a quasi-periodic structure and the zircon host grain. The EDS map of O (blue) shows no difference between the phases but it is missing in the amorphous feature. Si and Zr are absent in the amorphous feature and have a heterogeneous distribution within the reidite lamellae. Ca, Al and Y appear to be enhanced in the nanocrystalline domains and the zircon–reidite interfaces, especially the one with the quasi-periodic structure (right to the amorphous feature). Pb was not identified in the sample and the image represents the background noise.

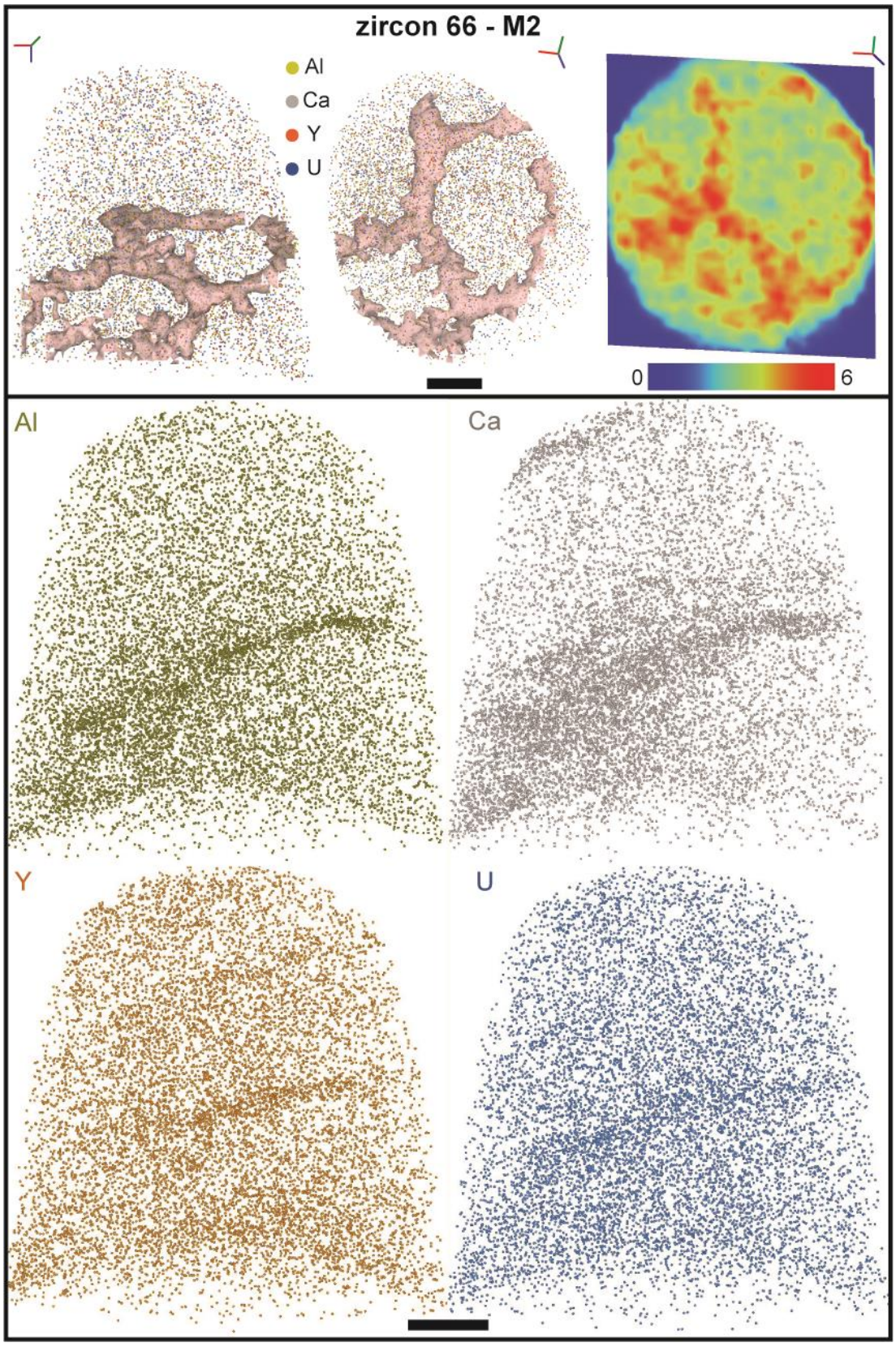

Figure 5.10 Atom probe 3D reconstruction of specimen M2 from zircon 66 with dislocation loops (~50 nm wide). Each sphere in the reconstruction represents a single detected atom (Al = yellow, Ca = grey, Y = orange and U = blue). The two

images at the top left are the same but differ by a rotation with the purpose of providing a better view of the dislocation loops. A concentration isosurface of a 0.5% of Al, Ca, Y and U was created to highlight the microstructures seen in the specimen. The image at the top right is a 2D density plot of Al, Ca, Y and U highlighting the dislocation loops. The four images at the bottom are individual images of each atom showing the enhancement of the atoms in the dislocation loops. The scale bar represents 20 nm.

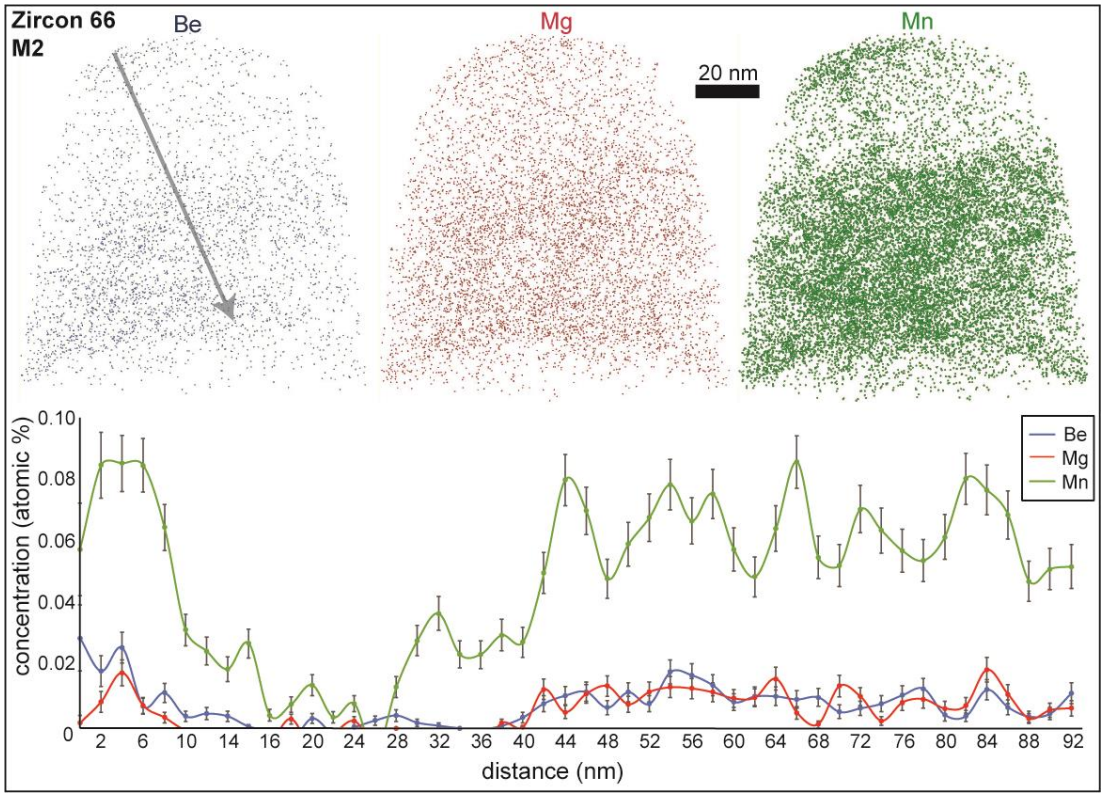

Figure 5.11 Atom probe 3D reconstruction of specimen M2 from zircon 66 showing a heterogeneous distribution of different trace elements. Each sphere in the reconstruction represents a single detected atom (Be = blue, Mg = red, Mn = green). The 1D concentration profile goes from the top left of the specimen to the bottom right (arrow) and it shows a region of low concentration of trace elements surrounded by two regions of a higher concentration. Notice that the Mn concentration from the higher concentration regions is ~8X of the low concentration region.

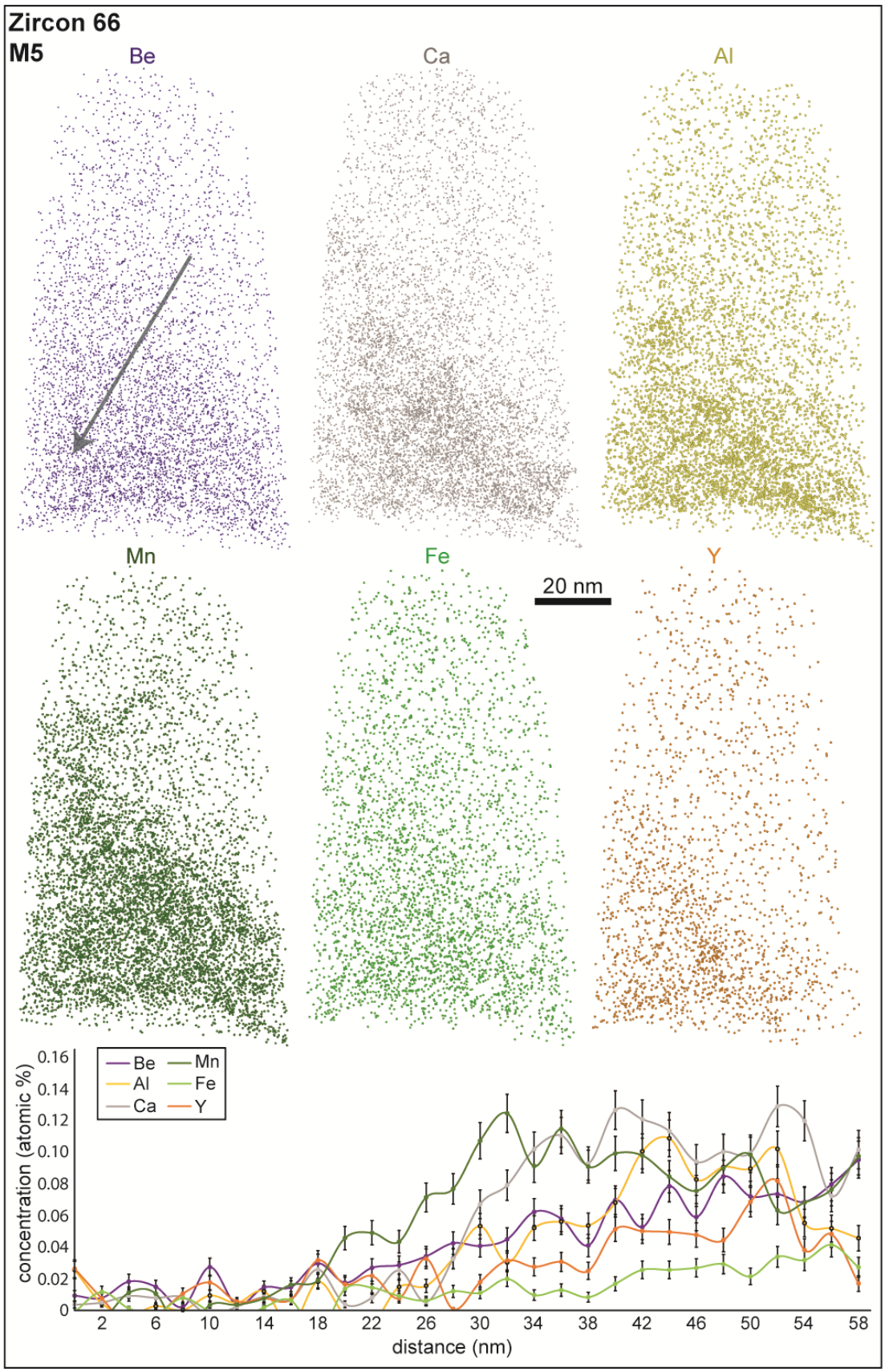

Figure 5.12 Atom probe 3D reconstruction of specimen M5 from zircon 66 showing a heterogeneous distribution of trace elements. The spheres represent a

single detected atom (Be = purple, Ca = grey, Al = yellow, Mn = dark green, Fe = light green and Y = orange). The 1D concentration profile goes from the top of the specimen to the bottom (arrow) showing a region of low concentration of trace elements and another region with a higher concentration of those elements. The difference of Mn concentration between region is ~ 7X.

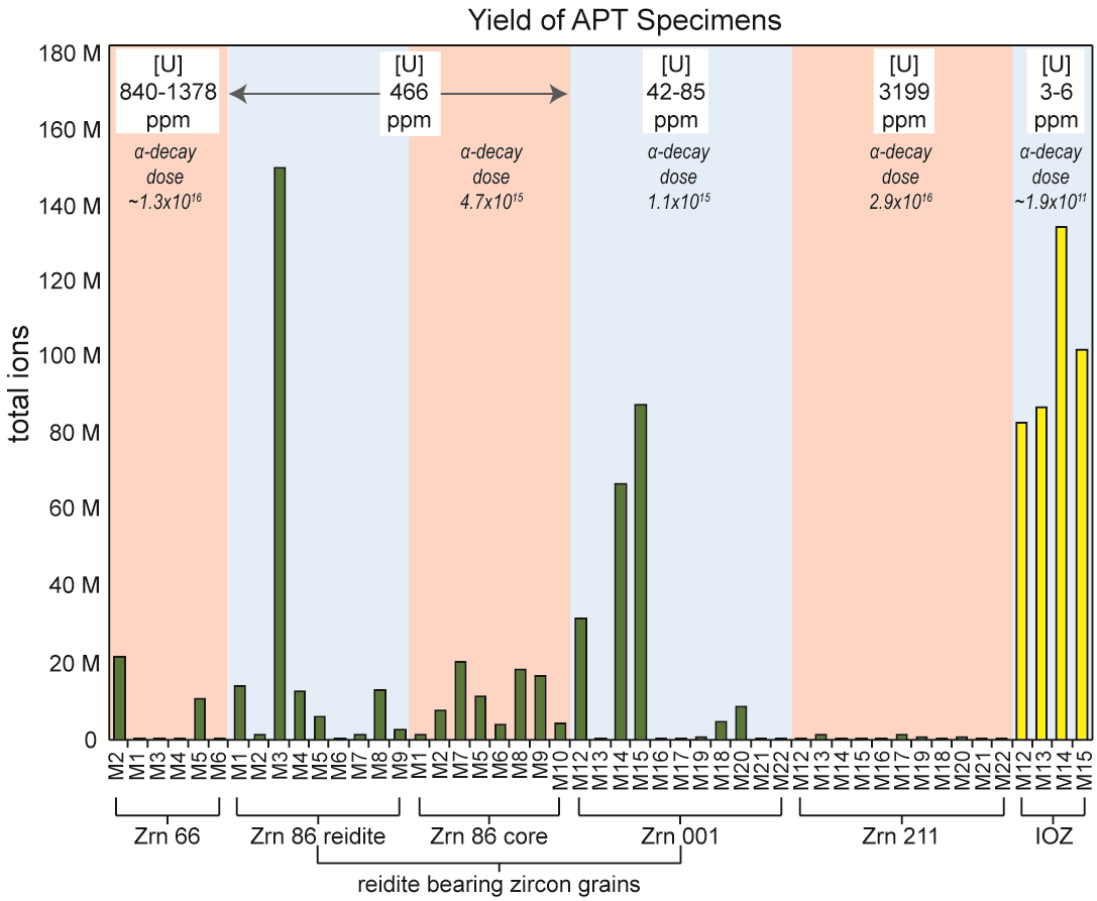

Figure 5.13 Yield of the APT specimens from the four shocked zircon grains (green bars) and the Indian Ocean zircon (IOZ - yellow bars) for comparison. The APT specimens that came from metamict areas are highlighted in red, while the samples from crystalline domains are highlighted in blue. The concentration of U from the SHRIMP analysis and the calculated α-decay dose are included. The SHRIMP data for IOZ was taken from Reddy et al. (2006). The APT analysis on the specimens were conducted with a variety of acquisition parameters (Table 5.2).

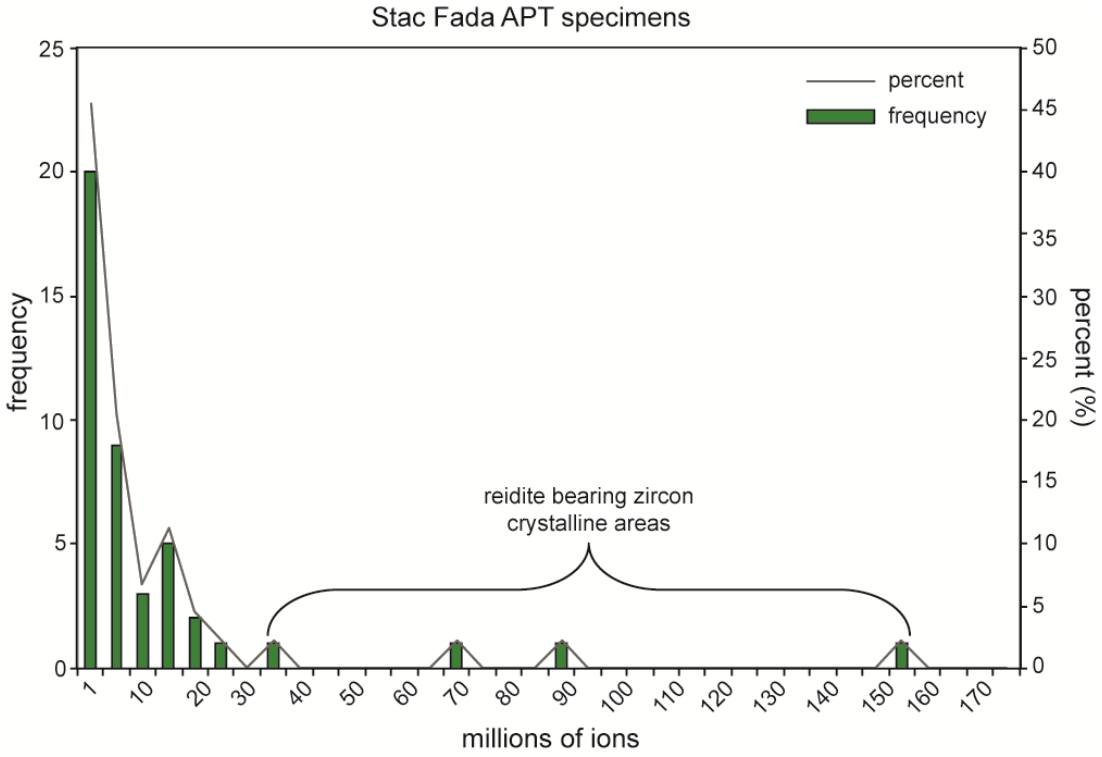

Figure 5.14 Histogram showing the relationship of the frequency and percent of the APT specimens with the number of ions collected. The crystalline areas of the reidite bearing zircon grains yielded the highest number of ions.

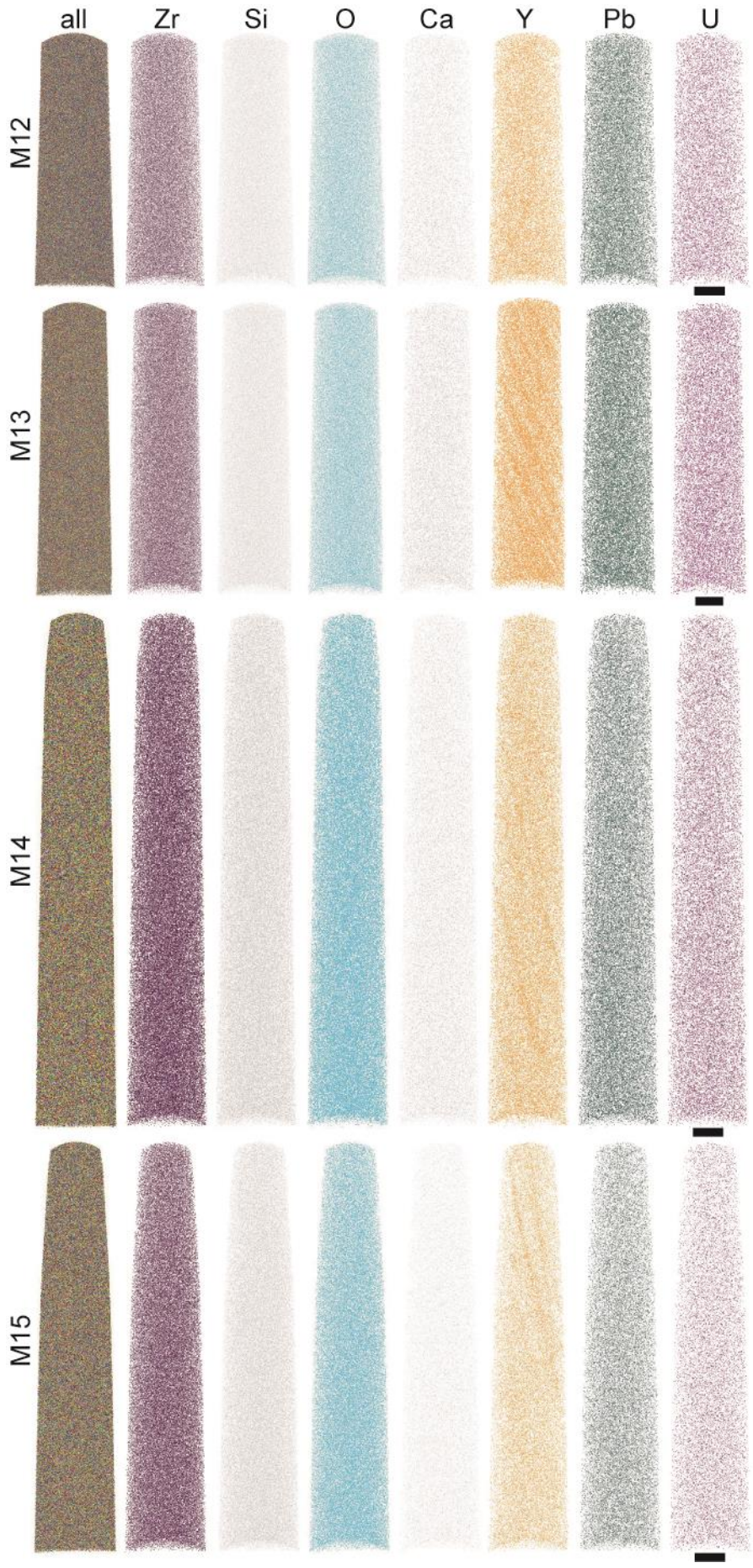
all
Zr
Si
O
Ca
Y
Pb
U
M12
M13
M14
M15

Figure 5.15 Atom probe 3D reconstruction of the specimens from the IOZ. The homogenous distribution of the elements can be seen in Zr, Si, O, Ca, Y, Pb and U. Planes enriched in Y can be seen in specimens M13, M14 and M15. Scale bar represents 40 nm.

Supplementary Material

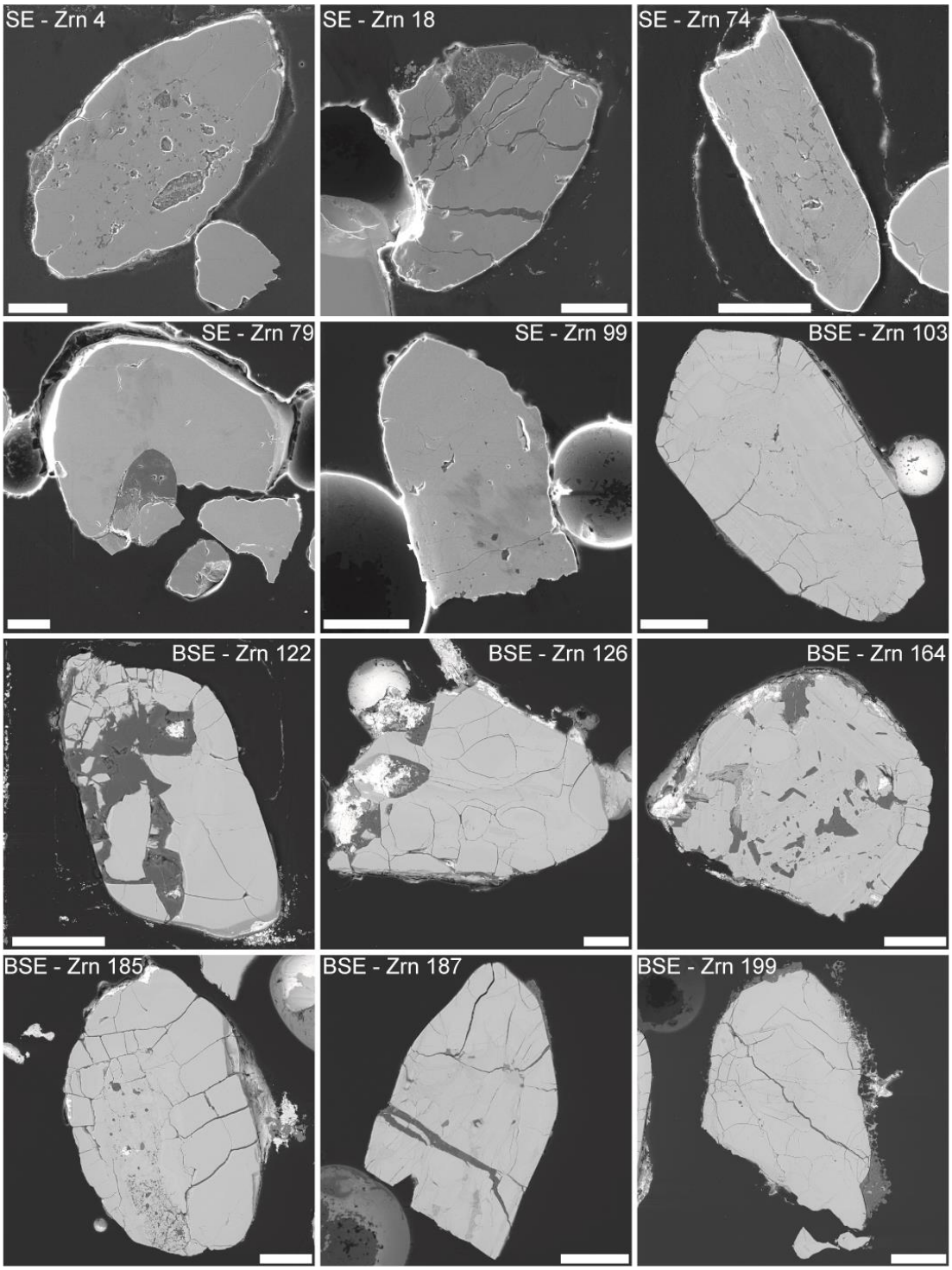

Suppl. Figure 5.1 Examples of SEM images (SE and BSE) of the interior of zircon grains from Stac Fada. Notice the complex internal structures, fractures and subhedral to anhedral form of the grains. Scale bar represents 50 µm.

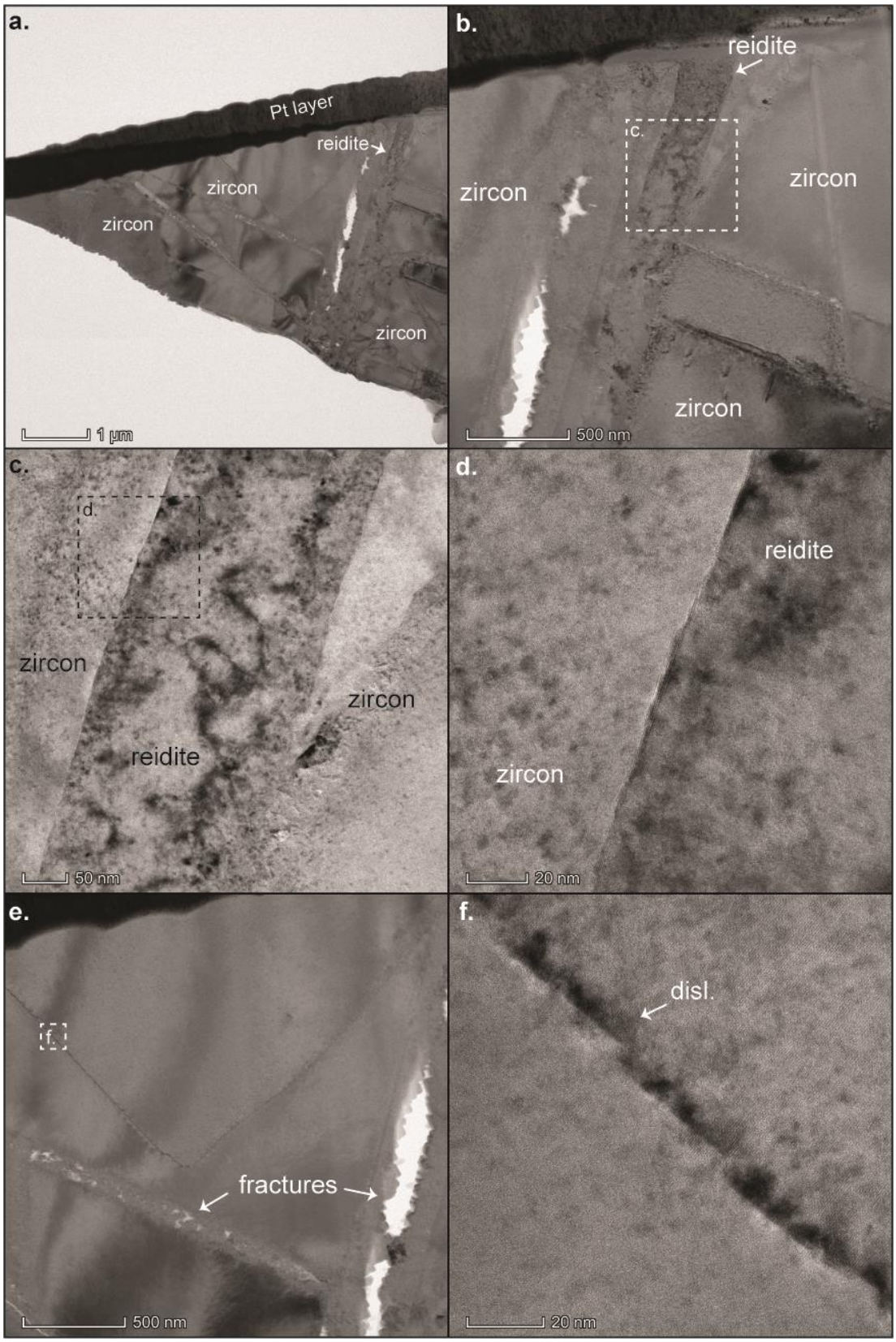

Suppl. Figure 5.2 TEM data of TEM foil 2 of the reidite bearing zircon grain 86. **(a)** BF STEM image of the foil where the protection Pt layer, a reidite lamella and the zircon host grain can be seen. **(b-c)** Detailed BF STEM images of the reidite

lamella. **(d)** Detailed BF STEM of the zircon–reidite interface with no quasi-periodic structure. **(e)** BF STEM image of the fractures in the zircon host grain. Notice parts of the fractures are filled (left one). **(f)** Detailed BF STEM image of the dislocations in the zircon phase.

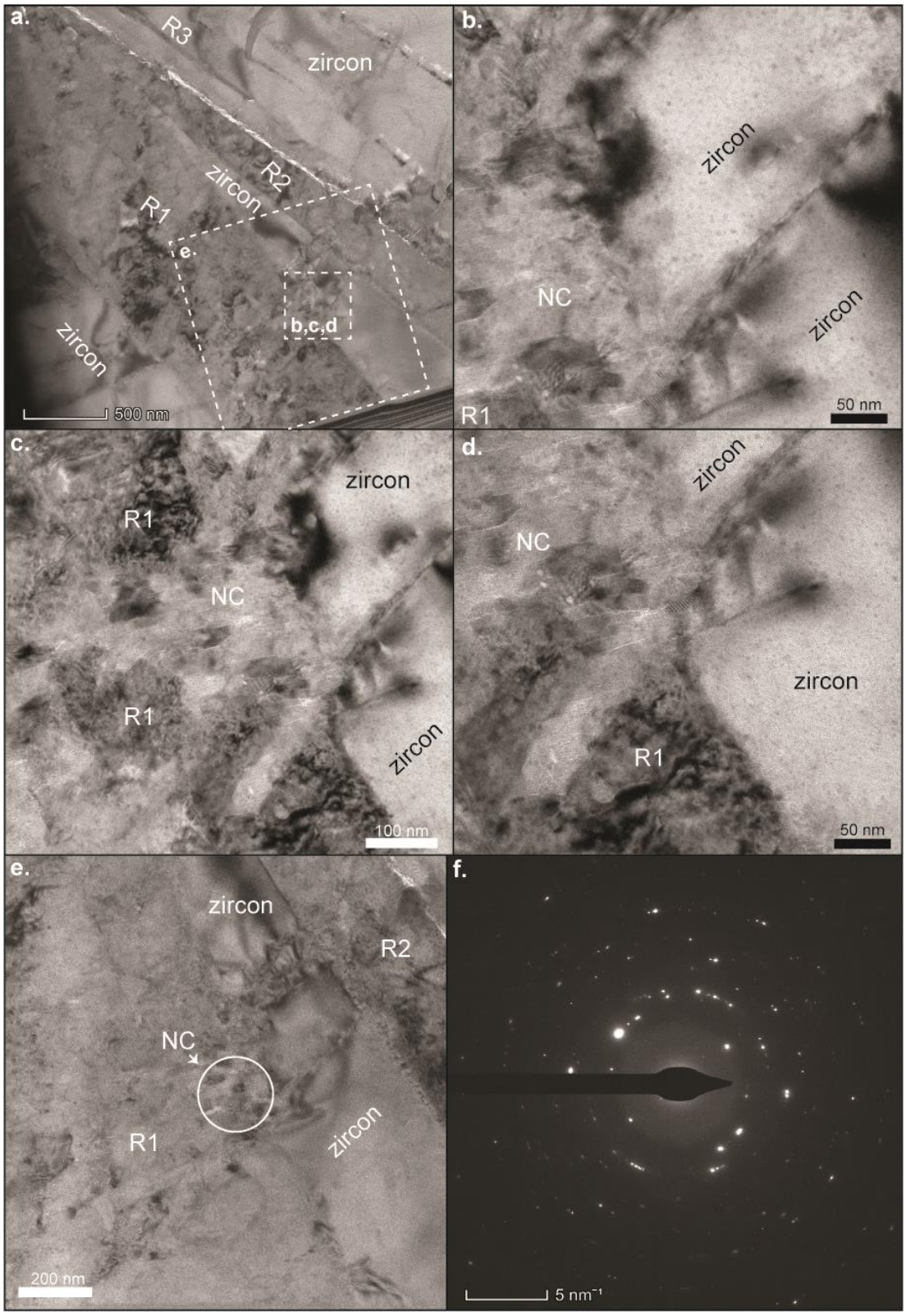

Suppl. Figure 5.3 **(a)** BF STEM image of the TEM foil 1 containing three reidite lamellae (R1–R3) and the approximate location of the following images. **(b-d)** Detailed BF STEM images of the area in the dashed square in image **(a)**. These images focused on the nanocrystalline (NC) domain identified within the reidite

lamellae R1. Notice the complexity of that structure and the effects it has on the zircon host. **(e)** BF STEM image with the location of the diffraction analysis. **(f)** Electron diffraction ring pattern of the nanocrystalline domain.

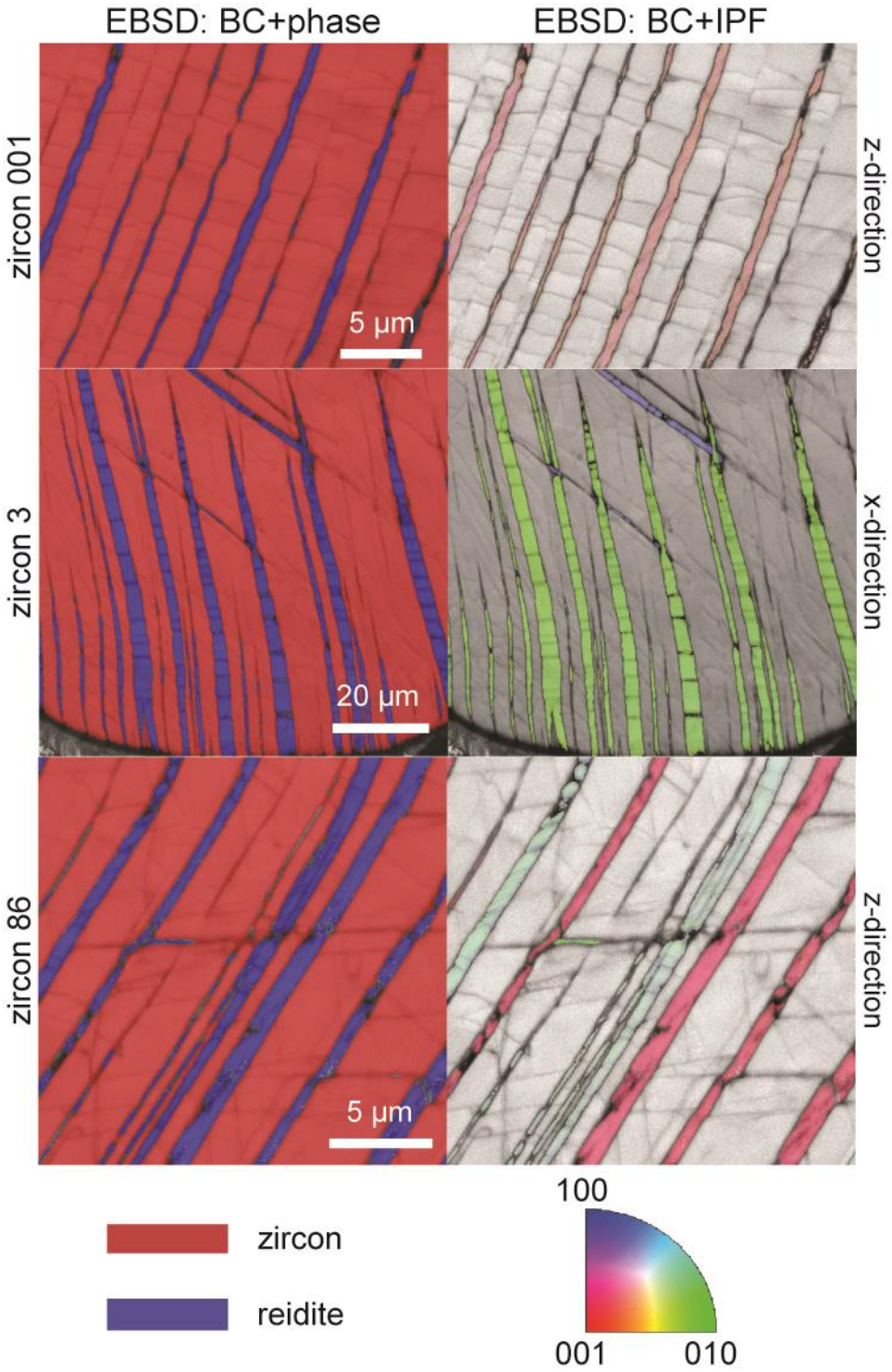

Suppl. Figure 5.4 Detailed EBSD maps of three zircon grains with reidite lamellae (zircon 001, 3 and 86). Band contrast (BC) maps combined with phase and

inverse pole figure (IPF) show the form of the lamellae and the different orientations (different colours in IPF). Colours in the EBSD phase map indicate zircon = red and reidite = blue. Notice that zircon 001 has one orientation of reidite lamellae, zircon 3 has two orientations, and zircon 86 has three different orientations of reidite lamellae.

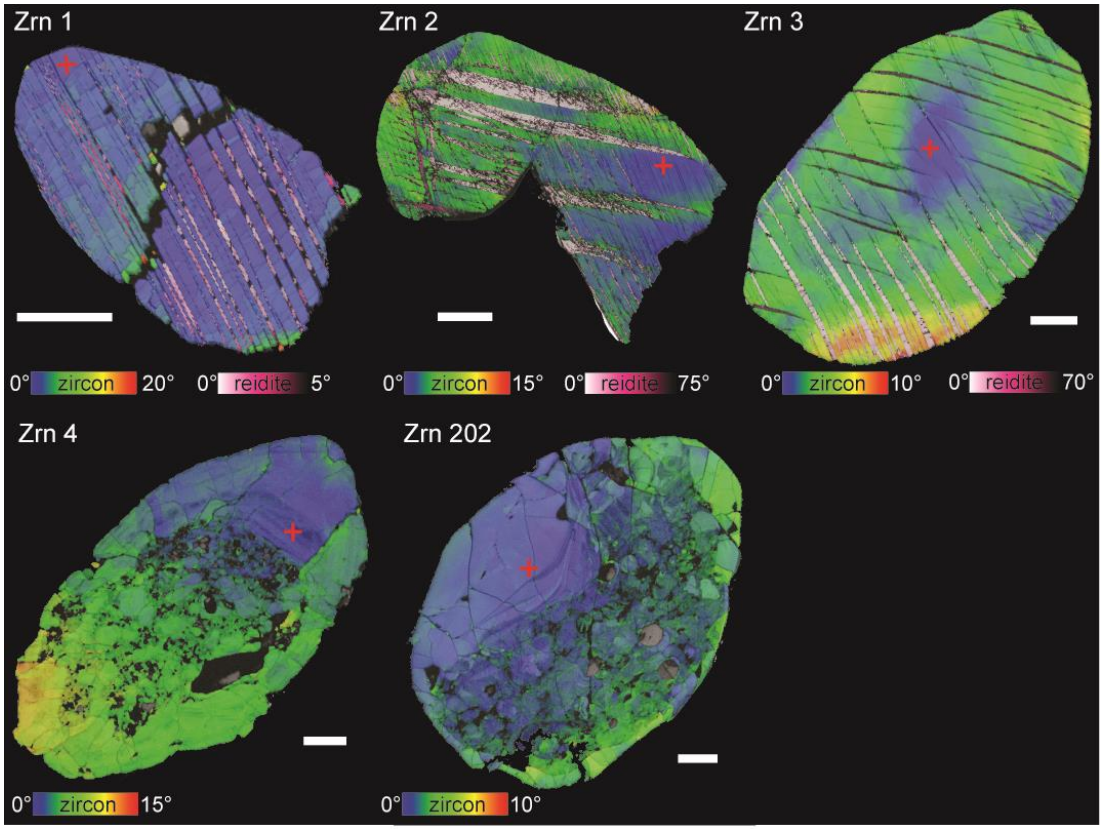

Suppl. Figure 5.5 EBSD maps with the misorientation of zircon grains (rainbow scale) and the misorientation of the reidite lamellae (fuchsia scale). The scale bar represents 25 µm.

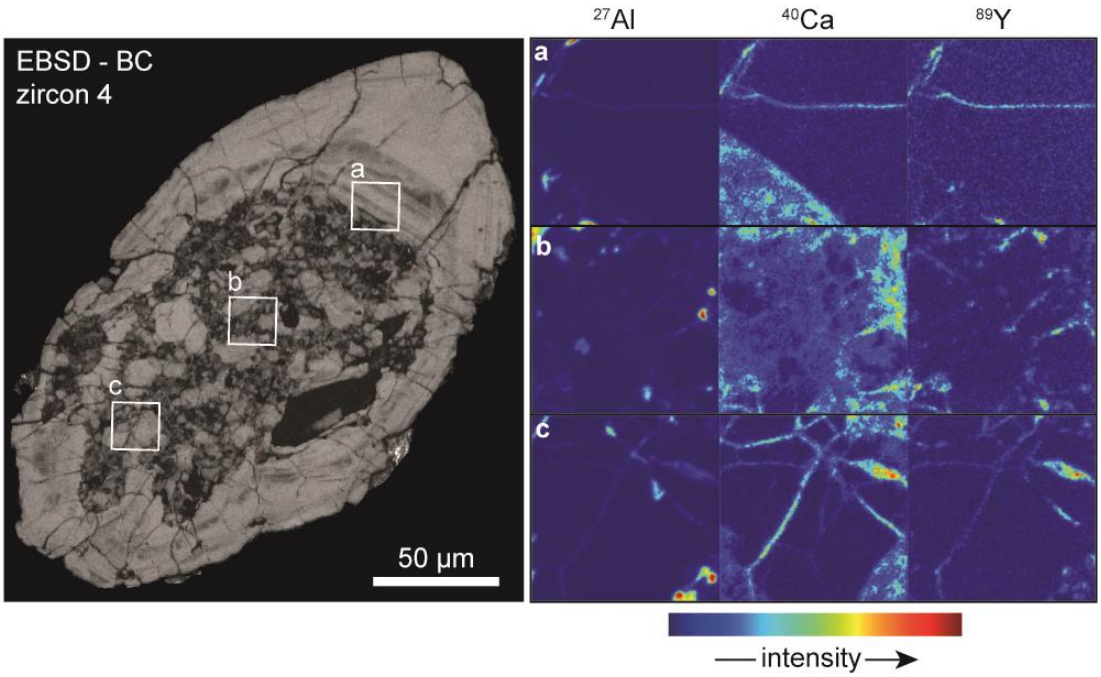

Suppl. Figure 5.6 Band contrast (BC) EBSD map and ToF-SIMS isotopic maps of zircon 4 showing the distribution of ^{27}Al, ^{40}Ca and ^{89}Y in the grain. The trace element enrichment occurs along fractures, zonation and clasts within metamict core.

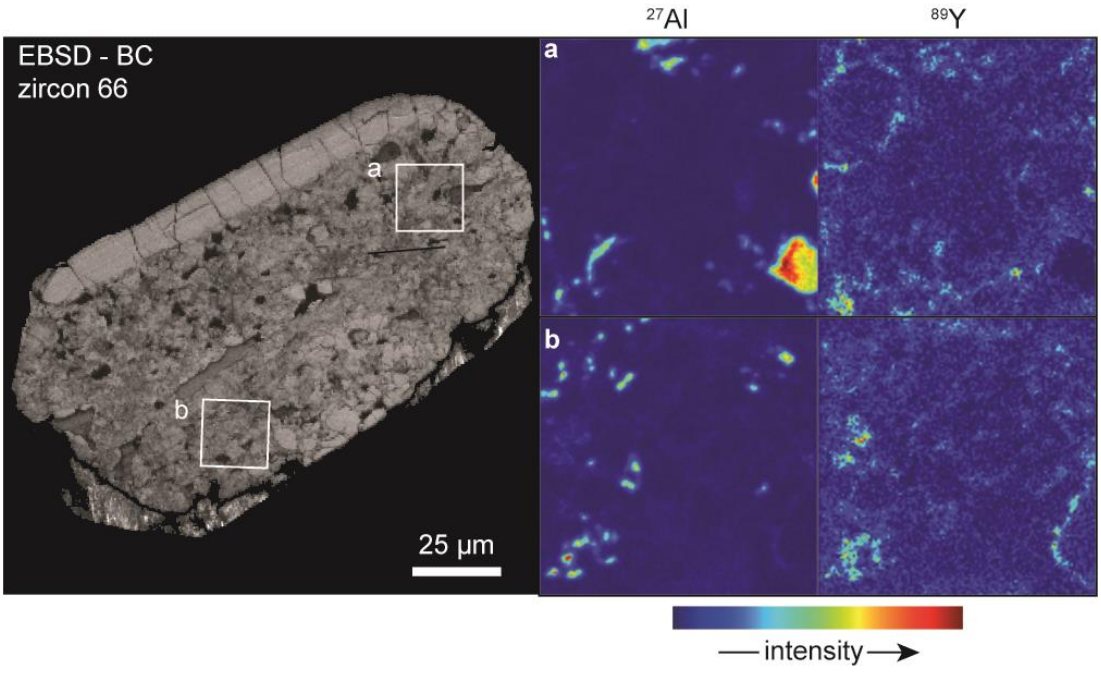

Suppl. Figure 5.7 Band contrast (BC) EBSD map and ToF-SIMS isotopic maps of zircon 66 displaying the distribution of ^{27}Al and ^{89}Y in the complex (metamict) core of the grain.

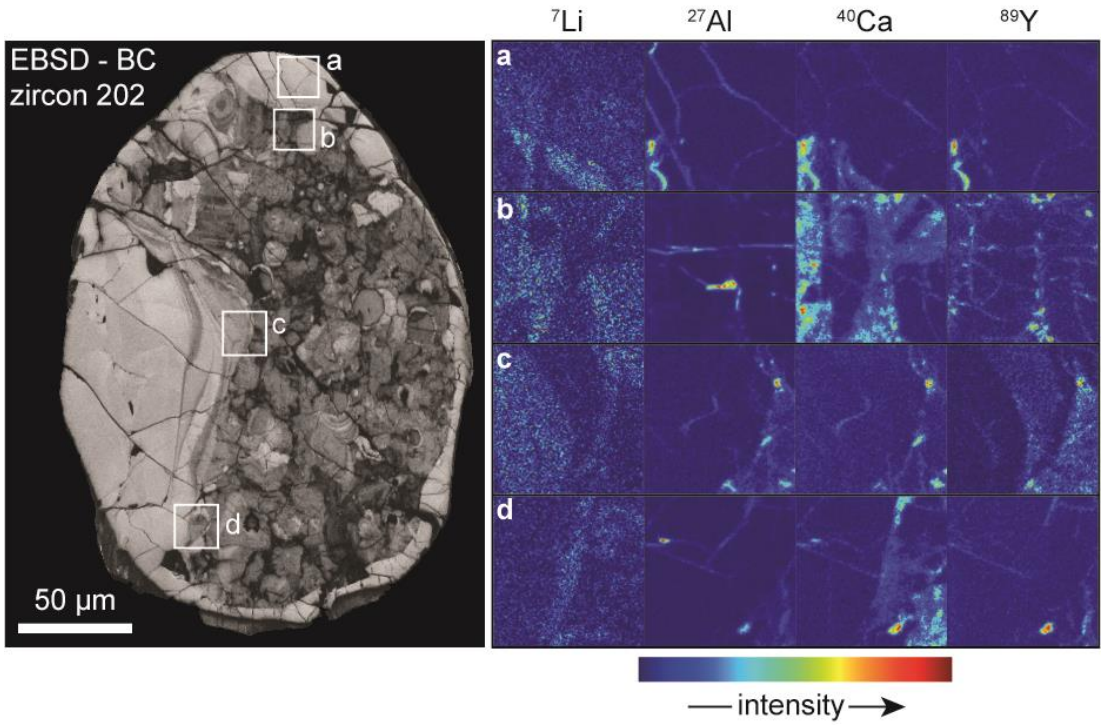

Suppl. Figure 5.8 Band contrast (BC) EBSD map and ToF-SIMS isotopic maps of zircon 202 showing the distribution of ^{7}Li, ^{27}Al, ^{40}Ca and ^{89}Y.

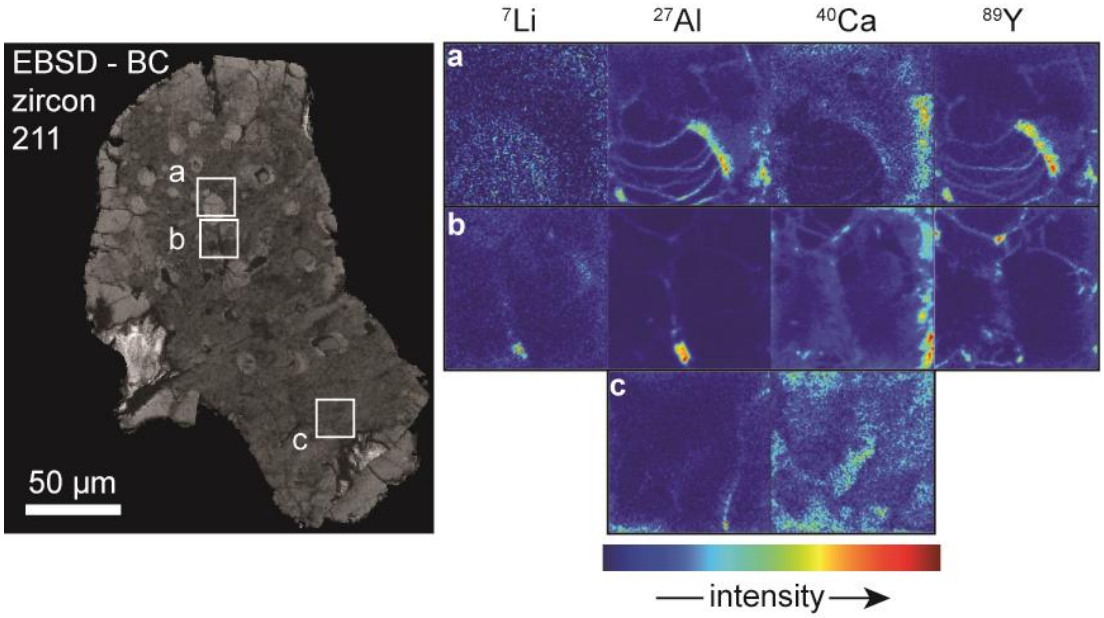

Suppl. Figure 5.9 Band contrast (BC) EBSD map and ToF-SIMS isotopic maps of zircon 211 with the distribution of ^{7}Li, ^{27}Al, ^{40}Ca and ^{89}Y from three areas in the grains. Notice the enhancement through the fractures of the clasts.

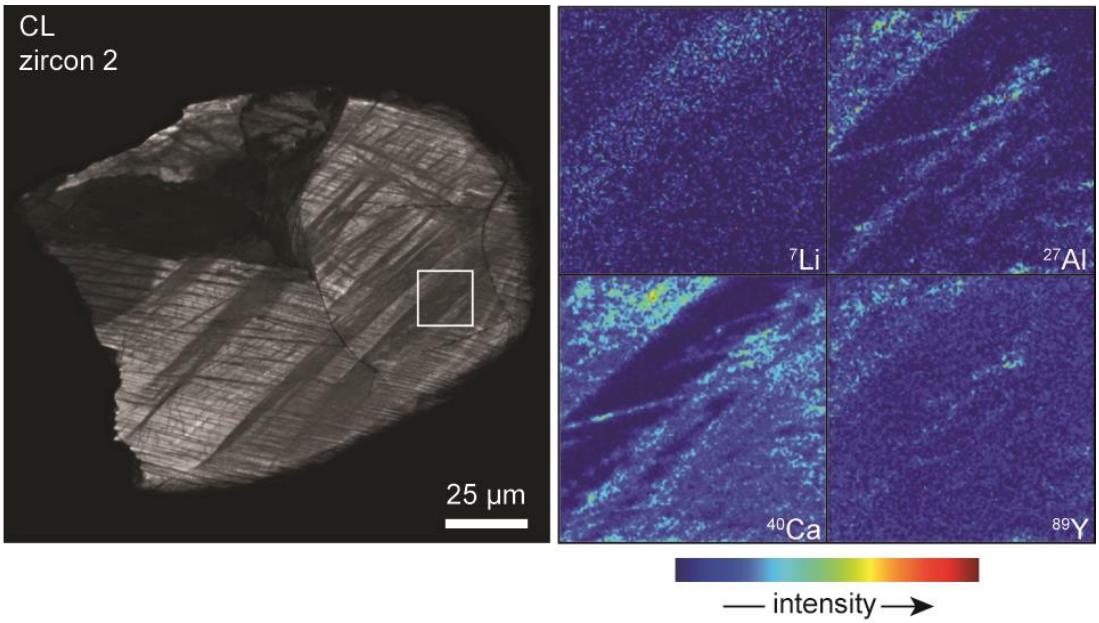

Suppl. Figure 5.10 CL images and ToF-SIMS isotopic maps of reidite bearing zircon 2 showing the distribution of ^{7}Li, ^{27}Al, ^{40}Ca and ^{89}Y in the grain.

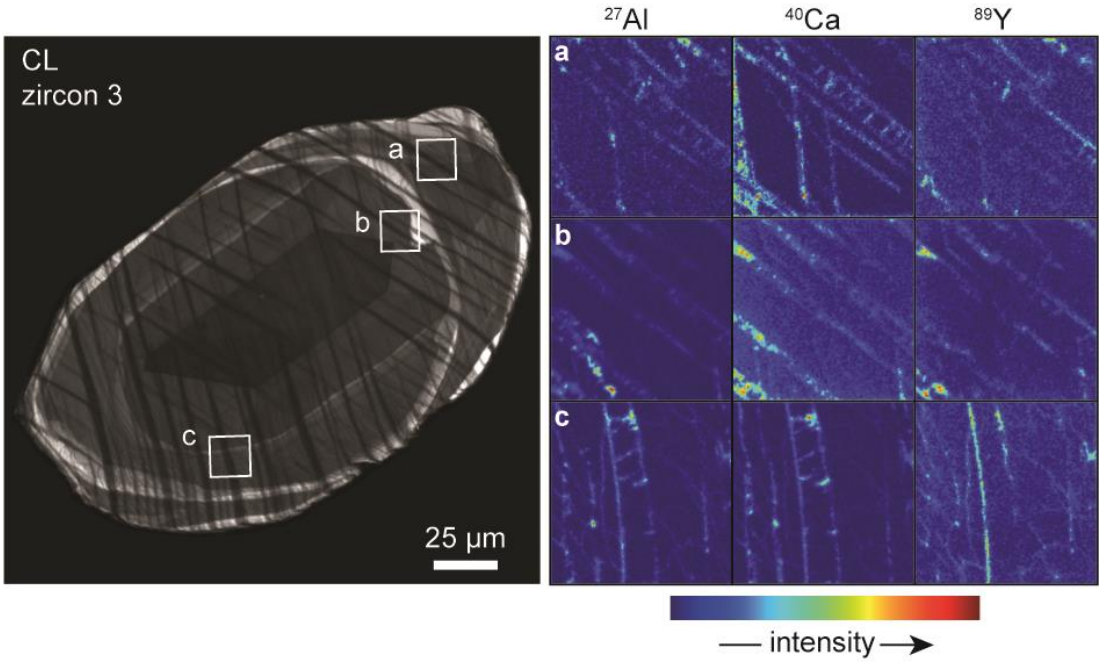

Suppl. Figure 5.11 CL images and ToF-SIMS isotopic maps of reidite bearing zircon 3 showing the distribution of ^{27}Al, ^{40}Ca and ^{89}Y.

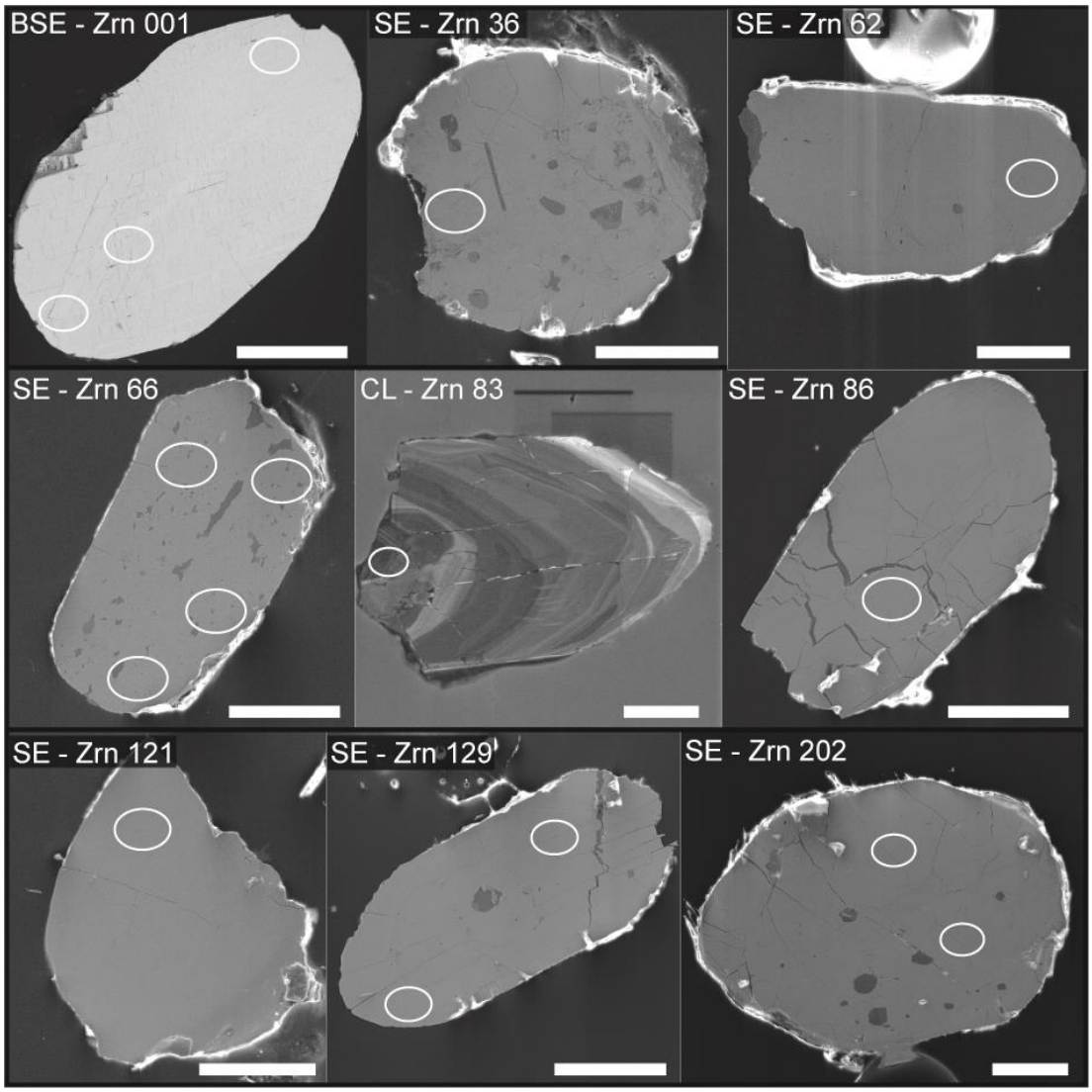

Suppl. Figure 5.12 BSE, SE and CL images of various zircon grains with the location of the SHRIMP spot analyses, including reidite bearing zircon 001 and zircon 86. The scale bars represent 50 µm.

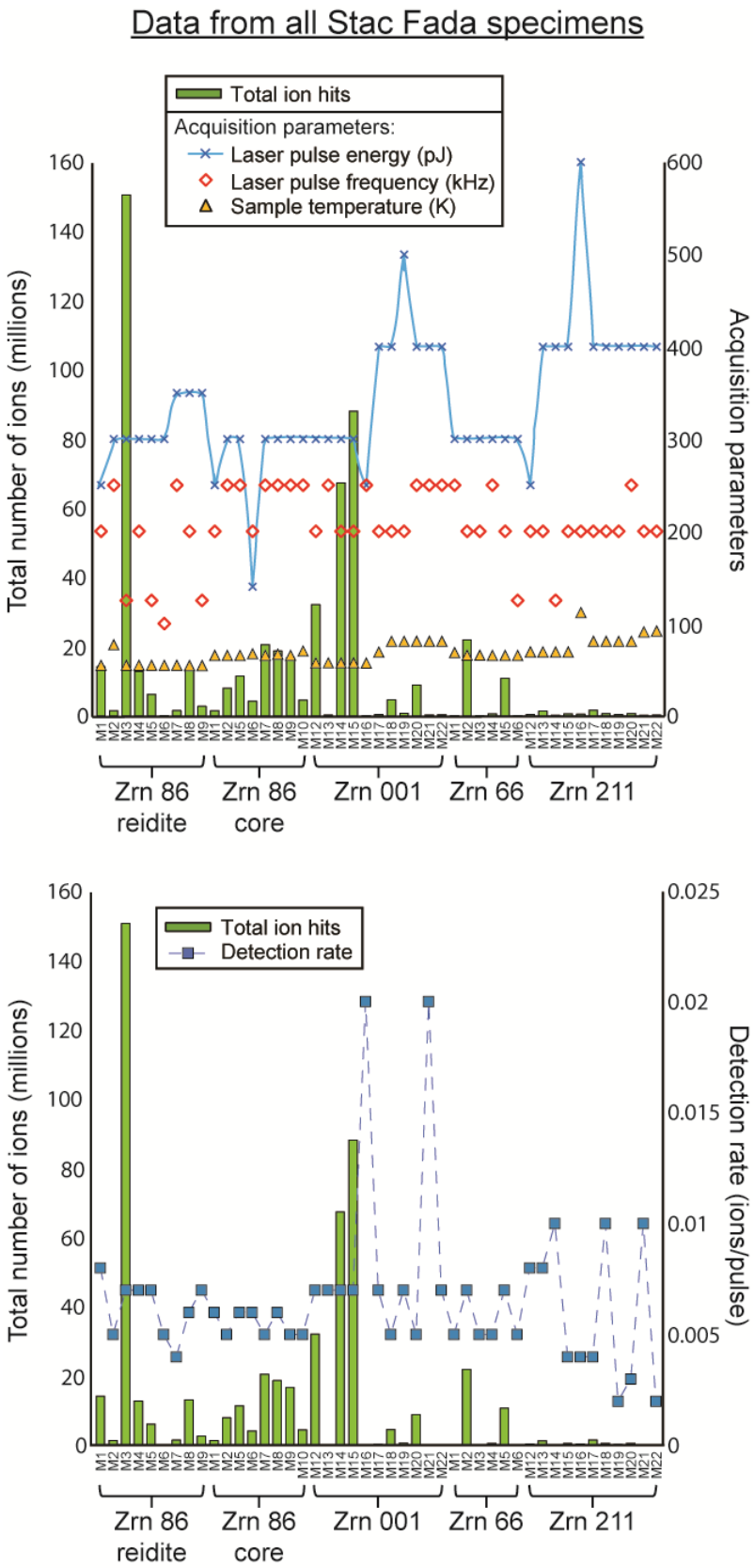

Suppl. Figure 5.13 APT yield of all the Stac Fada specimens with their respective acquisition parameters.

References

Branney, M. J., and Brown, R. J., 2011, Impactoclastic Density Current Emplacement of Terrestrial Meteorite-Impact Ejecta and the Formation of Dust Pellets and Accretionary Lapilli: Evidence from Stac Fada, Scotland: The Journal of Geology, v. 119, no. 3, p. 275-292.

Bursill, L. A., and McLaren, A. C., 1966, Transmission Electron Microscope Study of Natural Radiation Damage in Zircon (ZrSiO4): physica status solidi (b), v. 13, no. 2, p. 331-343.

Cavosie, A. J., Erickson, T. M., and Timms, N. E., 2015, Nanoscale records of ancient shock deformation: Reidite ($ZrSiO_4$) in sandstone at the Ordovician Rock Elm impact crater: Geology, v. 43, no. 4, p. 315-318.

Cherniak, D. J., 2010, Diffusion in accessory minerals: zircon, titanite, apatite, monazite and xenotime, *in* Zhang, Y., and Cherniak, D. J., eds., Diffusion in Minerals and Melts, Volume 72: Virginia, The Mineralogical Society of America, p. 827-869.

Cherniak, D. J., and Watson, E. B., 2003, Diffusion in Zircon, *in* Hanchar, J. M., and Hoskin, P. W. O., eds., Zircon, Volume 53: Washington, DC, Mineralogical Society of America, p. 113-143.

Erickson, T. M., Cavosie, A. J., Pearce, M. A., Timms, N. E., and Reddy, S. M., 2016, Empirical constraints on shock features in monazite using shocked zircon inclusions: Geology, v. 44, p. 635-638.

Finch, R. J., and Hanchar, J. M., 2003, Structure and chemistry of zircon and zircon-group minerals, *in* Hanchar, J. M., and Hoskin, P. W. O., eds., Zircon, Volume 53: Washington, DC, The Mineralogical Society of America, p. 1-25.

Fougerouse, D., Reddy, S. M., Kirkland, C. L., Saxey, D. W., Rickard, W. D., and Hough, R. M., 2019, Time-resolved, defect-hosted, trace element mobility in deformed Witwatersrand pyrite: Geoscience Frontiers, p. 55-63.

Geisler, T., Pidgeon, R. T., van Bronswijk, W., and Kurtz, R., 2002, Transport of uranium, thorium, and lead in metamict zircon under low-temperature hydrothermal conditions: Chemical Geology, v. 191, no. 1–3, p. 141-154.

Glass, B. P., Liu, S., and Leavens, P. B., 2002, Reidite: An impact-produced high-pressure polymorph of zircon found in marine sediments: American Mineralogist, v. 87, no. 4, p. 562-565.

Harley, S. L., and Kelly, N. M., 2007, Zircon Tiny but Timely: Elements, v. 3, no. 1, p. 13-18.

La Fontaine, A., Piazolo, S., Trimby, P., Yang, L., and Cairney, J. M., 2017, Laser-Assisted Atom Probe Tomography of Deformed Minerals: A Zircon Case Study: Microscopy and Microanalysis, p. 1-10.

Langenhorst, F., and Deutsch, A., 2012, Shock metamorphism of minerals: Elements, no. 1, p. 31-36.

Leroux, H., Reimold, W. U., Koeberl, C., Hornemann, U., and Doukhan, J. C., 1999, Experimental shock deformation in zircon: a transmission electron microscopic study: Earth and Planetary Science Letters, v. 169, no. 3, p. 291-301.

Lyon, I. C., Kusiak, M. A., Wirth, R., Whitehouse, M. J., Dunkley, D. J., Wilde, S. A., Schaumlöffel, D., Malherbe, J., and Moore, K. L., 2019, Pb nanospheres in ancient zircon yield model ages for zircon formation and Pb mobilization: Scientific reports, v. 9, no. 1, p. 13702.

Martin, L. A. J., Duchêne, S., Deloule, E., and Vanderhaeghe, O., 2008, Mobility of trace elements and oxygen in zircon during metamorphism: Consequences for geochemical tracing: Earth and Planetary Science Letters, v. 267, no. 1–2, p. 161-174.

Melosh, H. J., 1989, Impact Cratering: A Geologic Process: New York, USA, Oxford University Press, p. 245.

Montalvo, S. D., Reddy, S. M., Saxey, D. W., Rickard, W. D. A., Fougerouse, D., Quadir, Z., and Johnson, T. E., 2019, Nanoscale constraints on the shock-induced transformation of zircon to reidite: Chemical Geology, v. 507, p. 85-95.

Murakami, T., Chakoumakos, B. C., Ewing, R. C., Lumpkin, G. R., and Weber, W. J., 1991, Alpha-decay event damage in zircon: American Mineralogist, v. 76, p. 1510-1532.

Parnell, J., Mark, D., Fallick, A. E., Boyce, A., and Thackrey, S., 2011, The age of the Mesoproterozoic Stoer Group sedimentary and impact deposits, NW Scotland: Journal of the Geological Society, v. 168, no. 2, p. 349-358.

Peterman, E. M., Reddy, S. M., Saxey, D. W., Fougerouse, D., Snoeyenbos, D. R., and Rickard, W. D. A., 2019, Nanoscale processes of trace element mobility in metamorphosed zircon: Contributions to Mineralogy and Petrology, v. 174, no. 11, p. 92.

Peterman, E. M., Reddy, S. M., Saxey, D. W., Snoeyenbos, D. R., Rickard, W. D. A., Fougerouse, D., and Kylander-Clark, A. R. C., 2016, Nanogeochronology of discordant zircon measured by atom probe microscopy of Pb-enriched dislocation loops: Science Advances, v. 2, p. 9.

Piazolo, S., Austrheim, H., and Whitehouse, M., 2012, Brittle-ductile microfabrics in naturally deformed zircon: Deformation mechanisms and consequences for U-Pb dating: American Mineralogist, v. 97, no. 10, p. 1544-1563.

Piazolo, S., La Fontaine, A., Trimby, P., Harley, S., Yang, L., Armstrong, R., and Cairney, J. M., 2016, Deformation-induced trace element redistribution in zircon revealed using atom probe tomography: Nature Communications, p. 7.

Reddy, S. M., Johnson, T. E., Fischer, S., Rickard, W. D. A., and Taylor, R. J. M., 2015, Precambrian reidite discovered in shocked zircon from the Stac Fada impactite, Scotland: Geology, v. 43, no. 10, p. 899-902.

Reddy, S. M., Saxey, D. W., Rickard, W. D. A., Fougerouse, D., Montalvo, S. D., Verberne, R., and van Riessen, A., 2020, Atom probe tomography: development and application to the geosciences: Geostandards and Geoanalytical Research, v. 44, no. 1, p. 5-50.

Reddy, S. M., Timms, N. E., Pantleon, W., and Trimby, P., 2007, Quantitative characterization of plastic deformation of zircon and geological implications: Contributions to Mineralogy and Petrology, v. 153, no. 6, p. 625-645.

Reddy, S. M., Timms, N. E., Trimby, P., Kinny, P. D., Buchan, C., and Blake, K., 2006, Crystal-plastic deformation of zircon: A defect in the assumption of chemical robustness: Geology, v. 34, no. 4, p. 257-260.

Reddy, S. M., van Riessen, A., Saxey, D. W., Johnson, T. E., Rickard, W. D. A., Fougerouse, D., Fischer, S., Prosa, T. J., Rice, K. P., Reinhard, D. A., Chen, Y., and Olson, D., 2016, Mechanisms of deformation-induced trace element migration in zircon resolved by atom probe and correlative microscopy: Geochimica et Cosmochimica Acta, v. 195, p. 158-170.

Reimold, W. U., and Gibson, R. L., 2009, Meteorite Impact! The Danger from Space and South Africa's Mega-Impact The Vredefort Structure, Berlin, Heidelberg, Springer.
Rubatto, D., 2017, Zircon: The Metamorphic Mineral: Reviews in Mineralogy and Geochemistry, v. 83, no. 1, p. 261-295.
Sanders, I. S., and Johnston, J. D., 1989, The Torridonian Stac Fada Member: an extrusion of fluidised peperite?: Transactions of the Royal Society of Edinburgh: Earth Sciences, v. 80, no. 1, p. 1-4.
Simms, M. J., 2015, The Stac Fada impact ejecta deposit and the Lairg Gravity Low: evidence for a buried Precambrian impact crater in Scotland?: Proceedings of the Geologists' Association, v. 126, no. 6, p. 742-761.
Stewart, A. D., 2002, The Later Proterozoic Torridonian Rocks of Scotland: Their Sedimentology, Geochemistry and Origin, Geological society memoirs: UK, Geological Society of London, p. 130.
Timms, N. E., Erickson, T. M., Zanetti, M. R., Pearce, M. A., Cayron, C., Cavosie, A. J., Reddy, S. M., Wittmann, A., and Carpenter, P. K., 2017, Cubic zirconia in >2370 °C impact melt records Earth's hottest crust: Earth and Planetary Science Letters, v. 477, p. 52-58.
Timms, N. E., Kinny, P. D., and Reddy, S. M., 2006, Enhanced diffusion of Uranium and Thorium linked to crystal plasticity in zircon: Geochemical Transactions, v. 7, no. 1, p. 10.
Timms, N. E., and Reddy, S. M., 2009, Response of cathodoluminescence to crystal-plastic deformation in zircon: Chemical Geology, v. 261, no. 1–2, p. 12-24.
Valley, J. W., Cavosie, A. J., Ushikubo, T., Reinhard, D. A., Lawrence, D. F., Larson, D. J., Clifton, P. H., Kelly, T. F., Wilde, S. A., Moser, D. E., and Spicuzza, M. J., 2014, Hadean age for a post-magma-ocean zircon confirmed by atom-probe tomography: Nature Geoscience, v. 7, no. 3, p. 219-223.
Wheeler, J., Park, R. G., Rollinson, H. R., and Beach, A., 2010, The Lewisian Complex: insights into deep crustal evolution: Geological Society, London, Special Publications, v. 335, no. 1, p. 51-79.
White, L. F., Darling, J. R., Moser, D. E., Reinhard, D. A., Prosa, T. J., Bullen, D., Olson, D., Larson, D. J., Lawrence, D., and Martin, I., 2017, Atomic-scale age resolution of planetary events: Nature Communications, v. 8, p. 15597.
White, L. F., Moser, D. E., Tait, K. T., Langelier, B., Barker, I., and Darling, J. R., 2019, Crystallization and impact history of a meteoritic sample of early lunar crust (NWA 3163) refined by atom probe geochronology: Geoscience Frontiers, v. 10, no. 5, p. 1841-1848.
Wittmann, A., Kenkmann, T., Schmitt, R. T., and Stöffler, D., 2006, Shock-metamorphosed zircon in terrestrial impact craters: Meteoritics & Planetary Science, v. 41, no. 3, p. 433-454.
Yang, W., Lin, Y.-T., Zhang, J.-C., Hao, J.-L., Shen, W.-J., and Hu, S., 2012, Precise micrometre-sized Pb-Pb and U-Pb dating with NanoSIMS: Journal of Analytical Atomic Spectrometry, v. 27, no. 3, p. 479-487.

Chapter 6 CONCLUSION AND FUTURE RECOMMENDATIONS

The primary goal of this project was to develop the use of APT in geochemistry and geochronological studies for complex zircon grains. This was achieved by analysing microscale grains that were previously difficult to study (chapter 2), complex altered zones in a zircon grain (chapter 3) and shocked deformation features of a few microns in a zircon grain (chapters 4 and 5). This project has already produced one published manuscript (Montalvo et al., 2019) with two more (chapters 2 and 3) nearing submission. These individual manuscripts will increase the number of published works on zircon grains using APT. What is more, these manuscripts will be some of the few works conducted on complex zircon grains using APT (e.g. Peterman et al., 2019).

Distribution of trace elements in complex zircon grains

This project has proved the capability of APT to provide nanoscale geochemical data of complex zircon grains. The distribution of trace elements was examined in all the individual case studies with different goals in mind.

Micrometre size grains

Micrometre scale zircon grains from the Bunburra Rockhole meteorite (chapter 2) had not been studied previously due to their size (< 15 µm). Targeting populations of zircon grains of the sample with APT, allowed the geochemical data of the grains to be extracted. The trace element composition of the zircon grains was used to verify the classification of the meteorite and understand more about the formation and evolutional history of the parent body. This study has established that APT can resolve the chemistry of micrometre scale zircon grains. This study highlights the broader applications of APT to other minerals that have not been analysed due to their size.

Complex textures within a grain

In the zircon from the Lalla Rookh Sandstone (chapter 3), the nanoscale composition of the various textures of the grain identified different concentrations of trace elements, allowing an understanding of the different processes that affected the grain. The combination of micro and nanoscale analyses provided the necessary

information to extract and reconstruct the evolutional history of this detrital zircon grain.

The inclusions of uranium and fluid alteration elements observed in the nanoscale analysis, are associated to the defects derived from the metamictisation process. Radiogenic Pb in the grain migrated and segregated during a metamorphic event, creating nanoscale clusters enriched in Pb. The mechanism responsible for Pb clustering was found to be different than the ones previously known, suggesting another unknown mechanism. This study demonstrates the application of APT in obtaining the chemical information of complex features in a zircon grain, and how the APT data can be integrated with other techniques to understand the evolutional history of the grain.

Structures in shocked zircon grains: Insights into phase transformation

The distribution of trace elements in a suit of zircon grains altered by shock metamorphism varied (chapters 4 and 5). Heterogeneous distributions of trace elements were identified on highly radiation damaged zircon grains that is attributed to element diffusion through metamict areas. Nanostructures (dislocation loops, low-angle boundaries and interfaces) enriched in trace elements were detected from grains containing reidite lamellae and from metamict grains. These structures were formed during or immediately after the hypervelocity impact event. The dislocation loops enriched in trace elements, including uranium, formed by the annealing of the metamict areas. This study has shown the effects shock metamorphism has on the distribution of trace elements in shocked zircon grains. In addition, the identification of these nanoscale structures led to the understanding of the formation mechanisms.

The geochemical analysis of a shocked zircon grain containing reidite lamellae (chapter 4) revealed microstructures enriched in trace elements. A higher concentration of trace elements in low-angle boundaries within the reidite phase and in zircon–reidite interfaces indicates there was trace element mobility associated with the hypervelocity impact event. The trace element distribution in this shocked zircon grain provided the necessary information to propose a new model for the transformation of zircon to reidite lamellae during an impact event. This model comprises of a martensitic transformation and three additional short-range diffusional components. These components are the concentration of trace elements by the

migrating interface, a local diffusion through the migrating interface, and the coupled migration of trace elements and shock-induced defects.

Geochronological application of APT in zircon

The use of APT for geochronological studies in non-complex zircon has been demonstrated by Valley et al. (2014), Valley et al. (2015), Peterman et al. (2016), Blum et al. (2018). This project further develops the geochronological application of APT to complex zircon grains.

An altered zircon grain with a complexity of textures was found to contain clusters within the crystalline domain, enriched in Pb (chapter 3). APT was used to determine the age of the Pb enriched clusters however, the use of APT also lead to the discovery of a new mechanism of Pb migration and segregation. The other zircon samples that were analysed in this project did not have microstructures enriched in Pb therefore, these zircon samples could not be dated using APT.

To successfully use APT for geochronology on complex zircon grains an initial comprehensive, multi-technique study is needed. This would facilitate the identification of potential grains and areas within the grain for nanoscale geochronology. In this project it was found that suitable areas for APT geochronological analyses consist of crystalline or regions that are not heavily deformed.

APT specimen yield

For this project, a total of 99 APT specimens were manufactured, which covered zircon grains from the Stac Fada suite, Bunburra Rockhole meteorite, Lalla Rookh Sandstone and the Indian Ocean zircon (first used to learn the technique, then later incorporated in chapter 5 for comparison). A total of 1,938,202,199 atoms were collected from these specimens (Table 6.1), which corresponds to 492 hrs of data collection. From the 99 APT specimens, only 12 survived the APT run, with 87 fracturing (88%). It is known that the stress on the APT specimens during the analysis can cause the specimens to fracture (Larson et al., 2013), which reduces the specimen yield. However, the samples in this project are not pristine grains, they are

complex zircon grains that are either small or extremely deformed, which also contributes to the fracturing of the APT specimens.

As with any technique, APT is still developing in its application on geological materials. Hence, there are some limitations associated with the use of APT for geologic samples as discussed throughout this thesis. Although, the complications mentioned in chapters 3 and 5 are not the only ones that could occur during APT analysis, most of the problems that arose during this project were related to the sample integrity, making the study of complex zircon grains quite the challenge. Nevertheless, this project has shown the importance of a comprehensive characterization prior the use of APT to improve the probability of obtaining a high specimen yield.

In order to assess the geochemistry of zircon grains, a minimum APT yield of ~1.5 million ions was determined adequate for this study. Due to the complexity of the samples and the variability of deformation, the APT running conditions were adjusted individually to maximise the yield for each specimen (Table 6.1). It was not possible, nor within the scope of this study to determine an optimum set of APT acquisition parameters due to the variability of the samples and grain integrity. Crystalline samples or crystalline target areas tended to produce a higher yield, while heavily deformed or metamict zircon grains produced a low yield. The observed correlation between the sample integrity and the APT yield is discussed in chapters 3 and 5.

Commonly used APT parameters for zircon grains in this study are sample temperature of 81 K, laser pulse frequency of 200 kHz, a laser pulse energy of 300-400 pJ, and a detection rate of 0.005 ions per pulse (Table 6.1). For highly deformed or metamict zircon grains, or target areas that contained boundaries or interfaces, the laser pulse energy and the sample temperature were increased and the detection rate were decreased to try to reduce the stress on the specimens due to the electric field (e.g. SF-211 M21: 91 K, 200 kHz, 400 pJ, 0.01 ions/pulse). Figure 6.1 plots the APT running conditions against sample yield to offer a comparison. However, due to the constant changing of parameters to suit the knowledge of the particular specimen, there is no apparent correlation. Further studies could be undertaken to investigate the optimum running conditions for APT on different sample types.

Table 6.1 APT acquisition parameters of all specimens analysed in this project

Experiment ID	Sample	Specimen	Total ions	Sample temperature (K)	Laser pulse frequency (kHz)	Laser pulse energy (pJ)	Detection rate (ions/pulse)
1322	IOZ	M12	19136863	69.2	200	300	0.006
1323	IOZ	M12	64213137	69.1	200	200	0.006
1360	IOZ	M13	87337267	57.3	250	300	0.01
1362	IOZ	M14	134756852	57.3	250	200	0.006
1367	IOZ	M15	102720790	57.3	250	175	0.01
2843	BR-zrn5-CG	M1	52791	80.7	200	400	0.005
2844	BR-zrn5-CG	M2	98801	80.7	200	400	0.005
2845	BR-zrn5-CG	M3	90880921	80.7	200	300	0.005
2846	BR-zrn4-MG	M4	22333907	80.7	250	300	0.005
3020	BR-zrn4-MG	M7	59014	80.6	250	300	0.005
2962	BR-zrn4-MG	M8	60702	80.7	250	400	0.005
2949	BR-zrn4-MG	M10	30836913	69.7	250	400	0.006
2676	BR-zrn3-FGg	M12	17712853	80.9	200	400	0.006
2639	BR-zrn3-FGg	M13	56695600	80.7	200	400	0.006
2641	BR-zrn3-FGg	M14	67988533	80.7	200	400	0.006
2669	BR-zrn3-FGg	M15	74364532	79.9	200	400	0.006
2671	BR-zrn3-FGg	M16	62340391	80.7	200	400	0.007
2680	BR-zrn1-FGs	M17	20043	92	200	400	0.01
2678	BR-zrn1-FGs	M18	34756655	91.9	200	400	0.005
2637	BR-zrn2-FGs	M19	50660266	80.7	200	400	0.005
2636	BR-zrn2-FGs	M20	52639	80.7	200	400	0.01
2635	BR-zrn2-FGs	M21	25579	69.2	200	400	0.01
2634	BR-zrn2-FGs	M22	758286	69.2	200	400	0.005
1845	LR-D.C.	M9*	87229	80.7	200	400	0.005
1847	LR-D.C.	M10*	3265096	69.2	200	400	0.005
1849	LR-D.C.	M11*	1512345	80.6	200	400	0.005
2768	LR-D.C.	M1	219398	57.3	250	300	0.01
2769	LR-D.C.	M2	776821	87.8	250	250	0.005
2838	LR-D.C.	M3	955951		250	250	0.004
2841	LR-D.C.	M4	257274	92	250	250	0.005
1840	LR-int. D.C./L.C.	M8*	194976	80.7	200	400	0.01
1835	LR-L.C.	M6*	2528123	80.7	250	400	0.005
1839	LR-L.C.	M7*	54820359	80.7	200	400	0.005
2835	LR-L.C.	M5	71628730	92	250	250	0.006
2771	LR-L.C.	M7	4199538	92	250	300	0.007
2836	LR-L.C.	M9	55153010	92	250	250	0.005
2834	LR-L.C.	M10	63191407	91.4	250	250	0.005
2521	LR-L.C.	M19	94000943	92	250	250	0.005
2524	LR-L.C.	M20	75729049	92	250	250	0.005
1829	LR-L.R.	M3*	6036702	57.3	200	400	0.008
2483	LR-L.R.	M12	2194723	80.7	200	400	0.005
2495	LR-int. L.R./G.R.	M16	756246	92	250	300	0.005
1831	LR-G.R.	M4*	24634803	80.7	200	400	0.005
1833	LR-G.R.	M5*	1234332	80.7	200	400	0.005
2486	LR-G.R.	M15	6404792	88.5	250	250	0.005
2496	LR-G.R.	M17	263060	92	250	250	0.01
2522	LR-G.R.	M18	2749171	92	250	250	0.005
2484	LR-D.R.	M13	1568505	80.7	200	400	0.005
1823	LR-D.R.	M1*	844755	56.5	250	300	0.01
1827	LR-D.R.	M2*	430287	57.3	200	250	0.005
2561	LR-D.R.	M21	223377	91.8	250	250	0.01
2563	LR-D.R.	M22	173871	92	250	250	0.008

Experiment ID	Sample	Specimen	Total ions	Sample temperature (K)	Laser pulse frequency (kHz)	Laser pulse energy (pJ)	Detection rate (ions/pulse)
334	SF-86	M1	14180705	54.7	200	250	0.008
336	SF-86	M2	1458834	77	250	300	0.005
340	SF-86	M3	150494431	54.7	125	300	0.007
349	SF-86	M4	12827449	54.7	200	300	0.007
351	SF-86	M5	6176074	54.7	125	300	0.007
357	SF-86	M6	109005	54.7	100	300	0.005
358	SF-86	M7	1536333	54.7	250	350	0.004
360	SF-86	M8	13130596	54.6	200	350	0.006
362	SF-86	M9	2704485	54.6	125	350	0.007
690	SF-86core	M1	1470469	65.5	200	250	0.006
692	SF-86core	M2	7990867	65.5	250	300	0.005
696	SF-86core	M5	11453322	65.4	250	300	0.006
698	SF-86core	M6	4242983	67.1	200	140	0.006
694	SF-86core	M7	20532905	65.4	250	300	0.005
700	SF-86core	M8	18723751	66.7	250	300	0.006
833	SF-86core	M9	16749314	65.4	250	300	0.005
836	SF-86core	M10	4526156	70.1	250	300	0.005
1643	SF-001	M12	32127678	57.3	200	300	0.007
1652	SF-001	M13	199146	57.4	250	300	0.007
1654	SF-001	M14	67333613	57.3	200	300	0.007
1657	SF-001	M15	88025409	57.3	200	300	0.007
1661	SF-001	M16	77469	57.2	250	250	0.02
1692	SF-001	M17	380357	69.1	200	400	0.007
1696	SF-001	M18	4640756	80.7	200	400	0.005
1694	SF-001	M19	685009	80.7	200	500	0.007
1698	SF-001	M20	8930357	80.7	250	400	0.005
1701	SF-001	M21	239636	80.7	250	400	0.02
1702	SF-001	M22	302004	80.7	250	400	0.007
912	SF-66	M1	96476	68.5	250	300	0.005
910	SF-66	M2	21933309	65.6	200	300	0.007
913	SF-66	M3	66156	65.7	200	300	0.005
914	SF-66	M4	578638	65.5	250	300	0.005
915	SF-66	M5	10839295	65.5	200	300	0.007
917	SF-66	M6	55182	65.4	125	300	0.005
2097	SF-211	M12	430786	69.2	200	250	0.008
2098	SF-211	M13	1350543	69.2	200	400	0.008
2099	SF-211	M14	148319	69.2	125	400	0.01
2100	SF-211	M15	581654	69.2	200	400	0.004
2101	SF-211	M16	450420	111.9	200	600	0.004
2102	SF-211	M17	1592957	80.7	200	400	0.004
2103	SF-211	M18	629397	80.7	200	400	0.01
2107	SF-211	M19	376935	80.7	200	400	0.002
2108	SF-211	M20	653951	80.7	250	400	0.003
2109	SF-211	M21	157796	90.9	200	400	0.01
2110	SF-211	M22	220440	91.9	200	400	0.002
2850**	BR-zrn4-MG	M9	5377804	80.7	250	300	0.005
2785**	LLR-L.C.	M8	3516216	92	250	300	0.006
2485**	LLR-G.R.	M14	3998604	69.2	200	400	0.005

IOZ = Indian Ocean zircon; BR = Bunburra Rockhole; zrn = zircon; LLR = Lalla Rookh; SF = Stac Fada; CG = coarse-grained domain; MG = medium-grained domain; FGs = fined-grained domain (subophitic); FGg = fined-grained domain (granoblastic); D.C. = dark core; L.C. = light core; int. = interface; L.R. = light rim; G.R. = grey rim; D.R. = dark rim.

** APT instrument encountered a noise problem that corrupted the data.

Future Recommendations

One of the outcomes of this project is to understand the effects that sample integrity has to the APT specimen yield. This thesis shows that heavily deformed grains will produce a low yield, whether it be by metamictisation or deformation. Pristine crystalline grains will produce a higher number of ions from a specimen. This could partially explain the lack of published work of APT on complex grains.

In the case of further analysis of complex grains using APT, it is highly recommended that an extensive characterization of the structure of the grain is conducted before analysing it at the nanoscale. This characterization is necessary to identify target areas with a greater likelihood of a high APT yield resulting in improved results using multiple analytical techniques. Another recommendation would be to use coating layers to protect the integrity of the sample.

It is also recommended that during the microanalysis of the sample, the user choose multiple target areas and areas that contain a variety of microstructures (twining, zoning, interfaces, low-angle boundaries) (e.g. Piazolo et al., 2016; Fougerouse et al., 2019; Peterman et al., 2019; Taylor et al., 2019). This could increase the chances of obtaining a nanoscale structure enriched in trace elements (Pb for geochronology).

On the other hand, there have been studies where targeting areas with no visible microstructure have resulted in nanoscale structures in the APT specimens with trace element enrichment (e.g. Valley et al., 2014; Piazolo et al., 2016; Reinhard et al., 2018). This indicates nanoscale structures are not always visible at the microscale. To overcome this, the user needs to plan a suitable workflow and choose appropriate target areas to their research interest.

In summary, it will be useful for the user to conduct a thorough characterization of the sample prior to APT using a combination of analytical techniques depending on the focus of the research, identify several regions of interest within the analysed grain and, if possible, target microstructures, while avoiding defects. These suggestions will increase the chances for the user to get APT nanoscale data from their samples.

Figures

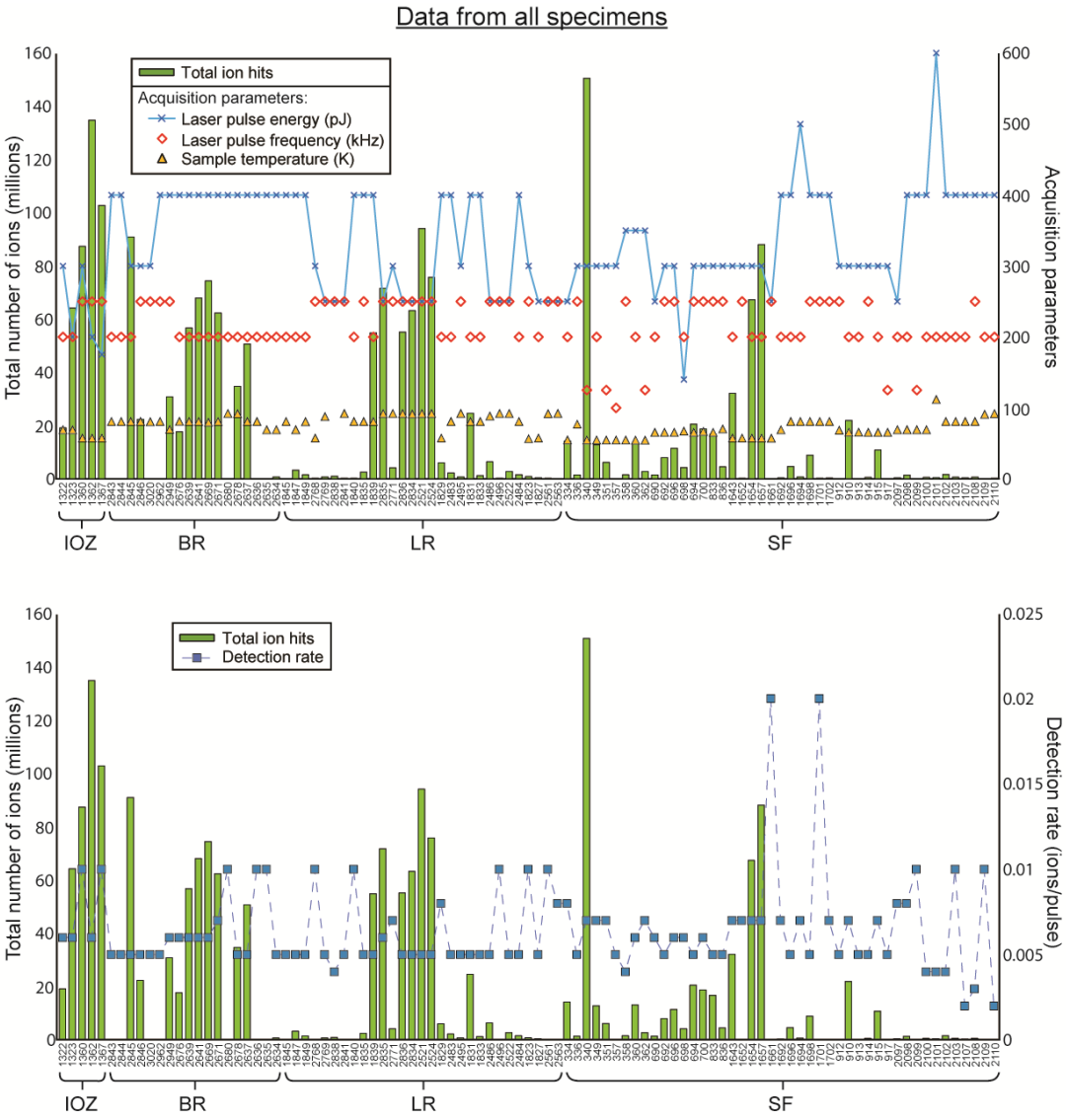
Data from all specimens
Total ion hits
Acquisition parameters:
Laser pulse energy (pJ)
Laser pulse frequency (kHz)
Sample temperature (K)
Total number of ions (millions)
Acquisition parameters
IOZ
BR
LR
SF
Total ion hits
Detection rate
Total number of ions (millions)
Detection rate (ions/pulse)
IOZ
BR
LR
SF

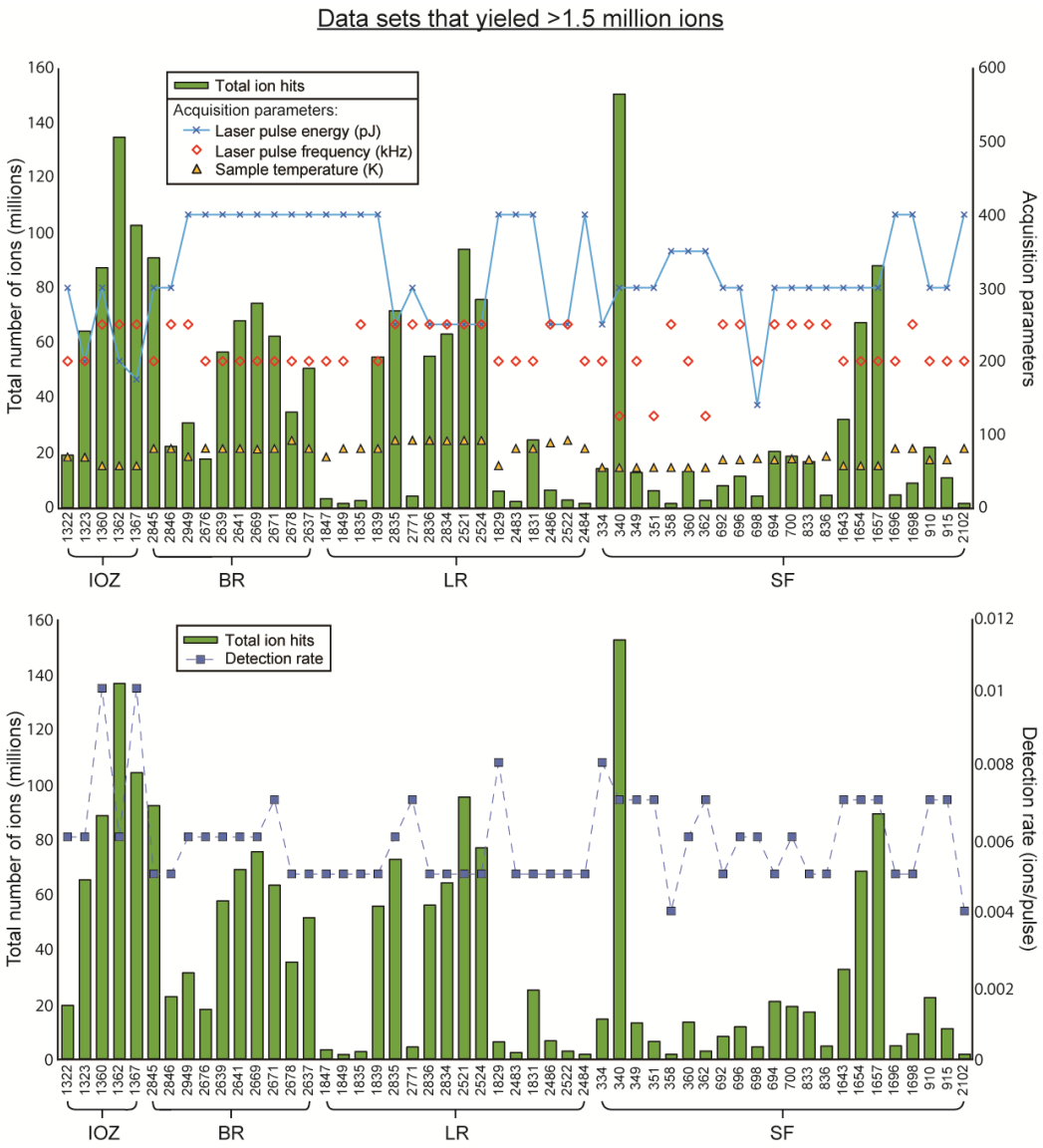

Figure 6.1 Plots showing the APT specimen yield and acquisition parameters (laser pulse anergy, laser pulse frequency, sample temperature and detection rate) from all the specimens in this project and from the specimens that yielded more than 1.5 million ions. No clear correlation was found between the yield and the APT acquisition parameters. A higher resolution version of the figure of all the data sets can be found in Appendix B.

References

Branney, M. J., and Brown, R. J., 2011, Impactoclastic Density Current Emplacement of Terrestrial Meteorite-Impact Ejecta and the Formation of Dust Pellets and Accretionary Lapilli: Evidence from Stac Fada, Scotland: The Journal of Geology, v. 119, no. 3, p. 275-292.

Bursill, L. A., and McLaren, A. C., 1966, Transmission Electron Microscope Study of Natural Radiation Damage in Zircon (ZrSiO4): physica status solidi (b), v. 13, no. 2, p. 331-343.

Cavosie, A. J., Erickson, T. M., and Timms, N. E., 2015, Nanoscale records of ancient shock deformation: Reidite ($ZrSiO_4$) in sandstone at the Ordovician Rock Elm impact crater: Geology, v. 43, no. 4, p. 315-318.

Cherniak, D. J., 2010, Diffusion in accessory minerals: zircon, titanite, apatite, monazite and xenotime, *in* Zhang, Y., and Cherniak, D. J., eds., Diffusion in Minerals and Melts, Volume 72: Virginia, The Mineralogical Society of America, p. 827-869.

Erickson, T. M., Cavosie, A. J., Pearce, M. A., Timms, N. E., and Reddy, S. M., 2016, Empirical constraints on shock features in monazite using shocked zircon inclusions: Geology, v. 44, p. 635-638.

Finch, R. J., and Hanchar, J. M., 2003, Structure and chemistry of zircon and zircon-group minerals, *in* Hanchar, J. M., and Hoskin, P. W. O., eds., Zircon, Volume 53: Washington, DC, The Mineralogical Society of America, p. 1-25.

Fougerouse, D., Reddy, S. M., Kirkland, C. L., Saxey, D. W., Rickard, W. D., and Hough, R. M., 2019, Time-resolved, defect-hosted, trace element mobility in deformed Witwatersrand pyrite: Geoscience Frontiers, p. 55-63.

Geisler, T., Pidgeon, R. T., van Bronswijk, W., and Kurtz, R., 2002, Transport of uranium, thorium, and lead in metamict zircon under low-temperature hydrothermal conditions: Chemical Geology, v. 191, no. 1–3, p. 141-154.

Harley, S. L., and Kelly, N. M., 2007, Zircon Tiny but Timely: Elements, v. 3, no. 1, p. 13-18.

Langenhorst, F., and Deutsch, A., 2012, Shock metamorphism of minerals: Elements, no. 1, p. 31-36.

Melosh, H. J., 1989, Impact Cratering: A Geologic Process: New York, USA, Oxford University Press, p. 245.

Montalvo, S. D., Reddy, S. M., Saxey, D. W., Rickard, W. D. A., Fougerouse, D., Quadir, Z., and Johnson, T. E., 2019, Nanoscale constraints on the shock-induced transformation of zircon to reidite: Chemical Geology, v. 507, p. 85-95.

Murakami, T., Chakoumakos, B. C., Ewing, R. C., Lumpkin, G. R., and Weber, W. J., 1991, Alpha-decay event damage in zircon: American Mineralogist, v. 76, p. 1510-1532.

Parnell, J., Mark, D., Fallick, A. E., Boyce, A., and Thackrey, S., 2011, The age of the Mesoproterozoic Stoer Group sedimentary and impact deposits, NW Scotland: Journal of the Geological Society, v. 168, no. 2, p. 349-358.

Peterman, E. M., Reddy, S. M., Saxey, D. W., Fougerouse, D., Snoeyenbos, D. R., and Rickard, W. D. A., 2019, Nanoscale processes of trace element mobility in metamorphosed zircon: Contributions to Mineralogy and Petrology, v. 174, no. 11, p. 92.

Peterman, E. M., Reddy, S. M., Saxey, D. W., Snoeyenbos, D. R., Rickard, W. D. A., Fougerouse, D., and Kylander-Clark, A. R. C., 2016, Nanogeochronology of

discordant zircon measured by atom probe microscopy of Pb-enriched dislocation loops: Science Advances, v. 2, p. 9.
Piazolo, S., La Fontaine, A., Trimby, P., Harley, S., Yang, L., Armstrong, R., and Cairney, J. M., 2016, Deformation-induced trace element redistribution in zircon revealed using atom probe tomography: Nature Communications, p. 7.
Reddy, S. M., Johnson, T. E., Fischer, S., Rickard, W. D. A., and Taylor, R. J. M., 2015, Precambrian reidite discovered in shocked zircon from the Stac Fada impactite, Scotland: Geology, v. 43, no. 10, p. 899-902.
Reddy, S. M., Saxey, D. W., Rickard, W. D. A., Fougerouse, D., Montalvo, S. D., Verberne, R., and van Riessen, A., 2020, Atom probe tomography: development and application to the geosciences: Geostandards and Geoanalytical Research, v. 44, no.1, p. 5-50.
Reddy, S. M., Timms, N. E., Trimby, P., Kinny, P. D., Buchan, C., and Blake, K., 2006, Crystal-plastic deformation of zircon: A defect in the assumption of chemical robustness: Geology, v. 34, no. 4, p. 257-260.
Reddy, S. M., van Riessen, A., Saxey, D. W., Johnson, T. E., Rickard, W. D. A., Fougerouse, D., Fischer, S., Prosa, T. J., Rice, K. P., Reinhard, D. A., Chen, Y., and Olson, D., 2016, Mechanisms of deformation-induced trace element migration in zircon resolved by atom probe and correlative microscopy: Geochimica et Cosmochimica Acta, v. 195, p. 158-170.
Reimold, W. U., and Gibson, R. L., 2009, Meteorite Impact! The Danger from Space and South Africa's Mega-Impact The Vredefort Structure, Berlin, Heidelberg, Springer.
Rubatto, D., 2017, Zircon: The Metamorphic Mineral: Reviews in Mineralogy and Geochemistry, v. 83, no. 1, p. 261-295.
Sanders, I. S., and Johnston, J. D., 1989, The Torridonian Stac Fada Member: an extrusion of fluidised peperite?: Transactions of the Royal Society of Edinburgh: Earth Sciences, v. 80, no. 1, p. 1-4.
Simms, M. J., 2015, The Stac Fada impact ejecta deposit and the Lairg Gravity Low: evidence for a buried Precambrian impact crater in Scotland?: Proceedings of the Geologists' Association, v. 126, no. 6, p. 742-761.
Stewart, A. D., 2002, The Later Proterozoic Torridonian Rocks of Scotland: Their Sedimentology, Geochemistry and Origin, Geological society memoirs: UK, Geological Society of London, p. 130.
Timms, N. E., Erickson, T. M., Zanetti, M. R., Pearce, M. A., Cayron, C., Cavosie, A. J., Reddy, S. M., Wittmann, A., and Carpenter, P. K., 2017, Cubic zirconia in >2370 °C impact melt records Earth's hottest crust: Earth and Planetary Science Letters, v. 477, p. 52-58.
Timms, N. E., Kinny, P. D., and Reddy, S. M., 2006, Enhanced diffusion of Uranium and Thorium linked to crystal plasticity in zircon: Geochemical Transactions, v. 7, no. 1, p. 10.
Valley, J. W., Cavosie, A. J., Ushikubo, T., Reinhard, D. A., Lawrence, D. F., Larson, D. J., Clifton, P. H., Kelly, T. F., Wilde, S. A., Moser, D. E., and Spicuzza, M. J., 2014, Hadean age for a post-magma-ocean zircon confirmed by atom-probe tomography: Nature Geoscience, v. 7, no. 3, p. 219-223.
Wheeler, J., Park, R. G., Rollinson, H. R., and Beach, A., 2010, The Lewisian Complex: insights into deep crustal evolution: Geological Society, London, Special Publications, v. 335, no. 1, p. 51-79.
White, L. F., Moser, D. E., Tait, K. T., Langelier, B., Barker, I., and Darling, J. R., 2019, Crystallization and impact history of a meteoritic sample of early lunar

crust (NWA 3163) refined by atom probe geochronology: Geoscience Frontiers, v. 10, no. 5, p. 1841-1848.
Wittmann, A., Kenkmann, T., Schmitt, R. T., and Stöffler, D., 2006, Shock-metamorphosed zircon in terrestrial impact craters: Meteoritics & Planetary Science, v. 41, no. 3, p. 433-454.

APPENDIX A STATEMENTS FROM CO-AUTHORS FOR CH. 4

To Whom It May Concern

I, Stephanie Dannett Montalvo Delgado, contributed in the sample preparation, data acquisition, analysis and interpretation, manuscript writing and editing of the publication entitled Nanoscale constrains on the shock-induced transformation of zircon to reidite.

I, as a Co-Author, endorse that this level of constitution by the candidate indicated above is appropriate.

Steven M. Reddy

David W. Saxey

William D.A. Rickard

Denis Fougerouse

Zakaria Quadir

Tim E. Johnson

APPENDIX B HIGHER RESOLUTION FIGURE 6.1

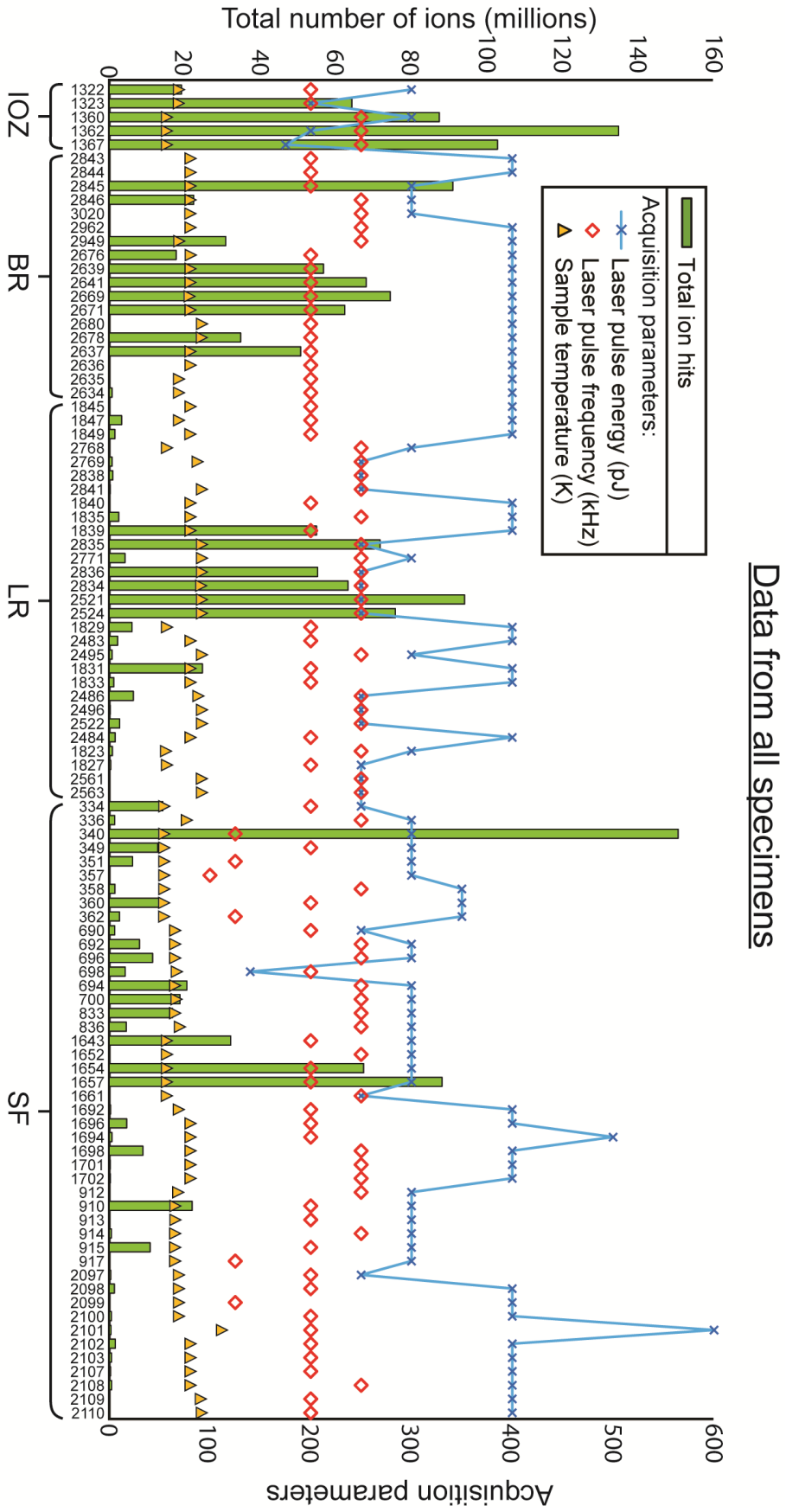
Total number of ions (millions)
0
20
40
60
80
100
120
140
160
Total ion hits
Acquisition parameters:
Laser pulse energy (pJ)
Laser pulse frequency (kHz)
Sample temperature (K)
IOZ
BR
LR
SF
1322
1323
1360
1362
1367
2843
2844
2845
2846
3020
2962
2949
2676
2639
2641
2669
2671
2680
2678
2637
2636
2635
2634
1845
1847
1849
2768
2769
2838
2841
1840
1835
1839
2835
2771
2836
2834
2521
2524
1829
2483
2495
1831
1833
2486
2496
2522
2484
1823
1827
2561
2563
334
336
340
349
351
357
358
360
362
690
692
696
698
694
700
833
836
1643
1652
1654
1657
1661
1692
1696
1694
1698
1701
1702
912
910
913
914
915
917
2097
2098
2099
2100
2101
2102
2103
2107
2108
2109
2110
0
100
200
300
400
500
600
Acquisition parameters
Data from all specimens

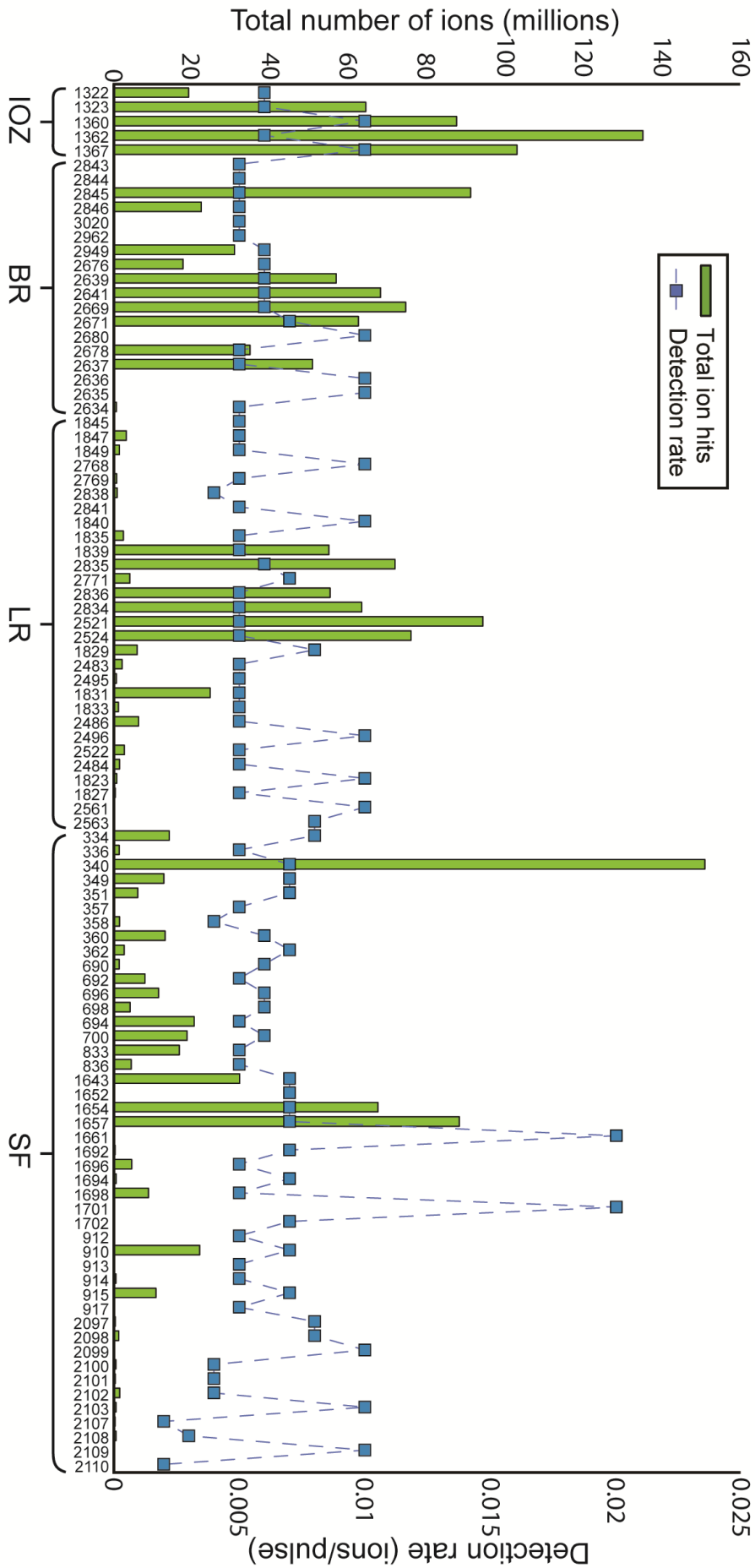
Total number of ions (millions)
0
20
40
60
80
100
120
140
160
Total ion hits
Detection rate
IOZ
BR
LR
SF
1322
1323
1360
1362
1367
2843
2844
2845
2846
3020
2962
2949
2676
2639
2641
2669
2671
2680
2678
2637
2636
2635
2634
1845
1847
1849
2768
2769
2838
2841
1840
1835
1839
2835
2771
2836
2834
2521
2524
1829
2483
2495
1831
1833
2486
2496
2522
2484
1823
1827
2561
2563
334
336
340
349
351
357
358
360
362
690
692
696
698
694
700
833
836
1643
1652
1654
1657
1661
1692
1696
1694
1698
1701
1702
912
910
913
914
915
917
2097
2098
2099
2100
2101
2102
2103
2107
2108
2109
2110
0
0.005
0.01
0.015
0.02
0.025
Detection rate (ions/pulse)

APPENDIX C ATTRIBUTION STATEMENTS

The following are the attribution of research outputs for each chapter.

Chapter 2: Trace element analysis of micrometre-scale zircons in Bunburra Rockhole meteorite

Percentage contribution by field of activity: percentage time each author contributed

Author and co-authors	Conception and design	Data acquisition	Data analysis	Interpretation and discussion	Manuscript writing and editing	Total % contribution
Stephanie D. Montalvo	85	80	80	75	80	80
Co-author 1 **Steven M. Reddy**	12.5	20	7.5	10	7.5	12
Co-author 1 acknowledgment: I acknowledge that these represent my contribution to the above research output Signed:						
Co-author 2 **David W. Saxey**	2.5		5	7.5	5	4
Co-author 2 acknowledgment: I acknowledge that these represent my contribution to the above research output Signed:						
Co-author 3 **William D.A. Rickard**			2.5	2.5	2.5	2
Co-author 3 acknowledgment: I acknowledge that these represent my contribution to the above research output Signed:						
Co-author 4 **Denis Fougerouse**			2.5	2.5	2.5	2
Co-author 4 acknowledgment: I acknowledge that these represent my contribution to the above research output Signed:						
Co-author 5 **Gretchen K. Benedix**			2.5	2.5	2.5	2
Co-author 5 acknowledgment: I acknowledge that these represent my contribution to the above research output Signed:						
Total %	**100**	**100**	**100**	**100**	**100**	

Chapter 3: Complex history of a detrital zircon obtained by textural and trace element analyses

Percentage contribution by field of activity: percentage time each author contributed

Author and co-authors	Conception and design	Data acquisition	Data analysis	Interpretation and discussion	Manuscript writing and editing	Total % contribution
Stephanie D. Montalvo	85	85	70	75	85	80
Co-author 1 **Steven M. Reddy**	15	5	15	10	5	11
Co-author 1 acknowledgment: I acknowledge that these represent my contribution to the above research output Signed:						
Co-author 2 **David W. Saxey**		5	7.5	5	2.5	4
Co-author 2 acknowledgment: I acknowledge that these represent my contribution to the above research output Signed:						
Co-author 3 **William D.A. Rickard**			2.5	5	2.5	2
Co-author 3 acknowledgment: I acknowledge that these represent my contribution to the above research output Signed:						
Co-author 4 **Denis Fougerouse**		2.5	2.5	2.5	2.5	2
Co-author 4 acknowledgment: I acknowledge that these represent my contribution to the above research output Signed:						
Co-author 5 **Chris Kirkland**		2.5	2.5	2.5		2
Co-author 5 acknowledgment: I acknowledge that these represent my contribution to the above research output Signed:						
Total %	**100**	**100**	**100**	**100**	**100**	

Chapter 4: Nanoscale constrains on the shock-induced transformation of zircon to reidite

Percentage contribution by field of activity: percentage time each Author contributed

Author and co-authors	Conception and design	Data acquisition	Data analysis	Interpretation and discussion	Manuscript writing and editing	Total % contribution
Stephanie D. Montalvo	80	85	80	80	82.5	82
Co-author 1 **Steven M. Reddy**	10	5	7.5	7.5	5	7
Co-author 1 acknowledgment: I acknowledge that these represent my contribution to the above research output Signed:						
Co-author 2 **David W. Saxey**	5	2.5	5	5	2.5	4
Co-author 2 acknowledgment: I acknowledge that these represent my contribution to the above research output Signed:						
Co-author 3 **William D.A. Rickard**		2.5	2.5	2.5	2.5	2
Co-author 3 acknowledgment: I acknowledge that these represent my contribution to the above research output Signed:						
Co-author 4 **Denis Fougerouse**		2.5	2.5	2.5	2.5	2
Co-author 4 acknowledgment: I acknowledge that these represent my contribution to the above research output Signed:						
Co-author 5 **Zakaria Quadir**		2.5	2.5	2.5	2.5	2
Co-author 5 acknowledgment: I acknowledge that these represent my contribution to the above research output Signed:						
Co-author 6 **Tim E. Johnson**	5				2.5	2
Co-author 6 acknowledgment: I acknowledge that these represent my contribution to the above research output Signed:						
Total %	**100**	**100**	**100**	**100**	**100**	

Chapter 5: Strategies for nanoscale analysis of shocked zircon grains

Percentage contribution by field of activity: percentage time each Author contributed

Author and co-authors	Conception and design	Data acquisition	Data analysis	Interpretation and discussion	Chapter writing and editing	Total % contribution
Stephanie D. Montalvo	90	90	85	85	90	88
Co-author 1 **Steven M. Reddy**	10	2.5	5	7.5	5	6
Co-author 1 acknowledgment: I acknowledge that these represent my contribution to the above research output Signed:						
Co-author 2 **Denis Fougerouse**		2.5	5	2.5	5	3
Co-author 2 acknowledgment: I acknowledge that these represent my contribution to the above research output Signed:						
Co-author 3 **David W. Saxey**		2.5	2.5	2.5		2
Co-author 3 acknowledgment: I acknowledge that these represent my contribution to the above research output Signed:						
Co-author 4 **William D.A. Rickard**		2.5	2.5	2.5		2
Co-author 4 acknowledgment: I acknowledge that these represent my contribution to the above research output Signed:						
Total %	**100**	**100**	**100**	**100**	**100**	

REFERENCES

Aaronson, H. I., 1975, Lectures on the theory of phase transformations: New York, American Institute of Mining, Metallurgical and Petroleum Engineers, p. 178.

Aaronson, H. I., Enomoto, M., and Lee, J. K., 2010, Mechanisms of diffusional phase transformations in metals and alloys: USA, CRC Press, p. 667.

Amor, K., Hesselbo, S. P., Porcelli, D., Thackrey, S., and Parnell, J., 2008, A Precambrian proximal ejecta blanket from Scotland: Geology, v. 36, no. 4, p. 303-306.

Anders, E., and Grevesse, N., 1989, Abundances of the elements: Meteoritic and solar: Geochimica et Cosmochimica Acta, v. 53, no. 1, p. 197-214.

Babinsky, K., De Kloe, R., Clemens, H., and Primig, S., 2014, A novel approach for site-specific atom probe specimen preparation by focused ion beam and transmission electron backscatter diffraction: Ultramicroscopy, v. 144, p. 9-18.

Balluffi, R. W., Allen, S. M., and Carter, W. C., 2005, Kinetics of materials: Hoboken, N.J., Wiley-Interscience, p. 645.

Barley, M. E., McNaughton, N. J., Williams, I. S., and Compston, W., 1994, Geologic Note: Age of Archaean volcanism and sulphide mineralization in the Whim Creek Belt, west Pilbara: Australian Journal of Earth Sciences, v. 41, no. 2, p. 175-177.

Barrat, J. A., Zanda, B., Moynier, F., Bollinger, C., Liorzou, C., and Bayon, G., 2012, Geochemistry of CI chondrites: Major and trace elements, and Cu and Zn Isotopes: Geochimica et Cosmochimica Acta, v. 83, p. 79-92.

Belousova, E., Griffin, W., O'Reilly, S. Y., and Fisher, N., 2002, Igneous zircon: trace element composition as an indicator of source rock type: Contributions to Mineralogy and Petrology, v. 143, no. 5, p. 602-622.

Benedix, G. K., Bland, P. A., Friedrich, J. M., Mittlefehldt, D. W., Sanborn, M. E., Yin, Q. Z., Greenwood, R. C., Franchi, I. A., Bevan, A. W. R., Towner, M. C., Perrotta, G. C., and Mertzman, S. A., 2017, Bunburra Rockhole: Exploring the geology of a new differentiated asteroid: Geochimica et Cosmochimica Acta, v. 208, p. 145-159.

Binzel, R. P., and Shui, X., 1993, Chips off of asteroid 4 Vesta: Evidence for the parent body: Science, v. 260, no. 5105, p. 186.

Bland, P. A., Spurný, P., Towner, M. C., Bevan, A. W. R., Singleton, A. T., Bottke, W. F., Greenwood, R. C., Chesley, S. R., Shrbený, L., Borovička, J., Ceplecha, Z., McClafferty, T. P., Vaughan, D., Benedix, G. K., Deacon, G., Howard, K. T., Franchi, I. A., and Hough, R. M., 2009, An Anomalous Basaltic Meteorite from the Innermost Main Belt: Science, v. 325, no. 5947, p. 1525-1527.

Blum, T. B., Darling, J. R., Kelly, T. F., Larson, D. J., Moser, D. E., Perez-Huerta, A., Prosa, T. J., Reddy, S. M., Reinhard, D. A., Saxey, D. W., Ulfig, R. M., and Valley, J. W., 2018a, Best practices for reporting atom probe analysis of geological materials, *in* Moser, D. E., Corfu, F., Darling, J. R., Reddy, S. M., and Tait, K., eds., Microstructural Geochronology: Planetary Records Down to Atom Scale: USA, American Geophysical Union, p. 416.

Blum, T. B., Reinhard, D. A., Chen, Y., Prosa, T. J., Larson, D. J., and Valley, J. W., 2018b, Uncertainty and sensitivity analysis for spatial and spectral processing of Pb isotopes in zircon by atom probe tomography, *in* Moser, D. E., Corfu, F., Darling, J. R., Reddy, S. M., and Tait, K., eds., Microstructural

Geochronology: Planetary Records Down to Atom Scale: USA, American Geophysical Union, p. 416.
Bostel, A., Blavette, D., Menand, A., and Sarrau, J. M., 1989, Toward a tomographic atom-probe: J. Phys. Colloques, v. 50, no. C8, p. C8-501-C508-506.
Bouvier, L. C., Costa, M. M., Connelly, J. N., Jensen, N. K., Wielandt, D., Storey, M., Nemchin, A. A., Whitehouse, M. J., Snape, J. F., Bellucci, J. J., Moynier, F., Agranier, A., Gueguen, B., Schönbächler, M., and Bizzarro, M., 2018, Evidence for extremely rapid magma ocean crystallization and crust formation on Mars: Nature, v. 558, no. 7711, p. 586-589.
Branney, M. J., and Brown, R. J., 2011, Impactoclastic Density Current Emplacement of Terrestrial Meteorite-Impact Ejecta and the Formation of Dust Pellets and Accretionary Lapilli: Evidence from Stac Fada, Scotland: The Journal of Geology, v. 119, no. 3, p. 275-292.
Bursill, L. A., and McLaren, A. C., 1966, Transmission Electron Microscope Study of Natural Radiation Damage in Zircon (ZrSiO4): physica status solidi (b), v. 13, no. 2, p. 331-343.
Cao, M., Evans, N. J., Reddy, S. M., Fougerouse, D., Hollings, P., Saxey, D. W., McInnes, B. I. A., Cooke, D. R., McDonald, B. J., and Qin, K., 2019, Micro- and nano-scale textural and compositional zonation in plagioclase at the Black Mountain porphyry Cu deposit: Implications for magmatic processes: American Mineralogist, v. 104, no. 3, p. 391-402.
Cavosie, A. J., Erickson, T. M., and Timms, N. E., 2015, Nanoscale records of ancient shock deformation: Reidite ($ZrSiO_4$) in sandstone at the Ordovician Rock Elm impact crater: Geology, v. 43, no. 4, p. 315-318.
Cavosie, A. J., Quintero, R. R., Radovan, H. A., and Moser, D. E., 2010, A record of ancient cataclysm in modern sand shock microstructures in detrital minerals from the Vaal River, Vredefort Dome, South Africa: Geological Society of America Bulletin, v. 122, no. 11, p. 1968-1980.
Cerezo, A., Godfrey, T. J., and Smith, G. D. W., 1988, Application of a position-sensitive detector to atom probe microanalysis: Review of Scientific Instruments, v. 59, no. 6, p. 862-866.
Chakoumakos, B. C., Murakami, T., Lumpkin, G. R., and Ewing, R. C., 1987, Alpha-Decay—Induced Fracturing in Zircon: The Transition from the Crystalline to the Metamict State: Science, v. 236, no. 4808, p. 1556-1559.
Chen, M., Yin, F., Li, X., Xie, X., Xiao, W., and Tan, D., 2013, Natural occurrence of reidite in the Xiuyan crater of China: Meteoritics & Planetary Science, v. 48, no. 5, p. 796-805.
Cherniak, D. J., 2010, Diffusion in accessory minerals: zircon, titanite, apatite, monazite and xenotime, *in* Zhang, Y., and Cherniak, D. J., eds., Diffusion in Minerals and Melts, Volume 72: Virginia, The Mineralogical Society of America, p. 827-869.
Cherniak, D. J., and Watson, E. B., 2003, Diffusion in Zircon, *in* Hanchar, J. M., and Hoskin, P. W. O., eds., Zircon, Volume 53: Washington, DC, Mineralogical Society of America, p. 113-143.
Cherniak, D. J., and Watson, E. B., 2010, Li diffusion in zircon: Contributions to Mineralogy and Petrology, v. 160, no. 3, p. 383-390.
Compston, W., and Williams, I. S., 1983, U-Pb Geochronology of Zircons from Breccia 73217 Using a Sensitive High Mass-Resolution Ion Microprobe (shrimp), Lunar and Planetary Science Conference, p. 130.

Corfu, F., Hanchar, J. M., Hoskin, P. W. O., and Kinny, P., 2003, Atlas of zircon textures, *in* Hanchar, J. M., and Hoskin, P. W. O., eds., Reviews in Mineralogy and Geochemistry: Zircon, Volume 53, p. 468-500.

Courtney-Davies, L., Ciobanu, C. L., Verdugo-Ihl, M. R., Slattery, A., Cook, N. J., Dmitrijeva, M., Keyser, W., Wade, B. P., Domnick, U. I., Ehrig, K., Xu, J., and Kontonikas-Charos, A., 2019, Zircon at the Nanoscale Records Metasomatic Processes Leading to Large Magmatic–Hydrothermal Ore Systems: Minerals, v. 9, no. 6, p. 1-34.

Dubosq, R., Rogowitz, A., Schweinar, K., Gault, B., and Schneider, D. A., 2019, A 2D and 3D nanostructural study of naturally deformed pyrite: assessing the links between trace element mobility and defect structures: Contributions to Mineralogy and Petrology, v. 174, no. 9, p. 72.

Erickson, T. M., Cavosie, A. J., Pearce, M. A., Timms, N. E., and Reddy, S. M., 2016, Empirical constraints on shock features in monazite using shocked zircon inclusions: Geology, v. 44, p. 635-638.

Erickson, T. M., Pearce, M. A., Reddy, S. M., Timms, N. E., Cavosie, A. J., Bourdet, J., Rickard, W. D. A., and Nemchin, A. A., 2017, Microstructural constraints on the mechanisms of the transformation to reidite in naturally shocked zircon: Contributions to Mineralogy and Petrology, v. 172, no. 1, p. 6.

Ewing, R. C., Meldrum, A., Wang, L., Weber, W. J., and Corrales, L. R., 2003, Radiation Effects in Zircon, *in* Hanchar, J. M., and Hoskin, P. W. O., eds., Zircon, Volume 53: Wagington, DC., The Mineralogical Society of America, p. 387-425.

Exertier, F., La Fontaine, A., Corcoran, C., Piazolo, S., Belousova, E., Peng, Z., Gault, B., Saxey, D. W., Fougerouse, D., Reddy, S. M., Pedrazzini, S., Bagot, P. A. J., Moody, M. P., Langelier, B., Moser, D. E., Botton, G. A., Vogel, F., Thompson, G. B., Blanchard, P. T., Chiaramonti, A. N., Reinhard, D. A., Rice, K. P., Schreiber, D. K., Kruska, K., Wang, J., and Cairney, J. M., 2018, Atom probe tomography analysis of the reference zircon gj-1: An interlaboratory study: Chemical Geology, v. 495, p. 27-35.

Fedo, C. M., Sircombe, K. N., and Rainbird, R. H., 2003, Detrital Zircon Analysis of the Sedimentary Record: Reviews in Mineralogy and Geochemistry, v. 53, p. 277-303.

Feng, R., Machado, N., and Ludden, J., 1993, Lead geochronology of zircon by LaserProbe-inductively coupled plasma mass spectrometry (LP-ICPMS): Geochimica et Cosmochimica Acta, v. 57, no. 14, p. 3479-3486.

Finch, R. J., and Hanchar, J. M., 2003, Structure and chemistry of zircon and zircon-group minerals, *in* Hanchar, J. M., and Hoskin, P. W. O., eds., Zircon, Volume 53: Washington, DC, The Mineralogical Society of America, p. 1-25.

Fougerouse, D., Reddy, S. M., Kirkland, C. L., Saxey, D. W., Rickard, W. D., and Hough, R. M., 2019, Time-resolved, defect-hosted, trace element mobility in deformed Witwatersrand pyrite: Geoscience Frontiers, p. 55-63.

Fougerouse, D., Reddy, S. M., Saxey, D. W., Erickson, T. M., Kirkland, C. L., Rickard, W. D. A., Seydoux-Guillaume, A. M., Clark, C., and Buick, I. S., 2018, Nanoscale distribution of Pb in monazite revealed by atom probe microscopy: Chemical Geology, v. 479, p. 251-258.

French, B. M., 1998, Traces of Catastrophe: Houston, TX, Lunar and Planetary Institude, p. 120.

Gamsjäger, E., Militzer, M., Fazeli, F., Svoboda, J., and Fischer, F. D., 2006, Interface mobility in case of the austenite-to-ferrite phase transformation: Computational Materials Science, v. 37, no. 1, p. 94-100.
Gault, B., Moody, M. P., Cairney, J. M., and Ringer, S. P., 2012, Atom Probe Microscopy: New York, Springer, p. 396.
Geisler, T., Pidgeon, R. T., Kurtz, R., van Bronswijk, W., and Schleicher, H., 2003, Experimental hydrothermal alteration of partially metamict zircon: American Mineralogist, v. 88, no. 10, p. 1496-1513.
Geisler, T., Pidgeon, R. T., van Bronswijk, W., and Kurtz, R., 2002, Transport of uranium, thorium, and lead in metamict zircon under low-temperature hydrothermal conditions: Chemical Geology, v. 191, no. 1–3, p. 141-154.
Geisler, T., Schaltegger, U., and Tomaschek, F., 2007, Re-equilibration of Zircon in Aqueous Fluids and Melts: Elements, v. 3, no. 1, p. 43-50.
Geoscience Australia and Australian Stratigraphy Commission, 2017, Australian Stratigraphic Units Database (accessed February 2020).
Gin, S., Jollivet, P., Barba Rossa, G., Tribet, M., Mougnaud, S., Collin, M., Fournier, M., Cadel, E., Cabie, M., and Dupuy, L., 2017, Atom-Probe Tomography, TEM and ToF-SIMS study of borosilicate glass alteration rim: A multiscale approach to investigating rate-limiting mechanisms: Geochimica et Cosmochimica Acta, v. 202, p. 57-76.
Glass, B. P., Liu, S., and Leavens, P. B., 2002, Reidite: An impact-produced high-pressure polymorph of zircon found in marine sediments: American Mineralogist, v. 87, no. 4, p. 562-565.
Gomer, R., 1994, Field emission, field ionization, and field desorption: Surface Science, v. 299-300, p. 129-152.
Gouné, M., Danoix, F., Ågren, J., Bréchet, Y., Hutchinson, C. R., Militzer, M., Purdy, G., van der Zwaag, S., and Zurob, H., 2015, Overview of the current issues in austenite to ferrite transformation and the role of migrating interfaces therein for low alloyed steels: Materials Science and Engineering: R: Reports, v. 92, p. 1-38.
Gray, M. B., and Zeitler, P. K., 1997, Comparison of clastic wedge provenance in the Appalachian foreland using U/Pb ages of detrital zircons: Tectonics, v. 16, no. 1, p. 151-160.
Griffith, W. P., 1970, Raman studies on rock-forming minerals. Part II. Minerals containing MO_3, MO_4, and MO_6 groups: Journal of the Chemical Society A: Inorganic, Physical, Theoretical, p. 286-291.
Gucsik, A., Koeberl, C., Brandstätter, F., Libowitzky, E., and Reimold, W. U., 2004, Cathodoluminescence, Electron Microscopy, and Raman Spectroscopy of Experimentally Shock Metamorphosed Zircon Crystals and Naturally Shocked Zircon from the Ries Impact Crater, *in* Dypvik, H., Burchell, M. J., and Claeys, P., eds., Cratering in Marine Environments and on Ice: Berlin, Springer, p. 281-322.
Haba, M. K., Yamaguchi, A., Horie, K., and Hidaka, H., 2014, Major and trace elements of zircons from basaltic eucrites: Implications for the formation of zircons on the eucrite parent body: Earth and Planetary Science Letters, v. 387, p. 10-21.
Harley, S. L., and Kelly, N. M., 2007, Zircon Tiny but Timely: Elements, v. 3, no. 1, p. 13-18.

Hinton, R. W., and Upton, B. G. J., 1991, The chemistry of zircon: Variations within and between large crystals from syenite and alkali basalt xenoliths: Geochimica et Cosmochimica Acta, v. 55, no. 11, p. 3287-3302.
Hoskin, P. W. O., 2005, Trace-element composition of hydrothermal zircon and the alteration of Hadean zircon from the Jack Hills, Australia: Geochimica et Cosmochimica Acta, v. 69, no. 3, p. 637-648.
Hoskin, P. W. O., and Black, L. P., 2000, Metamorphic zircon formation by solid-state recrystallization of protolith igneous zircon: Journal of Metamorphic Geology, v. 18, no. 4, p. 423-439.
Hoskin, P. W. O., Kinny, P. D., Wyborn, D., and Chappell, B. W., 2000, Identifying Accessory Mineral Saturation during Differentiation in Granitoid Magmas: an Integrated Approach: Journal of Petrology, v. 41, no. 9, p. 1365-1396.
Hoskin, P. W. O., and Schaltegger, U., 2003, The composition of zircon and igneous and metamorphic petrogenesis, *in* Hanchar, J. M., and Hoskin, P. W. O., eds., Zircon, Volume 53: Washington, DC, The Mineralogical Society of America, p. 27-62.
Hutchison, R., 2006, Meteorites: a petrologic, chemical, and isotopic synthesis, New York, Cambridge University Press.
Iizuka, T., Yamaguchi, T., Hibiya, Y., and Amelin, Y., 2015, Meteorite zircon constraints on the bulk Lu-Hf isotope composition and early differentiation of the Earth: Proceedings of the National Academy of Sciences of the United States of America, v. 112, no. 17, p. 5331-5336.
Ireland, T. R., and Wlotzka, F., 1992, The oldest zircons in the solar system: Earth and Planetary Science Letters, v. 109, no. 1, p. 1-10.
Johnstone, G. S., and Mykura, W., 1989, British Regional Geology: Northern Highlands of Scotland: London, UK, p. 219.
Jourdan, F., Benedix, G., Eroglu, E., Bland, P. A., and Bouvier, A., 2014, 40Ar/39Ar impact ages and time–temperature argon diffusion history of the Bunburra Rockhole anomalous basaltic achondrite: Geochimica et Cosmochimica Acta, v. 140, p. 391-409.
Karahka, M., and Kreuzer, H. J., 2015, Field evaporation of insulators and semiconductors: Theoretical insights for ZnO: Ultramicroscopy, v. 159, p. 156-161.
Kellogg, G. L., and Tsong, T. T., 1980, Pulsed-laser atom-probe field-ion microscopy: Journal of Applied Physics, v. 51, no. 2, p. 1184-1193.
Kelly, T. F., Camus, P. P., Larson, D. J., Holzman, L. M., and Bajikar, S. S., 1996, On the many advantages of local-electrode atom probes: Ultramicroscopy, v. 62, no. 1, p. 29-42.
Kelly, T. F., Gribb, T. T., Olson, J. D., Martens, R. L., Shepard, J. D., Wiener, S. A., Kunicki, T. C., Ulfig, R. M., Lenz, D. R., Strennen, E. M., Oltman, E., Bunton, J. H., and Strait, D. R., 2004, First data from a commercial local electrode atom probe (LEAP): Microscopy and Microanalysis, v. 10, no. 3, p. 373-383.
Kelly, T. F., and Larson, D. J., 2012, Atom Probe Tomography 2012: Annual Review of Materials Research, v. 42, no. 1, p. 1-31.
Kohn, M. J., Corrie, S. L., and Markley, C., 2015, The fall and rise of metamorphic zircon: American Mineralogist, v. 100, no. 4, p. 897-908.
Krapez, B., and Barley, M. E., 1987, Archaean strike-slip faulting and related ensialic basins: Evidence from the Pilbara Block, Australia: Geological Magazine, v. 124, no. 6, p. 555-567.

Kusaba, K., Syono, Y., Kikuchi, M., and Fukuoka, K., 1985, Shock behavior of zircon: phase transition to scheelite structure and decomposition: Earth and Planetary Science Letters, v. 72, no. 4, p. 433-439.
Kusaba, K., Yagi, T., Kikuchi, M., and Syono, Y., 1986, Structural considerations on the mechanism of the shock-induced zircon-scheelite transition in ZrSiO4: Journal of Physics and Chemistry of Solids, v. 47, no. 7, p. 675-679.
Kusiak, M. A., Dunkley, D. J., Wirth, R., Whitehouse, M. J., Wilde, S. A., and Marquardt, K., 2015, Metallic lead nanospheres discovered in ancient zircons: Proceedings of the National Academy of Sciences, v. 112, no. 16, p. 4958-4963.
La Fontaine, A., Piazolo, S., Trimby, P., Yang, L., and Cairney, J. M., 2017, Laser-Assisted Atom Probe Tomography of Deformed Minerals: A Zircon Case Study: Microscopy and Microanalysis, p. 1-10.
Langenhorst, F., and Deutsch, A., 2012, Shock metamorphism of minerals: Elements, no. 1, p. 31-36.
Larson, D. J., Gault, B., Geiser, B. P., De Geuser, F., and Vurpillot, F., 2013a, Atom probe tomography spatial reconstruction: Status and directions: Current Opinion in Solid State and Materials Science, v. 17, no. 5, p. 236-247.
Larson, D. J., Prosa, T. J., Ulfig, R. M., Geiser, B. P., and Kelly, T. F., 2013b, Local Electrode Atom Probe Tomography: A user's guide: New York, Springer, p. 318.
Lawson, D. E., 1972, Torridonian volcanic sediments: Scottish Journal of Geology, v. 8, no. 4, p. 345-362.
Lee, J. K. W., 1995, Multipath diffusion in geochronology: Contributions to Mineralogy and Petrology, v. 120, no. 1, p. 60-82.
Lee, J. K. W., and Tromp, J., 1995, Self-induced fracture generation in zircon: Journal of Geophysical Research: Solid Earth, v. 100, no. B9, p. 17753-17770.
Lee, J. K. W., and Williams, I. S., 1993, Microstructural controls on U-Pb mobility in zircons, Volume 74: Washington, DC, Washington, DC, United States: American Geophysical Union, p. 650-651.
Leroux, H., Reimold, W. U., Koeberl, C., Hornemann, U., and Doukhan, J. C., 1999, Experimental shock deformation in zircon: a transmission electron microscopic study: Earth and Planetary Science Letters, v. 169, no. 3, p. 291-301.
Lodders, K., 2003, Solar system abundances and condensation temperatures of the elements: The Astrophysical Journal, v. 591, no. 2, p. 1220-1247.
Ludwig, K., 2009, SQUID 2: A user's manual: Berkeley Geochronology Center Special Publication No. 5, p. 110.
-, 2012, User's manual for Isoplot 3.75: A geochronological toolkit for microsoft excel: Berkeley Geochronology Center Special Publication No. 5, p. 75.
Lyon, I. C., Kusiak, M. A., Wirth, R., Whitehouse, M. J., Dunkley, D. J., Wilde, S. A., Schaumlöffel, D., Malherbe, J., and Moore, K. L., 2019, Pb nanospheres in ancient zircon yield model ages for zircon formation and Pb mobilization: Scientific reports, v. 9, no. 1, p. 13702.
Ma, C., and Rossman, G. R., 2005, Microanalysis of Hafnian Zircon: Microscopy and Microanalysis, v. 11, no. S02, p. 1304-1305.
Martin, L. A. J., Duchêne, S., Deloule, E., and Vanderhaeghe, O., 2008, Mobility of trace elements and oxygen in zircon during metamorphism: Consequences for

geochemical tracing: Earth and Planetary Science Letters, v. 267, no. 1–2, p. 161-174.
Marvin, U. B., and Klein, C., 1964, Meteoritic Zircon: Science, v. 146, no. 3646, p. 919-920.
Mattinson, J. M., Graubard, C. M., Parkinson, D. L., and McClelland, W. C., 1996, U-Pb Reverse Discordance in Zircons: The Role of Fine-Scale Oscillatory Zoning and Sub-Micron Transport of Pb, *in* Basu, A., and Hart, S., eds., Earth Processes: Reading the Isotopic Code: USA, American Geophysical Union, p. 437.
McComb, D. W., Brydson, R., Hansen, P. L., and Payne, R. S., 1992, Qualitative interpretation of electron energy-loss near-edge structure in natural zircon: Journal of Physics: Condensed Matter, v. 4, no. 43, p. 8363-8374.
McSween, H. Y., 1999, Meteorites and their parent planets, New York, Cambridge University Press, p. 310.
McSween Jr, H. Y., Mittlefehldt, D. W., Russell, C. T., and Raymond, C. A., 2013, Overview of the composition of asteroid 4 Vesta: Constraints from the Dawn spacecraft mission and HEDs: Meteoritics & Planetary Science, v. 48, no. 11, p. 2073-2075.
Melosh, H. J., 1989, Impact Cratering: A Geologic Process: New York, USA, Oxford University Press, p. 245.
Meredith, P., 2007, An investigation of chemical mobility and variability within a metamict zircon from the Georgeville Granite, Nova Scotia, using ToF-SIMS, Atlantic Universities Geological Conference, Volume 43, Atlantic Geology, p. 117-118.
Miller, M. K., 1986, Atom probe field ion microscopy, Annual joint meeting of the Electron Microscopy Society of America and the Microbeam Analysis Society: Albuquerque, NM (USA).
Miller, M. K., and Forbes, R. G., 2009, Atom probe tomography: Materials Characterization, v. 60, no. 6, p. 461-469.
Miller, M. K., and Forbes, R. G., 2014, Atom-probe tomography: The local electrode atom probe: New York, Springer, p. 423.
Misawa, K., Yamaguchi, A., and Kaiden, H., 2005, U-Pb and 207Pb-206Pb ages of zircons from basaltic eucrites: Implications for early basaltic volcanism on the eucrite parent body: Geochimica et Cosmochimica Acta, v. 69, no. 24, p. 5847-5861.
Montalvo, S. D., Reddy, S. M., Saxey, D. W., Rickard, W. D. A., Fougerouse, D., Quadir, Z., and Johnson, T. E., 2019, Nanoscale constraints on the shock-induced transformation of zircon to reidite: Chemical Geology, v. 507, p. 85-95.
Moser, D. E., Arcuri, G. A., Reinhard, D. A., White, L. F., Darling, J. R., Barker, I. R., Larson, D. J., Irving, A. J., McCubbin, F. M., Tait, K. T., Roszjar, J., Wittmann, A., and Davis, C., 2019, Decline of giant impacts on Mars by 4.48 billion years ago and an early opportunity for habitability: Nature Geoscience, v. 12, no. 7, p. 522-527.
Moser, D. E., Chamberlain, K. R., Tait, K. T., Schmitt, A. K., Darling, J. R., Barker, I. R., and Hyde, B. C., 2013, Solving the Martian meteorite age conundrum using micro-baddeleyite and launch-generated zircon: Nature, v. 499, no. 7459, p. 454.
Müller, E. W., 1956, Field Desorption: Physical Review, v. 102, no. 3, p. 618-624.

Müller, E. W., Panitz, J. A., and McLane, S. B., 1968, The Atom-Probe Field Ion Microscope: Review of Scientific Instruments, v. 39, no. 1, p. 83-86.
Münker, C., Pfänder, J. A., Weyer, S., Büchl, A., Kleine, T., and Mezger, K., 2003, Evolution of Planetary Cores and the Earth-Moon System from Nb/Ta Systematics: Science, v. 301, no. 5629, p. 84-87.
Murakami, T., Chakoumakos, B. C., Ewing, R. C., Lumpkin, G. R., and Weber, W. J., 1991, Alpha-decay event damage in zircon: American Mineralogist, v. 76, p. 1510-1532.
Nasdala, L., Irmer, G., and Wolf, D., 1995, The degree of metamictization in zircon: a Raman spectroscopic study: European Journal of Mineralogy, v. 7, no. 3, p. 471-478.
Nasdala, L., Lengauer, C. L., Hanchar, J. M., Kronz, A., Wirth, R., Blanc, P., Kennedy, A. K., and Seydoux-Guillaume, A.-M., 2002, Annealing radiation damage and the recovery of cathodoluminescence: Chemical Geology, v. 191, no. 1, p. 121-140.
Neves, J. M. C., Nunes, J. E. L., and Sahama, T. G., 1974, High hafnium members of the zircon-hafnon series from the granite pegmatites of Zambézia, Mozambique: Contributions to Mineralogy and Petrology, v. 48, no. 1, p. 73-80.
Nishikawa, O., and Kimoto, M., 1994, Toward a scanning atom probe — computer simulation of electric field: Applied Surface Science, v. 76-77, p. 424-430.
Ono, A., 1976, Chemistry and zoning of zircon from some Japanese granitic rocks: The Journal of the Japanese Association of Mineralogists, Petrologists and Economic Geologists, v. 71, no. 1, p. 6-17.
Panitz, J. A., 1973, The 10 cm Atom Probe: Review of Scientific Instruments, v. 44, no. 8, p. 1034-1038.
Parnell, J., Mark, D., Fallick, A. E., Boyce, A., and Thackrey, S., 2011, The age of the Mesoproterozoic Stoer Group sedimentary and impact deposits, NW Scotland: Journal of the Geological Society, v. 168, no. 2, p. 349-358.
Patzer, A., Pack, A., and Gerdes, A., 2010, Zirconium and hafnium in meteorites: Meteoritics & Planetary Science, v. 45, no. 7, p. 1136-1151.
Peterman, E. M., Reddy, S. M., Saxey, D. W., Fougerouse, D., Snoeyenbos, D. R., and Rickard, W. D. A., 2019, Nanoscale processes of trace element mobility in metamorphosed zircon: Contributions to Mineralogy and Petrology, v. 174, no. 11, p. 92.
Peterman, E. M., Reddy, S. M., Saxey, D. W., Snoeyenbos, D. R., Rickard, W. D. A., Fougerouse, D., and Kylander-Clark, A. R. C., 2016, Nanogeochronology of discordant zircon measured by atom probe microscopy of Pb-enriched dislocation loops: Science Advances, v. 2, p. 9.
Piazolo, S., Austrheim, H., and Whitehouse, M., 2012, Brittle-ductile microfabrics in naturally deformed zircon: Deformation mechanisms and consequences for U-Pb dating: American Mineralogist, v. 97, no. 10, p. 1544-1563.
Piazolo, S., La Fontaine, A., Trimby, P., Harley, S., Yang, L., Armstrong, R., and Cairney, J. M., 2016, Deformation-induced trace element redistribution in zircon revealed using atom probe tomography: Nature Communications, p. 7.
Pidgeon, R. T., Nemchin, A. A., and Cliff, J., 2013, Interaction of weathering solutions with oxygen and U–Pb isotopic systems of radiation-damaged zircon from an Archean granite, Darling Range Batholith, Western Australia: Contributions to Mineralogy and Petrology, v. 166, no. 2, p. 511-523.

Pidgeon, R. T., Nemchin, A. A., Roberts, M. P., Whitehouse, M. J., and Bellucci, J. J., 2019, The accumulation of non-formula elements in zircons during weathering: Ancient zircons from the Jack Hills, Western Australia: Chemical Geology, v. 530, p. 119310.

Pond, R. C., Celotto, S., and Hirth, J. P., 2003, A comparison of the phenomenological theory of martensitic transformations with a model based on interfacial defects: Acta Materialia, v. 51, no. 18, p. 5385-5398.

Priester, L., 2001, "Dislocation–interface" interaction — stress accommodation processes at interfaces: Materials Science and Engineering: A, v. 309-310, p. 430-439.

Rainbird, R. H., Hamilton, M. A., and Young, G. M., 2001, Detrital zircon geochronology and provenance of the Torridonian, NW Scotland: Journal of the Geological Society, v. 158, no. 1, p. 15-27.

Rayman, M. D., and Mase, R. A., 2014, Dawn′s exploration of Vesta: Acta Astronautica, v. 94, no. 1, p. 159-167.

Reddy, S. M., Johnson, T. E., Fischer, S., Rickard, W. D. A., and Taylor, R. J. M., 2015, Precambrian reidite discovered in shocked zircon from the Stac Fada impactite, Scotland: Geology, v. 43, no. 10, p. 899-902.

Reddy, S. M., Saxey, D. W., Rickard, W. D. A., Fougerouse, D., Montalvo, S. D., Verberne, R., and van Riessen, A., 2020, Atom probe tomography: development and application to the geosciences: Geostandards and Geoanalytical Research, v. 44, no. 1, p. 5-50.

Reddy, S. M., Timms, N. E., Pantleon, W., and Trimby, P., 2007, Quantitative characterization of plastic deformation of zircon and geological implications: Contributions to Mineralogy and Petrology, v. 153, no. 6, p. 625-645.

Reddy, S. M., Timms, N. E., Trimby, P., Kinny, P. D., Buchan, C., and Blake, K., 2006, Crystal-plastic deformation of zircon: A defect in the assumption of chemical robustness: Geology, v. 34, no. 4, p. 257-260.

Reddy, S. M., van Riessen, A., Saxey, D. W., Johnson, T. E., Rickard, W. D. A., Fougerouse, D., Fischer, S., Prosa, T. J., Rice, K. P., Reinhard, D. A., Chen, Y., and Olson, D., 2016, Mechanisms of deformation-induced trace element migration in zircon resolved by atom probe and correlative microscopy: Geochimica et Cosmochimica Acta, v. 195, p. 158-170.

Reid, A. F., and Ringwood, A. E., 1969, Newly observed high pressure transformations in Mn_3O_4, $CaAl_2O_4$, and $ZrSiO_4$: Earth and Planetary Science Letters, v. 6, no. 3, p. 205-208.

Reimold, W. U., and Gibson, R. L., 2009, Meteorite Impact! The Danger from Space and South Africa's Mega-Impact The Vredefort Structure, Berlin, Heidelberg, Springer, p. 337.

Reinhard, D. A., Moser, D. E., Martin, I., Rice, K. P., Chen, Y., Olson, D., Lawrence, D., Prosa, T. J., and Larson, D. J., 2018, Atom Probe Tomography of Phalaborwa Baddeleyite and Reference Zircon BR266, *in* Moser, D. E., Corfu, F., Darling, J. R., Reddy, S. M., and Tait, K., eds., Microstructural Geochronology: Planetary Records Down to Atom Scale, American Geophysical Union & John Wiley and Sons, Inc., p. 315-326.

Romer, R. L., 2003, Alpha-recoil in U–Pb geochronology: effective sample size matters: Contributions to Mineralogy and Petrology, v. 145, no. 4, p. 481-491.

Roszjar, J., Whitehouse, M. J., and Bischoff, A., 2014, Meteoritic zircon – Occurrence and chemical characteristics: Chemie der Erde - Geochemistry, v. 74, no. 3, p. 453-469.
Rout, S. S., Heck, P. R., Isheim, D., Stephan, T., Zaluzec, N. J., Miller, D. J., Davis, A. M., and Seidman, D. N., 2017, Atom-probe tomography and transmission electron microscopy of the kamacite–taenite interface in the fast-cooled Bristol IVA iron meteorite: Meteoritics & Planetary Science, v. 52, no. 12, p. 2707-2729.
Rubatto, D., 2017, Zircon: The Metamorphic Mineral: Reviews in Mineralogy and Geochemistry, v. 83, no. 1, p. 261-295.
Sanders, I. S., and Johnston, J. D., 1989, The Torridonian Stac Fada Member: an extrusion of fluidised peperite?: Transactions of the Royal Society of Edinburgh: Earth Sciences, v. 80, no. 1, p. 1-4.
Saxey, D. W., Moser, D. E., Piazolo, S., Reddy, S. M., and Valley, J. W., 2018a, Atomic worlds: Current state and future of atom probe tomography in geoscience: Scripta Materialia, p. 115-121.
Saxey, D. W., Reddy, S. M., Fougerouse, D., and Rickard, W. D. A., 2018b, The Optimization of Zircon Analyses by Laser-Assisted Atom Probe Microscopy: Insights from the 91500 Zircon Standard, *in* Moser, D. E., Corfu, F., Darling, J. R., Reddy, S. M., and Tait, K., eds., Microstructural Geochronology: Planetary Records down to Atom Scale, American Geophysical Union & John Wiley and Sons, Inc., p. 293-313.
Saxey, D. W., Fougerouse, D., Rickard, W. D. A., and Reddy, S., 2019, Spatial Reconstruction of Atom Probe Data from Zircon: Microscopy and Microanalysis, v. 25, p. 2536-2537.
Schwartz, J. J., John, B. E., Cheadle, M. J., Wooden, J. L., Mazdab, F., Swapp, S., and Grimes, C. B., 2010, Dissolution–reprecipitation of igneous zircon in mid-ocean ridge gabbro, Atlantis Bank, Southwest Indian Ridge: Chemical Geology, v. 274, no. 1–2, p. 68-81.
Scott, E. R. D., Greenwood, R. C., Franchi, I. A., and Sanders, I. S., 2009, Oxygen isotopic constraints on the origin and parent bodies of eucrites, diogenites, and howardites: Geochimica et Cosmochimica Acta, v. 73, no. 19, p. 5835-5853.
Seydoux-Guillaume, A. M., Fougerouse, D., Laurent, A. T., Gardés, E., Reddy, S. M., and Saxey, D. W., 2019, Nanoscale resetting of the Th/Pb system in an isotopically-closed monazite grain: A combined atom probe and transmission electron microscopy study: Geoscience Frontiers, v. 10, no. 1, p. 65-76.
Silver, L. T., and Deutsch, S., 1963, Uranium-Lead Isotopic Variations in Zircons: A Case Study: The Journal of Geology, v. 71, no. 6, p. 721-758.
Simms, M. J., 2015, The Stac Fada impact ejecta deposit and the Lairg Gravity Low: evidence for a buried Precambrian impact crater in Scotland?: Proceedings of the Geologists' Association, v. 126, no. 6, p. 742-761.
Skrotzki, W., 1994, Dislocation-interface interactions in exsolved augite: Materials Science and Engineering: A, v. 175, no. 1, p. 149-158.
Sliwinski, J. T., Kueter, N., Marxer, F., Ulmer, P., Guillong, M., and Bachmann, O., 2018, Controls on lithium concentration and diffusion in zircon: Chemical Geology, v. 501, p. 1-11.
Spanos, G., and Aaronson, H. I., 1990, The interfacial structure and habit plane of proeutectoid cementite plates: Acta Metallurgica et Materialia, v. 38, no. 12, p. 2721-2732.

Speer, J. A., 1980, Zircon: Reviews in Mineralogy and Geochemistry, v. 5, no. 1, p. 67-112.
Spivak-Birndorf, L. J., Bouvier, A., Benedix, G. K., Hammond, S., Brennecka, G. A., Howard, K., Rogers, N., Wadhwa, M., Bland, P. A., Spurný, P., and Towner, M. C., 2015, Geochemistry and chronology of the Bunburra Rockhole ungrouped achondrite: Meteoritics & Planetary Science, v. 50, no. 5, p. 958-975.
Spurný, P., Bland, P. A., Shrbený, L., Borovička, J., Ceplecha, Z., Singelton, A., Bevan, A. W. R., Vaughan, D., Towner, M. C., McClafferty, T. P., Toumi, R., and Deacon, G., 2012, The Bunburra Rockhole meteorite fall in SW Australia: fireball trajectory, luminosity, dynamics, orbit, and impact position from photographic and photoelectric records: Meteoritics & Planetary Science, v. 47, no. 2, p. 163-185.
Stacey, J. S., and Kramers, J. D., 1975, Approximation of terrestrial lead isotope evolution by a two-stage model: Earth and Planetary Science Letters, v. 26, no. 2, p. 207-221.
Stephan, T., 2001, TOF-SIMS in cosmochemistry: Planetary and Space Science, v. 49, no. 9, p. 859-906.
Stern, R. A., Bodorkos, S., Kamo, S. L., Hickman, A. H., and Corfu, F., 2009, Measurement of SIMS Instrumental Mass Fractionation of Pb Isotopes During Zircon Dating: Geostandards and Geoanalytical Research, v. 33, no. 2, p. 145-168.
Stern, R. A., Fletcher, I. R., Rasmussen, B., McNaughton, N. J., and Griffin, B. J., 2005, Ion microprobe (NanoSIMS 50) Pb-isotope geochronology at <5μm scale: International Journal of Mass Spectrometry, v. 244, no. 2, p. 125-134.
Stewart, A. D., 1988, The Stoer Group, Scotland, *in* Winchester, J. A., ed., Later Proterozoic Stratigraphy of the Northern Atlantic Regions: Glasgow, Blackie and Son Ltd., p. 97-103.
-, 2002, The Later Proterozoic Torridonian Rocks of Scotland: Their Sedimentology, Geochemistry and Origin, Geological society memoirs: UK, Geological Society of London, p. 130.
Stüeken, E. E., and Buick, R., 2018, Environmental control on microbial diversification and methane production in the Mesoarchean: Precambrian Research, v. 304, p. 64-72.
Svoboda, J., Fischer, F. D., and Gamsjäger, E., 2002, Influence of solute segregation and drag on properties of migrating interfaces: Acta Materialia, v. 50, no. 5, p. 967-977.
Takeda, H., 1997, Mineralogical records of early planetary processes on the howardite, eucrite, diogenite parent body with reference to Vesta: Meteoritics & Planetary Science, v. 32, no. 6, p. 841-853.
Tanabe, K., and Hiraishi, J., 1980, Correction of finite slit width effects on Raman line widths: Spectrochimica Acta Part A: Molecular Spectroscopy, v. 36, no. 4, p. 341-344.
Tange, Y., and Takahashi, E., 2004, Stability of the high-pressure polymorph of zircon ($ZrSiO_4$) in the deep mantle: Physics of the Earth and Planetary Interiors, v. 143-144, p. 223-229.
Taylor, S. D., Liu, J., Zhang, X., Arey, B. W., Kovarik, L., Schreiber, D. K., Perea, D. E., and Rosso, K. M., 2019, Visualizing the iron atom exchange front in the Fe(II)-catalyzed recrystallization of goethite by atom probe tomography:

Proceedings of the National Academy of Sciences, v. 116, no. 8, p. 2866-2874.
Tennent, R. M., 1976, Science Data Book: UK, Oliver & Boyd, p. 104.
Thomson, O. A., Cavosie, A. J., Moser, D. E., Barker, I., Radovan, H. A., and French, B. M., 2014, Preservation of detrital shocked minerals derived from the 1.85 Ga Sudbury impact structure in modern alluvium and Holocene glacial deposits: GSA Bulletin, v. 126, no. 5-6, p. 720-737.
Tilton, G. R., Patterson, C., Brown, H., Inghram, M., Hayden, R., Hess, D., and Larsen, A. J., 1955, Isotopic composition and distribution of lead, Uranium, and Thorium in a Precambrian granite: GSA Bulletin, v. 66, no. 9, p. 1131-1148.
Timms, N. E., Erickson, T. M., Pearce, M. A., Cavosie, A. J., Schmieder, M., Tohver, E., Reddy, S. M., Zanetti, M. R., Nemchin, A. A., and Wittmann, A., 2017a, A pressure-temperature phase diagram for zircon at extreme conditions: Earth-Science Reviews, v. 165, p. 185-202.
Timms, N. E., Erickson, T. M., Zanetti, M. R., Pearce, M. A., Cayron, C., Cavosie, A. J., Reddy, S. M., Wittmann, A., and Carpenter, P. K., 2017b, Cubic zirconia in >2370 °C impact melt records Earth's hottest crust: Earth and Planetary Science Letters, v. 477, p. 52-58.
Timms, N. E., Kinny, P. D., and Reddy, S. M., 2006, Enhanced diffusion of Uranium and Thorium linked to crystal plasticity in zircon: Geochemical Transactions, v. 7, no. 1, p. 10.
Timms, N. E., and Reddy, S. M., 2009, Response of cathodoluminescence to crystal-plastic deformation in zircon: Chemical Geology, v. 261, no. 1–2, p. 12-24.
Tomaschek, F., Kennedy, A. K., Villa, I. M., Lagos, M., and Ballhaus, C., 2003, Zircons from Syros, Cyclades, Greece—Recrystallization and Mobilization of Zircon During High-Pressure Metamorphism: Journal of Petrology, v. 44, no. 11, p. 1977-2002.
Trinquier, A., Birck, J. L., and Allegre, C. J., 2007, Widespread ^{54}Cr Heterogeneity in the Inner Solar System: The Astrophysical Journal, v. 655, no. 2, p. 1179-1185.
U.S. Geological Survey, 2006, GDC Digital Cartographic Standard for Geologic Map Symbolization (available at http://pubs.usgs.gov/tm/2006/11A02/).
Ushikubo, T., Kita, N. T., Cavosie, A. J., Wilde, S. A., Rudnick, R. L., and Valley, J. W., 2008, Lithium in Jack Hills zircons: Evidence for extensive weathering of Earth's earliest crust: Earth and Planetary Science Letters, v. 272, no. 3–4, p. 666-676.
Utsunomiya, S., Palenik, C. S., Valley, J. W., Cavosie, A. J., Wilde, S. A., and Ewing, R. C., 2004, Nanoscale occurrence of Pb in an Archean zircon: Geochimica et Cosmochimica Acta, v. 68, no. 22, p. 4679-4686.
Valley, J. W., Cavosie, A. J., Ushikubo, T., Reinhard, D. A., Lawrence, D. F., Larson, D. J., Clifton, P. H., Kelly, T. F., Wilde, S. A., Moser, D. E., and Spicuzza, M. J., 2014, Hadean age for a post-magma-ocean zircon confirmed by atom-probe tomography: Nature Geoscience, v. 7, no. 3, p. 219-223.
Valley, J. W., Reinhard, D. A., Cavosie, A. J., Ushikubo, T., Lawrence, D. F., Larson, D. J., Kelly, T. F., Snoeyenbos, D. R., and Strickland, A., 2015, Nano- and micro-geochronology in Hadean and Archean zircons by atom-probe tomography and SIMS: New tools for old minerals: American Mineralogist, v. 100, no. 7, p. 1355-1377.

Van Kranendonk, M., 2008, Structural geology of the central part of the Lalla Rookh - Western Shaw structural corridor, Pilbara Craton, Western Australia Geological Survey of Western Australia, p. 29.
Van Kranendonk, M. J., Hickman, A. H., Smithies, R. H., Nelson, D. R., and Pike, G., 2002, Geology and Tectonic Evolution of the Archean North Pilbara Terrain, Pilbara Craton, Western Australia: Economic Geology, v. 97, no. 4, p. 695-732.
Vonlanthen, P., Fitz Gerald, J. D., Rubatto, D., and Hermann, J., 2012, Recrystallization rims in zircon (Valle d'Arbedo, Switzerland): An integrated cathodoluminescence, LA-ICP-MS, SHRIMP, and TEM study: American Mineralogist, v. 97, no. 2-3, p. 369-377.
Weber, J., Barthel, J., Brandt, F., Klinkenberg, M., Breuer, U., Kruth, M., and Bosbach, D., 2016, Nano-structural features of barite crystals observed by electron microscopy and atom probe tomography: Chemical Geology, v. 424, p. 51-59.
Weisberg, M. K., Smith, C., Benedix, G., Folco, L., Righter, K., Zipfel, J., Yamaguchi, A., and Chennaoui Aoudjehane, H., 2009, The Meteoritical Bulletin, No. 95: Meteoritics & Planetary Science, v. 44, no. 3, p. 429-462.
Welten, K. C., Meier, M. M. M., Caffee, M. W., Laubenstein, M., Nishizumi, K., Wieler, R., Bland, P. A., Towner, M. C., and Spurný, P., 2012, Cosmic-ray exposure age and preatmospheric size of the Bunburra Rockhole achondrite: Meteoritics & Planetary Science, v. 47, no. 2, p. 186-196.
Wheeler, J., Park, R. G., Rollinson, H. R., and Beach, A., 2010, The Lewisian Complex: insights into deep crustal evolution: Geological Society, London, Special Publications, v. 335, no. 1, p. 51-79.
White, L. F., Darling, J. R., Moser, D. E., Reinhard, D. A., Prosa, T. J., Bullen, D., Olson, D., Larson, D. J., Lawrence, D., and Martin, I., 2017, Atomic-scale age resolution of planetary events: Nature Communications, v. 8, p. 15597.
White, L. F., Moser, D. E., Tait, K. T., Langelier, B., Barker, I., and Darling, J. R., 2019, Crystallization and impact history of a meteoritic sample of early lunar crust (NWA 3163) refined by atom probe geochronology: Geoscience Frontiers, v. 10, no. 5, p. 1841-1848.
Wilde, S. A., Valley, J. W., Peck, W. H., and Graham, C. M., 2001, Evidence from detrital zircons for the existence of continental crust and oceans on the Earth 4.4 Gyr ago: Nature, v. 409, p. 175.
Wittmann, A., Kenkmann, T., Schmitt, R. T., and Stöffler, D., 2006, Shock-metamorphosed zircon in terrestrial impact craters: Meteoritics & Planetary Science, v. 41, no. 3, p. 433-454.
Yang, W., Lin, Y.-T., Zhang, J.-C., Hao, J.-L., Shen, W.-J., and Hu, S., 2012, Precise micrometre-sized Pb-Pb and U-Pb dating with NanoSIMS: Journal of Analytical Atomic Spectrometry, v. 27, no. 3, p. 479-487.
Young, G. M., 2002, Stratigraphy and geochemistry of volcanic mass flows in the Stac Fada Member of the Stoer Group, Torridonian, NW Scotland: Transactions of the Royal Society of Edinburgh: Earth Sciences, v. 93, no. 1, p. 1-16.
Zhang, W. Z., and Weatherly, G. C., 2005, On the crystallography of precipitation: Progress in Materials Science, v. 50, no. 2, p. 181-292.

Every reasonable effort has been made to acknowledge the owners of copyright material. I would be pleased to hear from any copyright owner who has been omitted or incorrectly acknowledged.